PEROVSKITE SOLAR CELL FOR GREENHOUSE APPLICATIONS

LINDA YEN-CHIEN CHEN
MPhil, **University of Auckland, 2014**

A thesis submitted
in partial fulfilment of the requirements for the degree of

DOCTOR OF PHILOSOPHY

In

ELECTRICAL AND COMPUTER ENGINEERING

Department of Electrical and Computer Engineering
University of Canterbury
CHRISTCHURCH, NEW ZEALAND

Abstract

Greenhouse with the rooftop semi-transparent solar cell is a better way of controlling plantation environmental conditions with reduced electricity costs without utilizing extra land for solar panel installation. However, the semi-transparent thin film solar cells that are suitable for rooftop installation have low power conversion efficiency (PCE) and less stable when compared with silicon solar cells. The semi-transparent perovskite solar cell (PSC), with potential for high PCE, is suitable for rooftop electricity generation while allowing partial light to pass through.

Using PSCs with different colours for electricity generation allows light with a particular wavelength range to pass through for different plantation needs. This could be achieved either externally with nanostructures on the transparent substrate, or internally by modifying the perovskite thin film composition to tune the optical absorbance position with band gap tuning. Applying nanostructures on PSC can improve the device's performance by minimizing the reflected incident light. Besides, doping plasmonic nanoparticles within the nanostructures could increase absorbance at the particular wavelength range or blue-shifts incident light with a shorter wavelength depending on the nanoparticle size. Modifying the composition of the perovskite thin film is another way to achieve wavelength selectivity. While the occurrence of PL peak shiftings due to the change of anion concentrations within the perovskite composition has been reported by literature for perovskite solar cells, I/Br mixture, and Br/Cl mixture, there was no report on the full spectrum of caesium contained perovskite solar cell with various anion mixtures, including I/Cl mixture.

This research first looked into the possibility to fabricate the perovskite solar cell with the common semiconductor fabrication environment with little control over humidity. Different fabrication methods and conditions of each layer within the device have been experimented and characterised. The PCE of the fabricated device reached close to 10 %. A comparison of common performance results of the device fabricated without humidity control and with some of the humidity control has

been looked at to show the effect of humidity on the device.

The second part of the research looked into the application of nanoimprinted upright nanopyramids on perovskite solar cell for PCE improvement and the possibility of doping the UV curable resist with solvent based $Au_9(PPh_3)_8(NO_3)_3$ nanoclusters to form the nanopyramids with nanoclusters within the nanopyramids. The change in the nanostructure's physical and optical characteristics when it is doped with $Au_9(PPh_3)_8(NO_3)_3$ has been investigated. Moreover, the robustness of the nanopyramids and the long term stability of the nanostructure with or without $Au_9(PPh_3)_8(NO_3)_3$ have been studied. The maximum temperature for the nanostructures to maintain reasonable optical transmittance dropped from over 250 °C for undoped nanopyramids to less than 200 °C for $Au_9(PPh_3)_8(NO_3)_3$ doped nanopyramids.

The final part of this research studies the possibility of achieving wavelength selectivity by modifying anions in the composition of caesium contained triple cation PSC with the control sample based on the popular $Cs_{0.05}MAFAPb(Br_{0.17}I_{0.83})_3$ composition published by Saliba et al [1]. The result shows that increasing the Br concentration blue shifts the optical absorbance and the PL peak to wavelengths shorter than 550 nm. Sample with Br/Cl mixed anion further blue shifts the absorbance even further to wavelengths with 500 nm or even shorter. The spectral response of the devices incorporating different anion mixtures agrees with the UV-Vis absorbance spectrum and PL spectrum.

The research outcome shows that it is possible to achieve wavelength selectivity with the PSC, either by the application of nanopyramids on the device or by modifying the perovskite layer. Further optimization of the overall performance of the PSC is still required. The long term stability of the device also requires further investigation. Testing on the solar cell with the application of $Au_9(PPh_3)_8(NO_3)_3$ doped nanopyramids is needed to investigate the change in device PCE. The perovskite thin films of different anion concentrations need to be further optimized to find better ratios between the cations and anions for better electrical performance of the devices with different light wavelength range.

Acknowledgment

A lot of people offered assistance from time to time during my whole research period. Without their help, I do not think this research could work.

I would like to express my gratitude to my main supervisor, Professor Maan Alkaisi, for his guidance and support throughout the whole research. He has been very helpful during my experiments and offered suggestions for the research aspects that I have missed out on. At the same time, he gave me a lot of freedom to plan and decide what I would like to try out for my research. Furthermore, he has spent a lot of time carefully read through my writings and gave clear comments on where should be modified or elaborate and the reason for that. I would also like to thank my co-supervisor, Associate professor Martin Allen, for sharing some of his experimental tips and knowledge regarding Gallium oxide wide bandgap semiconductor (not exactly relevant to my research, but still an interesting topic to learn) whenever he drops by in the lab.

Many thanks to all other people at the Nanolaboratory, University of Canterbury, for offering assistance for my experiments. In particular, Research Engineer Gary Turner, for the training of the various complicated equipment and the background theory for the equipment. Moreover, he is the main helper in designing and constructing the glovebox. Great thanks to the laboratory technician, Helen Devereux, for the assistance in purchasing any chemicals and the spin coater for perovskite solar cell fabrications. I am also grateful to have Dr. Almaraj Peter Amalthas for teaching me interference lithography and nanoimprint lithography for the application of light trapping.

Many thanks to the people I worked with in the lab during working hours or after hours. Working with them makes my time in the laboratory exciting: Dr. Volker Nock, Postdoctoral research fellows Rebecca Soffe, Claude Meffan, Azadeth Hashemi and Ayelen Tayagui; Ph.D. students Yiling Sun, Caixia Hou, Sevgi Onal, Nicola Altenhuber, Christine Franke, and Miguel Reis; people who have completed their project and left: Dr. Alana Hyland, Dr. Louise Orcheston Finlay, Dr. Tobias Baldhoff, and Dr. Nor Abd Wahid.

I would also like to thank Dr. Siriluck Tesana and Associate Professor Vladimir Golovko at the Department of Physical and Chemical Science, University of Canterbury, for providing the synthesized gold nanoclusters for part of this research. Great thanks also to Professor Roger Reeves and his postdoc Dr. Rodrigo Martinez Gazoni, for their help on UV-Vis spectrometry and Photoluminescence spectrometry.

Great thanks to Associate Professor Geoff Waterhouse and his research fellow, Dr. Wan Ting Chen, for the help on using their UV-Vis spectrometry with an integrated sphere for nanopyramids optical

transmittance measurements. I would also like to thank Professor Jyh-Ming Ting, Professor Tsung-Fang Kuo, and Professor Peter Chen at the National Cheng Kung University, where I learned the initial basics of perovskite solar cells.

Many thanks to the Department of Electrical and Computer Engineering at the University of Canterbury, for the energetic and vibrant research atmosphere. I would also like to thank the administrator Deborah Eureti, for all the administration related works and her assistance on my dispute with the boarding house management company.

Finally, many thanks to my family for their support and encouragement during this period. Without their support, it is difficult to go through this whole research.

.

List of publication and presentations

4 Publication of conference proceeding

4.1 L. Y. Chen and M. M. Alkaisi, "Investigation of Nanopyramids coatings on Perovskite Solar Cell for Performance Enhancement", 2018 IEEE 7th World Conference on Photovoltaic Energy Conversion (WCPEC) (A Joint Conference of 45th IEEE PVSC, 28th PVSEC & 34th EU PVSEC), Waikoloa Village, HI, 2018, pp. 0472-0476, doi: 10.1109/PVSC.2018.8547970.

5 Conference presentations

5.1 **L. Y. Chen**, Siriluck Tesana, Vladimir B. Golovko, and M. M. Alkaisi, "Gold nanoclusters for solar cells applications", 9th International Conference on Advanced Materials and Nanotechnology (AMN9) , Wellington, New Zealand, Feb 10-14, 2019 (Oral presentation).

5.2 **L. Y. Chen**, Siriluck Tesana, Vladimir B. Golovko, and M. M. Alkaisi, "Nanopyramids with Gold nanoclusters", Materials@UC, Christchurch, New Zealand, Dec 3-4 (Poster presentation)

5.3 **L. Y. Chen** and M. M. Alkaisi, "Investigation of Nanopyramids coatings on Perovskite Solar Cell for Performance Enhancement", 2018 IEEE 7th World Conference on Photovoltaic Energy Conversion (WCPEC), Waikoloa Village, HI, June 10-15, 2018 (Poster presentation)

5.4 **L. Y. Chen** and M. M. Alkaisi, "Performance of MAPbI3 Based Perovskite Solar Cell Fabricated with Anti-solvent Method in Air", 2018 International Conference On Nanoscience and Nanotechnology (ICONN 2018), Wollongong, NSW, Australia, Jan 29-Feb 2, 2018 (Poster and short talk presentation)

5.5 **L. Y. Chen** and M. M. Alkaisi, "The effect of mesoporous TiO2 layer with 200nm particle size on perovskite solar cell performance" 8th International Conference on Advanced Materials and Nanotechnology (AMN8), Queenstown, New Zealand, Feb 12-16, 2017 (Poster presentation).

Contents

Figures

1. Introduction

Greenhouse plantation has always been a very useful way to control the conditions of growing environments for plants. However, an excess amount of electricity for heat generation is required to control the environment for plant growth, especially during the wintertime in cold climate places such as New Zealand. In consequence, a price surge in vegetables in the winter season can be observed. This can range from less than $4 per Kg in summer to over $10 per Kg in winter for tomatoes in retail shops [2] and less than $5 per Kg in summer to over $15 per Kg in winter for cucumbers [3].

Solar cell powered greenhouse can provide greenhouse the heat required without utilizing electricity from the grid, reducing the cost of greenhouse plantation. However, utilizing conventional silicon solar cells requires a huge land area to accommodate the electricity generation the greenhouse needs. If the cells are placed on top of the greenhouse structure, all light will be absorbed or reflected by silicon solar cells before reaching the plants in the greenhouse, resulting in plants not receiving the required light intensity and quality for their growth cycle. According to a comparison study

Thin film photovoltaics that is transparent or semi-transparent can overcome this kind of problem by allowing light with certain wavelengths that are not absorbed by the solar cells to pass on to plants. Light with wavelengths shorter than 525 nm and wavelength longer than 640 nm, for example, is essential for plant photosynthesis. Moreover, a recent study by P. Bombelli's research group revealed that there is an overall financial gain of 2.5 % when transparent amorphous silicon solar panels (with 8 % power conversion efficiency) are installed on the greenhouse rooftop. While, depending on the type of plants, there is a certain amount of yield loss in marketable biomass, the amount of protein in the plant has increased, and a redirection of plant metabolic energy toward tissues above ground can be seen. [4] However, the overall power conversion efficiency of these transparent photovoltaic is usually incomparable with conventional silicon cells. The emergence

of the perovskite solar cell since 2009 shows huge potential in overtaking the silicon solar cell in overall power conversion efficiency. The theoretical power conversion efficiency (PCE) of the perovskite solar cell is close to 31 % [5], which is very close to the 32 % PCE limit of the silicon solar cell [6].

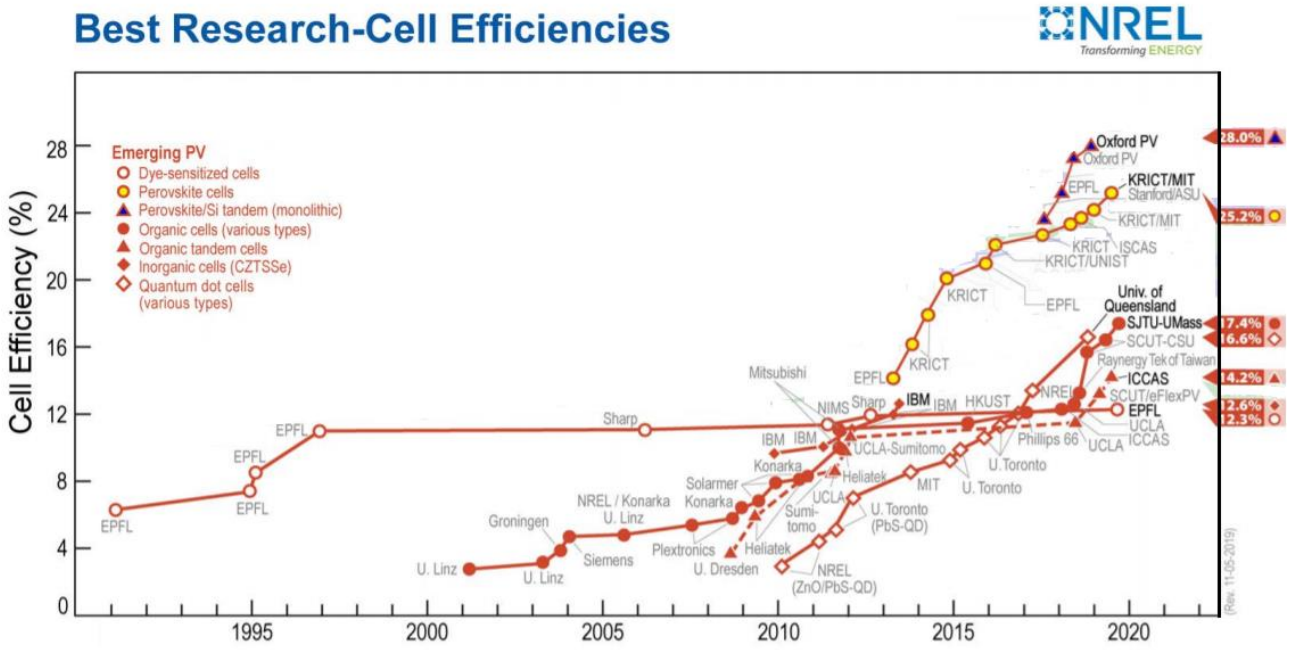

Figure 1-1 Progress in the performances of emerging photovoltaics. The recorded power conversion efficiency of the perovskite solar cell has reached over 25 %. This plot is courtesy of the National Renewable Energy Laboratory, Golden, CO [7].

Perovskite solar cell (PSC) is one of the third generation solar cells with tremendous potential in solar-electricity power conversion. It was first introduced by Miyasaka's research group in 2009 by using the hybrid organic-inorganic lead halide material with perovskite crystal structure as the active photon absorbing dye for Quantum dot dye sensitized solar cell (QDDSSC), resulting in a power conversion efficiency of 3.8 % [8]. However, little attention was given to this research outcome due to the poor stability of perovskite quantum dots in the liquid electrolyte. The power conversion efficiency of the device was later improved in 2012 to 9 % when the liquid electrolyte was replaced by the solid thin film of the hole transport layer for the solid-state dye sensitized solar cell [9]. While the operation mechanism of the dye sensitized solar cell is usually explained via the photoelectrochemical system approach, the perovskite solar cell system is usually explained with the semiconductor p-n junction approach. Since then, more researchers had started their

Perovskite solar cell research. The overall power conversion efficiency of PSC improved from 3.8 % to 21 % in 6 years [8, 10], with the most recent recorded best overall power conversion efficiency of 25.2 % for single-junction perovskite solar cells. Figure 1-1 shows the progress of PSC performances in comparison with other types of emerging photovoltaics.

Furthermore, the UV-Vis absorption spectra of PSC, as shown in Figure 1-2, indicated that PSC absorption in the visible light region (300 nm-700 nm) is relatively high, but it can be tuned according to the type of anions used. Noh et al. has compared samples with different iodine and bromine content with Methylammonium based perovskite solar cell and deduced that increasing the concentration of bromine in $MAPbI_3$ based perovskite results in a blue shift of optical absorbance. [11]

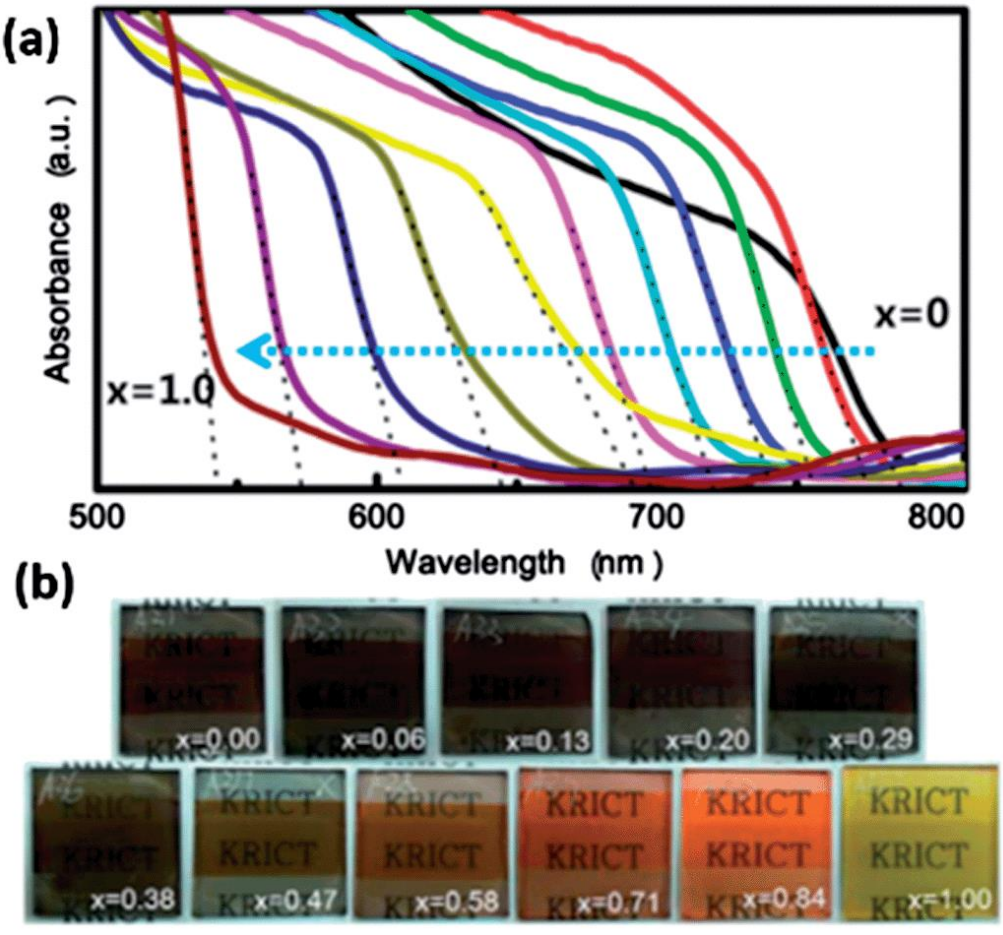

Figure 1-2 (a) UV-Vis wavelength absorbance at room temperature for $Pb(I_{(1-x)}Br_x)_3$, where $(I(1-x)Br_x)_3$ is the anion for PSC with different ratios of iodine and bromine (b) Sample images of $MAPb(I_{(1-x)}Br_x)_3$ thin film with different concentration of iodine and bromine on glass substrates. Reprinted with permission from Noh, J. H.; Im, S. H.; Heo, J. H.; Mandal, T. N.; Seok, S. I. *Nano Lett.* **2013,** 13, (4), 1764-1769. Copyright *© 2013* American Chemical Society [11].

This provides a possibility to let the light pass through the device with a certain wavelength for certain plantation needs while absorbing other light wavelengths for electricity via PSC. [12, 13] Despite having high absorbance in visible light, PSC can also be made as a semi-transparent device with transparent electrodes [14, 15]. This makes PSC a potential candidate as a greenhouse electricity provider when used on greenhouse rooftop.

Similar to silicon solar cells, apart from the original p-i-n solar cell structure, additional features on the device can improve the overall performance. More noticeable research regarding the use of coating micro/nanostructures on the devices for light trapping to improve the percentage of the light being absorbed and the application of encapsulation for long term stability is getting more attention [16, 17].

While most of the wavelength tuning was done by adding extra layers on the PSC or combining another device with the PSC [18-20], very little research was focusing on modifying the active perovskite layer itself for wavelength selectivity. It is known that changing the concentration of iodine, bromine, or chlorine in the perovskite mixture would change the possible range of wavelength absorption spectrum. There are few publications on $MAPbX_3$, or $CsPbX_3$ based perovskite solar cell bandgap tuning [21], but so far not much research relating to triple cation perovskite solar cell bandgap tuning, as well as no report on how far can the absorbance redshifts or blueshifts with the modification of compositions. Furthermore, the only triple cation related reports regarding tuning the bandgap were for laser purposes and presented only the results from iodine/bromine or bromine chlorine mixture for anion modifications [22].

1.1 Light for plantation

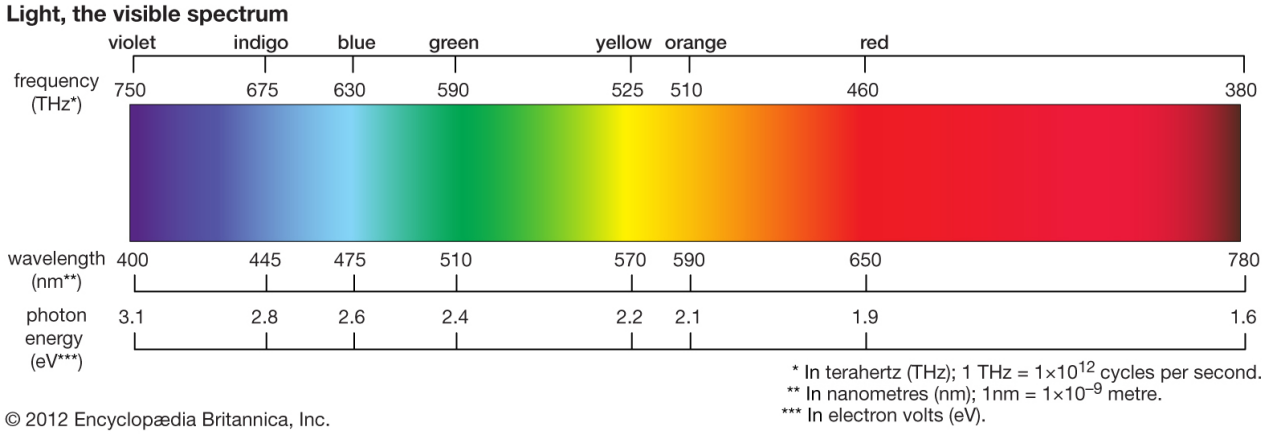

Figure 1-3 Visible wavelength range with corresponding colors. Reproduced with permission from Encyclopaedia Britannica [23].

There are two factors in light energy that have a great effect on the plant's growth cycle. One is the light intensity, a primary parameter when investigating the plant's photosynthesis process. The other one is the spectral distribution of radiation, as shown in Figure 1-3, which has various effects on plant colour, taste (regarding edible plants), aroma, and photosynthesis depending on which particular wavelength the plant absorbed [23]. Below is a brief review of the effect of different light wavelengths on plant growth.

Near UV light (380 -400 nm) is one of the main contributors to plant colour, taste, and aroma. This is the shortest wavelength in the visible light region that could be absorbed by the plant without the occurrence of any damages. The absorption of near UV light enhances the antioxidant activity of plant extracts. Other UV light with shorter wavelengths (UV-B and UV-C, λ<380 nm) are mainly harmful to plants. The violet and blue light (400 -500 nm) have a strong influence on photosynthesis and vegetation growth through root growth. Therefore, light wavelengths within this range are usually used as one of the light sources for seedlings or young plants. The green and yellow light (500 -600 nm) have less influence on vegetation growth. Light wavelength in this region is the least efficient in the photosynthesis process compared with the light wavelength in the

other region. However, the green and yellow light are still important for plants. For growing tomato in an enclosed environment, for example, the plant grows better under a mixture of green and red light compared with growing under a mixture of blue and red light [24]. The red light (600 -700 nm) is the most important light source for photosynthesis, flowering, and fruit production [25, 26]. Singh et al. from Germany sorted a list of research done by various researchers in the past regarding vegetable growth in relation to light wavelengths [26]. The study shows that most vegetables grow best under exposure to red light. This is mainly because the red light is absorbed by the phytochrome system in plants [27]. The phytochrome system helps the plant to grow away from the shadow towards the sun. Far-red and infrared light (700 -1000 nm) is also absorbed by the phytochrome system. It is one of the necessary light sources for short-day plants [25]. This wavelength dependence of plant growth is shown in Figure 1-4. Different components in the plant absorb different light at different wavelengths.

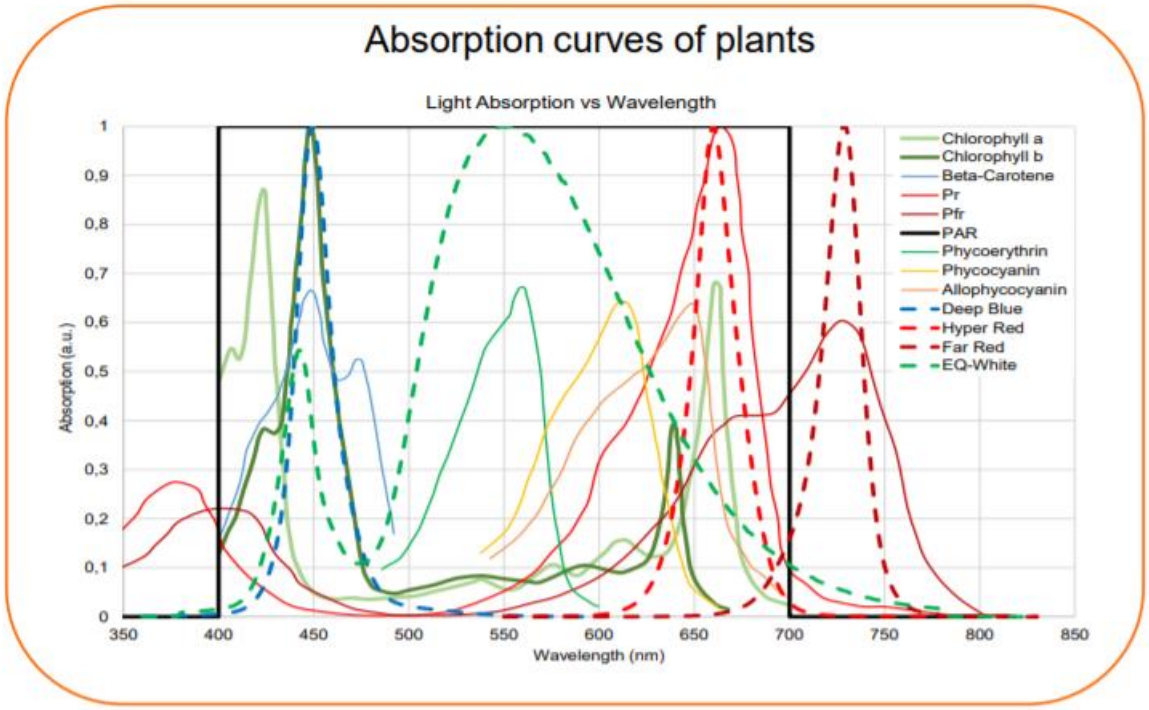

Figure 1-4 Different components of the plants absorb light in different wavelength regions and the comparison of LED light wavelength ranges. Reproduced with permission from OSRAM GmBH [28].

1.2 Research Goals

The first part of this research looks into the possibility of fabricating and optimizing perovskite solar cells with the facilities at The Nanofabrication Laboratory, the University of Canterbury in New Zealand. The expected goal is to fabricate devices with reproducible PCE at over 5 % for initial fabrication tests, taking the effect of moisture into account, following the commonly used recipe adapted by most perovskite solar cell researchers for $MAPbI_3$ based perovskite solar cell. Once the initial 5 % PCE is achieved, further improvements in PCE by trying different fabrication methods and parameter optimizations.

The second part of the research is looking at the possibility of applying upright nanopyramids on perovskite solar cells, and the possibility of doping the nanopyramids with nanoparticles or nanoclusters to change the transmittance or absorbance at particular wavelength regions. The long term stability of the nanopyramids regarding the physical and optical characteristics will also be examined. Nanopyramids are usually highly hydrophobic, the hydrophobicity of the features after doping nanoclusters will also be tested.

The final part of the research is to fabricate perovskite solar cells with different colours by changing the composition of the active perovskite layer. The composition with the I/Cl anion mixture will also be examined to understand why this particular mixture has been left out by the published literature. This could confirm the possibility of achieving wavelength selectivity with solar cells for greenhouse applications.

1.3 Present work

The outcome of perovskite solar cell fabrication with uncontrolled humidity is the first goal for this research, examining the possibility of fabricating the device without the requirement highly expensive chamber for humidity control. The second part of this research looks into the possibility of exploring the use of nanopyramid structure coatings on the Perovskite solar cell with the structure

and fabrication optimized in the first part to minimize the incident light being reflected and study the possibility of doping the nanopyramids with nanoparticles to achieve wavelength selectivity. The final part of the research looks into the possibility of modifying the composition of the active perovskite layer for wavelength selectivity.

In chapter 1, current progress in perovskite research, including the performance of perovskite solar cells and the factors that affect the stability of perovskite solar cells will be discussed in detail. Chapter 2 provides the description and explanations of thin film deposition and characterization techniques used in perovskite solar cell fabrications, as well as the technique used for solar cell performance characterizations. Chapter 3 describes the various deposition methods used for optimizing perovskite solar cells, such as one-step spin coating, sequential deposition, and anti-solvent method, and how the different factors affect the performance of the fabricated solar cells. The use of nanopyramids on the perovskite solar cell has been applied and tested and presented in chapter 4. This includes studying the possibility of doping the nanopyarmids with nanoparticles or nanoclusters to observe their influence on the absorbance of perovskite material at a particular wavelength region. A different approach in achieving wavelength selectivity with perovskite solar cells is described in chapter 5. This is done by alternating the composition of the active photon absorbing layer to obtain perovskite solar cells with different colour absorbance spectrum. The final chapters, chapter 6 and chapter 7, provides the conclusions that summarize the overall research work in this thesis and suggestions for future work that can be performed based on the present research.

1.4 Conclusions

Generating electricity with the solar cell for greenhouse rooftop applications require semi-transparent solar cells with different colours that allow light with different wavelengths to pass through for different stages of plant growth. Perovskite solar cell is considered as the most promising new solar cell to substitute conventional crystalline silicon solar cell with a recorded

power conversion efficiency reaching over 25 % for the single-junction perovskite solar cell. This particular solar cell has high efficiency and at the same time is semi-transparent, making it a good candidate for greenhouse rooftop electricity generation without affecting the greenhouse plantations. However, the fabrication of the device required an expensive glovebox to minimise the effect of moisture, UV light, and temperature on the active film crystallization. This research looked into the possibility of fabricating the perovskite solar cell for wavelength selectivity with a laboratory environment that only has a certain level of humidity and temperature control. Moreover, additional light trapping with upright nanopyramids for overall power conversion efficiency improvement and the possibility in and the long term stability of the nanopyramids was also investigated.

2. Photovoltaic Device

2.1 Converting sunlight to electricity

There are two main methods of converting solar energy into electricity. One is the use of solar light to produce heat for electricity generation. This is usually approached by using a mirror/ reflector to collect the sunlight, then redirect and focused the light to the receiver. The heat transfer fluid is then being heated to produce steam that used for power generation. The second method is the conversion of photon energy to generate electricity, such as solar cells. For conventional silicon solar cells, the operation theory is based on the photovoltaic effect in p-n junction semiconductor theory. When a p-type semiconductor connects to an n-type semiconductor, a depletion region is formed at the interface. Under the illumination condition, when the photon energy from sunlight is similar to the bandgap energy of the semiconducting material, then the photon energy is absorbed by the material to generate electron-hole pair in the depletion region. The electron and holes are then separated and transported in opposite direction to the edge of the depletion region, toward the p-type and n-type material. When the device is operated without light illumination, it is essentially a diode with a p-n junction.

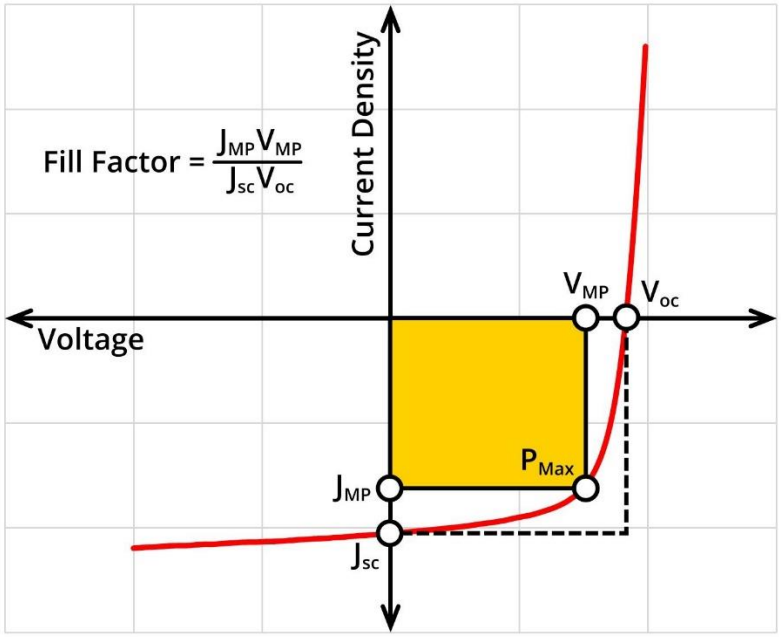

Figure 2-1 Typical solar cell IV characteristics showing the related parameters that are important for the solar cell. The image remains the copyright of Ossila Ltd. Taken with permission from Ossila.com. [29]

2.1.1 Solar cell characteristics

To calculate how much light has been converted into electricity, several important parameters need to be looked at. Figure 2-1 shows a typical IV characteristic of a solar cell under light illumination. The measurement of the solar cell is usually done by using an indoor light which is calibrated to the same intensity as sunlight. The current of the device is then measured using a source meter with a voltage sweep under light illumination. Detailed characterization techniques, including the equipment used, are provided in section 2.4. $\mathbf{J_{SC}}$, short circuit current density, is a measure of the electric carriers in the device generated by light. The measured $\mathbf{J_{SC}}$ does not get affected by the active area of the device. The open circuit voltage, $\mathbf{V_{OC}}$, refers to the maximum voltage that can be generated by the solar cell. $\mathbf{J_{MP}}$ and $\mathbf{V_{MP}}$ refer to the current density and voltage where maximum power ($\mathbf{P_{MP}}$) occurs. Fill factor looks into the ratio between maximum power output measured from the device and the product of device $\mathbf{J_{SC}}$ and $\mathbf{V_{OC}}$. The device power conversion efficiency, $\boldsymbol{\eta}$, can then be calculated with equation 2-1 when the above parameters are known:

$$\boldsymbol{\eta}(\%) = \frac{\boldsymbol{P_{OUT}}}{\boldsymbol{P_{IN}}} = \frac{\boldsymbol{V_{OC}}(V)\boldsymbol{I_{SC}}(A)\boldsymbol{FF}}{\boldsymbol{P_{IN}}(W)} \qquad (2\text{-}1)$$

Where P_{IN} is the input power from the light, and I_{SC} is the active area dependent short circuit current of the device, which can be converted to J_{SC} with equation 2-2:

$$I_{SC}(A) = J_{SC}(A/cm^2) \times A(cm^2) \quad (2\text{-}2)$$

where ***A*** is the active area of the device.

In addition to the parameters mentioned above, the internal resistance in solar cells is also important as it affects the voltage and current output of the solar cell. The equivalent electrical circuit of a solar cell is illustrated in Figure 2-2. The internal resistances are greatly affected by the quality of the thin film material, the quality of the interface between thin films. R_{SH} refers to the internal shunt resistance and R_S refers to the internal series resistance.

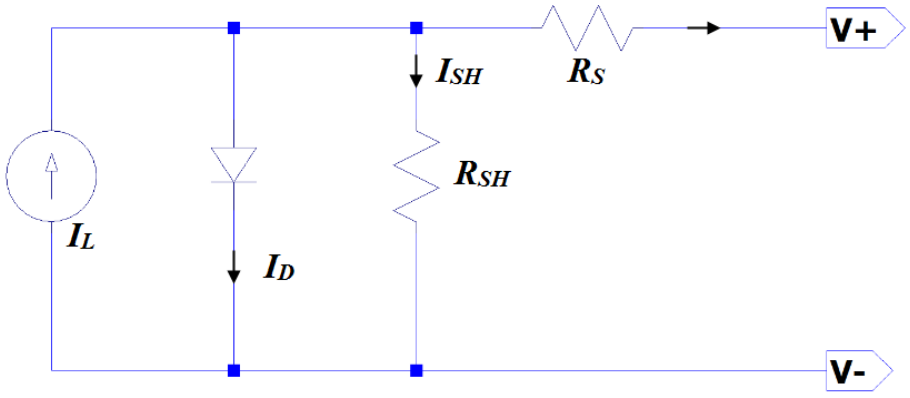

Figure 2-2 Equivalent electrical circuit of a solar cell. The current and voltage of the device are greatly affected by the internal shunt resistance and series resistance.

2.2 Perovskite solar cell

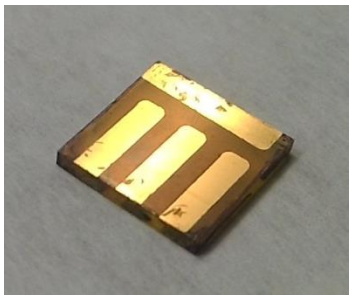

Figure 2-3 Image of perovskite solar cell sample fabricated at the University of Canterbury showing the counter gold electrode.

Perovskite solar cell (PSC) was announced as one of the major science breakthroughs by Science

magazine in 2013 [30]. Figure 2-3 shows the perovskite solar cell fabricated in this work at the University of Canterbury. The first time perovskite crystal structure material was used as an active photon sensitizer in Dye sensitized solar cell (DSSC) was in 2009 by Miyasaka's group [8]. The material consists of crystal structure form of ABX_3, with A refers to the monovalent cation such as methylammonium$^+$ (MA^+), B as the divalent transition metal cation such as Pb^{2+}, and X is the halide anion such as I^-. The MA^+ cations form a cage around the octahedron PbI_6 crystal, as shown in Figure 2-4.

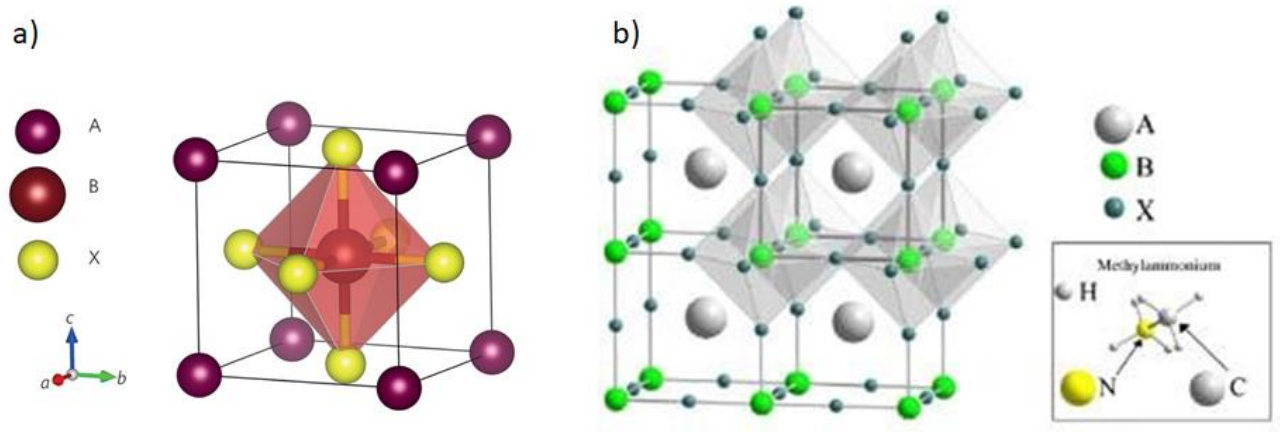

Figure 2-4 a) Perovskite generic crystal structure [31]. A refers to the organic monovalent cation such as MA^+, B refers to the inorganic cation such as Pb^{2+}, and X, such as I^- is the anion that links the crystal with adjacent Pb^{2+} in the perovskite crystal lattice. The MA^+ cations form a "cage" around the octahedron PbI_6. b) An equivalent way of demonstrating perovskite $MAPbI_3$ crystal [32]. The MA^+ cation is surrounded by the octahedron PbI_6 crystals. Reproduced with permission from Samual D. Stranks et al [31] and Muzammal uz Zaman et al [32].

The overall efficiency was not attractive, standing at just above around 3.8 %. The cell's performance increased to around 6% when Park's group spin coated perovskite on top of TiO_2 as the photon absorbing layer in solid-state DSSC instead of soaking TiO_2 in a solution containing perovskite material [33]. In just one year, the same research group, in collaboration with Michael Grätzel's research group at EPFL, managed to improve the cell further to nearly 10 % efficiency by replacing the liquid electrolyte with a solid-state hole transmitting thin film, Spiro-omeTAD for solid-state dye sensitized solar cell [9]. In the same year, Snaith et al. published a breakthrough in PSC efficiency and overall performance. The power conversion efficiency of PSC was officially recorded over 10%, which is near the highest efficiency record for DSSC [34]. At the same time, further understanding of PSC principle conversion mechanisms was postulated Snaith's group replaced the commonly used

conductive TiO_2 with non-conductive Al_2O_3 and found that Perovskite material can transport holes and electrons itself [35, 36].

The rapid growth in PSC performance did not stop here. Until this point, the mesoporous layer was necessary for PSC structure with high efficiency. In 2013, Snaith's group managed to remove the mesoporous layer and fabricated planar PSC with a dual-source thermal evaporator [37]. This method helped to boost the PSC efficiency record to over 15 % with pin-holes minimized in the structure. By the end of 2014, researchers from the Korea Research Institute of Chemical Technology (KRICT) had obtained PSC performance certification with a record of 20.1 % [38]. This record was achieved by blending the most commonly used monovalent cation, Methylammonium (MA), with Formamidinium (FA). Shortly after 1 year, Grätzel's group along with Greatcell Solar (Dyesol as the previous name) announced a new certified record of the power conversion efficiency at 21.02 % [39].

The race for breakthroughs of perovskite solar cells efficiency records continued. Research published in 2016 stated that the addition of cesium to the MA and FA blend results in a highly efficient triple cation perovskite solar cell with much better environmental stability when compared with the previously published results [1]. Currently, the best result so far was published by collaborative research between the Massachusetts Institute of Technology and Korea Research Institute of Chemical Technology with a 25.2 % for single-junction perovskite solar cell [7].

2.2.1 Typical structures of perovskite solar cells in research

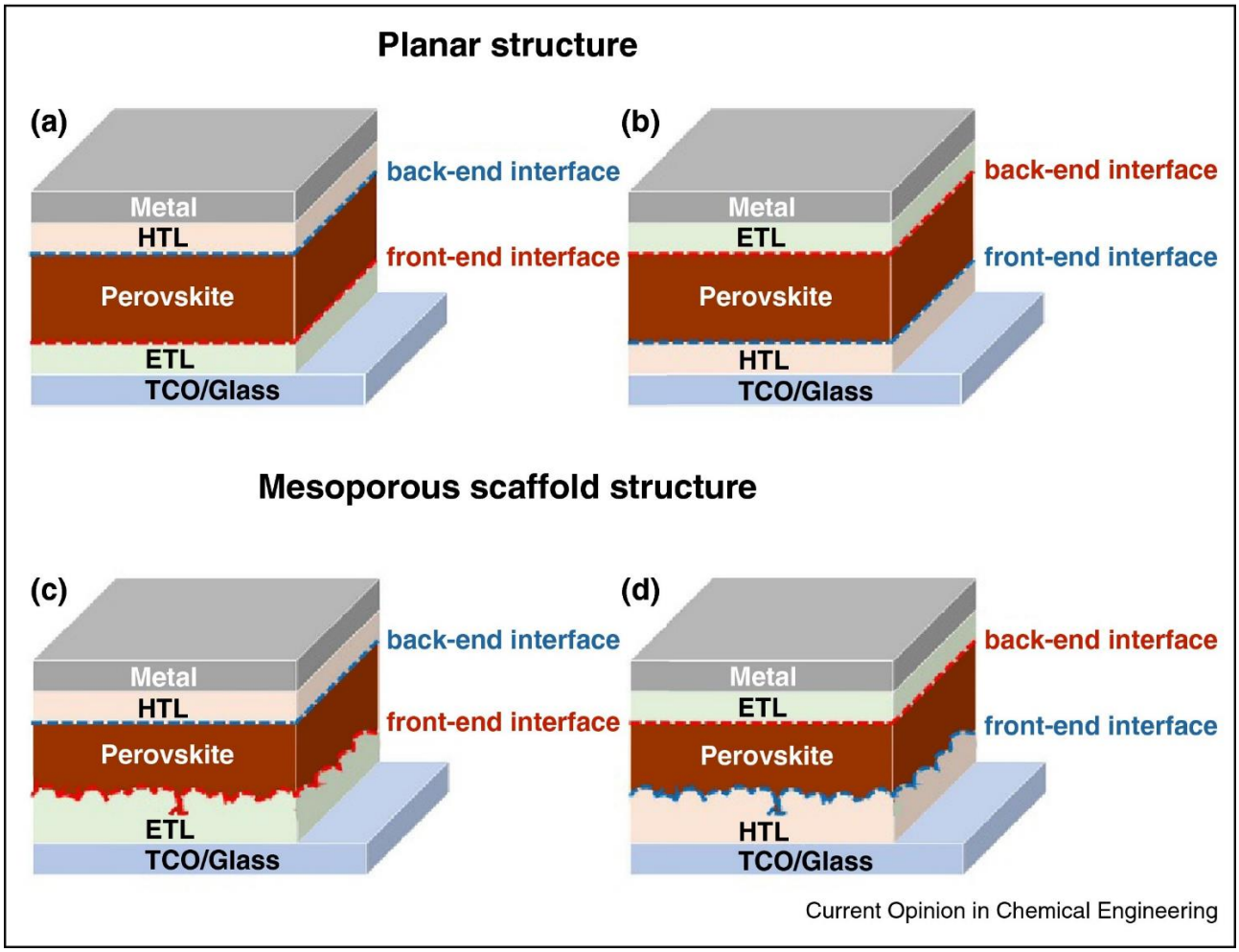

Figure 2-5 Different structures of the perovskite solar cell that have been published by researchers: (a) upright planar structure, (b) inverted planar structure, (c) mesoscopic upright structure, and (d) inverted mesoscopic structure. ETL refers to the electron transport layer, and HTL is the hole transport layer. Reproduced with permission from Chris Manspeaker et al [40]

Figure 2-5 shows the different types of structures of perovskite solar cells that have been published in the past years. The best efficiency was usually achieved with the mesoscopic structure that is similar to the dye sensitized solar cell structure, containing mesoporous metal oxides as the electron transport layer, with conversion efficiency reaching over 23 % [36, 41, 42]. In this approach, the actual interface area between perovskite and metal oxide layers is much larger allowing for better carrier transport. Devices with the planar structure are also very popular in perovskite solar cell research, especially with an inverted planar structure based on organic photovoltaics, with

conductive polymers or small molecules materials instead of semiconductors, achieving an overall power conversion efficiency of over 20 % [41, 43]. Popular metal oxide for electron transport layer include TiO_2 [44-46], ZnO [47-50], and SnO_2 [42, 51-53]. While iodine-based perovskite material, such as $MAPbI_3$, mixed cation, or triple cation perovskite are the main choices for active perovskite layer, some of the research have put their effort into lead-free perovskite to minimise the impact on the environment [54]. For the hole transport layer, lithium ion doped spiro-omeTAD is commonly the first choice in upright structure perovskite solar cells [55-57]. Organic materials such as PCBM and PEDOT are commonly the main material used in perovskite solar cells with an inverted structure for the electron transport layer and hole transport layer respectively [14, 58-61]. Alternatively, metal oxides such as NiO_x can also be used as an efficient hole transport layer for perovskite solar cells with an inverted structure [62, 63].

2.2.2 Mixed cation mixed halide perovskite solar cell

Perovskite solar cells with mixed monovalent cations showed high performances since 2016, when Saliba et al. published the highly efficient triple cation solar cell, with the addition of caesium cation in the mixed [1, 41]. Triple cation refers to the addition of another 2 monovalent cations to the MA^+ in conventional $MAPbI_3$ perovskite. While the original $MAPbI_3$ has a diffusion length of around 400 nm depending on the preparation method, the addition of FA^+ and bromine in the compound could increase the diffusion length to close to several micrometres [64]. Moreover, because of the larger molecular size of FA^+ when compared with MA^+, the size of the crystal structure expands and the optical absorbance of the active material broadened with the addition of FA^+ [65]. However, with the addition of FA^+ in the crystal, some of the tetragonal crystal structures originally from $MAPbI_3$ collapsed and formed the trigonal phase of the α-$FAPbI_3$ and hexagonal phase of δ-$FAPbI_3$ crystal structure, as shown in Figure 2-6. For solar cell applications, α-$FAPI_3$ (black colour material with a trigonal crystal structure) is more favourable compared to δ-$FAPbI_3$ (yellow colour material with a hexagonal crystal structure) due to the weak optical absorbance of δ-$FAPbI_3$ at visible

wavelengths [66, 67]. However, it is difficult to suppress the formation of δ-$FAPbI_3$ because the hexagonal crystal structure is easier to form compared to α-$FAPI_3$ with a trigonal crystal structure at a temperature below 120 °C [66].

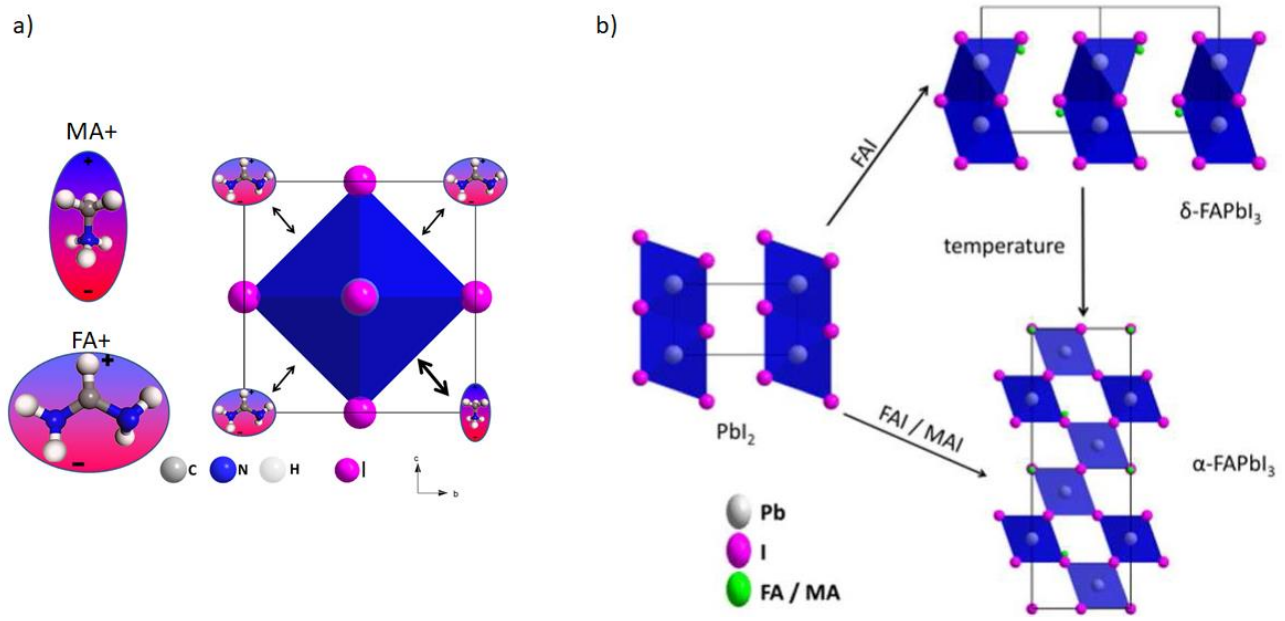

Figure 2-6 a) interaction of MA^+ cation and FA^+ cation with PbI_3 crystal. Pb is in the center of the crystal which is invisible from this viewing angle. MA^+ has a stronger interaction with the PbI_6 octahedron structure compared with the interaction between PbI_6 and FA^+. b) When FA^+ cation is incorporated in the crystal structure, the overall crystal size expands due to the larger molecular size of FA^+ compared with MA^+ 2 possible crystal structures. This results in 2 different crystal phases during the deposition of perovskite film—α-$FAPbI_3$ and δ-$FAPbI_3$ [66]. Reprinted with permission from A. Binek, F. C. Hanusch, P. Docampo, and T. Bein, "Stabilization of the Trigonal High-Temperature Phase of Formamidinium Lead Iodide," *The Journal of Physical Chemistry Letters,* vol. 6, pp. 1249-1253, 2015/04/02 2015. Copyright 2015 American Chemical Society [66]

The addition of Cs^+ cation to the $MAFAPbI_3$ partially replaced the large FA^+ with smaller Cs^+ in the crystal structure helps suppress the undesired δ-$FAPbI_3$, and strengthens the bonding of the "cation cage" surrounding the PbI_6 octahedrons. This results in a more stable device at ambient conditions [68]. Since then, more researchers has tried to find an explanation of why mixed cation performs better in both PCE and stability [1, 69]. Figure 2-7 shows the crystal structure of triple cation perovskite formed with Cs^+, FA^+, and MA^+ in the A site of ABX_3 perovskite crystal structure.

With the success of the triple cation perovskite solar cell, various research adopted the addition of alternative cations in perovskite. This includes quadruple cations, quintuple cation perovskites [70-72].

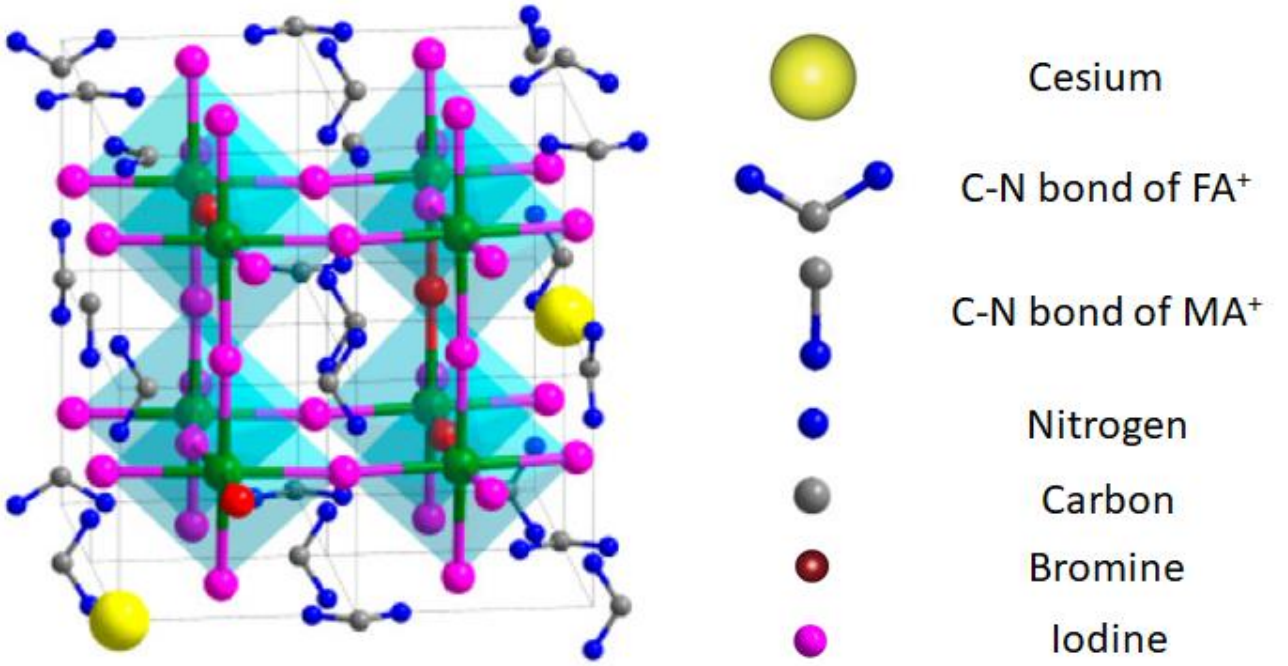

Figure 2-7 Crystal structure of triple cation perovskite. One of the iodine ions is replaced by bromine in the PbI_6 octahedron crystal. Caesium partially replaced the FA^+ in the "cubic cage" formed by MA^+ and FA^+ cations. The addition of caesium helps suppress the occurrence of the δ-$FAPbI_3$ phase, stabilized the perovskite crystal structure. Reprinted with permission from L. Chen, Y.-Y. Tan, Z.-X. Chen, T. Wang, S. Hu, Z.-A. Nan*, et al.*, "Toward Long-Term Stability: Single-Crystal Alloys of Cesium-Containing Mixed Cation and Mixed Halide Perovskite," *Journal of the American Chemical Society,* vol. 141, pp. 1665-1671, 2019/01/30 2019. Copyright 2019 American Chemical Society [73].

Despite the flying high record in PSC power conversion efficiency, there are some obstacles that researchers are yet to overcome. Stability and hysteresis are the main two issues that affect the performance of the perovskite solar cell [74-78].

Hysteresis in solar cells was defined by the difference in IV curves that appeared during the IV characteristic measurements when the sweeping direction is different [74, 79]. The occurrence of hysteresis is still a debatable subject in recent research in PSC [75, 79]. In 2014, Snaith et al. published a paper in the Journal of Physical Chemistry Letters, comparing the hysteresis that occurs in three different PSC structures: planar, mesoscopic TiO_2, and mesoscopic Al_2O_3 [74]. By varying the IV scanning conditions, hysteresis in the planar structure became more obvious when the scan rate is reduced. Moreover, from the data his research group collected, he believed that hysteresis is present mainly due to the perovskite layer in the cell. He then stated three possible hypotheses in the reason for hysteresis occurrence: (i) The defect at the contact between perovskite and other

materials; (ii) the ferroelectric properties and slow polarization observed in perovskite materials; and (iii) the possibility of excess ions in the film [74]. In recent years, more in-depth research has been done on the hysteresis effects and attempts were made on eliminating or minimising the effect [80-85].

Another major issue that hinders the performance of perovskite solar cells is their stability under light and natural environmental conditions. It is known that moisture and UV radiation are the two main factors affecting PSC degradation [31, 48, 78, 86-90]. Figure 2-8 shows the effect of moisture on conventional $CH_3NH_3PbI_3$ ($MAPbI_3$) perovskite crystal structure [76]. It can be explained via several chemical equilibrium equations describing the formation and degradation of $MAPbI_3$ [91, 92].

$$CH_3NH_2 + HI \rightarrow CH_3NH_3I \quad (2\text{-}3)$$

$$CH_3NH_3I + PbI_2 \rightarrow CH_3NH_3PbI_3 \quad (2\text{-}4)$$

Equation 2-3 denotes the formation of MAI from methylamine and hydrogen iodide. Equation 2-4 describes the formation of perovskite from MAI and PbI_2, forming octahedron PbI_6 surrounding MA^+, resulting in the cubic structure shown in Figure 2-4.

$$CH_3NH_3PbI_3 + H_2O \rightarrow CH_3NH_3PbI_3 \cdot H_2O \quad (2\text{-}5)$$

$$4(CH_3NH_3PbI_3) + 2H_2O \rightarrow (CH_3NH_3)_4PbI_6 \cdot 2H_2O + 3PbI_2 \quad (2\text{-}6)$$

$$(CH_3NH_3)_4PbI_6 \cdot 2H_2O \xrightarrow{H_2O} 4CH_3NH_3I + PbI_2 + 2H_2O \quad (2\text{-}7)$$

When the material is exposed to moisture, the moisture distorted the alignment of the perovskite structure, forming a perovskite monohydrate, as described in equation 2-5. The perovskite monohydrate changes to perovskite dihydrate when the material is further exposed to moisture. At the same time, PbI_2 is also produced, as shown in equations 2-6. This can be further degraded back to MAI and PbI_2 by the moisture, as shown in Figure 2-8.

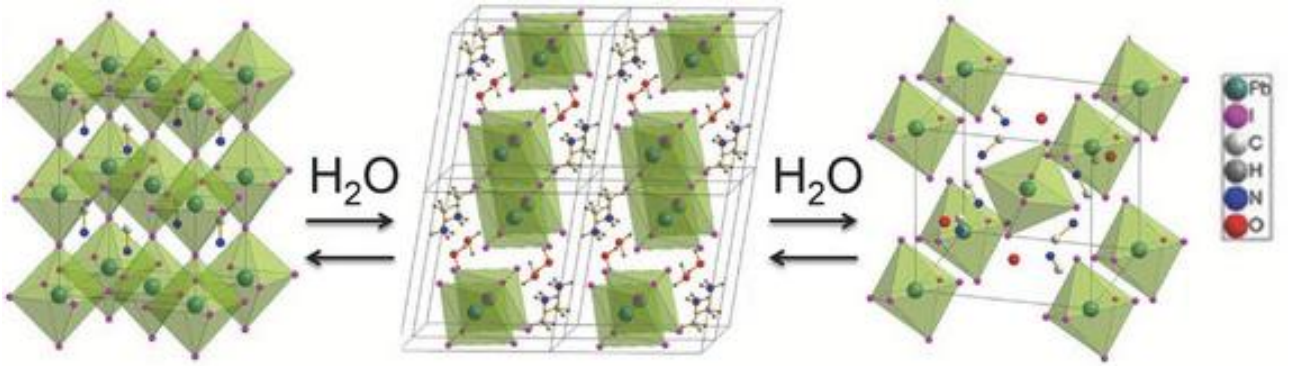

Figure 2-8 Change in Perovskite crystal structure after moisture exposure [76, 92]. The leftmost image represents an as-deposited perovskite crystal with octahedron PbI_6 crystals surrounding the cation MA^+. The PbI_6 crystals are connected via the shared Iodine ion and aligned with the interaction with MA^+ cations. When the perovskite is exposed to moisture, the introduction of H_2O in the crystal lattice separated the connection between PbI_6 crystals, transforming the material to perovskite monohydrate, as the image in the center. When the material is further exposed with H_2O, the perovskite monohydrate transitioned to perovskite dihydrate with PbI_2 formed at the same time. The perovskite dihydrate can then decomposes into MAI and PbI_2, as mentioned in equation 1-5. Reprinted (adapted) with permission from A. M. A. Leguy, Y. Hu, M. Campoy-Quiles, M. I. Alonso, O. J. Weber, P. Azarhoosh*, et al.*, "Reversible Hydration of CH3NH3PbI3 in Films, Single Crystals, and Solar Cells," *Chemistry of Materials,* vol. 27, pp. 3397-3407, 2015/05/12 2015. Copyright 2015 American Chemical Society [92].

In 2015, researchers led by Prof. Yang Yang at UCLA announced improved stability when the n-type oxide and p-type hole transmitting material was replaced by Nickel Oxide and ZnO [48]. After the publication of triple cation perovskite solar cells in 2016 highly efficient nonencapsulated device stability was also improved in 2017. The PSC was tested for over 1000 hours at maximum power output and under 1 sun illumination where 95% of the initial 20% PCE efficiency was retained [93]. In the same year, Grancini et al. published stable 2D/3D perovskite solar cells with a one-year stability record, but with lower initial efficiency of approximately 12 % [94]. Furthermore, the encapsulated perovskite solar cells were also tested for over 180 days and retaining 100% of the initial PCE efficiency of over 20% [95]. Despite this, PSC stability still has a long road to go to achieve similar stability as conventional silicon based solar cells which have over 20 years of stability.

2.2.3 Current challenges on perovskite solar cells

Apart from improving the overall PSC performance and investigating or minimising the known issues of cell stability and hysteresis, there are some other aspects in PSC research that attracted attention.

This could be separated into several categories. Among these, the simulation of optimum PSC performance [5, 96], fabricating PSC on flexible substrates [87, 90, 97-99], the pinholes occurrence with solution processing [48, 99-104], and the charge separations in PSC [35, 78, 105]. There are also published papers on utilizing plasmonic nanoparticles on PSC to enhance PSC's optical absorption [19, 106]. Because PSC can be flexible and transparent, another popular research area involves fabricating tandem solar cells with PSC and other types of solar cells such as silicon solar cells[107, 108], to improve the overall power conversion efficiency of the cell.

The applications of perovskite material in various areas are also another popular topic in perovskite-related research. While bandgap tuning is one of the mainstream in perovskite LEDs [31, 109], there are similar attempts in the perovskite solar cell research [13, 21, 110]. Apart from modifying perovskite composites as one of the mainstreams in tuning the bandgap of perovskite solar cells, there are other attempts to achieve the required changes in absorbing wavelengths [18, 20, 111]. Furthermore, the utilisation of micro/nanostructures on perovskite solar cells have started to get some attention as well. The application of micro/nanostructures helps improve the percentage of the incident light reaching the active perovskite layer for the efficient light conversion process. This helps improve the device's overall conversion efficiency [112, 113].

2.3 Micro/nanostructures for solar cell light trapping

Light trapping structures have been widely used in minimising the incident light reflection in most solar cell technologies [114, 115]. This effectively increases the number of photon generated carriers and improves the overall performance of the solar cells. While most of the research regarding the use of nanostructures for light trapping is related to conventional crystalline solar cells, adding nanostructures is also effective for thin film-based solar cells for light-harvesting improvement [116]. Depending on the solar cell type and the structures used, the overall photocurrent generation could improve up to 20 % when compared with the device without light trapping nanostructures [116, 117]. For PSC, an estimation of 15% to 17% power conversion

efficiency improvement with submicron inverted cones with PSC on a flat substrate has been reported back in 2016 [118]. However, most of the research regarding nanostructure incorporation on PSC are simulation based only [17, 112, 113], with very few published research include the actual fabricated results [119-121].

Depending on the material and structure used, different fabrication methods for applying nanostructures on solar cells. For conventional silicon solar cells, is using chemical etching to form random upright pyramids on the front surface of the solar cells [122]. While chemical etching is fast and low cost for module size solar cells, the requirement for a large amount of acid or base possesses a huge impact on the environment. The alternative way is to fabricate the textured structures using dry etching with reactive gases. Popular methods including reactive ion etching (RIE) or inductively coupled plasma etching (ICP). Detailed descriptions regarding these techniques will be given in chapter 3. Since all dry etchings are a combination of physical bombardment and chemical reaction, it is difficult to fabricate pyramidal-shaped nanostructure on the device with only dry etchings. Therefore a combination of wet and dry etching was proposed to form uniform pyramid-like features and other various types of nanostructures have been investigated [115, 122, 123].

For thin film based solar cells such as perovskite solar cell, dye sensitized solar cell, and organic solar cell, it is difficult to incorporate the nanostructure on the transparent substrate with dry/wet etching since the devices have very little chemical and plasma resistance. Therefore, techniques based on pattern replication with a mould or stamp such as nanoimprinting or nano-embossing are popular for solar cell surface texturing applications [119, 124].

Also, to enhance the light trapping effect in thin film solar cells, the incorporation of plasmonic materials such as nanoparticles in conjunction with surface textured nanostructures have started getting attention [125, 126].

2.3.1 Nanoclusters/nanoparticles on light trapping nanostructures

The incorporation of plasmonic nanoparticles for solar cell applications has been very popular in recent years. There are reports where the addition of nanoparticles on light trapping features for solar cell application improved the absorption of lights for photon-electron conversion, resulting in an increase in device photocurrent under illumination [125, 127]. Moreover, there is an increase in demand for colourful rooftop solar cells, for both functional and aesthetic purposes. The addition of metal nanoparticles/nanoclusters with different sizes has the potential to modify the solar cell colour while maintaining the power efficiency of the device [128]. While most of the studies are based on the incorporation of nanoparticles, research in nanoclusters is gaining more attention in recent years due to the possibility of adjusting cluster size and distance between atoms for different optical light absorbance wavelengths [129, 130].

2.4 Photovoltaic device characterizations

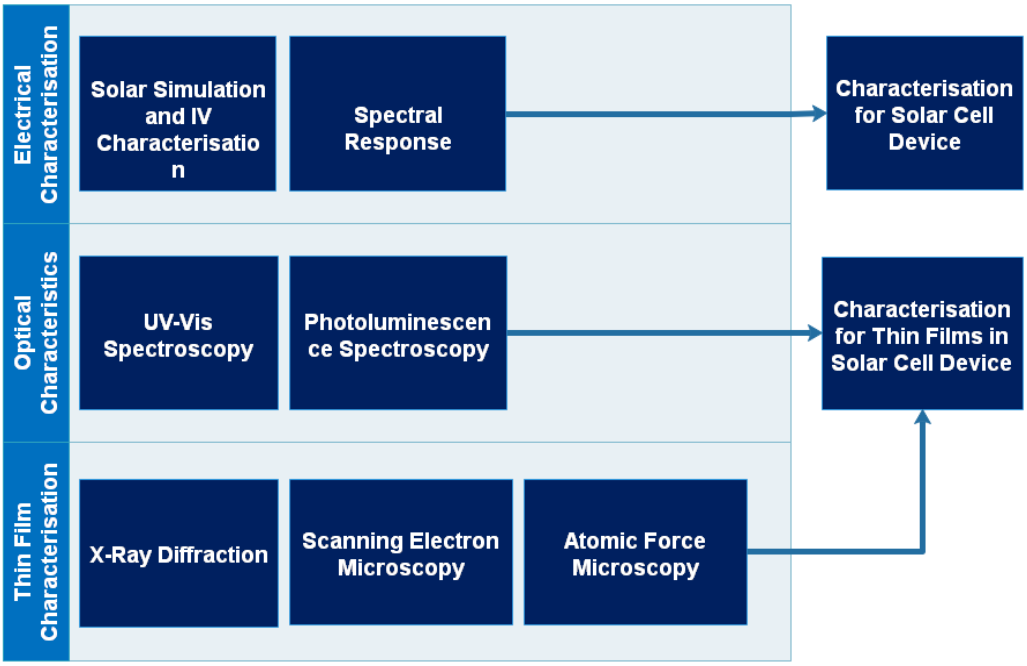

Figure 2-9 Different characterisation techniques employed for solar cells analysis and testing

After fabricating a solar cell device, it is important to test its performance and understand the device's operation mechanisms [131, 132]. To understand how each layer affects the overall performance of the device, including the optical and electrical characteristics, each of the thin films in the solar cell needs to be characterized and compared with published works. There are several methods in characterizing the solar cell devices and the thin films incorporated in the device, as shown in Figure 2-9. The Solar simulation and current Voltage IV characterization look at the device's performance under white light that has similar spectral irradiance and light intensity when compared with the typical natural sunlight. The spectral response looks at how much of the incident photons from the light source power have been converted into electrons and electrical power. For thin film surface morphology analysis, scanning electron microscopy and atomic force microscopy are the commonly used techniques. X-ray diffraction looks at the crystal structure of the thin film. Photoluminescence and UV-Vis spectroscopy look at the optical characteristics of the thin films. This section gives a brief explanation of these techniques that have been used for this project.

2.4.1 Solar simulation

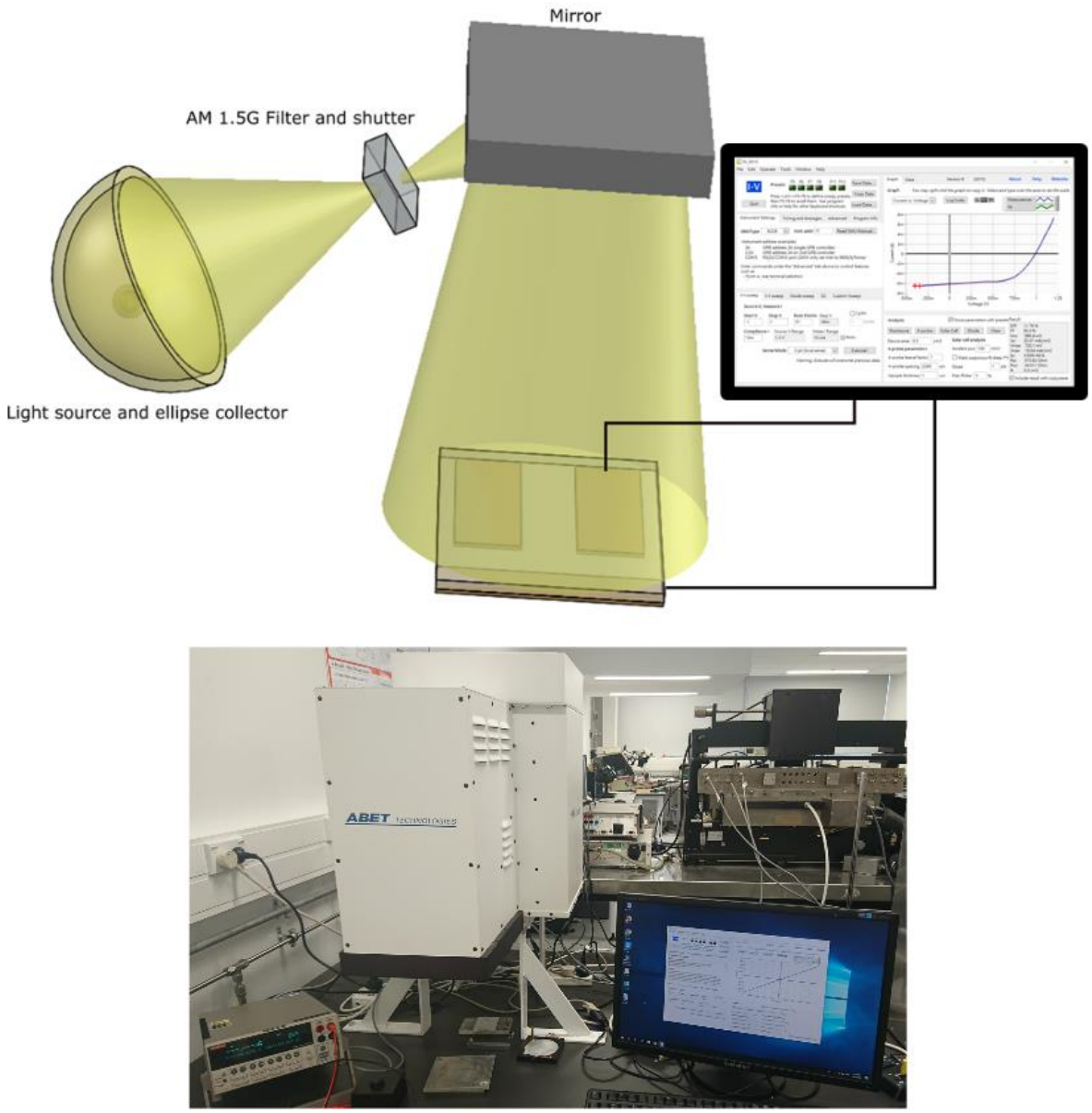

Figure 2-10 Top: schematic of the ABET solar simulator. The light from the light source was collected and concentrated via the eclipse collector, then passed through the AM 1.5 G filter and reflected by the mirror to reach the sample stage. Bottom: the setup of ABET AAA 3000 solar simulator for artificial sunlight, Keithley source meter for IV sweeping, and IV software by at the nanofabrication laboratory, University of Canterbury. The sample stage was maintained at room temperature via placing a commercially available ice gel pack underneath the metal sample stage.

The solar simulation is used to mimic the natural sunlight conditions when a solar cell is operating. A white light that's calibrated to have a similar spectral response to sunlight is used as the light source, as shown in Figure 2-10. The simulator used for this research was ABET Sun3000 solar

simulator with AM 1.5 G calibration and AAA classification. AM 1.5 G (Air mass 1.5 Global) is the yearly average atmosphere thickness at mid-latitude on earth, where most of the countries are located. The AAA classification refers to the factor of a spectral mismatch at visible wavelengths within 0.75-1.25, the non-uniformity of irradiance at the over 100 mm diameter sample stage smaller than 2 %, and the long term irradiance instability smaller than 2%. To ensure the consistency of light intensity, the solar simulator is calibrated with a shunted reference cell, to ensure the intensity of the light is maintained at 100 W/cm^2.

The light exposed device is concurrently connected to a Keithley 2400 source meter which measures the device current when different bias voltages are applied to the device. The data is then sent to the computer for IV plot and analysis to obtain essential information such as series and shunt resistances, fill factor, and efficiency that is key to the device performance. The Labview based software, IV_2015, used for IV plot and analysis was developed by Michael Kelzenberg, an alumnus from the California Institute of Technology [133].

For conventional silicon solar cells, a single voltage sweep from -1 to 1 V is sufficient to obtain devices' IV characteristics under illumination as shown in Figure 2-1 in section 2.1.1. For perovskite solar cell, due to the hysteresis characteristics of the device mentioned in section 2.2.2, a forward sweeping from negative bias to positive bias and a reverse sweeping from positive bias to negative bias shown in Figure 2-11 is needed to obtain a more accurate IV characteristic.

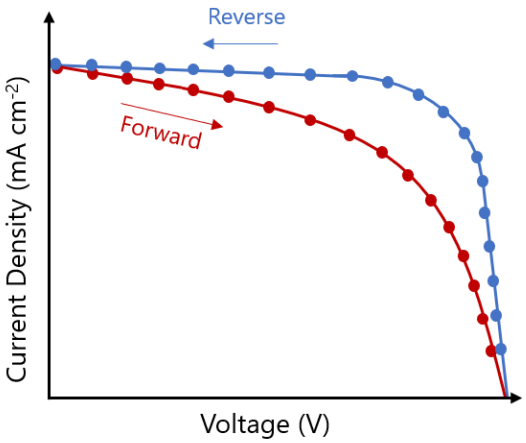

Figure 2-11 IV characteristics measurement for perovskite solar cell, showing the difference in forward and reverse voltage sweeping. [134]

2.4.2 Photoluminescence Spectrometry

Photoluminescence Spectroscopy is an essential non-destructive method in understanding the photon-electron characteristics of photosensitive materials. In general, when the material is excited by the incident photons, radiation energy is emitted from the sample which can be used to extract data regarding defects and impurities in the material. The emitted radiation energy, passing through several focusing filters, is collected by a detector to measure the number of photons being emitted by the sample.

Figure 2-12 is a typical set up of PL spectroscopy. When the sample material is excited by a light source, which is usually a laser or white light depending on the required excitation energy, photons are generated from the sample and travel through a set of focus lenses and filters before arriving at the detector. The detector measures the intensity of the photons generated, in photon counts, at different photons energy levels. This could then be processed to obtain plots of photons generated from the sample versus photons wavelengths.

For this research, a continuous laser with 1 mW intensity and 405 nm wavelength was used as the light source, and a silicon based charge-coupled detector was used for detecting the photons generated from the samples. The OceanView software from Ocean Optics was used to record the data. Various neutral density filters with different optical densities were also used to reduce the intensity of the laser down further, preventing the degradation of perovskite film with laser overexposure during measurements. Two collimating lenses were used to collect the photons excited from the sample and focus the photons to the detector. The environmental noise, which was the signal received by the detector in the dark without the incident laser, was first removed from the measurement, to ensure the signal obtained is solely from the sample. A long-pass filter (LP 497) was also used to filter out any scattered laser light being recorded by the detector.

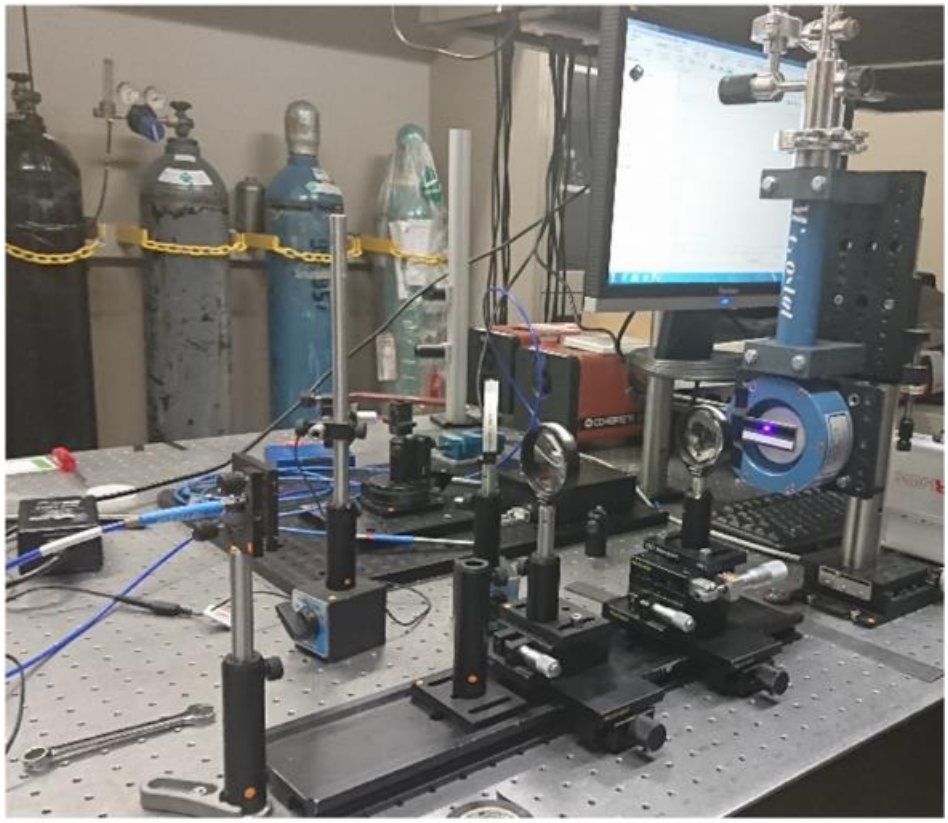

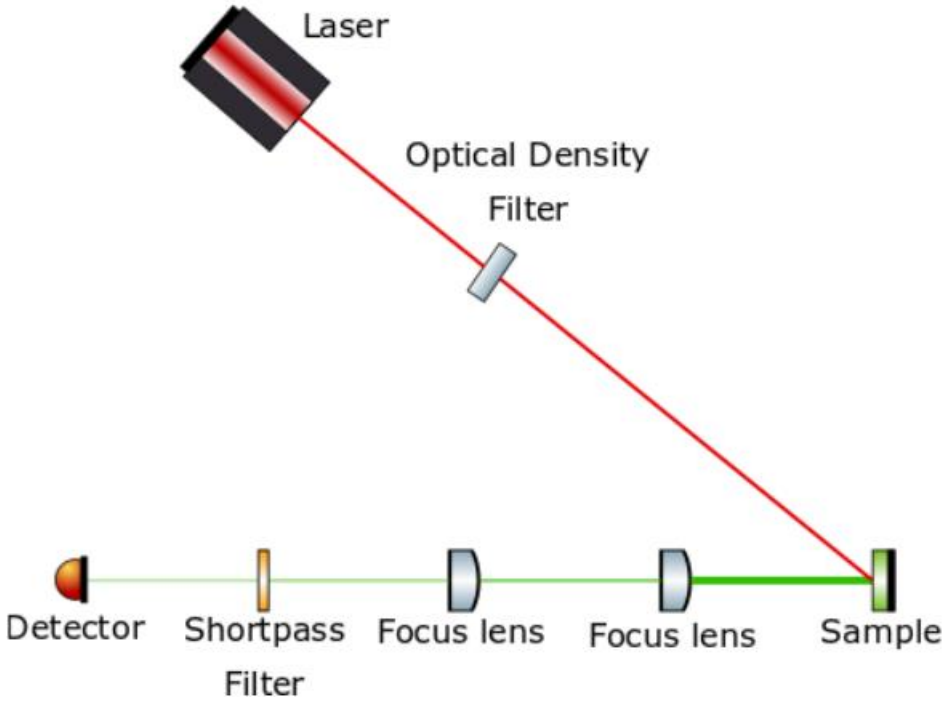

Figure 2-12 Image of the photoluminescence spectroscopy set up and a top view schematic of each component. The snapshot of the PL set up at Physics Department, University of Canterbury was taken during setting up major components.

2.4.3 Spectral Response

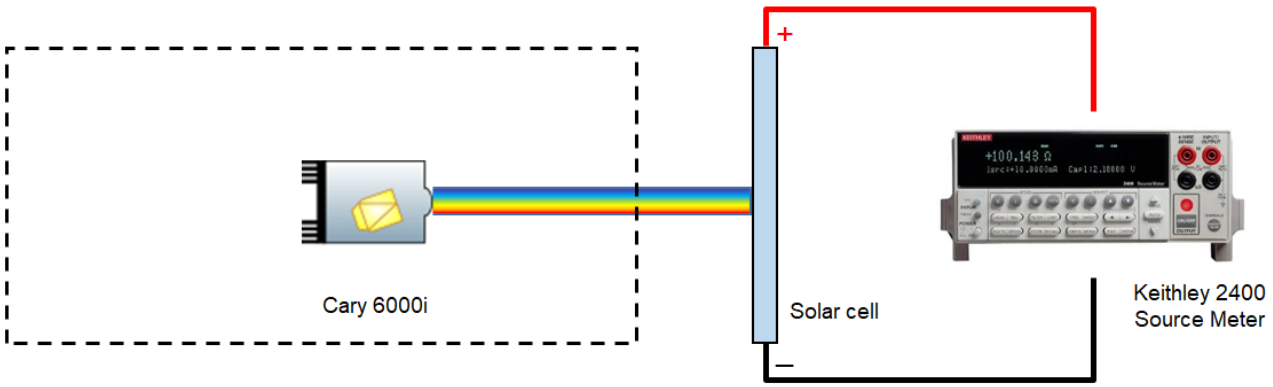

Figure 2-13 Spectral response set up using a UV-Vis spectrometer as a light source with different wavelength for the device, and a source meter for measuring current at 0V when the device is exposed to the light.

Spectral response is used to measure the spectral sensitivity of the device to the light at different wavelengths. This could also provide vital information regarding the percentage of incident light being converted to electricity at different wavelengths. Instead of purchasing sophisticated equipment specifically measuring device spectral response, this could be achieved by using a UV-Vis spectrometer to expose light at different wavelengths to a sample connected with a source meter for measuring the short circuit current output of the device as a function of the light wavelengths. A customized set up for spectral response measurement for this research is shown in Figure 2-13.

A reference sample, a heterojunction with intrinsic layer thin layer (HIT) solar cell obtained from Taiwan Semiconductor Research Institute in Taiwan, was used to calibrate the light source. The measured data for the reference cell was recorded in external quantum efficiency (EQE, %) versus wavelength, as shown in Figure 2-14.

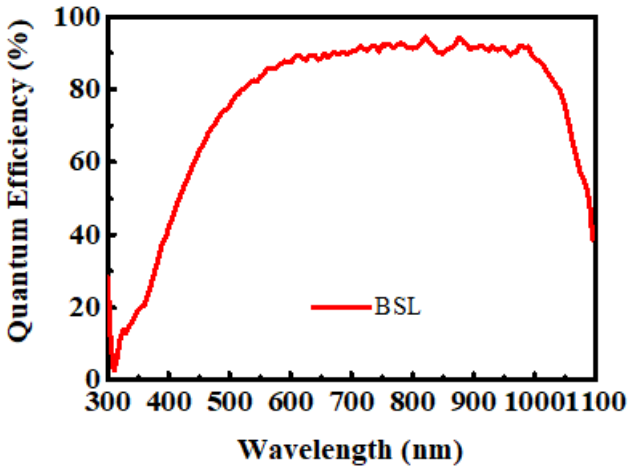

Figure 2-14 Plot of EQE versus wavelength of the reference cell. The EQE value is then converted to Spectral response values for quantifying the power output of the incident light at each wavelength.

Therefore, it is required to convert the data into spectral response versus wavelength. The relationship between **EQE** and spectral response (**SR**) in A/W is given by

$$\boldsymbol{SR} = \frac{\mathbf{EQE}(\%)}{100} \times \frac{\boldsymbol{\lambda} \times \boldsymbol{q}}{\boldsymbol{h} \times \boldsymbol{c}} \tag{2-8}$$

Where **λ** is the wavelength of the visible light; ***q*** is the charge of the electron, which is a constant of $1.602176634 \times 10^{-19}$ in coulombs; ***h*** is the Planck's constant of 6.63×10^{-34} J.S; ***c*** is the speed of light with 3×10^{9} meters per second.

The converted **SR** is then used to quantify the power output of the spectrometry with equation 2-9.

$$\boldsymbol{P}_{light\ \ source,\lambda} = \frac{|\Delta \boldsymbol{J}_{\boldsymbol{\lambda}}|}{\boldsymbol{SR}_{reference,\lambda}} \tag{2-9}$$

The spectral responsivity **SR** of the perovskite sample, in Amp/Watt, can be obtained by equation 2-10,

$$\mathbf{SR}_{\lambda} = \frac{|\Delta \boldsymbol{J}_{\boldsymbol{\lambda}}|}{\boldsymbol{P}_{light\ \ source,\lambda}} \tag{2-10}$$

where $\boldsymbol{P}_{light\ source,\lambda}$ refers to the incident light irradiation at the particular wavelength and $\Delta \boldsymbol{J}_{\boldsymbol{\lambda}}$ is the difference of device short circuit current with or without light exposure at that wavelength.

The device's short circuit current density, $\boldsymbol{J}_{\boldsymbol{SC}}$, can then be estimated with the spectral response obtained, with equation 2-11.

$$\boldsymbol{J}_{\boldsymbol{SC}} = \int \boldsymbol{S}(\boldsymbol{\lambda}) \times \boldsymbol{P}_{\boldsymbol{0}}(\boldsymbol{\lambda}) d\lambda \tag{2-11}$$

where $\boldsymbol{S(\lambda)}$ is the spectral response obtained from measurement, and $\boldsymbol{P_0(\lambda)}$ is the AM 1.5 irradiance reference spectrum obtained from National Renewable Energy Laboratory [135].

2.5 Conclusions

Perovskite solar cell is a new type of solar cell that has many application potentials. Although there are still challenges in the stability of the material, since the fabrication process is mainly solution processed, the device can be fabricated in various ways and utilize in different applications. The measurement method for determining the device characteristics according to international standards is vital for accurate characterizations, this chapter also provided the characterization techniques used and the related background theory.

3. Nanofabrication and Characterization Techniques for Solar Cells

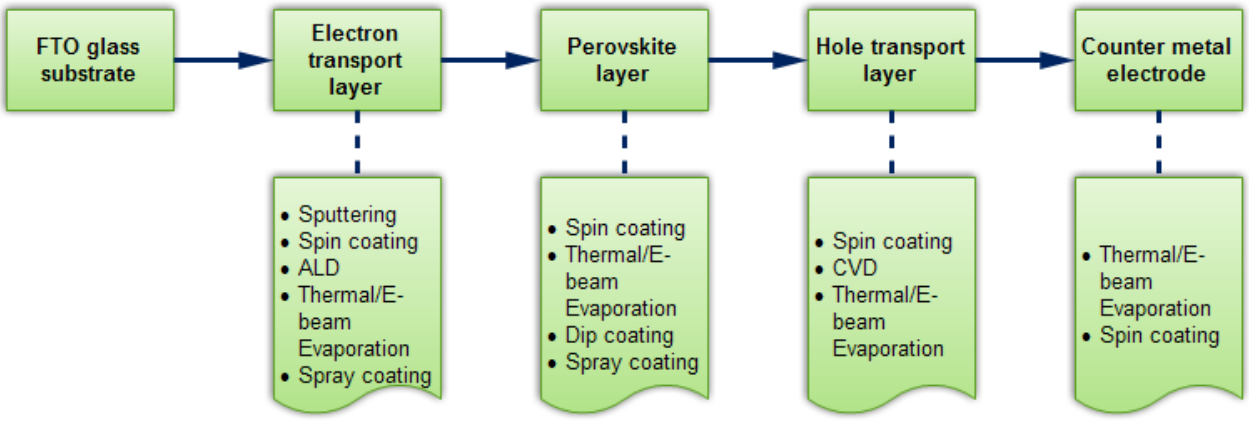

Figure 3-1 General fabrication flow chart of a perovskite solar cell

The fabrication of the solar cell involves many different fabrication technologies [136]. For this research, various fabrication processes that are commonly used in photovoltaic and semiconductor devices have been used for fabricating the thin film based perovskite solar cell. A simplified fabrication flow chart of perovskite solar cells is shown in Figure 3-1. This section provides a brief description and explanation of the techniques used. This includes different types of lithography followed in defining the active area and electrode patterns of solar cells to ensure the device is fabricated as designed. The completed device needs to be tested to determine the performance of the device under sunlight conditions. This is also to verify if the hypothesized device operation theory works as expected. Moreover, the structure of the solar cell for this research is a thin film based solar cell structure, with a stack of thin films composed of different materials. Therefore, it is necessary to optimize each layer to achieve the highest possible efficiency. To achieve this, the thin films were characterized electrically, optically, and structurally with different thin film characterization techniques, which will be explained in section 3.4.

3.1 Lithography for pattern transfer

Lithography is a key technique for all electronic devices and it is used in the photovoltaic fabrication process. The active area for which a solar cell is used for photon-electron conversion is usually defined with a predesigned pattern using different lithography techniques depending on pattern size, materials thicknesses, and ease of scaling up. In this section, different lithography techniques that have been used in fabricating perovskite solar cells and related features were described and explained.

3.1.1 Photolithography with Mask Aligner

Photolithography, or optical lithography [137], is probably the most common method used in defining the active area and metal contact positions for photovoltaic devices. A photosensitive polymer based material is exposed to UV light through a mask that contains the pattern of interest, as shown in Figure 3-2. The predesigned features were defined on a "mask", then transferred onto the substrate via the mask aligner. The mask aligner, Karl Suss MA-6, is used to align the position of the predesigned pattern to the desired position on the substrate. The substrate was covered with approximately 1.8 μm of positive photoresist AZ 1518, for direct transfer of the pattern from the mask on the substrate. The photoresist onto the substrate is then exposed to 365 nm UV light, through the mask for approximately 8 seconds, with 5 mW/cm^2 irradiation intensity. Similar to the conventional photography operation theory, the exposed substrate coated with a positive type photoresist is then developed with the alkaline developer to remove the exposed photoresist.

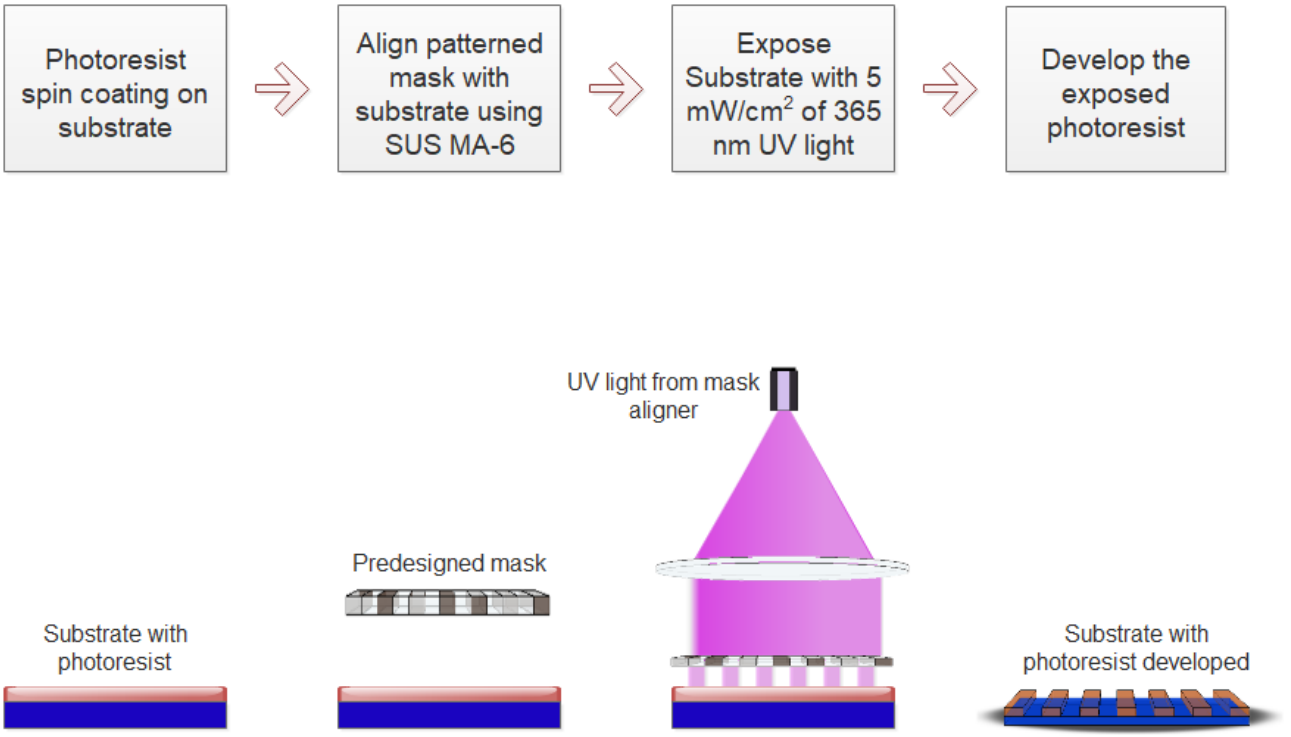

Figure 3-2 Schematic of the Photolithography process. The substrate with photoresist deposited on top is aligned with the predesigned mask with a mask aligner. The aligned mask and substrate are then exposed with UV light to crosslink the photoresist. For positive photoresist, the area that was not covered by the mask can be rinsed off with the developer, whereas when the negative resist cross-linked into solid form when exposed to UV light.

3.1.2 Laser Interference Lithography (LIL)

Laser interference lithography (LIL) can be utilized to produce periodic patterns with scalable potential at a cheaper cost [138, 139]. As opposed to conventional lithography, the predesigned mask is not required for interference lithography to pattern periodic lines or dots in nanometer sizes. Since LIL is a maskless technique, there is no need for the expensive Mask Aligner for mask and substrate alignment. This is particularly useful in patterning periodic holes or gratings on solar cells for light trapping features. The simplified setup is shown in Figure 3-3. A class 2B, 325 nm laser with 20 mW intensity is used as a light exposure source for making periodic patterns on the substrate. A mirror directly perpendicular to the substrate holder is used to reflect the incoming laser onto the substrate so that the reflected beam from the mirror and the incident beam from the laser to the sample could form an interference pattern. This forms regions of high and low light intensity (constructive or destructive interference). The angle θ between the mirror and the substrate

determines the period and separation of each line. Patterning dots can be achieved by double expose the sample with the sample rotate with a certain angle for second exposure (usually 90°). The spatial filter is used to produce a clean Gaussian beam without undesired fringes. Moreover, the laser beam diameter could be expanded, via the spatial filter, to cover larger areas. The current limit for the system at Nanofabrication laboratory, University of Canterbury, however, is that the maximum exposure area with interference lithography is around 1.2 cm × 1.2 cm. Increasing the distance between the substrate and the spatial filter could potentially increase the exposure area, but the intensity of the laser reaching the sample would be reduced at the same time, resulting in a longer exposure time for each sample. The laser intensity reaching the sample with the current set up is approximately 170 µW to 180 µW. This is the technique used to form the nanopyramids in this research, which will be covered in Chapter 5.

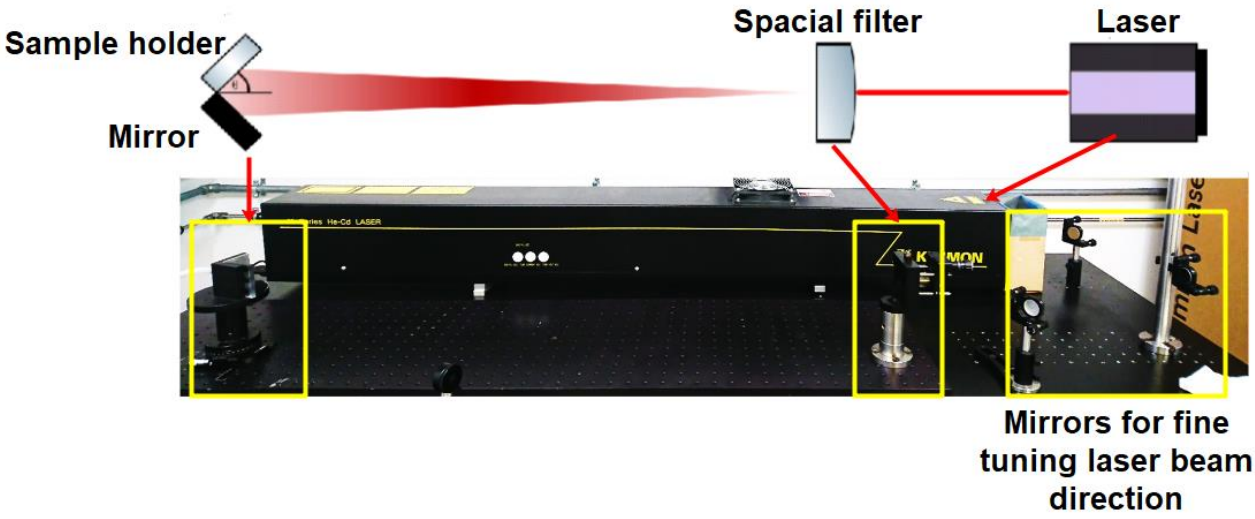

Figure 3-3 Top: The schematic of a simplified setup of interference lithography. Bottom: the LIL set up at the University of Canterbury. The laser was reflected by 3 optic mirrors to fine tuning the direction of the laser beam. The laser is then passed through the special filter and the pinhole to expand the laser's exposure area and produce a clean Gaussian profile of the laser beam to the sample with spatial noise removed. Part of the laser beam did not expose to the sample directly, instead, a mirror was used to reflect the partial laser beam onto the sample. The portion of the laser that exposed directly onto the sample was coincided with the reflected laser light, resulting in an interference effect.

3.1.3 Nanoimprint Lithography

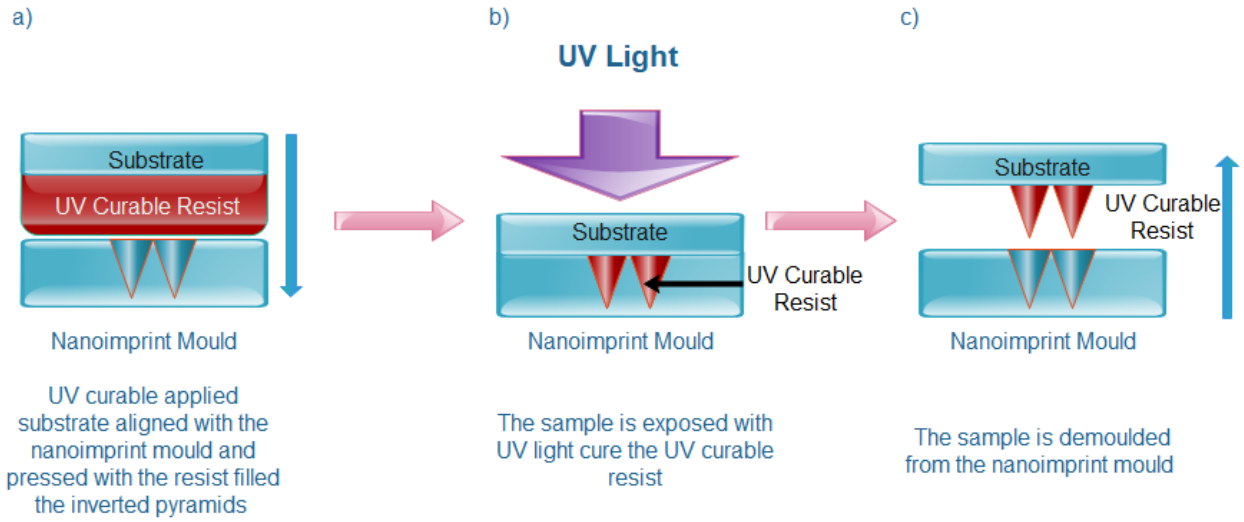

Figure 3-4 Nanoimprinting process flow. The nanoimprinting mould with inverted periodic nanopyramids was patterned with interference lithography and fabricated with dry and wet etchings. A UV curable resist was first dispensed on the substrate then aligned and pressed on the nanoimprinting mould with the required force. The sample is then exposed to UV light to crosslink and cure the resist. Once the resist is cured, the substrate is then demoulded from the nanoimprinting mould. The demoulding process can be done automatically or manually depending on the available equipment. At the nanofabrication laboratory at the University of Canterbury, the sample and nanoimprinting mould are aligned and press down by the Suss MA6 mask aligner, where the demoulding process is done manually.

Nanoimprint lithography is a useful technique in replicating large areas of 3D structures without losing detailed features in nanometers size. For this research, it was used to fabricate the upright nanopyramids for light trapping features which were predefined using interference lithography [140, 141]. The overall process is shown in Figure 3-4. The sample is overlapped on the imprint mould with a UV curable resist in the middle. The overlapped substrate-mould pair is usually clamped down with a constant force during UV light exposure to ensure the equal flow of the resist across the whole area. The UV curable resist would solidify during UV exposure. Once the resist is cured, the substrate is demoulded from the imprint mould. The replication of 3D structures is greatly affected by the physical characteristics of the resist such as the resist viscosity, and the feature profile on the mould. This will be covered in more detail in Chapter 5.

3.2 Thin film deposition

Thin film deposition techniques were used for depositing different types of thin films, such as metals, semiconductors, or insulating materials in nanofabrication processes. Different techniques would result in different thin film characteristics, uniformity, and will affect the performance of the fabricated device. Below is a brief description of the various techniques used in the perovskite solar cell fabrications.

3.2.1 Spin coating

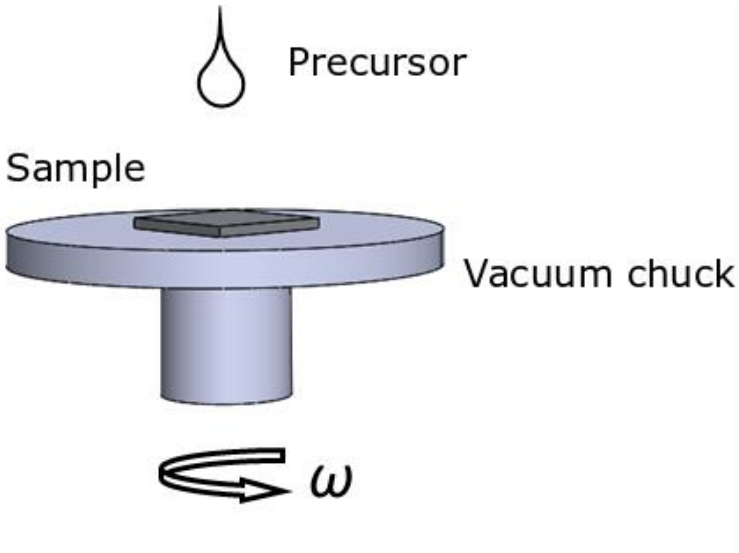

Figure 3-5 Set up of spin coating materials with sample fixed on sample holder by vacuum illustrating the sample holder (pedestal)

Spin coating is one of the simplest and cost-effective methods in thin film deposition. For 3rd generation solar cells, spin coating is one of the popular ways to fabricate multilayer thin films. [33, 100, 103, 142, 143] This technique is simple to use and low in setup costs. This is done by spinning the sample with a precursor solution at an angular speed ω, as shown in Figure 3-5. The centrifugal force that occurred from spinning the sample pushes the precursor material away from the center resulting in a uniform thin film of precursor on top of the substrate. Several factors determine the thickness and uniformity of the film deposited. This includes the viscosity of the precursor, the hydrophilicity of the substrate, the speed, acceleration, and duration of the spin

coating process. Depositing the precursor material before or after the spinning starts (static or dynamic spin coating respectively) also affects the result. Dynamic spin coating is a more controlled process with less material required to achieve the target thin film thickness, but with a risk of not getting complete coverage on the substrate. Therefore it is more suitable for high spin speed processes or low viscosity materials. Static spin coating, on the other hand, is a better way for viscous materials such as photoresists and low spin speed process due to stronger centrifugal force at the start of the spinning. Spin coating is the main method used for research for coating most of the layers for the perovskite solar cell in Chapters 4 to 6. This includes the mesoporous TiO_2 layer, active perovskite $MAPbI_3$ or CsMAFAPbIBr perovskite layer, and the spiro-omeTAD hole transport layer.

3.2.2 DC Magnetron Sputtering for metal oxides

DC magnetron sputtering is a widely used technique in depositing various dense thin films with high purity, especially metallic materials, under low pressure, at around 10^{-3} mbar, instead of requiring much lower pressure (around 10^{-6} mbar) for thermal or electron beam evaporation [144, 145]. It can deposit thinner and higher quality thin films, eliminating the possibility of pinholes on the film when compared with thin films deposited with spin coating or dip coating methods. This is essential for thin film based solar cells since the pinholes result in a higher electron-hole recombination rate or route for short circuit. A high electric field is generated by the sputtering system power source to ionize the processing gas, which usually high atomic weight gas such as Argon. The energized argon ions bombard the sputtering target ejecting target atoms and deposited onto the substrate. In our system, Magnetron Sputtering, there are magnets underneath the sputtering target, producing a magnetic field as shown in Figure 3-6.

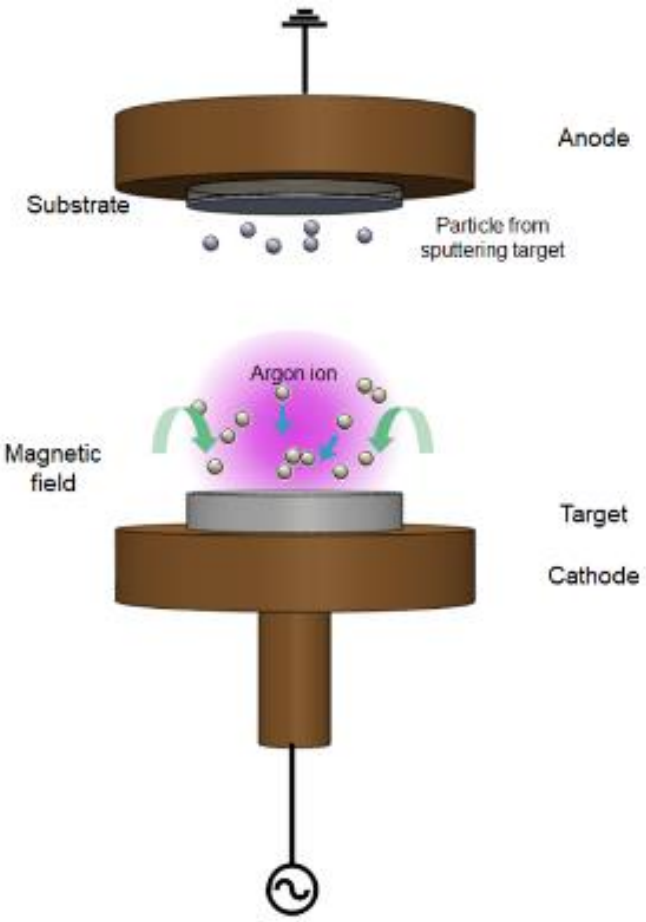

Figure 3-6 Right: Edwards Auto 500 system with 2 different sputtering depositions and electron beam evaporation. Left: an illustration of the target/substrate arrangement. The target is connected to the RF/DC power source, the substrate is placed on the sample holder held at ground potential. The RF/DC power excited Argon ions are used for bombarding the target molecules from the target. The energy from Argon ions is transferred to the target molecules, allowing them to travel upward toward the substrate. When the molecules reached the substrate, it is slightly cooled and accumulated on the substrate.

This magnetic field is used to confine the Argon ions within the target area increasing the ionization efficiency, inducing high density ions, and increasing the sputtering yield. The ability to deposit thin films under low pressure results in higher purity of the sputtered material deposited onto the substrate with fewer contaminations from the atmosphere. For the deposition of metal oxide films for perovskite solar cell applications such as TiO_2, additional energized oxygen ions are required to react with the Titanium atoms, forming metal oxide particles before resting on the substrate. The amount of oxygen used during this process is dependent on the stoichiometry of the material. Sputtering of transparent TiO_2 with anatase phase, for example, requires a high flow rate of oxygen gas to reach the required stoichiometry. This deposition system contains RF and DC sputtering

sources in addition to the Electron Beam Evaporation source.

3.2.3 Electron Beam Evaporation

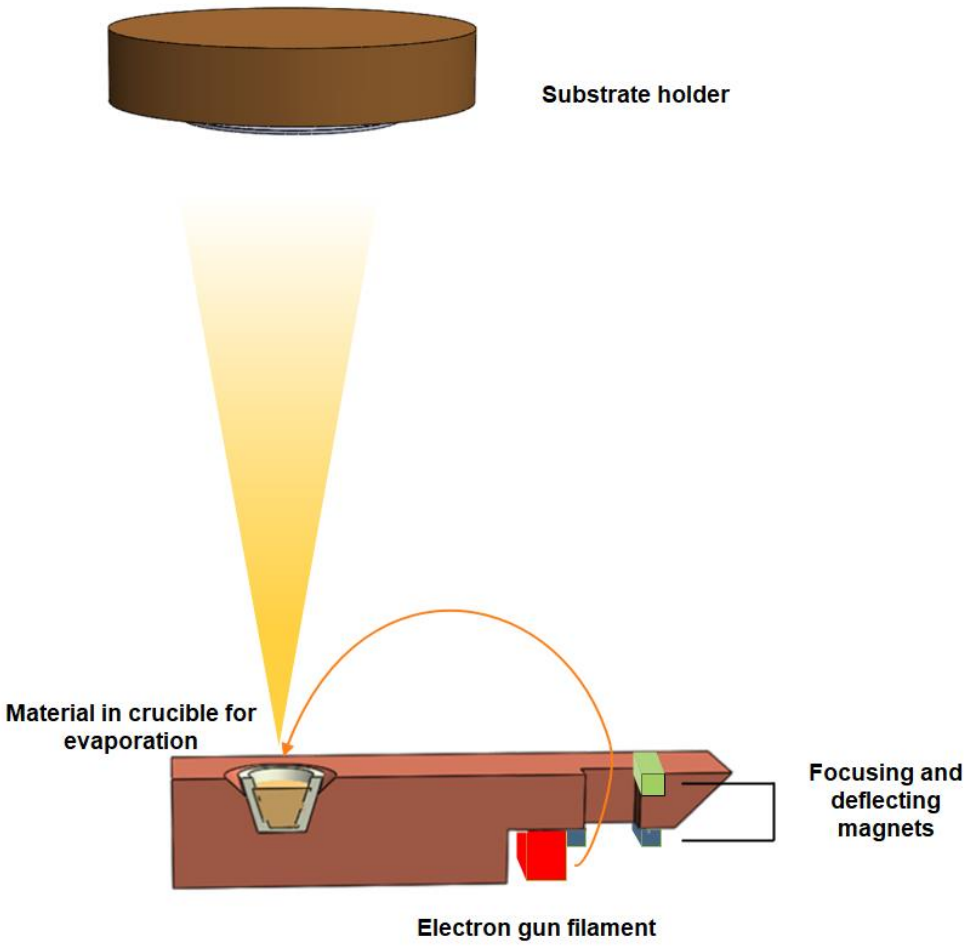

Figure 3-7 An illustration of the Electron beam evaporation mechanism. The substrate is held on the sample holder (top), the crucible containing the material to be evaporated (bottom) is exposed to the high energy electron beam.

The electron beam evaporation is the only metal deposition technique employed in this research, to deposit the contact metal without causing damages to the already deposited polymer films on the substrates [146, 147]. This is essential for perovskite solar cells deposition since some of the layers in the perovskite solar cells are polymer based and don't withstand high temperature processing. The E-Beam Evaporation set up is part of the Edward Auto 500 sputterer system described in Section 3.2.2. It uses an electron gun shooting high energy electrons directed towards the material inside the crucible at the cathode via magnetic fields, as shown in Figure 3-7. The bombarded material gets heat up above its melting temperature and evaporate and condense on the substrate.

Electron beam evaporation could effectively evaporate high melting point materials such as SiO_2, and Al_2O_3 at high vacuum, since the electron beam can produce much higher power density compared to conventional resistive evaporation deposition (thermal evaporation).

3.3 Material etching

While the lithography is for defining the patterns, etching is a subtractive pattern transfer method used to remove unwanted materials and form the final structures with the required profile and dimensions. This is a relatively delicate technique, especially when a pattern needs to be transferred through several layers, or if different patterns are required for each thin film layers in a device like thin film solar cells. In general, materials etching can be separated into wet or dry etching [148]. Wet etching is simple to set up and has very high selectivity between materials compared with dry etching. However, the etchants used for wet etchings do get degraded, so frequent change in etchant is required for larger numbers of samples. Although dry etching could eliminate the problems encountered with wet etching, it requires expensive equipment, such as reactive ion etching or inductively coupled plasma etching to perform the etching process. This section gives a brief description of the techniques used for this research.

3.3.1 Wet etching

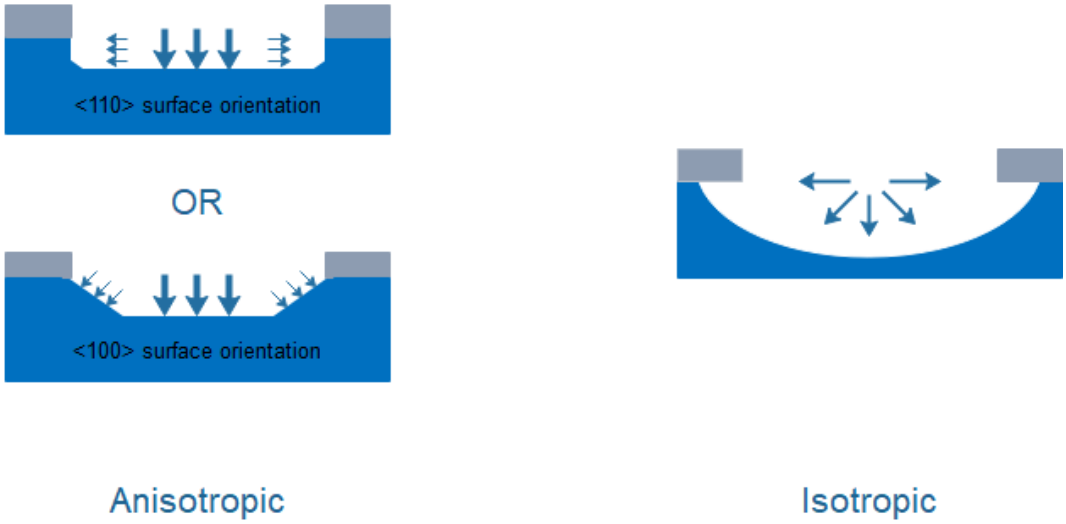

Figure 3-8 Anisotropic and Isotropic wet etchings. The arrows refer to the etch rate at vertical and lateral directions. Isotropic etching has an equal etch rate at both lateral and vertical etching directions. Anisotropic has a higher vertical etch rate compared to etching in the lateral direction. The anisotropic lateral etching is strongly dependent on the orientation of crystal growth.

Wet etching is one of the most commonly used methods in semiconductor device fabrication. It essentially relies on the chemical reaction between the substrate surface and the etchant to remove the targeted material from the substrate. It is easy to set up, with just glass or plastic beakers and does not require advanced equipment to carry out the etching process. However, due to the toxicity of the acids or alkali used and the toxic gas produced during the process, it is necessary to work under a well-ventilated fume hood with required personal protective equipment such as gloves, safety glasses, and acid/alkali resistant gloves. Wet etching could also be separated into anisotropic or isotropic etching, as shown in Figure 3-8. Isotropic etching and bigger undercuts of the substrate below the masking material Etching a silicon substrate with <1 0 0> orientation, for example, results in 54.74 ° angled sidewalls. For this research, anisotropic etching was used to fabricate the inverted pyramids into the silicon substrate as a master mold for nanoimprinting. The detailed fabrication process will be presented in Chapter 5.

3.3.2 Inductively coupled plasma etching (ICP)

Dry etching is the process of using gases to perform the material removal process. It is a combination of the chemical reaction to form volatile radicals and the physical bombardment to knock atoms off the target. The resultant etching can have very steep sidewall profiles with no undercut problems that are usually found in wet etching.

ICP is a relatively new dry etching technique used to etch substrates or thin films without the use of hazardous acids or solvents. In comparison with the conventional reactive ion etching (RIE), ICP can etch materials deeper, with high aspect ratios in much shorter times even when the feature sizes are in the nanometer scale. The energized ions from the reactive gas, such as SF_6 for silicon etching, reacts with the surface of the substrate and form volatile gas molecules (SiF_4 for example, produced from the reaction between silicon and SF_6) with the substrate atoms. These molecules are then get removed from the chamber via vacuum pumps.

Figure 3-9 shows the schematic of the Oxford PlasmaPro 100 Cobra ICP chamber with an illustration of the main components shown on the left. It is a cylindrical chamber with copper coils externally wrapped around the chamber wall. The wafer stage is temperature controlled by an externally connected fluid re-circulating chiller. Helium gas backing can also be used for better temperature control. The RF power, which can be as large as 1500W, applied to the coils creates an electric field in the upper half of the chamber to generate and control the high density ionic plasma (ion density $> 10^{11}$ cm^3). A much smaller RF power (< 200 W) is applied to the substrate holder to control the energy of the ions approaching the sample. This enables a high etching rate while maintaining the chamber at relatively low chamber pressure. Moreover, higher selectivity for etching the substrate while the damage to the masking layer is minimized can be achieved, since the high energy ions result in better anisotropy when compared with the conventional reactive ion etching [149]. Depending on the process gas used during etching, different masking materials are required for etchings with good selectivity. While an acid or alkali resistant polymer such as AZ1518

photoresists is enough to act as the masking layer with good selectivity for wet etching, the mask selection for plasma deep etching need to be more robust to the highly energized ions and has minimal reaction to the reactive gas. Therefore, metal masks such as Aluminum, and Chromium are commonly used for dry etchings.

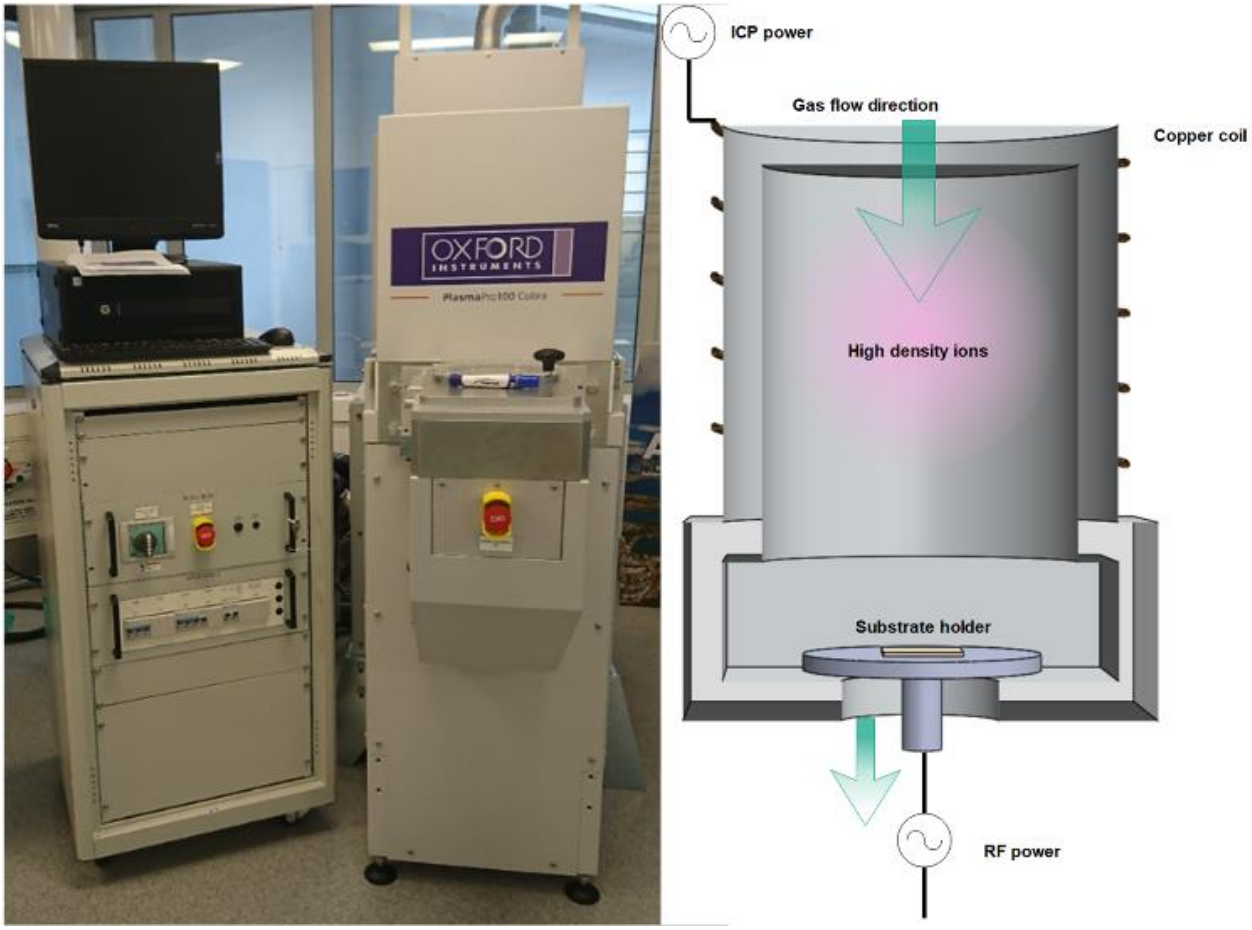

Figure 3-9 Image of Oxford 100 Cobra ICP (left) and a schematic of the inside of the ICP chamber (right). The temperature of the substrate holder is controlled by the chiller with fluid re-circulation. The copper coil wrapped around the chamber produced an electric field in the chamber by applying high RF power (usually 1000 W or above), results in high density ion plasma when the process gas is introduced.

3.4 Thin film characterizations

3.4.1 Atomic Force Microscopy

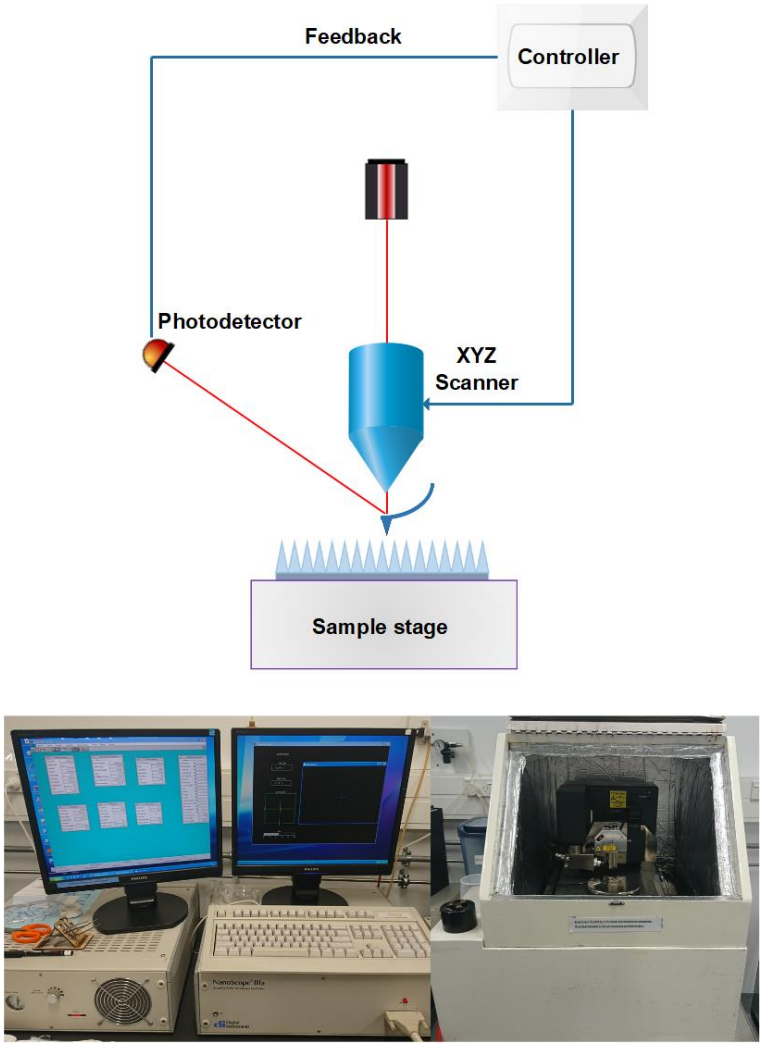

Figure 3-10 Top: The schematic of AFM set up. The sharp tip attached cantilever was controlled by a piezoelectric motor which oscillates the cantilever at its resonance frequency (270 kHz to 330 kHz for silicon tip from Budget Sensor Tap-300G) to tap the surface of the thin film at few nanometers above the thin film surface, using the atomic force between the atom at the cantilever tip and the atom at the material surface to detect the thin film surface features. The cantilever tip is deflected at different heights while scanning the features of the sample surface. The difference in cantilever deflection magnitude is detected by the photodetector, which converts the difference in angle and position of the reflected laser light from the cantilever into signals that could be sent through a feedback loop to the electronic controller and recorded as the change in Z directions. The information is then sent to the XYZ scanner which fine tunes the position of the tip above the surface so that the amplitude of tip deflection does not exceed the limit. Bottom: The DI 3100 Nanoscope III AFM from VEECO at The nanofabrication laboratory, University of Canterbury.

Atomic force microscopy (AFM) is a high-resolution method for imaging thin film's surface morphology without charging problems. This method can obtain information regarding surface roughness, pattern dimensions down to nanometer scale, grain size, and thin film thickness. Obtaining this information helps understand the interfaces between the different thin film layers that form the perovskite solar cells. Digital Instruments (DI) 3100 Nanoscope III AFM from Veeco Instruments Inc. in tapping mode was used for this research and the simplified operation mechanism is shown in Figure 3-10. AFM in tapping mode refers to the measurement of the sample by "tapping" the surface of the sample with the sharp tip attached cantilever.

A cantilever with a less than 10 nm diameter sharp tip attached at the end was oscillated by the piezoelectric motor at the cantilever's resonance frequency. The cantilever was allowed to move in X and Y directions, at a few nm above the sample surface. The unevenness of the surface of the thin film causing a change in the force between the atoms at the tip and the sample surface. To maintain a constant force between the tip and the surface, the cantilever is deflected from the sample surface. The magnitude of the deflection causes the laser focusing on the back of the cantilever to be reflected at different angles. The photodetector detects the reflection of the laser beam and converts it to electrical signals that feed through the feedback loop to the electronic controller and recorded as the change in the Z direction at the particular X-Y position. The recorded data sets containing the position of the tip at X, Y, and Z direction could then be converted to a 3D image of the sample. While AFM can measure surface morphology at resolution in less than 10 nm, it does come into contact with the measured thin film. Therefore, if the thin film measured is not robust enough, the probe of the AFM can easily scratch the surface and result in incorrect measurements of the sample.

3.4.2 Scanning Electron Microscopy

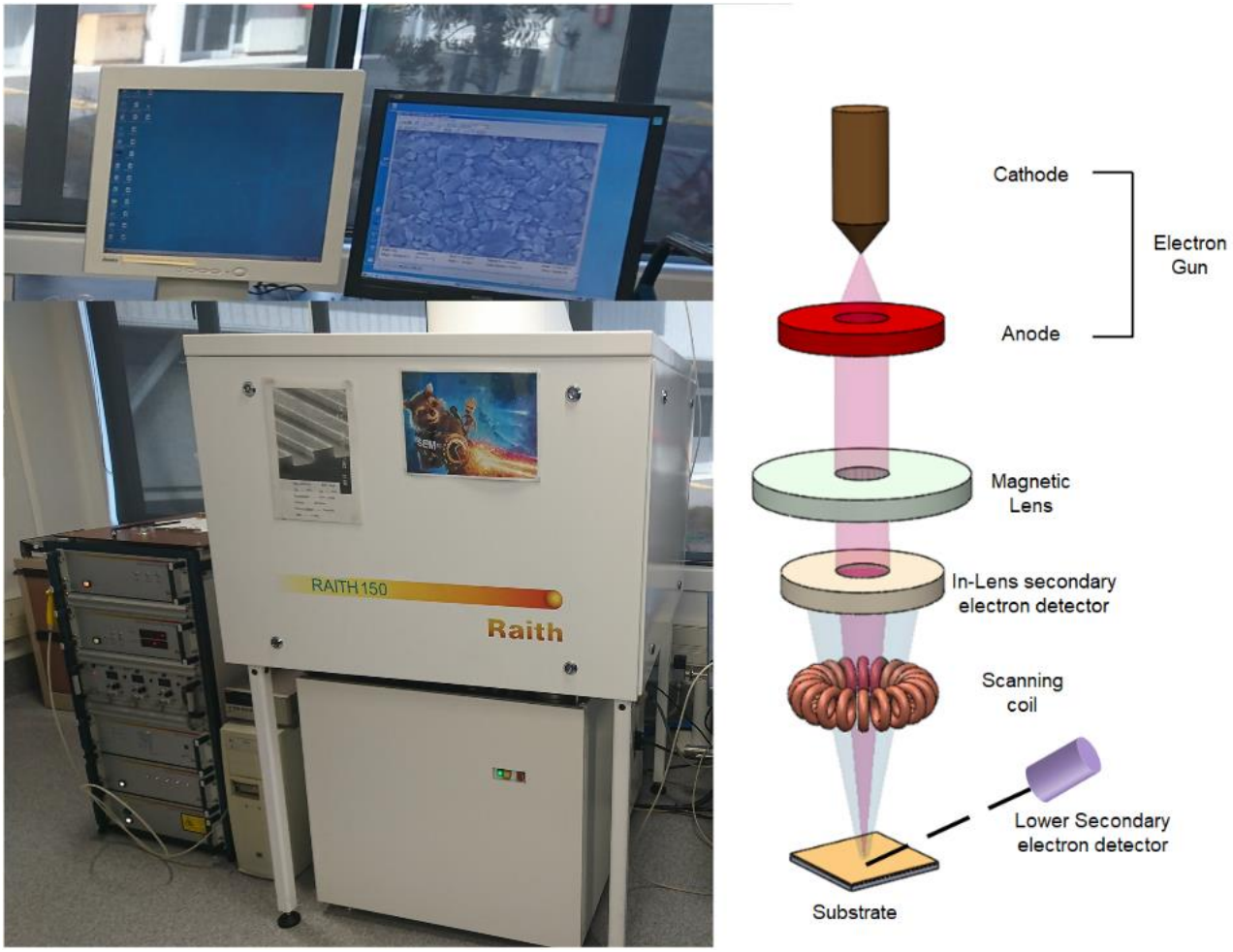

Figure 3-11 Left: Raith 150 for electron beam lithography at the University of Canterbury. SEM is an add-on feature in Raith 150. Right: Simple operation schematic of the SEM system. The cathode of the electron gun produces a cloud of electrons which are collected by the positively charged anode to form the electron beam. Several magnetic lenses were used to control the diameter of the electron beam and directs the electron beam towards the sample stage. The scanning coil, or deflector coil, is used to deflect the beam from side to side to scan the desired area. Two secondary detectors (inLens and lower SE, inLens is more commonly used) are used to collect the secondary electrons from the substrate and convert it to signals that then convert to the image with the software.

Scanning Electron Microscopy (SEM) is another method of acquiring thin film surface morphology down to nanometer scales. Moreover, it is a contactless imaging method, so there is much less risk in scratching the sample when compared with AFM. The SEM used in this research is an add-on feature from the Raith's Electron Beam Lithography (Raith 150) for patterning substrates with complicated features down to ~30 nm resolution. Figure 3-11 shows the image of the equipment

and the brief operation principle of the equipment. An electron gun fires high energy electrons, which was collected by the anode metal plate and gets focused on the substrate by the magnetic lenses. The scanning coil deflects the electrons in the X and Y direction to scan the surface in a 2-dimensional motion. When the beam of electrons scans the sample surface, different types of electrons were generated from the sample surface. This includes backscatter electrons, secondary electrons, and different types of x-rays that are generated and deflected from the substrate. An inLens secondary detector and a lower secondary electron detector were used to collect the secondary electrons that were generated from the substrate during electron beam scanning. The collected secondary electrons were then converted to digital signals, which is the main information source of the acquired image. A thin layer of metal (approximately 2 nm is usually enough) is usually required for non-conductive materials due to the charging effect of the electrons on the surface of the material.

3.4.3 UV-Vis Spectrometry

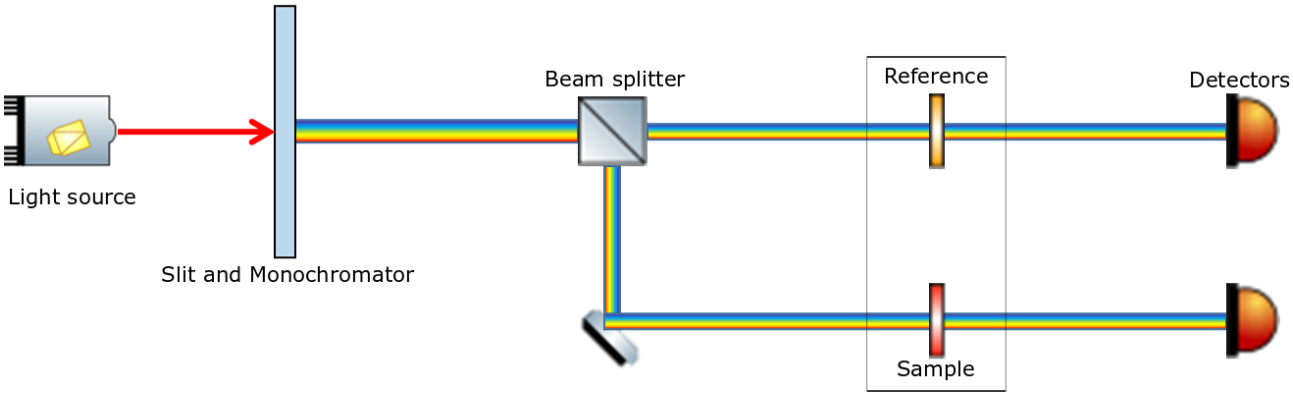

Figure 3-12 Illustration of the optical setup of Cary 6000i UV-Vis spectrometer. The white light/UV light passes through the slit and monochromator to allow light with a single wavelength to reach the sample.

Cary 6000i UV-Vis spectrometer from Agilent is the essential tool in studying the optical characteristics of the photon sensitive active layers of the perovskite solar cells. This includes measuring the transparency of the transparent conductive oxide electrode. High transparency is required to ensure most of the incident light passes through the electrode for efficient photon-electron conversion at the photoactive layer. For the photoactive thin films in photovoltaic

applications, this is looking at the light absorbance at the visible light wavelengths corresponding to the sunlight irradiance. As shown in Figure 3-12, a beam of broadband light was passed through the slit and monochromator to allow the exposure of monochromatic light on the sample. A reference sample was used to compare with the testing sample to compensate for the light absorbance of the substrate and normalize the results.

The intensity of the light that went through the sample was collected by the detector held behind the sample and compared with the intensity of the incident light. The result was sent to the computer and converted into absorbance, with the ratio between the incident light and the light collected by the detector following Beer's Law:

$$\mathrm{A} = \log_{10} \frac{I_0}{I} \tag{3-1}$$

where A refers to the absorbance of the material, I_0 refers to the incident light intensity and I refers to the intensity of the transmitted light reaching the detectors. This could also be used to determine the transmittance T and reflectance R of the sample film by the following equations:

$$T(\%) = \frac{I_0}{I} \times 100 \tag{3-2}$$

$$100(\%) = \%T + \%R + \%A \tag{3-3}$$

3.4.4 X-Ray Diffraction Crystallography (XRD)

XRD is one of the common tools in material analysis to study the crystal structure of the material. In particular, glancing/grazing angle XRD is the main method used for thin film analysis. When the incident x-ray beam reaches the surface of the thin film material at a small incidence angle (usually around 1 °), it would be scattered by the thin film atoms. The low incidence angle ensures the incident laser only reaches the topmost thin film layer, without picking up signals from the substrate. A diffraction effect occurs when two or more scattered x-ray beams with some phase differences are superimposed onto each other. The intensities of the scattered signals are then collected by the detector to obtain the diffraction pattern of the measured sample with signal intensity versus the

phase angle. Different materials with different crystal structures have a unique diffraction pattern.

Figure 3-13 shows the XRD equipment used for analyzing the crystal phase of TiO_2.

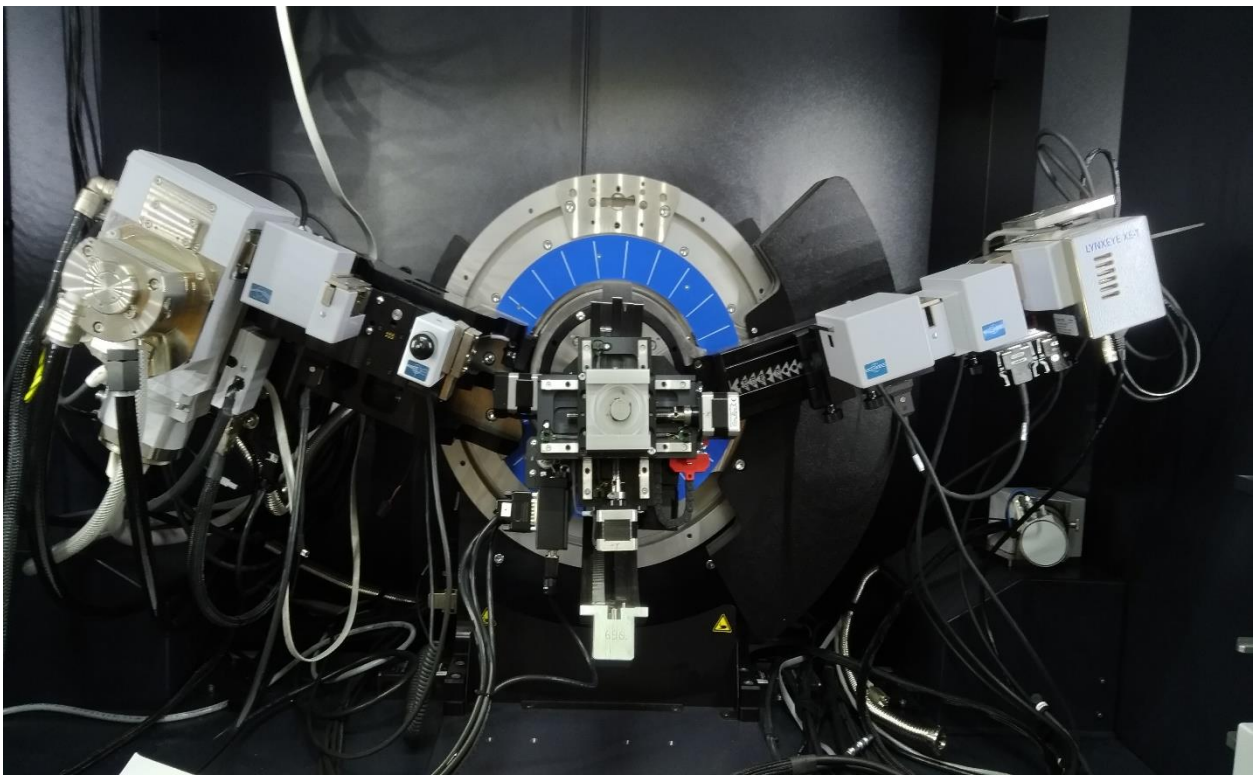

Figure 3-13 Brucker D8 Discovery multipurpose XRD with rotating anode.

3.5 Humidity controlled glovebox

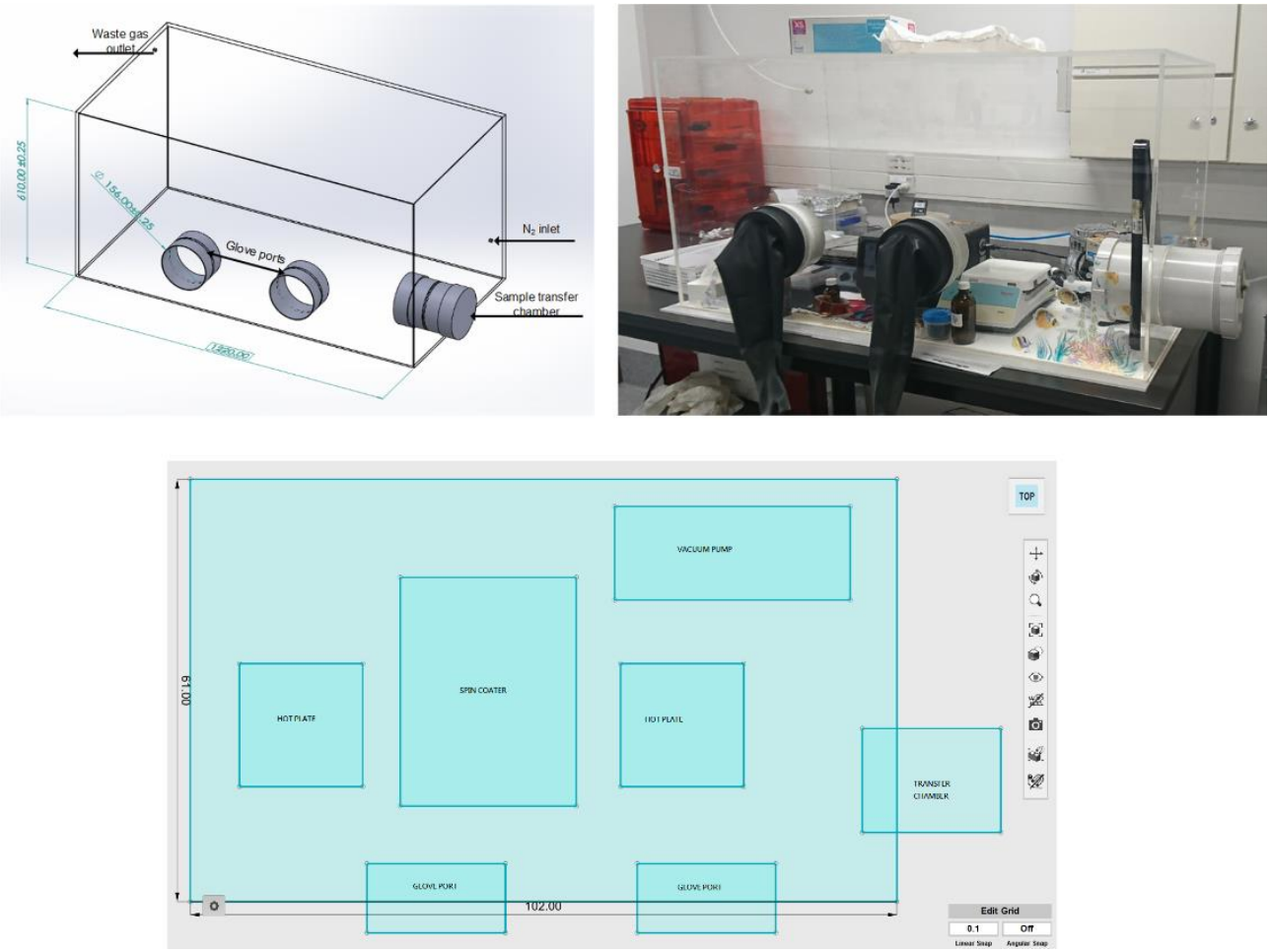

Figure 3-14 Top left: the schematic of the glovebox cover, showing the positions of glove ports and sample transfer chamber. Top right: the completed glovebox with a polypropylene base. The gaps between the glove box cover and the base were sealed with rubber to minimize air leakage into the box. Bottom: The setup of spin coater and hotplates in the glove box.

The fabrication of perovskite materials for solar cells is strongly dependent on environmental conditions such as humidity, oxygen level, and temperature [150]. There are various literature stated that the perovskite thin film quality, such as the grain size and structure, number of pinholes, and the smoothness of the film surface is greatly influenced by the moisture and temperature during the synthesis and deposition processes. Therefore, controlling the process fabrication environment is important. Most of the perovskite solar cells fabrication related research were carried out in humidity and oxygen controlled glovebox. These could cost over $50K NZD for a complete set up that operate to lower the humidity to almost 0% and close to 0 ppm for oxygen

content. This is achieved by removing the moisture contained in atmospheric air and replace it with dry air such as high purity nitrogen gas. However, the fabrication process for perovskite solar cells, especially for the devices with mesoporous structure, did not necessarily require zero humidity. There are reports verified that perovskite film quality is better when assisted by low levels of humidity. Therefore, it is possible to build a cheap humidity-controlled processing work station for the fabrication of perovskite solar cells provided it is performed in a Nitrogen atmosphere.

Figure 3-14 shows the design and setup of the glovebox built in house at the Nanofabrication Laboratory, Electrical and Computer Engineering Department, University of Canterbury for this research. An 8 mm thick of transparent acrylic panels were used for the glovebox case, and polypropylene was selected as the working bench surface due to its good chemical resistance. PVC pipe was used for the transfer passage and glove portal to lower the cost. The total cost was kept at around $1000 NZD to build.

To maintain the glovebox at a lower humidity level, approximately 5 L/min of nitrogen gas from the vaporization of liquid nitrogen was purged into the glovebox during the fabrication process with a ventilation outlet on the opposite side. The high flow rate of the gas is to ensure the evaporation of the excess solvent vapour after spin coating and to maintain a constant humidity level in the glovebox. While compact TiO_2 and mesoporous TiO_2 can be fabricated in air, both the photosensitive perovskite layer and the hole transport layer, spiro-omeTAD were deposited with the spin coating method in the glovebox. Post annealing of the deposited films was also done inside the glovebox. The samples were only removed right before the deposition of counter gold electrodes. The fabricated samples were kept either in the dry box with less than 10% humidity before characterisation and were stored in containers under low vacuum after measurements.

3.6 Conclusions

The majority of the perovskite solar cell fabrication was done with spin coating multiple thin film layers on the substrates. Sputtering was used for compact TiO_2 deposition to ensure a dense layer

between the transparent conductor and photosensitive perovskite layer, minimizing electron-hole pair recombinations. E-beam evaporation was used for counter gold electrode instead of sputtering, to ensure the polymer based spiro-omeTAD hole transport layer is not damaged by the sputtering plasma. A customized low-cost glovebox was built to control the humidity to below 15 % during spin coating the photoactive layer.

Most of the layers, apart from the spiro-omeTAD layer, has been characterized with thin film characterization techniques such as SEM, and AFM for film surface morphology, UV-VIS spectrometry for optical characteristics, and Photoluminescence spectrometry for electrical characteristics. The completed devices have been tested with the solar simulator for the I-V relationship to determine the device's overall power conversion efficiency, short circuit current density, open circuit voltage and fill factors. The devices with different perovskite compositions were also tested with the customized spectral response measurements to determine at which wavelength the devices generate current.

4. $MAPbI_3$ Perovskite Solar Cell Fabrication Optimization

Perovskite was initially referring to the calcium titanate mineral named after the famous mineralogist Lev Perovski [151, 152]. It was first discovered in 1839 by Gustav Rose in Ural Mountain, Russia. Calcium Titanate has a cubic crystal structure of ABX_3, as shown in Figure 4-1. The name Perovskite was later expanded to all materials with the same ABX_3 crystal structure, where A refers to the cation with a larger size, B is the other cation with a smaller size and X is the anion in the material. Since the beginning of the perovskite solar cell research in 2009, there are now several different perovskite compositions synthesized [153]. For this chapter, Perovskite refers to $CH_3NH_3PbI_3$ ($MAPbI_3$), where $CH_3NH_3^+$ (MA) is the monovalent cation A, Pb is the small cation B and Iodine is the halide anion X.

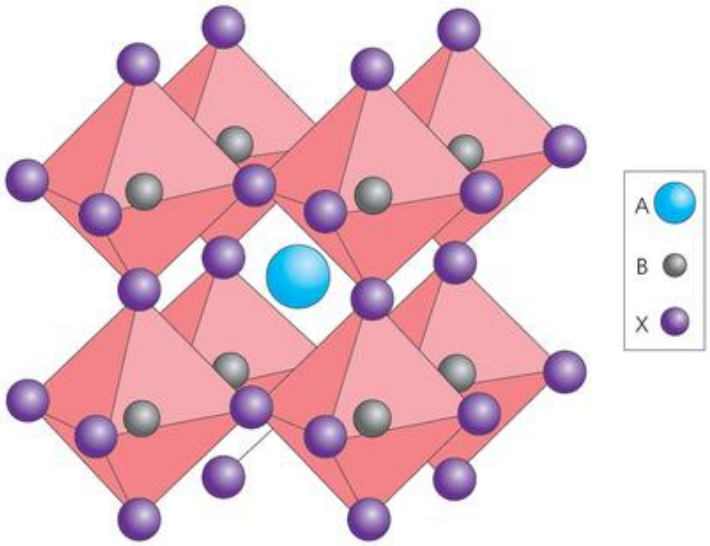

Figure 4-1 generic perovskite crystal structure, where both A and B are cations with different sizes, and X is the anion in the composition. Reproduced with permission from Martin A. Green et al [36]. For the perovskite material used in perovskite solar cell related applications, cation A usually refers to the larger organic monovalent cations such as $CH_3NH_3^+$, B refers to the smaller inorganic cation such as Pb^{2+}. X is the anion such as I^-, Br^-, or Cl^-.

One of the major issues with the perovskite solar cell fabrication is that the moisture in the ambient affects the crystallization of the $MAPbI_3$ thin film, as well as degrading the already crystallized material [16, 48, 83]. Therefore, the glovebox is required for perovskite preparation, with a controlled amount of oxygen and moisture in the chamber which must be kept at a level close to 0 ppm. The cost of such equipment is very expensive, looking at over $NZ 500,000. If the use of glovebox can be avoided, then the total cost of perovskite solar cells fabrication can be lowered significantly.

In this chapter, the perovskite solar cell structure and composition have been examined and tested for performance optimization without the use of a glovebox. The optimized cells are then used as the control samples for different experiments such as coating the cells with nanostructures and bandgap tuning for wavelength selectivity. The optimization in this study was mainly focused on the electron transport layer (TiO_2) and the active photon absorbing perovskite layer $CH_3NH_3PbI_3$.

4.1 Principles of Operation of Perovskite solar cells

The structure of PSC is similar to DSSC as shown in Figure 4-2. While there is a perovskite solar cell with different structures, PSC with mesoscopic structure was used for this research. PSC with mesoscopic structure has better performance and stability when compared with planar structure when this project commenced.

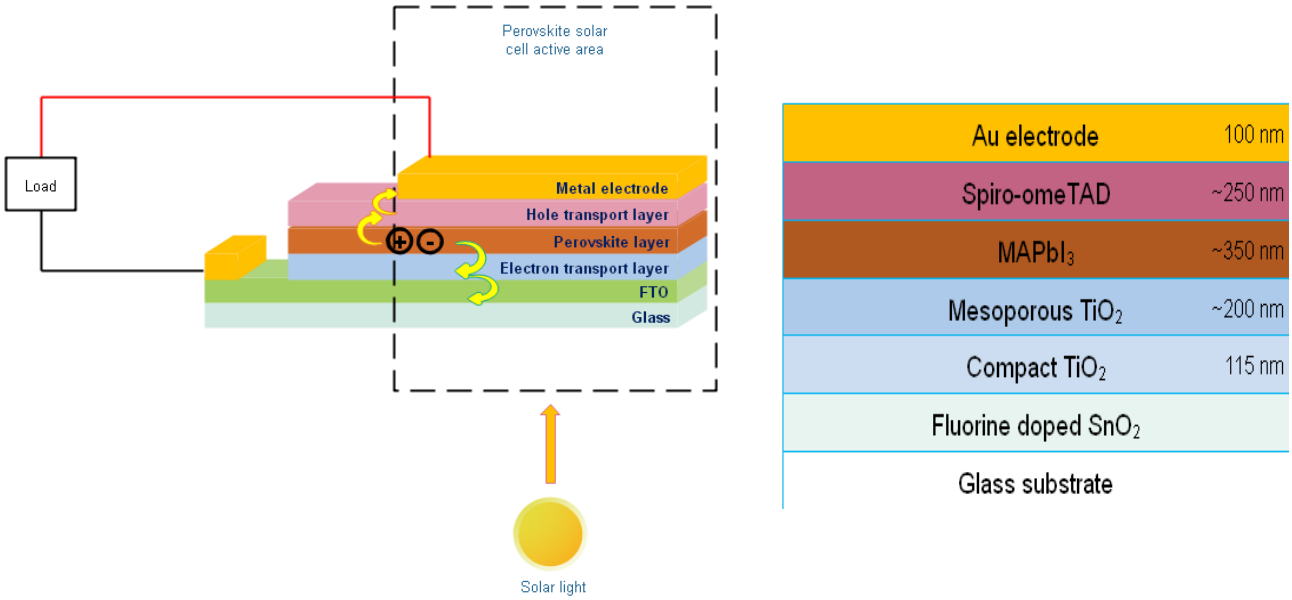

Figure 4-2 Left: A typical perovskite solar cell structure with an illustration of the electron and holes transport direction. The active area of the device is defined as the area directly below the metal electrode. The electron transport layer is usually highly transparent so that the light from the sun could travel through to the active photon absorbent perovskite layer. The perovskite layer absorbs the photon and generates an electron-hole pair, which then got separated and travel in opposite directions to the load. Right: Structure of the perovskite solar cell used in this research. Commercially available FTO glass was used for this research. The electron compact and mesoporous TiO_2 are the layers for the electron transport layer, $MAPbI_3$ is the active perovskite thin film, and spiro-omeTAD is the hole transport layer.

A substrate, such as glass or plastic is generally used as a base for building the multilayer structure of the perovskite solar cells. A transparent oxide layer, typically Fluorine doped Tin Oxide (FTO) or Indium doped Tin Oxide (ITO), is then deposited onto the glass substrates via spray pyrolysis. For this work, commercially available FTO glass or ITO glass was used to reduce one deposition step for the PSCs fabrication. The compact TiO_2 layer is then deposited onto the substrate as an electron transport layer, as well as a hole blocking layer. The 100 to 200 nm of mesoporous TiO_2 on top of the compact layer is generally used for enhancing the electron transmission in the perovskite solar cell and can also act as a light trapping material to trap the light inside the cell due to the porous surface of the film. The active layer, perovskite, normally deposited via spin coating or dip coating, is the main active layer for photon absorption and hole-electron pairs generation. The active layer is equivalent to the intrinsic layer if PSC is viewed as a p-i-n junction structure. The hole transmitting layer, typically Spiro-omeTAD, is the layer for transmitting the holes, as well as acts as the electron blocking layer for minimising recombination. The final layer in PSC structure is the

contact electrode, Au or Ag metals (or Ag/Al for inverted PSC structure) are the popular choices due to the high conductivity of the material and the small potential difference in valence band energy of the electrode and spiro-omeTAD in the universal energy chart shown in Figure 4-3

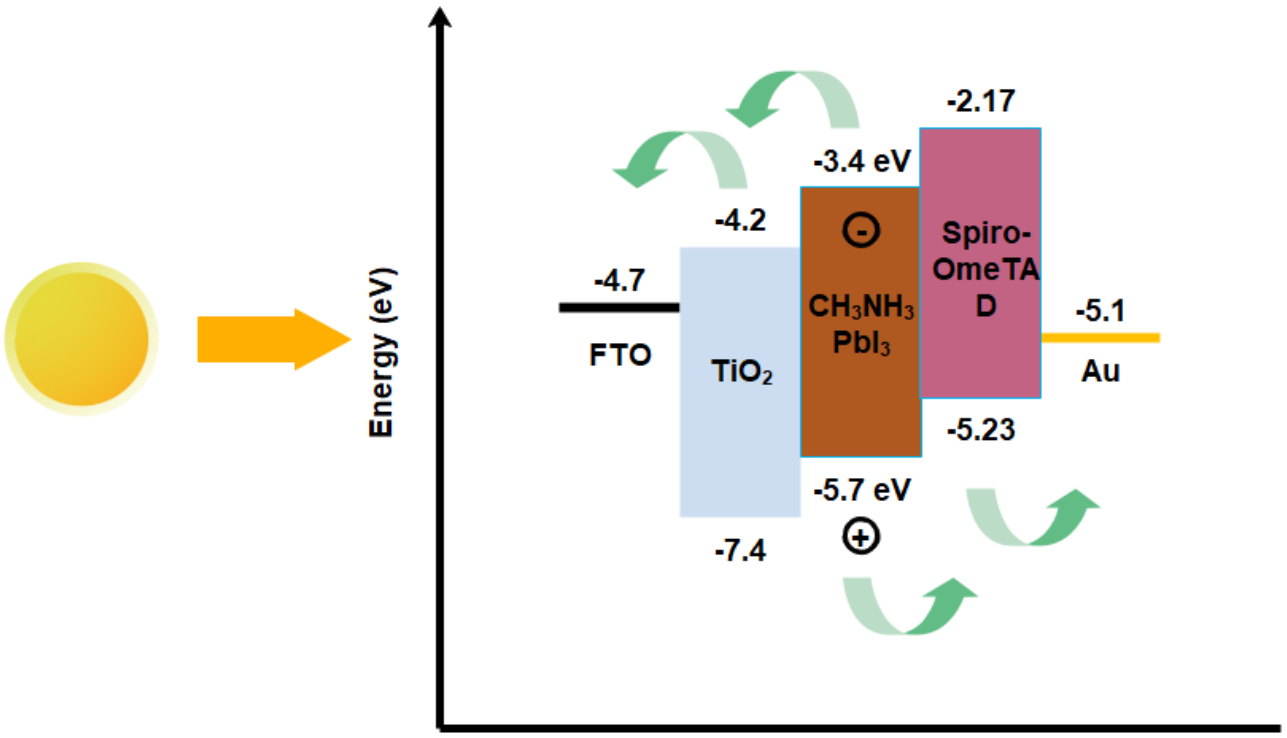

Figure 4-3 The universal bandgap energy alignment of perovskite solar cells and electron-hole pairs hopping towards the electrodes when the device is under sunlight condition. When the perovskite is exposed to the sunlight, the active $MAPbI_3$ perovskite layer absorbs the photons from the sunlight and generates electron-hole pair, which flow in different directions towards the load.

The basic theory in PSC operation, as shown in Figure 4-2, is relatively similar to how DSSC operates, where the photon-sensitive dye is the active photon absorbent material in DSSC. However, the operation of the DSSC device is based on the reduction-oxidation (REDOX) principle, where the dye absorbs the photon and excites the electron higher energy level. This enables the electron to be free from dye molecules and then get injected into the wide bandgap semiconductor and then diffused toward the load. Perovskite materials used for the perovskite solar cell applications, however, have various diffusion lengths (could range from a few nm to over 1 µm) depending on the material compositions. The active layer (Perovskite) absorbs the photons from the sunlight and generates electron and hole pairs. The electrons are then transferred to a load via the electron

transmitting layer (TiO_2) and the transparent conductive oxide (FTO or ITO). On the other hand, the holes travel in the opposite direction through the hole transmitting layer (Spiro-omeTAD) reaching the contact electrode (gold or silver) through to the load.

The conduction band (CB) energy of the wide bandgap oxide (TiO_2) is lower than the CB energy of perovskite, promoting a smooth electron transfer between the layers while minimizing the loss of energy during transportation. At the same time, the huge valence band (VB) energy of the two materials prevents the hole from traveling towards TiO_2, reducing the possibility of electron-hole recombination in TiO_2. A similar situation occurs between the perovskite layer and hole transmitting layer (Spiro-omeTAD), where a small VB energy difference (approximately 0.5 eV difference) between the two materials allows the holes to travel to contact electrode smoothly and a huge CB energy difference (approximately 1.3 eV difference) prevents electrons to enter from perovskite layer. The CB energy for the perovskite layer can be controlled by changing the small cation (eg. Pb, or Sn), while the VB energy depending on the difference in anion X (eg. I, Br, or Cl) [12, 13].

4.2 Fabrication Process for Perovskite solar cells

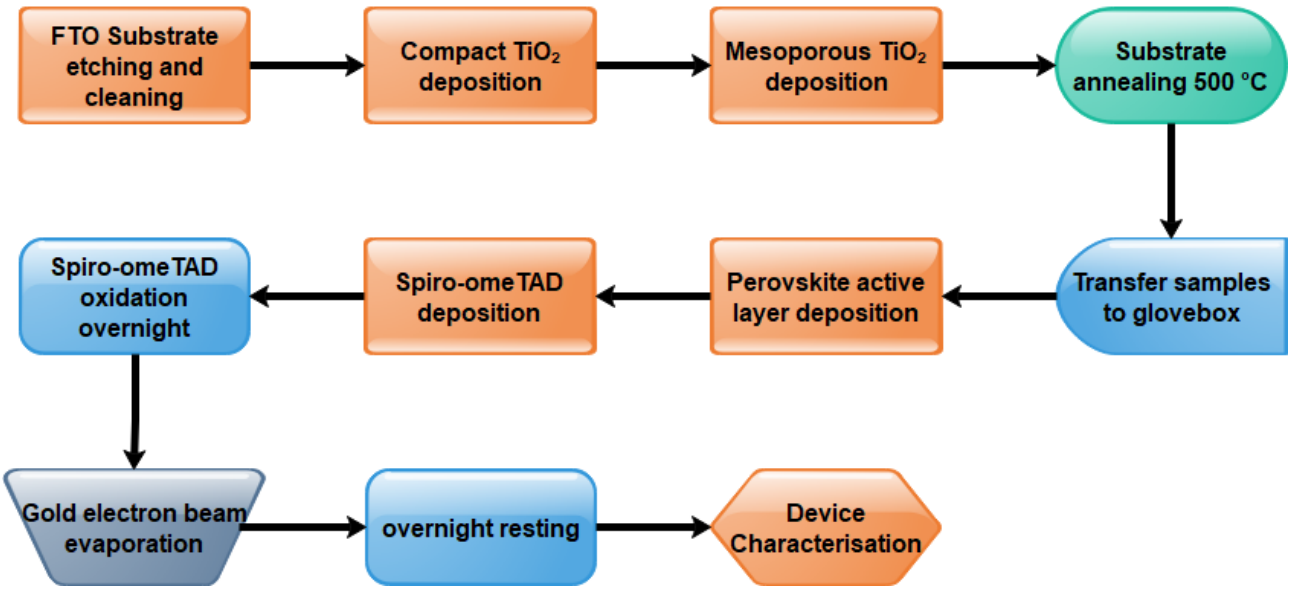

Figure 4-4 A general flow chart of the perovskite solar cell fabrication process. The fabrication process is following the bottom-up approach. Apart from the compact TiO_2 layer and the gold electrodes that were deposited with DC

sputtering and electron beam evaporation respectively, all the other layers were deposited via spin coating.

The fabrication of perovskite solar cells involved depositing several layers of thin films deposited mainly by spin coating with the bottom-up approach. The structure of the perovskite solar cell for this part of the research is shown in Figure 4-2 and the basic fabrication process of the device is shown in Figure 4-4. The total thickness of a complete device, including FTO film on the commercially available FTO substrate (300 nm on soda lime glass, MSE supplies, 7-10 Ω/sq) is around 1 to 1.3 µm. This is composed of a 115 nm thick of compact TiO_2, a 200 nm -300 nm of mesoporous TiO_2 layer, an approximately 300 nm thick of perovskite active layer, a spiro-omeTAD layer with thickness around 200 nm, and a 100 nm thick gold electrode. The commercially available FTO thin film is approximately 300 nm thick.

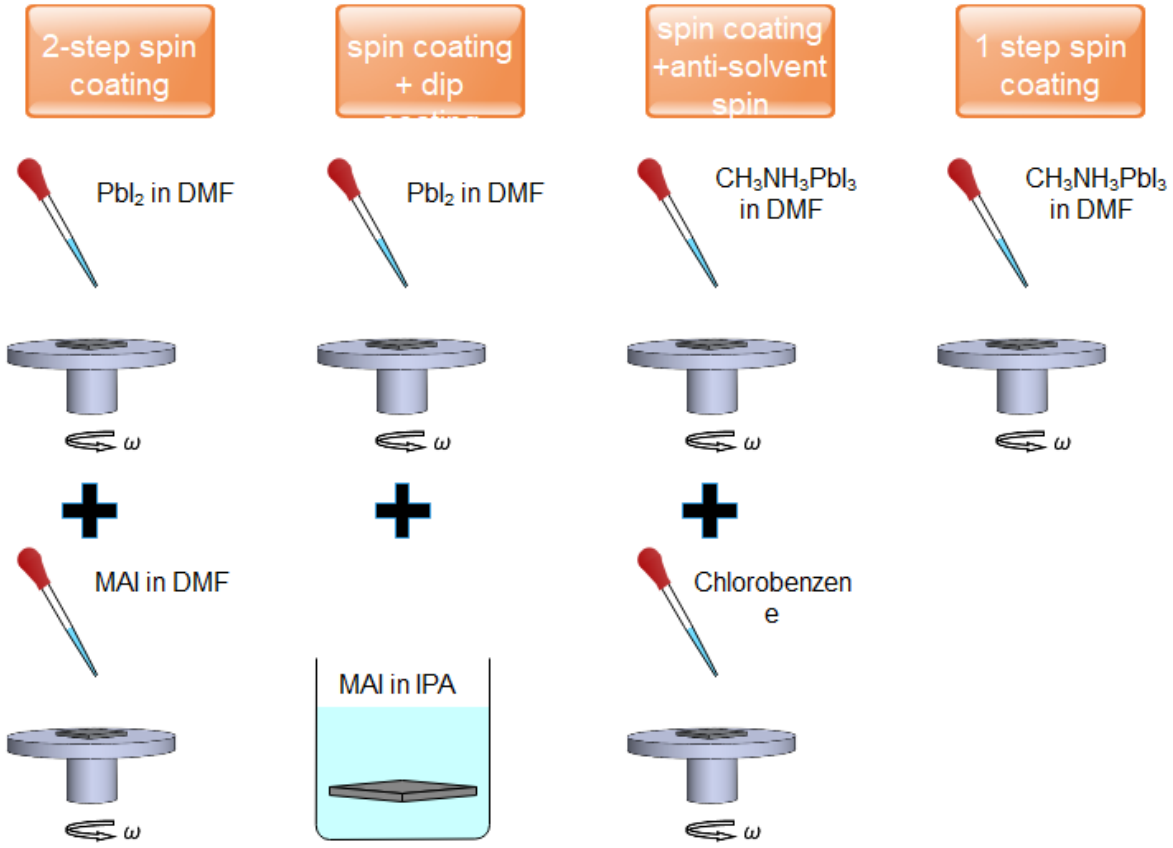

Figure 4-5 Different fabrication methods for perovskite photoactive film deposition. All 4 methods were tested in this research.

Initially, we were attempting to fabricate perovskite solar cells in a normal laboratory atmosphere without the use of a glovebox, given that our nanofabrication laboratory has some temperature and humidity control. While the fabrication of the electron and hole transport layers and metal

electrodes have well know protocols, there are several different fabrication methods for fabricating the photoactive perovskite films [80, 83, 154]. Figure 4-5 shows the fabrication methods used for this research. The one-step spin coating is the simplest method but could be greatly affected by ambient environmental conditions such as humidity and temperature. The 2 step spin coating and spin coating + dip-coating method appear to be slightly more moisture resistant during the deposition process when compared with 1 step spin coating, but lots of pinholes still appeared in the film, resulting in recombination path for electron-hole pair generated. The spin coating+ anti-solvent method, which is the one adopted in this research minimized the influence of the moisture on the film but does require more precise control over manual handling for reproducibility. Several methods have been tried and compared via SEM or AFM to determine which method produces perovskite films with suitable properties for solar cell applications.

4.2.1 Precursor preparations

Apart from the compact TiO_2 thin film and gold electrode (Sputtering and E-beam evaporation), all other thin films employed in optimized perovskite solar cell fabrication are deposited with spin coating. This requires preparations for the precursors used.

Both DC sputtering and spin coating depositions for the compact TiO_2 layer were tested for performance comparison. The precursor preparation for spin coating compact TiO_2 includes mixing equal parts of 0.245 mol of titanium isopropoxide (TTIP, Sigma-Aldrich, 97%) in ethanol (Thermofisher, absolute) and 0.02 mol of HCl (HCL, Univar, 32%) in ethanol with a magnetic stirrer and spin bar to obtain a clear colourless solution.

For mesoporous TiO_2 thin film, initial research was focused on mesoporous bi-layer TiO_2. This consists of a TiO_2 nanoparticles paste with 18 nm particle size (Taiwan DSC PV, transparent) and a TiO_2 nanoparticles paste containing 30% of TiO_2 nanoparticles with 200 nm particle size (Taiwan DSC PV, opaque). Both pastes were diluted separately in ethanol with a 1:4 w/w ratio. This is later changed to single layer mesoporous TiO_2 in an attempt to reduce the mesoporous TiO_2 thickness to

improve the short circuit current density of the device, as new studies show that the optimum total thickness for compact TiO_2 with mesoporous TiO_2 need to be within 400nm to ensure reasonable resistivity of the film with optimum active surface area and pore volume of TiO_2 [155]. A solution of 150 mg/mL diluted TiO_2 (Great solar cell, 30 N-RD) in Ethanol was prepared at least an hour before spin coating the solution on the compact TiO_2 sputtered substrate. The solution was maintained in a beaker on the magnetic hotplate stirrer at 50 °C and 200 rpm at all times to minimise the possibility of agglomeration of the TiO_2 nanoparticles when dispensed onto the substrate.

Methods of preparing the precursors for depositing the $MAPbI_3$ films with different spin coating methods are shown in Table 4-1. The main materials used for precursor preparations are PbI_2 powder (Lumtec, 99.999% trace metal basis), CH_3NH_3I crystals (MAI, Great Cell Solar, >99.5%), Dimethylformamide (DMF, Thermofisher Scientific, 99.5% certified AR), Dimethylsulfoxide (DMSO, Fisher Scientific, ≥99.7%), and Isopropanol alcohol (IPA, Labserv Pronalys, AR ACS).

Table 4-1 Precursor preparation for different perovskite thin film deposition methods

1 step spin coating and spin coating with anti-solvent methods
Dissolve 1:1 mol ratio of PbI_2 and MAI powder in a mixed solvent of DMF and GBL (8:2) to make a 40% w/w ratio of $CH_3NH_3PbI_3$ in solution. The solution is then stirred at 70 °C overnight to achieve a homogeneous clear yellow solution for spin coating. The solution is maintained at 70 °C during the spin coating process. [156]
2 step spin coating and spin coating with dip coating methods
2 separate solutions were prepared. The first precursor is prepared by dissolving 1 mol of PbI_2 in a mixed solvent of DMF and GBL (8:2) and stirred at 70 °C overnight to achieve a homogeneous clear yellow solution for spin coating. The solution is maintained at 70°C during spin coating. The second precursor is a solution that consists of MAI in IPA with a concentration of 10 mg/mL. This is prepared immediately before spin coating the first precursor.

The precursor for the Spiro-omeTAD hole transport layer is usually prepared before deposition. 80mg of Spiro-omeTAD is dissolved in 1 mL of chlorobenzene, followed by the addition of 28.5 µL of

4-tert-Butylpyridine and 17.5 µL of Lithium salt in acetonitrile (520mg/mL of Bis(trifluoromethylsulfonyl)amine lithium salt in acetonitrile) to the mixture.

4.2.2 Device Fabrication

Substrate cleaning:

A quarter section of the FTO film area of the commercially available FTO glass (10 × 10 mm^2 or 20 × 20 mm^2, MSE supplies, 1.1 mm, 7-10 Ω/sq.) was etched away by mixing zinc powder (Sigma-Aldrich, purum) and diluted 2 mol of Hydrochloric acid on the unwanted area of FTO. [157] This is to prevent short-circuiting the top and bottom electrodes. The substrates are then cleaned with diluted lemon detergent (any detergents that has a label with "leaves no residue" would work) in hot water to remove zinc chloride from the reaction of zinc and HCl. This is followed by 3 times rinsing in hot water to ensure the detergent has been rinsed off completely. The substrates are then cleaned, in the ultrasonic bath, with acetone for 5 minutes, followed by methanol for 10 minutes and Isopropyl alcohol for 5 minutes. The cleaned substrates were then placed inside the 95 °C oven for at least 5 minutes to remove the solvent residues.

Compact TiO_2 deposition:

Table 4-2 Change in parameters for compact TiO_2 optimization

Change in Ar:O_2 gas ratio for DC sputtering, thickness fixed at 115 nm			
2:1	1:1	1:2	
Change in TiO_2 film thickness, process gas ratio fixed at 1:2			
65 nm	80 nm	100 nm	115 nm

DC sputtering was used for the compact TiO_2 deposition. Before the deposition of compact TiO_2, the cleaned substrates were soaked under 100 W of O_2 plasma with the plasma asher (Quorum Technologies K1050X) to clean off any residues that are left on the substrates. The O_2 plasma also improved the hydrophilicity of FTO films so that there's a better adhesion of the TiO_2 thin film on

FTO. After O_2 plasma clean, another 1/4 section of the substrates were covered with polyamide tape to ensure part of FTO film is not exposed to TiO_2 sputtering. Different thicknesses of the compact TiO_2 film were deposited with 200 W of DC magnetron sputtering power using pure Titanium target (99.9999% check purity) with a mixture of Argon and Oxygen gas. Different processing gas ratios were also tested for optimization. The chamber processing pressure was maintained at approximately 4.8×10^{-3} torr. The change in parameters for TiO_2 optimization is shown in Table 4-2.

Mesoporous TiO_2 deposition:

For the Bi-layer mesoporous TiO_2 layer, the prepared precursors were spun coated onto the compact TiO_2 coated substrate with the rotation speed of 5000 rpm, acceleration at 2500 rpm/second, and 10-second duration subsequently. The precursor containing TiO_2 nanoparticles with 18 nm particle size was first deposited, followed by 5 minutes of baking at 60 °C, before the deposition of mesoporous TiO_2 with 200 nm particle size. For devices with a single mesoporous TiO_2 layer consisting of 30 nm particle size, the prepared precursor was spin coated with 5000 rpm rotation speed, 2500 rpm/second acceleration, and 10 seconds of duration. After spin coating, the substrates were annealed on a hot plate at 100 °C for 5 minutes to remove excess solvent. The samples were then annealed at 500 °C with the several intermediate temperatures and annealing durations shown in Table 4-3 followed by cooling slowly down to 100 °C. The substrates can then be stored in a 95 °C oven if subsequent procedures are carried-on within a week. If longer waiting times are required, the substrates can be stored under a low vacuum with minimal light to prevent the degradation from UV light or the excess of moisture that can condense on film.

Table 4-3 Annealing parameters for mesoporous TiO_2

Temperature (°C)	**100**	**220**	**300**	**380**	**460**	**500**
Duration (min)	5	5	5	5	5	30

$CH_3NH_3PbI_3$ perovskite film deposition:

As mentioned at the beginning of the section, several different spin coating methods for perovskite thin film deposition have been tried for the optimisation of materials. A detailed description of

each method is given in Table 4-4.

Table 4-4 Description of each deposition method tried for $CH_3NH_3PbI_3$ deposition methods

1-step spin coating
Substrates coated with compact and mesoporous TiO_2 were preheated at 70 °C before spin coating. The precursor prepared with recipe described in section 3.2.1 was first spin coated onto the substrate with low speed 1000 rpm and acceleration setting of 500 rpm/second for 3 seconds to ensure full substrate coverage, followed by high speed spin coating at 4000 rpm and 2000 rpm/second for 5 seconds to define the thickness. The spin coated substrates were immediately annealed at 70 °C for 10 minutes to remove any residual excess solvent.
Spin coating with dip coating
The PbI_2 precursor was first spin coated on 70 °C preheated substrate for 3 seconds with the low spin speed setting at 1000 rpm and acceleration at 500 rpm/second. The spinning speed is then immediately increased to 4000 rpm with acceleration set at 2000 rpm/second for 5 seconds. The substrates were then placed on a 70 °C hotplate for 5 minutes to remove excess solvent then cooled down to room temperature for dip coating. The PbI_2 spun coated substrate was then submerged in the MAI/IPA solution for 5 minutes, followed by a quick rinse with IPA, then dried on a 70 °C hotplate for 5 minutes.
2 step spin coating
The 70 °C preheated substrate was spun coated with PbI_2 precursor at 1000 rpm and 500 rpm/second for 3 seconds followed by 4000 rpm and 2000 rpm/second for 5 seconds. The substrate was then annealed at 70 °C for 5 minutes then cooled down to room temperature for 2^{nd} spin coating. The MAI/IPA solution was then spun coated onto the substrate with 6000 rpm, 2000 rpm/second, and 10 seconds duration.
Spin coating with anti-solvent
The $CH_3NH_3PbI_3$ precursor was spin coated on the preheated substrate with 1000 rpm and 500 rpm/second for 3 seconds, followed by 4000 rpm and 2000 rpm/second for 10 seconds. 200 µL

of chlorobenzene was dripped onto the substrate 5 seconds before the end of the spin coating. The spin-coated substrate was then annealed at 70 °C for 5 minutes.

Spiro-OmeTAD deposition:

The perovskite layer which was deposited on the substrate was first cooled to room temperature before the spiro-omeTAD spin coating. A 200 µL of the prepared spiro-omeTAD precursor was spun coated on the substrate at 4000 rpm, 1000 rpm/second for 30 seconds. The substrate was then placed in a dry cabinet, under dark, to oxidize the spiro-omeTAD layer further for at least 8 hours to improve the hole conductivity of the layer. Moreover, during spin coating, the Li^+ ions tend to stay closer to the interface between the spiro-omeTAD and active $MAPbI_3$ layer. Letting the thin film "rest" in dark, allowing the Li^+ ions to redistribute evenly in the spiro-omeTAD film [56, 57, 158].

Gold counter electrode deposition:

A total of 100 nm of gold (24ct pure gold, Regal Castings Ltd)was evaporated onto the sample using the electron beam evaporation in Edward Auto 500 sputtering system described in chapter 2. The deposition rate is shown in Table 4-5. The 5 kV electron beam with approximately 32 to 38 mA beam current was used. The chamber pressure was kept at around 1×10^{-5} during evaporation.

Table 4-5 Gold electrode deposition rate

Deposition rate (nm/sec)	**0.01-0.02**	**0.06-0.08**
Thickness (nm)	5	95

4.2.3 Thin Film and Device Characterisation

The completed device was rested in a dry place under dark overnight. This is first to allow Lithium ions to redistribute in the hole transport layer and slightly diffused into the $MAPbI_3$. This allows the Li^+ to accumulate at the grain boundaries of perovskite film, resulting in the higher potential difference at the grain boundaries, which attracts the electrons and repels the holes more easily, minimising the recombination of electron-hole pair at the perovskite layer [159]. The device was

then tested under simulated solar light for the current vs. voltage characterisation. The simulated light is maintained at 100 W/cm^2 irradiation, equivalent to the midday sunlight intensity at the equator. The 21 measurement points to construct the current-voltage curve was taken between 0 V and 1 V.

The electron transport layer, TiO_2 films were characterised via UV-Vis spectrometry for transparency and XRD for crystal phase confirmation. Thin films of the perovskite solar cells were also characterised individually on compact TiO_2 coated quartz substrate. The compact TiO_2 acted as the buffer layer since the $CH_3NH_3PbI_3$ film does not adhere well to the quartz substrate. Scanning electron microscopy SEM and Atomic Force Microscopy AFM were used for the thin film surface morphology imaging and UV-Vis spectrometry was used for the active layer light absorbance measurements.

4.3 Device thin film optimizations

The main focus of the optimization was on the deposition methods, the thicknesses, and film morphologies of the compact TiO_2, mesoporous TiO_2, and $MAPbI_3$ layers. The hole transporting layer, lithium doped spiro-omeTAD, was kept unmodified, following the synthesis and fabrication method described by previously published literature [57, 160, 161].

4.3.1 Compact TiO_2 optimization

DC magnetron sputtering deposition method was used for compact TiO_2 thin film deposition. DC sputtering produces a much denser and higher quality of TiO_2 thin film when compared with the spin coating method. While the 4 hour deposition time for growing a 115 nm thin film seems long when compared with spin coating, a large number of samples can be prepared at the same time, as opposed to one sample at a time for spin coating. Moreover, the film also appears to be more robust when compared with TiO_2 film deposited with spin coating. Figure 4-6 shows the SEM images of the 115 nm DC sputtered TiO_2 thin films deposited on indium doped tin oxide (ITO) coated

glass. The surface roughness of the film measured using the AFM was approximately 5.6 nm, which was very similar to the surface roughness of the ITO coated substrate of 5.8 nm. This indicates that the thin film itself is very smooth. The average grain size is approximately 120 nm. This is larger than the TiO_2 deposited with RF sputtering published by C H Wei et al [162].

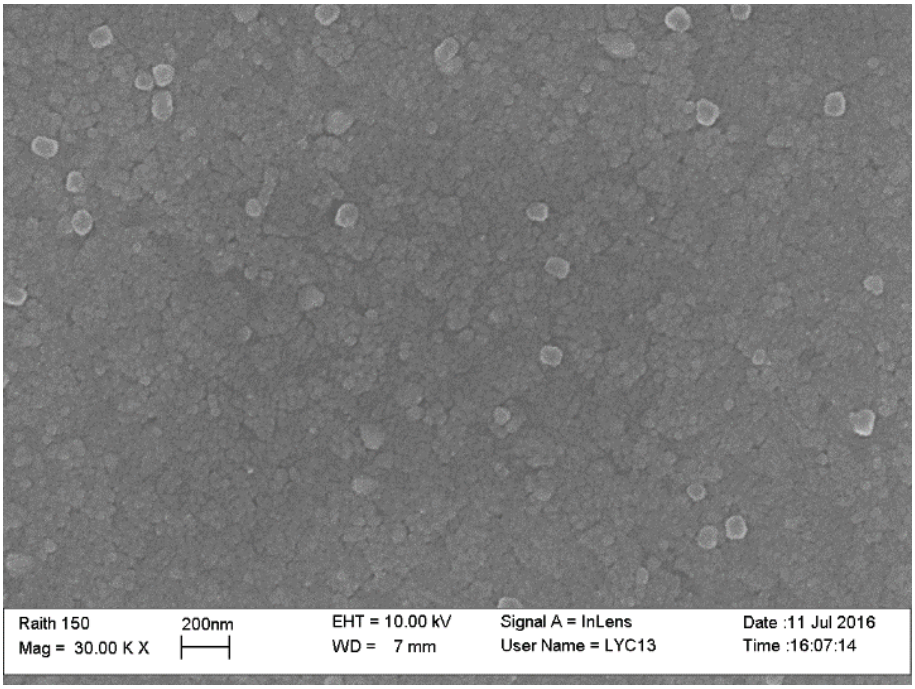

Figure 4-6 SEM image of DC sputtered TiO_2 film, showing grains in the range from 80 nm to 150 nm.

The DC sputtering power was maintained at 200 W for a reasonable deposition rate (30 nm per hour), and for the sputtering chamber to maintain below 100 °C. The chamber temperature could increase to 100 °C for a long period of sputtering at high power.

The performance of perovskite solar cells with different TiO_2 thickness of deposited films was studied, as shown in Table 4-6. Due to the sputtering system's limitation, the maximum thickness of the film that can be deposited via DC sputtering is 115nm. The short circuit current density increased from less than 4 mA/cm^2 to over 8.8 mA/cm^2 when the compact TiO_2 thickness increased to over 100 nm. Moreover, the open circuit voltage also improved from 0.55 V to 0.8 V. This results in an improvement in the perovskite solar cell's overall power conversion efficiency from less than 1.3 % to 3.79 % for the champion sample.

Table 4-6 Perovskite solar cell overall performance with different compact TiO_2 thickness. An increase of short circuit current density from less than 4 mA to close to 9 mA when the thickness increased to 115 nm, resulting in an overall

power efficiency conversion improvement from 1.3 % to 3.8%. 3 samples with 3 isolated cells each for each variable have been fabricated in the same batch to ensure the validity of the result.

TiO_2 thickness (nm)	Jsc (mA/cm^2)	Voc (V)	Fill Factor	Efficiency (%)
65	3.765	0.675	0.517	1.315
80	3.432	0.550	0.323	0.609
100	8.893	0.750	0.501	3.345
115	8.850	0.800	0.530	3.790

The device performance of the compact TiO_2 DC sputtered with different processing gas ratio is shown in Table 4-7. The thickness of the compact TiO_2 on all samples was 115nm. The best result was obtained when the oxygen flow rate was twice the argon flow rate. The working chamber pressure was maintained between 4.8 and 5.5 $*10^{-3}$ mbar. When the ratio of oxygen increased during sputtering, the colour of the compact TiO_2 changed from semi-transparent slightly greyish/metallic colour to transparent film with a tint of green colour. The overall power conversion efficiency increased from 1% to close to 3 %, with short circuit density increased to almost 10 mA/cm^3. The low efficiency of the device would be mainly due to the active film and the mesoporous TiO_2 which were not yet optimized.

Table 4-7 Average device performance of perovskite solar cells with 115 nm compact TiO_2 deposited with different processing gas ratios, the perovskite layer, and the mesoporous TIO_2 layers were not optimized yet. 3 individual substrates containing 3 isolated cells on each sample for each gas ratio. All samples were fabricated in the same batch for processes from mesoporous TiO_2 spin coating onwards. Each isolated cell is tested at least 3 times with the same IV sweeping range

Argon:Oxygen	Jsc (mA/cm^2)	Voc (V)	Fill Factor	Efficiency (%)
2:1	5.40	0.67	0.30	1.08
1:1	4.51	0.61	0.24	0.67
1:2	9.40	0.77	0.42	2.97

The sputtered samples were sent to The Instrument Centre of National Cheng Kung University, Taiwan for glancing angle XRD measurements with a multipurpose X-Ray Thin-Film Micro Area Diffractometer (Brucker D8 Discover). This is to understand which crystal structure does the

sputtered TiO_2 thin film has, since anatase is the desired crystal structure. TiO_2 with the anatase phase exhibits the best photocatalytic properties for solar cells. The incidence angle was set at 1 ° with the other set up conditions of 40 kV, 100mA and 2θ: 20 ° - 80 °. The XRD patterns of DC magnetron sputtered TiO_2 thin films are shown in Figure 4-7. All as-deposited TiO_2 film sputtered using different gas mixture appeared to be amorphous. However, after high temperature annealing at 450 °C, TiO_2 with anatase phase characteristics started to appear. The film XRD pattern appeared to be similar to the ones in the literature. [163, 164] The crystal structure appeared to be slightly different from the variation of sputtering gas. The peaks at 25 ° and near 40 ° correspond to the <101> and <004> reflections of anatase structure. There is also a small peak at around 48°, which is closely related to <200> reflection of anatase structure. The peak at 55 °is possibly related to the <211> and <105> reflection of anatase structure. TiO_2 sample deposited with an Ar/O_2 gas ratio of 1:2 shows a higher intensity count after annealing at 450 °C. One small peak appeared at near 20 ° for the samples with Ar/O_2 process gas ratios of 1:1 and 1:2. This was not part of the anatase peaks shown in the literature and only appeared after annealing. It could be from the glass substrate that got picked up by the XRD measurement, and could also possible from the thin film impurities during sputtering such as different material particles that react with the oxygen and landed on the substrate during the sputtering process.

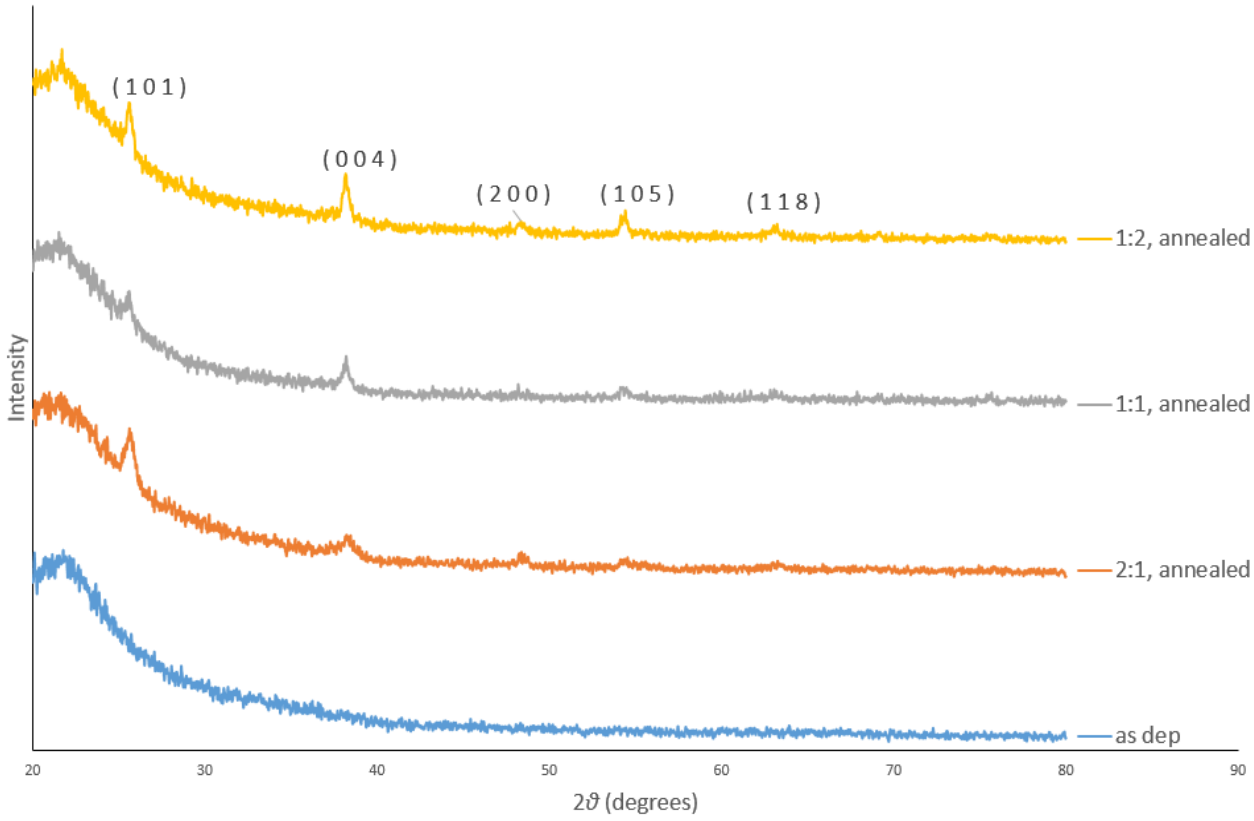

Figure 4-7 XRD measurements of 115 nm TiO_2 thin film deposited with DC magnetron sputtering using different process gas mixtures. (a) as-deposited TiO_2 thin film (b) TiO_2 film deposited in a mixture of Ar/O_2 ratio 2:1, annealed at 450 °C for 30 minutes (c) TiO_2 film deposited in a mixture of Ar/O_2 ratio 1:1, annealed at 450 °C for 30 minutes (d) TiO_2 film deposited with Ar/O_2 ratio 1:2, annealed at 450 °C for 30 minutes.

The transparency measurement of the compact TiO_2 is shown in Figure 4-8. The sample was tested using ITO coated microscope glass comparing to air reference for baseline correction. The compact TiO2 film allows over 80% of the light to pass through in most regions except when the wavelength is shorter than 350 nm. The peak positioned around 400 nm shows the highest, with approximately 98 % transmittance.

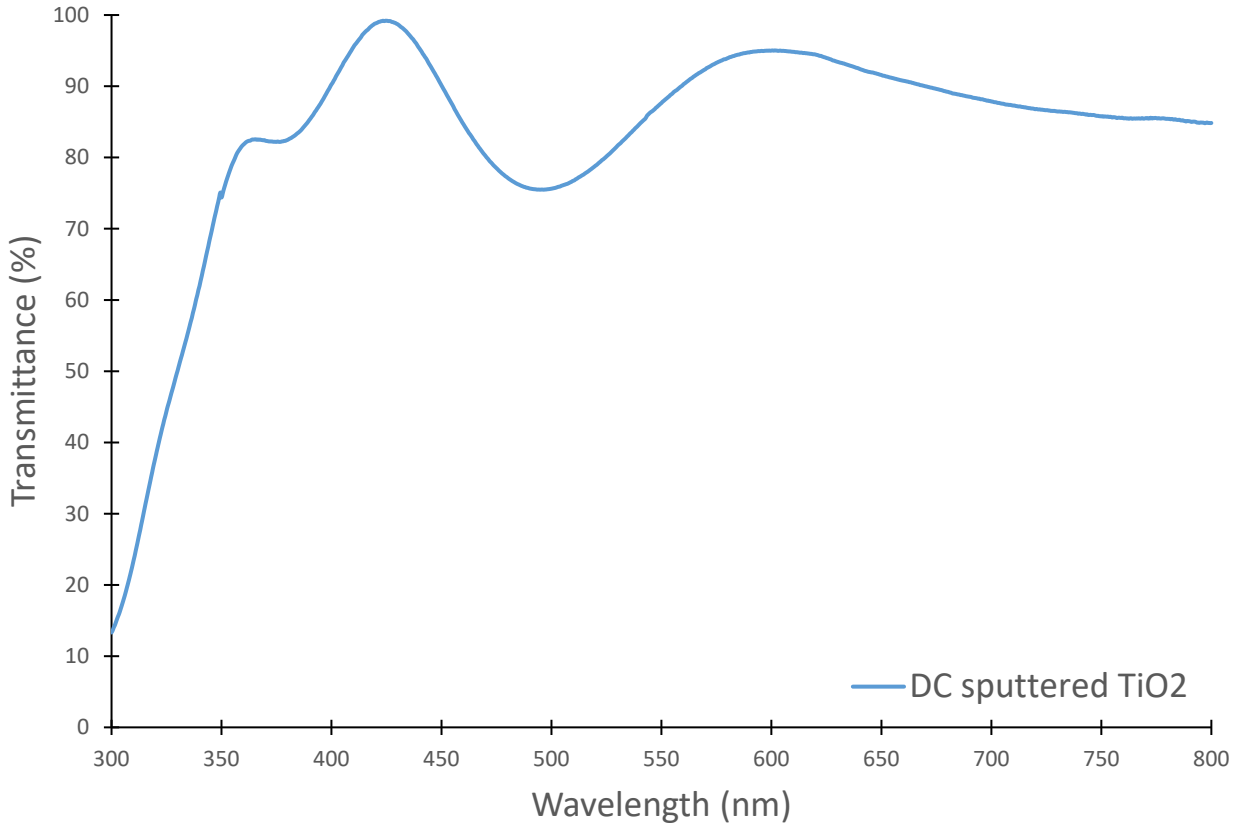

Figure 4-8 Transparency measurement of the compact TiO_2 film on ITO using UV-Vis spectrometer, with ITO coated glass substrate as the baseline. The combination of ITO glass+ compact TiO_2 might have allowed slightly more light to pass through at 400 nm wavelength when compared with ITO glass alone.

4.3.2 Mesoporous TiO_2 layer for device overall power conversion efficiency optimization

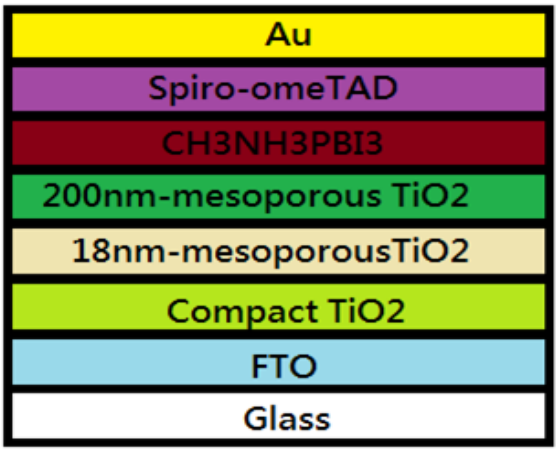

Figure 4-9 Position of the mesoporous TiO_2 with different particle sizes in the perovskite solar cell structure.

Mesoporous TiO_2 is an important material for perovskite solar cells with a mesoscopic structure. This layer is used to increase the interface area between the active perovskite layer and the electron transport layer. Moreover, due to the aggregation of the submicron-sized TiO_2 nanoparticles that can diffuse light at UV and visible light regions, mesoporous TiO_2 can act as a light scattering layer to improve the amount of incident light reaching the perovskite active layer [165].

Bi-layer mesoporous TiO_2 with 18 nm and 200 nm particle sizes

The initial test was carried out with a bi-layer of TiO_2 with 2 different particle sizes—18 nm and 200 nm, with sequential spin coating then dip coating for the $MAPbI_3$ layer. There were reports regarding dye sensitized solar cells that suggest using double layers of mesoporous TiO_2 would improve the overall device performance [166]. Figure 4-9 shows the position of the mesoporous TiO_2 with different particle sizes for devices with bi-layer mesoporous TiO_2. The effect of using a bi-layer of mesoporous TiO_2 is presented in Table 4-8. The spin coating speed of both layers was kept at 5000 rpm, which gives approximately 800 nm thickness in total for the bilayer mesoporous TiO_2, and 300 nm for a single layer without the 200 nm particle-sized TiO_2 layer.

Table 4-8 Perovskite Solar Cells performance under sunlight simulator with single and double layer of mesoporous TiO_2 or without mesoporous TiO_2 layer. 3 samples with 3 isolated cells each for each variable have been fabricated in the same batch to ensure the validity of the result.

Perovskite solar cells key parameters with or without mesoporous TiO2				
PSC structure	Jsc (mA/cm^2)	Voc (V)	Fill Factor	Efficiency (%)
With double TiO_2 layer	11.71	0.75	0.50	4.35
Without 200nm particle size mp-TiO_2	4.73	0.65	0.52	1.60
Without TiO_2 layer	6.88	0.85	0.15	0.87

Various thicknesses of each mesoporous TiO_2 layer were also examined to determine the best thickness for each layer. The result is shown in Table 4-9 and Table 4-10. While there seems to be an improvement in both short circuit current density and open circuit voltage, it seems like the improvement of the overall electrical performance has reached a limit, since it is difficult to further reduce the TiO_2 layer with 200 nm particle size.

Table 4-9 Device performance obtained for different thicknesses of mesoporous TiO_2 with 18 nm particle size. 3 samples

with 3 isolated cells each for each variable have been fabricated in the same batch to ensure the validity of the result.

Perovskite solar cells with different thicknesses of 18 nm mesoporous TiO2 and fixed 200 nm mesoporous TiO2 (600 nm)				
18 nm particle size TiO_2 layer thickness (nm)	Jsc (mA/cm^2)	Voc (V)	Fill Factor	Efficiency (%)
450	2.38	0.75	0.44	0.79
350	3.60	0.73	0.39	1.01
300	5.04	0.75	0.37	1.37
280	4.39	0.82	0.45	1.56
270	4.41	0.88	0.49	1.82

Table 4-10 Device performance for different thicknesses of mesoporous TiO_2 with 200 nm particle size. 3 samples with 3 isolated cells each for each variable have been fabricated in the same batch to ensure the validity of the result.

Perovskite solar cells with different thickness of 200 nm mesoporous TiO2 and fixed 18 nm mesoporous TiO2 (270 nm)				
200 nm particle size TiO_2layer thickness (nm)	Jsc (mA/cm^2)	Voc (V)	Fill Factor	Efficiency (%)
1050	3.34	0.55	0.31	0.57
600	7.95	0.70	0.29	1.59
500	11.50	0.75	0.51	4.37
450	11.27	0.85	0.56	5.35

Single-layer mesoporous TiO_2 with 30 nm particle size

While there was an improvement in the overall device performance, the overall efficiency of the device was capped at 5% regardless of the change in $MAPbI_3$ deposition methods. The result from Table 4-9 and Table 4-10 indicated that the thickness of mesoporous TiO_2 needs to be as thin as possible. However, the 200 nm particle size for the 2nd mesoporous TiO_2 layer limits the extent to which the thickness of mesoporous TiO_2 can be reduced. The reduction of the thickness not just improved the transparency of the film for photons reaching the active perovskite layer, the transportation path between the perovskite layer and the electrode is shorter, minimizing the electron-hole pair recombination at the TiO_2 layer. Therefore, alternative material for mesoporous TiO_2 needs to be investigated for further improvement in device performance. For this reason, TiO_2 paste containing TiO_2 with a particle size of 30 nm was used in the next sets of experiments. Table 4-11 shows the comparison of the electrical characteristics of perovskite solar cells using 30 nm

particle size mesoporous TiO_2 with the device using bi-layer mesoporous TiO_2, showing an improvement in both short circuit current density and open circuit voltage. Mesoporous TiO_2 with 30 nm particle size can both increase the interface area between the perovskite layer and TiO_2 layers, and scatter the incident light, especially in the wavelength region shorter than 600 nm, to minimize the reflected light. Moreover, due to the small particle size, the average mesoporous TiO_2 thickness can be reduced down to approximately 200 nm. The $MAPbI_3$ film quality and thickness optimization for an overall improvement on the perovskite solar cell in the next section were based on mesoporous TiO_2 with 30 nm particle size.

Table 4-11 Comparison of key parameters of PSC device fabricated with bi-layer mesoporous TiO_2 with 18 nm and 200 nm particle size and single layer TiO_2 with 30 nm particle size. 3 samples with 3 isolated cells each for each variable have been fabricated in the same batch to ensure the validity of the result.

PSC structure	**Jsc (mA/cm^2)**	**Voc (V)**	**Fill Factor**	**Efficiency (%)**
With double TiO_2 layer (total 270+450 nm)	11.71	0.75	0.50	4.4
Single TiO_2 layer with 30 nm particle size (~200 nm)	13.36	0.89	0.42	5.1

4.3.3 Active perovskite layer optimization

Deposition method selection:

As mentioned in Section 4.2, there are several different ways for depositing $CH_3NH_3PbI_3$ that have been reported, but most of the published device fabrications were performed in ultra-low humidity glovebox. Here we attempted to fabricate the device structure in ambient air, with common laboratory atmosphere humidity of approximately 35 %, as opposed to the glovebox environment with near 0% humidity that most researchers used. The result is shown in Table 4-12. Due to the limitation of IV measurement software used in this part of the study, only forward sweeping was done for the comparison shown in Table 4-12. The method that gave the best results for the perovskite layer was the spin coating with the anti-solvent method. The power conversion efficiency (PCE) has increased from less than 1 % to over 8 % by just changing the deposition method,

both the short circuit current density and open circuit voltage also increased dramatically.

Table 4-12 Device performance with different deposition methods for the perovskite active layer. 3 samples with 3 isolated cells each for each variable have been fabricated in the same batch to ensure the validity of the result.

	Jsc (mA/cm^2)	Voc (V)	Fill Factor	Efficiency (%)
1 step spin coating	10.36	0.70	0.37	2.72
spin coating + dip coating	11.27	0.85	0.52	4.99
spin coating + spin coating	12.13	0.90	0.62	6.78
spin coating + anti-solvent	17.73	0.90	0.51	8.26

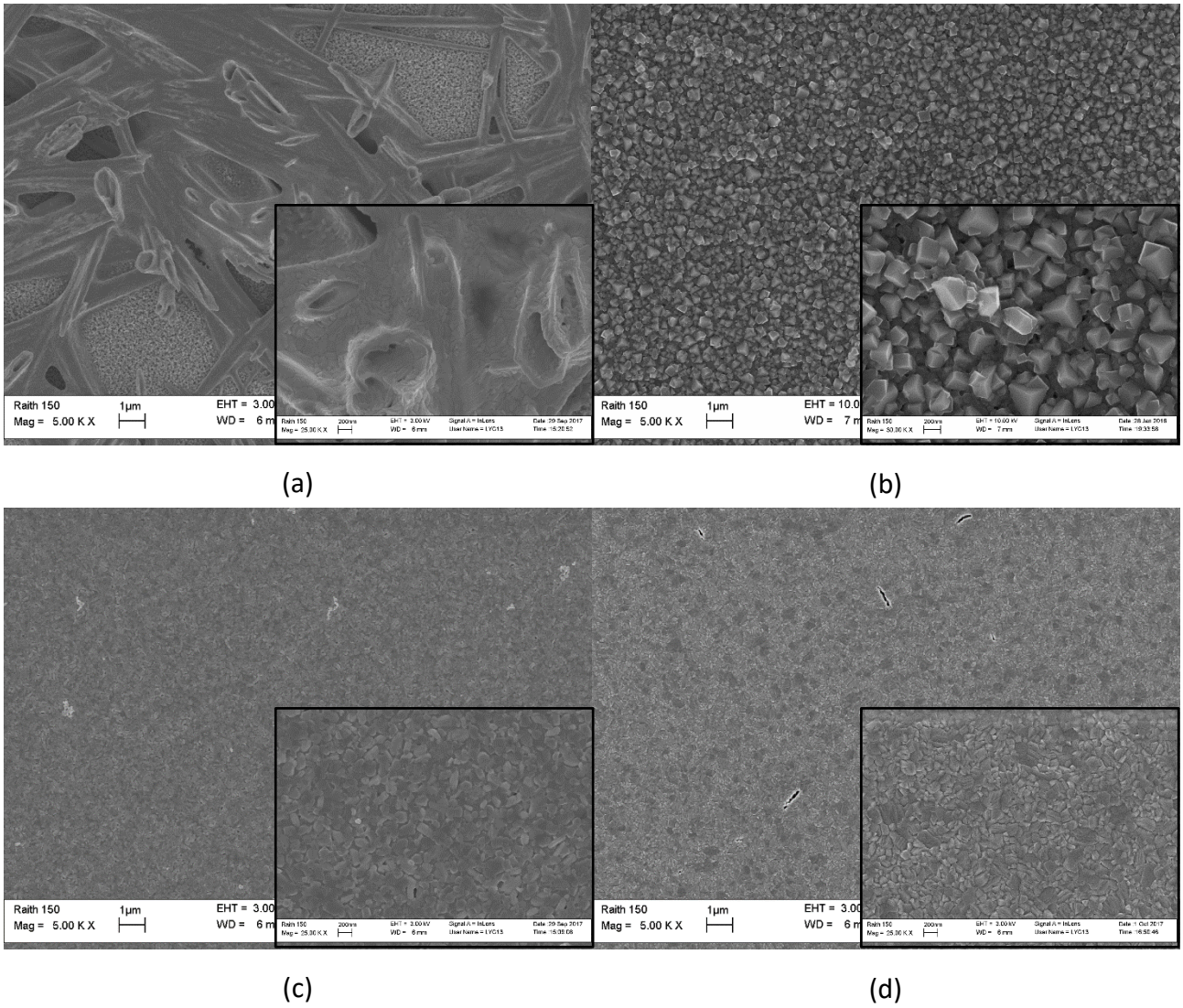

Figure 4-10 SEM images of $MAPbI_3$ deposited on mp-TiO_2 coated substrates with different deposition methods. (a) one-step spin coating, (b) spin coating PbI_2 with dip coating MAI, (c) spin coating PbI_2 with spin coating MAI, and (d) one-step spin coating with chlorobenzene anti-solvent spin coating.

The SEM images of the surface morphologies of $MAPbI_3$ deposited with different deposition methods are shown in Figure 4-10. For 1-step spin coating, it can be seen from the image that the

spin coated $MAPbI_3$ forms woven like pattern that did not provide full coverage of the material on the sample. The underlying mesoporous TiO2 can be seen clearly, leading to a massive electron-hole pair recombination path at the interface between TiO_2 and spiro-omeTAD. While the spin coating PbI_2 with dip coating MAI method shows much better surface coverage when compared with the 1 step spin coating method, but with a very rough surface (with roughness over 100 nm) and the grains appeared to be cubic crystals, ranging from 300 nm to 1 μm in size, that loosely sits on the surface. There are still lots of gaps between the cubic grains which provide a recombination path for the electron-hole pair. The sequential spin coating of spin coat PbI_2 followed by MAI appears to be smoother when compared with the spin coating with the dip coating method. The grain size, however, decreased to less than 200 nm on average. Moreover, the grains were formed in flaky irregular shapes, with no clear grain boundaries. For spin coating with anti-solvent dispensing, the film appeared to be smooth (with surface roughness roughly 10 nm) and with clear grain boundaries. The grains are shaped in polygons, with sizes ranged from 100 nm to close to 1 μm.

Optimization of spin coating with anti-solvent method prepared $MAPbI_3$ film morphology for device overall performance improvement

Although spin coating with anti-solvent achieved the highest efficiency solar cell in this study, the control for several variables with this method is challenging since the samples are fabricated in an uncontrolled environment and that the manual handling of the anti-solvent dispensing is critical to the crystallization of $MAPbI_3$. The variables that can be controlled, such as the amount and the timing of chlorobenzene being dispensed during spin coating, were adjusted to the parameters that achieved the best result. This includes the timing for the deposition of the chlorobenzene on the substrate during perovskite precursor spin coating, and the amount of chlorobenzene needed. Figure 4-11 shows the surface morphology of $MAPbI_3$ with different amount of chlorobenzene used as anti-solvent material. The substrate used for imaging was 10*10 cm^2 for imaging convenience.

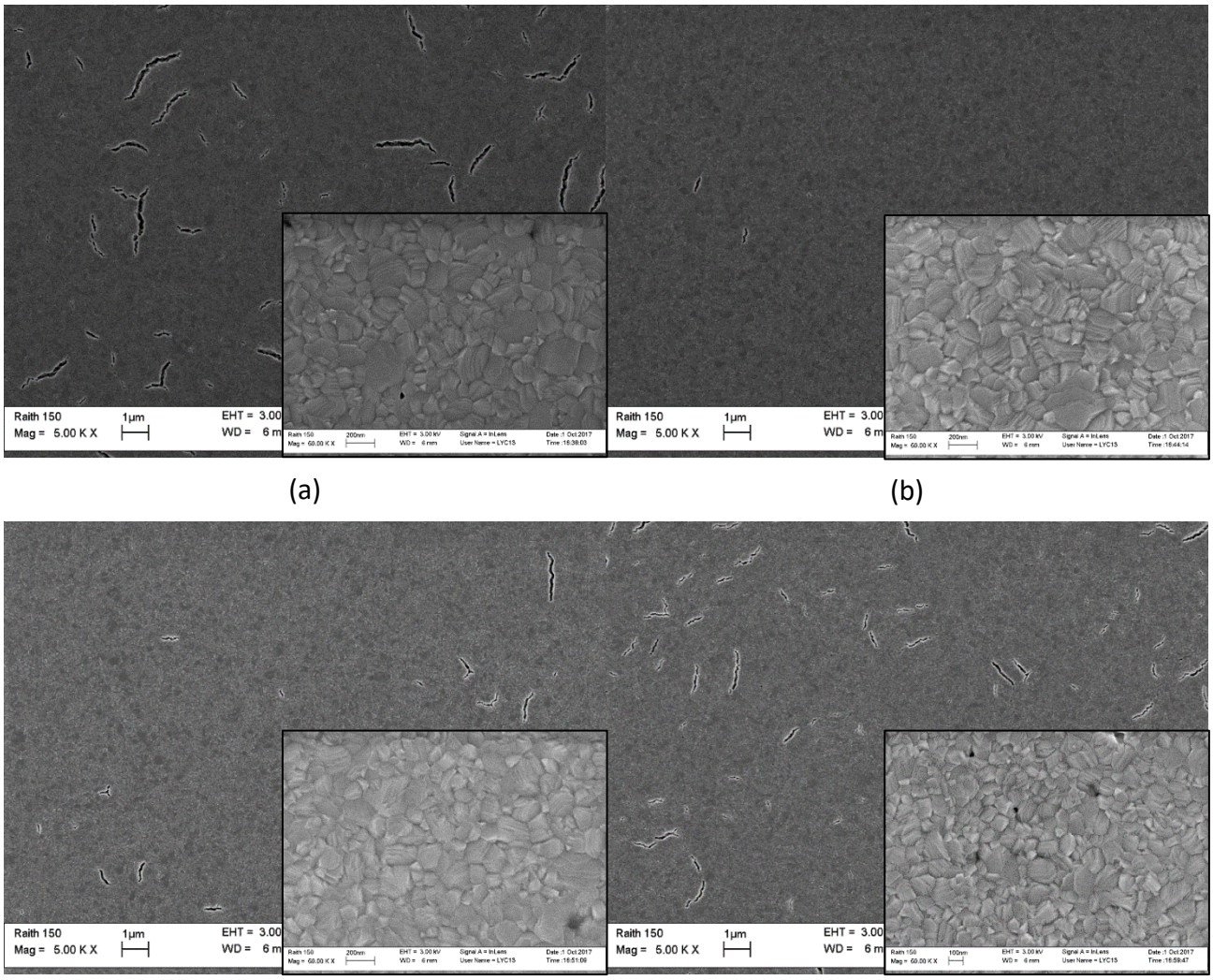

Figure 4-11 Perovskite thin film morphology with (a) 60 μL, (b) 80 μL, (c) 100 μL, and (d)120 μL of chlorobenzene used as anti-solvent to wash remove the precursor solvent during spin coating. The scale bars of the larger images are 1 μm and the scale bars for the insert images are 200 nm. The substrate size was 10*10 mm^2 for imaging convenience and the film is approximately 400 nm thick. When there are too little or too much chlorobenzene dispensed during spin coating, cracks between grain boundaries could be formed.

When there are little or too much chlorobenzene dispensed on the sample during spin coating, cracks with length up to more than 1 μm formed between grain boundaries. There are few suggestions of why this might occur. The most possible explanation refers to the existence of precursor solvent (such as DMF, DMSO, or GBL) or chlorobenzene residue remained in the film after dispensing chlorobenzene. The purpose of chlorobenzene dispensing during spin coating the perovskite precursor on the substrate is to remove the precursor solvent earlier, promoting the perovskite crystal formation with intact grains. When insufficient chlorobenzene is used, there is

a high chance that the precursor solvent was only partially removed. The residue of the precursor solvent that was not washed away by chlorobenzene remained in the film at the grain boundaries. Therefore, cracks are formed when the residue is evaporated during the annealing process. On the other hand, when excess chlorobenzene is used, while all precursor solvents were removed during the thin film formation, the excess chlorobenzene remained in the film between grains. Therefore cracks occurred when chlorobenzene is evaporated. [167]

Table 4-13 Characterization of solar cells fabricated on 25*25 mm^2 substrates with different amount of chlorobenzene used for the anti-solvent deposition. 3 samples with 3 isolated cells each for each variable have been fabricated in the same batch to ensure the validity of the result.

Chlorobenzene (mL)	Sweeping direction	η (%)	Fill Factor	Voc (mV)	Jsc (mA/cm^2)
250 µL	Forward	5.51	37.60	908.10	16.15
	Reverse	6.77	47.40	932.80	15.32
	Average	6.14	42.50	920.45	15.74
500 µL	Forward	3.70	27.80	861.70	15.42
	Reverse	4.43	39.90	846.50	13.13
	Average	4.07	33.85	854.10	14.28

The devices were initially fabricated on 10*10 mm substrates, but the small size results in the rapid cooling down of the substrate before depositing the precursor material. Consequently, there is an immediate temperature drop of the preheated precursor as the precursor is dispensed onto the substrate. The drop in temperature indicates that less solvent is being evaporated at the beginning of the spin coating when compared with precursors dispensed that could be maintained at the elevated temperature. The longer the solvent remained on the substrate during spin coating resulting in an intermediate phase which is extremely sensitive to moisture before the nucleation of perovskite taking place [168]. This is also one of the reasons for the anti-solvent method to be more effective when compared with other spin coating methods since it removes the solvent before the intermediate phase taking place, and speeds up the nucleation of perovskite crystals before being attacked by the moisture. Therefore, for device performance comparison, larger substrates, 25*25 mm^2 was used for device fabrication. The larger the substrate size, the larger the amount

of chlorobenzene is required. Table 4-13 and Figure 4-12 show the difference in performance when the different amount of chlorobenzene was used during $MAPbI_3$ thin film deposition. The active area of the device is 0.3 mm^2.

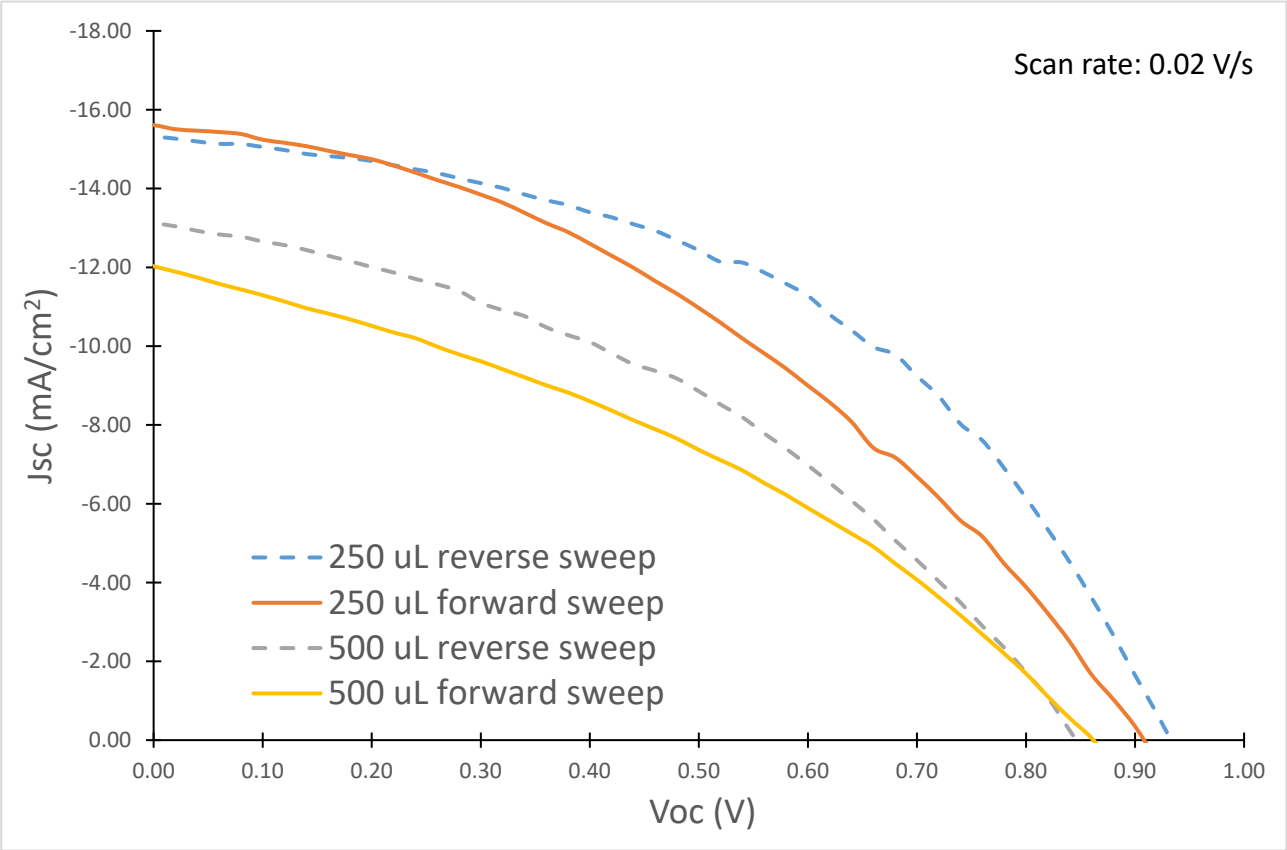

Figure 4-12 IV curve comparison between devices with different amount of chlorobenzene for anti-solvent deposition. Both forward and reverse sweepings were plotted with the ABET 3000A solar simulator, Keithly source meter, and IV plotting software by Kelzenberg which was described in chapter 2 [133]. The fill factor is approximately 37 % on average. The device with the perovskite layer fabricated using the anti-solvent method with 250 µL chlorobenzene shows the better result.

This is also the first time that we utilized an alternative software, described in Section 2.4.1 for IV measurement and plotting [133]. The device is measured with a voltage sweep from -0.4 V to 1.2 V for forward sweeping and 1.2 V to -0.4 V for reverse sweeping, with 20 mV as the step size. Hysteresis effect, which is the presence of a difference between forward and reverse sweeping can be seen. Hysteresis is one of the major topics in tailoring an accurate measurement for perovskite solar cell electrical performances. While the open circuit voltage appears to be relatively close between forward and reverse sweeping, the short circuit density shows an improvement from 14.28 mA/cm^2 to 15.74 mA/cm^2 with averaged forward and reverse sweeping measurement, which leads

to over 10% differences in fill factor. In consequence, there is an approximately 1 % difference in power conversion efficiency.

The timing for depositing the chlorobenzene is also a critical factor in producing good quality perovskite films. If chlorobenzene was dispensed too early, the precursor gets washed away before the material could adhere to the substrate. On the other hand, if the chlorobenzene was dispensed too late, the nucleation of $MAPbI_3$ becomes too slow and may be affected by the moisture in the air, resulting in a hazy coloured film instead of the mirror-like film as desired. Spin coating $MAPbI_3$ requires 2 different spin coating speeds. One at a low speed of 1000 rpm to ensure the precursor is fully covered. The duration of this part was kept very short, at 3 seconds, to minimize the effect of moisture during the whole process. The spin speed was then increased to 5000 rpm for 25 seconds. Chlorobenzene was dispended at either 5 seconds before the high spin speed ends or 20 seconds before the high speed spin coating ends. Figure 4-13 shows the IV curve and Table 4-14 shows the device performance of samples with chlorobenzene dispensing at different timings, displaying the effect of the anti-solvent dispensing timing on the illuminated current-voltage characteristics of the fabricated solar cells. An increase in the fill factor, Voc, and Jsc of the device with chlorobenzene dispensed at 20 seconds before the high speed spin coating step ends. This indicates the perovskite film fabricated with chlorobenzene dispensed at 20 seconds before the high speed spin step ends has fewer defects compared to the device with chlorobenzene dispensed at 5 seconds before the spin coating step finished.

Table 4-14 Device performance for different Chlorobenzene dispensing times. Forward and reverse sweeps were conducted because of the hysteresis phenomena found in perovskite solar cells discussed in chapter 2. 3 samples with 3 isolated cells each for each variable have been fabricated in the same batch to ensure the validity of the result.

		η (%)	Fill Factor (%)	Voc (mV)	Jsc (mA/cm^2)
5 second	forward	4.43	36.3	766.9	15.89
	reverse	6.35	46.2	835.5	16.48
20 second	forward	6.12	41.9	810.8	18.02
	reverse	7.74	50.7	839.3	18.18

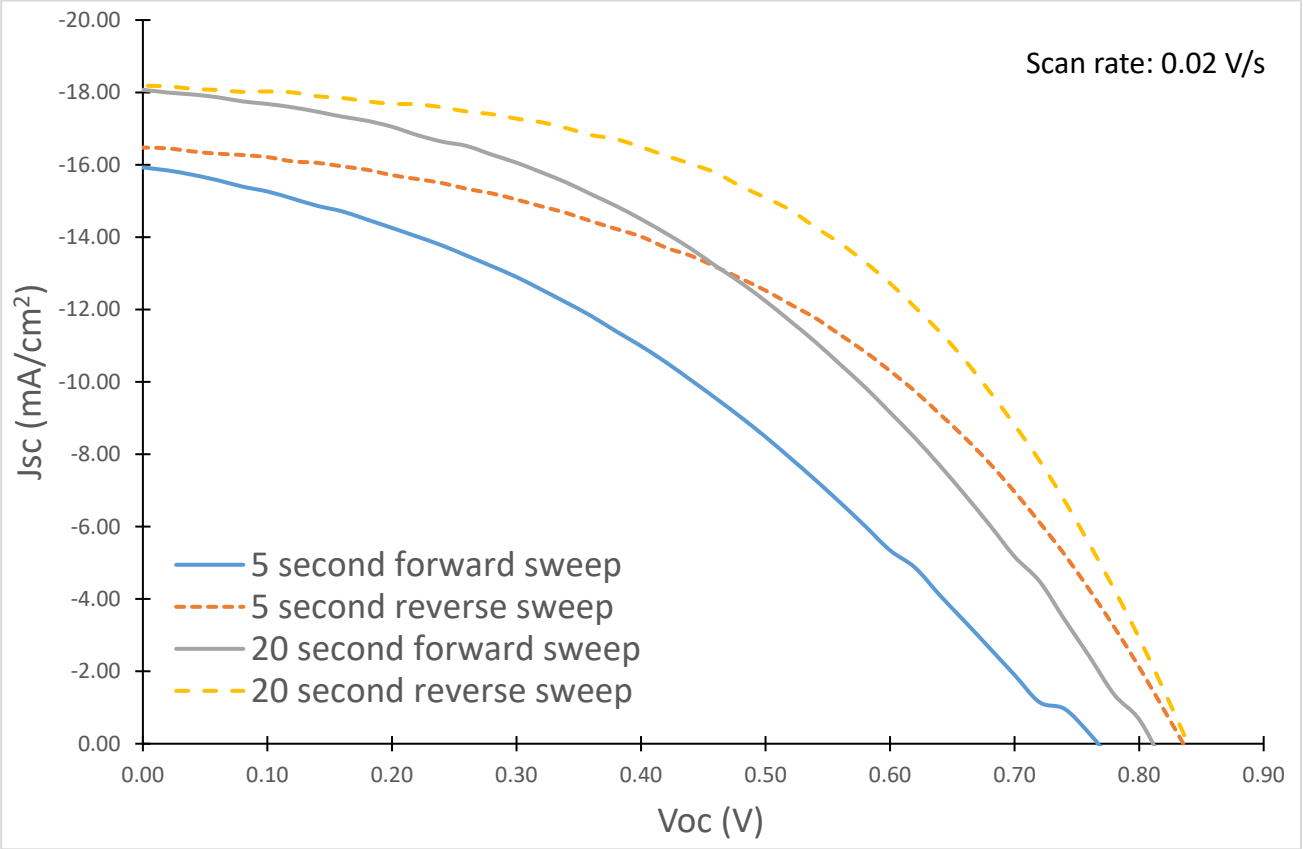

Figure 4-13 Illuminated forward and reverse sweep of the I-V curve for perovskite cells prepared with chlorobenzene at different dispensing times before the high speed spin coating step finished. The highest efficiency was obtained for chlorobenzene dispensing at 20 seconds before the high speed spin coating step finished, with short circuit density and open circuit voltage both increased.

It was also observed that the duration of the high spinning speed needs to be shortened as humidity increases. When the ambient humidity during sample preparation was increased to over 40 %, the duration of the high spin coating step needed to be shortened to 10 seconds. Whereas when the humidity is around 20%, the spin coating duration has to be extended to 25 seconds. The critical factor here is to keep the remaining spin coating time after the chlorobenzene dispensing step to 5 seconds. Long spinning time after dispensing the chlorobenzene resulted in degradation of the crystalized $MAPbI_3$ film due to moisture inclusion.

4.3.4 Best Device Performance for perovskite solar cell fabricated with little control on humidity

The best performance obtained in this work for perovskite solar cells fabricated in the air is shown in Table 4-15 and Figure 4-14, with an active area of 0.3 mm^2. The highest open circuit voltage achieved was over 900 mV, and the short circuit current reached a maximum of 17 mA/cm^2. The best power conversion efficiency achieved was close to 10 %. The fill factor, however, was low, less than 60 %. The low fill factor is possibly due to the low value of shunt resistance and the relatively high value for series resistance when compared with the one published. Several reasons could lead to high series resistance. This includes the interfaces between the active perovskite film and the electron transport layer and the hole transport layer.

Table 4-15 Champion device performance, with an efficiency close to 10 % at reverse sweeping.

	Efficiency (%)	Fill Factor (%)	Voc (V)	Jsc (mA/cm^2)	Rseries(Ωcm^2)	Rshunt(Ωcm_2)
Forward sweeping	6.64	42.8	869.4	17.82	12	540.1
Reverse sweeping	9.88	59.6	939.9	17.63	15	660.1

The hysteresis effect was also observed in the device during I-V characteristic sweeping. The power conversion efficiency of the forward sweeping is approximately 30% lower than the reverse sweeping. There are several reasons for the hysteresis effect in perovskite solar cells. The charge accumulation at the interface between the compact TiO_2 and the perovskite solar cells is usually one of the main causes, which have been explained by several published literature. [85, 169]

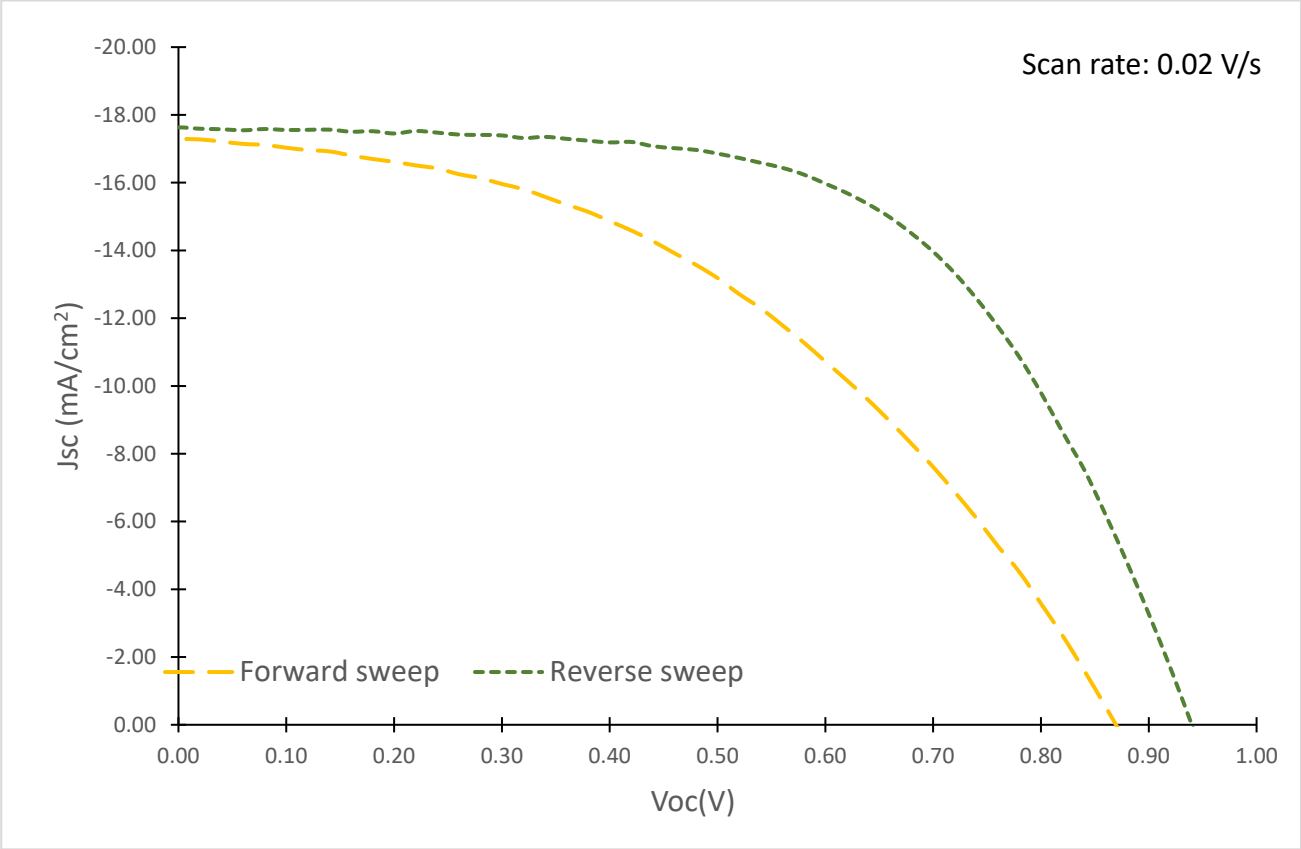

Figure 4-14 IV curve under simulated sunlight for the best efficiency of perovskite solar cell fabricated by this work in air, with a short circuit current close to 18 mA/cm^2 and open circuit voltage around 0.9 V.

4.3.5 Comparison between devices fabricated with or without humidity controlled environment

While it is possible to fabricate perovskite solar cells without controlling the environmental conditions, the performances of the cells are limited when compared with the devices fabricated in the environmental condition controlled atmosphere. Table 4-16 shows the difference in device performance under light conditions. While the fill factor seems to be similar for each case, there is a definite increase in the open circuit voltage and short circuit current density. The open circuit voltage was able to increase to close to 1 V, with some devices occasionally reaching slightly over 1V, similar to the results published in the literature. The short circuit current density also increased to approximately 15 mA/cm^2 on average for devices fabricated in a humidity controlled chamber, as compared to 12 mA/cm^2 for devices fabricated without the humidity control. This indicates that

the paths for electron-hole pair recombination are reduced in the devices fabricated with humidity controlled environment. The higher short circuit current density of devices fabricated in a controlled environment indicates fewer defects within the device, or at the interface between thin films. In consequence, there are fewer traps within the device that traps electrons from flowing to the load before recombines with the holes.

Table 4-16 Common device performances with the solar simulator of perovskite solar cells fabricated with or without a humidity controlled environment. The device with the best performance is excluded in this table, to show the most common result obtained with or without a glovebox.

Without glovebox (average humidity 35 %)				With glovebox (average humidity 15%)			
Efficiency (%)	Fill Factor (%)	Voc (mV)	Jsc (mA/cm^2)	Efficiency (%)	Fill Factor (%)	Voc (mV)	Jsc (mA/cm^2)
5.13	54.33	850.00	11.12	7.6	52.3	996.6	14.59
3.05	35.41	862.05	10.00	7.85	50.4	988.8	15.75
4.37	50.66	750.00	11.50	7.09	43.3	1010.2	16.22
6.13	52.09	850.00	13.85	6.63	45.9	856	16.86
3.31	43.01	862.05	8.93	6.83	46.6	919.3	15.93

4.4 Optimized PSC fabrication protocol

Compact TiO_2 deposition

200 W DC sputtering using Ti sputtering target (99.995%, 3" Dia) with Ar/O_2 gas ratio 1:2 and the pressure set at 4.8×10^{-3} torr to achieve a thickness of 115 nm.

Mesoporous TiO_2 deposition

The TiO_2 paste (Dyesol, 30NR-D Titania) with 30 nm particle size is diluted in Ethanol (150 mg/mL). The prepared precursor is then spin coated on the sample at 5000 rpm spin coating speed with 2500 rpm/sec for 10 seconds. The spin coated sample is then annealed at various temperatures described in Table 4-3 in Section 4.2.2.

$MAPbI_3$ deposition

The Precursor is prepared by dissolving a 1:1 mol ratio of PbI_2:MAI in DMF/GBL(8:2). The prepared precursor is deposited on the substrate using spin coating with the anti-solvent method. The spin

coating speed is set at 1000 rpm speed and 1000 rpm/sec acceleration for 3 seconds, followed by 4000 rpm and 2000 rpm/sec for 25 seconds. Approximately 250 uL of chlorobenzene is dispensed at 5 seconds before the final spin coating duration ends. The sample is then annealed at 70 ° for 5 minutes.

Spiro-OMeTAD deposition

A premade precursor with 80 mg Spiro-OMeTAD dissolved completely in 1 mL of chlorobenzene. 17.5 µL of 520 mg/mL of Li-TFSi salt in acetonitrile and 28.5 µL of TBP is then added to the mixture to form a homogeneous and slightly yellow solution. The material is then spin coat on the sample at 4000 rpm speed and 1000 rpm/sec acceleration for 30 seconds.

After the deposition of spiro-OMeTAD, the samples are stored overnight in dark in the desiccator (<10 RH%) before counter electrode deposition

Au electrode deposition

100 nm of gold is deposited via electron beam evaporation with a 5 kV gun and current between 32 mA and 38 mA at a low pressure of 1×10^{-5} torr.

The completed device is then stored overnight in dark in the desiccator before characterization

4.5 Conclusions

Both compact and mesoporous TiO_2 layers have been tested to optimize the device's overall electrical performances through characterisations such as thin film surface imaging, optical transmittance, or absorbance. The overall thickness of the two layers in combination needs to be below 400 nm to allow electrons to transport effectively from the active perovskite layer to FTO, the transparent conductive electrode. Different deposition methods and parameters of the $MAPbI_3$ perovskite layer has been tried and tested. The anti-solvent method proves to be the better method for depositing $MAPbI_3$ film with minimal cracks or pinholes. The hole transport layer, spiro-omeTAD, and counter electrode were kept constant for this research. The best power conversion efficiency device fabricated without humidity control could reach to 9.88 % in reverse sweeping.

Most of the devices fabricated without humidity control shows lower Voc and Jsc when compared with the devices fabricated in a controlled environment. This indicates that there are more electron-hole pair recombination and defects in the device.

5. Submicron upright pyramids with Au nanoclusters for Perovskite Solar Cell Applications

5.1 Introduction

The application of light trapping structures onto perovskite solar cells (PSC) has the potential of improving the amount of incident light reaching the active photon absorption layer. Moreover, with increased interest in multicolor solar cells [20, 170], integrating metallic nanoclusters within the light trapping nanostructures can be utilised to fine tune the absorption spectra of the wavelength of interest. This is providing that these structures maintain the required transparency for visible light to enter the device. [128] Furthermore, the degradation of the various layers by UV radiation is one of the main factors that determine the stability of perovskite solar cells. The addition of metallic nanoclusters should potentially improve the long term stability of the device while not compromising the efficiency of the device.

The use of nanostructured light trapping features for reducing reflections and enhancing incident light absorption is a well-established technique [114, 123, 171]. While a few researchers are focusing on applying nanostructures onto the transparent substrate for PSC devices, most of the works were focused on theoretical modelling and simulations [17, 113, 172], with very few that include experimental demonstrations. Shi et al. tried to use pre textured substrates in their experiments, but the textured substrate they used was commercially available FTO glass from Asahi glass. The textured substrate was achieved by depositing fluorine doped tin oxide (FTO) in a particular way that the surface roughness of the film was much higher than the commonly available FTO on glass [173]. This requires special deposition methods that are not readily available in most labs and are solely provided by one particular company [173-175]. Tavakoli et al. have published a method utilizing nanocones fabricated with PDMS on willow glass for flexible PSCs applications [176].

Their structures show an increase of 9 % on power conversion efficiency, from 12% to 13.14%. Although this method improved the overall performance slightly, however, the fabrication was time-consuming since PDMS needs to be thermally cured at 80 °C for at least 2 hours. The coating of nanostructures directly on the substrates via nanoimprinting, as reported by Amalraj et al. would reduce the required time dramatically [140, 141].

Furthermore, the demand for colourful photovoltaic panels is one of the demands for rooftop applications [18, 19, 111, 177]. One of the possible ways to achieve multicolour solar cells is to incorporate metal nanoclusters on or within the nanostructures. Metal nanoclusters, such as Al, Ag, or Au, have been studied [114, 178]. Their optical absorbance spectrum can be adjusted, depending on the material type choice, cluster size, the number of atoms per cluster, and the distance between the nanoclusters [129, 130]. Adding nanoclusters to surface textured substrates can be used to achieve both light scattering and device colour tuning. Conventionally, the nanoclusters are usually deposited on the surfaces after the surface nanostructures are formed.

Here we investigate the effect of adapting the use of upright sub-micron pyramids on the commercially available, non-textured FTO glass employing nanoimprinting lithography (NIL) for pattern transfer. The coated PSC device was then compared with the samples without nanostructures or clusters features. It is worth mentioning that the UV curable resist (Ormostamp) used in this research is widely used as a stamping material for the nanoimprint process. Long term stability of the nanostructures under outdoor conditions was not fully examined in the past. Therefore, the durability of the nanopyramids was also studied in this thesis under different external conditions.

We also attempted to dope the nanopyramids with nanoclusters instead of coating the nanopyramids. Solvent compatible $Au_9(PPh_3)_8(NO_3)_3$ was selected as the possible candidate in doping the solvent based UV curable resist. $Au_9(PPh_3)_8(NO_3)_3$ has been studied extensively by Professor Golovko's group at the University of Canterbury [179, 180]. Figure 5-1 shows the chemical structure of $Au_9(PPh_3)_8(NO_3)_3$, obtained from the Cambridge structure database.

$Au_9(PPh_3)_8(NO_3)_3$ is small in size (1.8 nm on average) and can be dispersed in solvents such as Dichloromethane or Isopropanol alcohol, which are compatible with the UV curable Ormostamp resist. For this research, $Au_9(PPh_3)_8(NO_3)_3$ nanoclusters were mixed into the UV curable polymer and the physical and optical characteristics of the Au nanocluster doped nanopyramids with the undoped samples were compared. Furthermore, the effect of Au nanoclusters on the nanopyramids' self-cleaning characteristics was also examined.

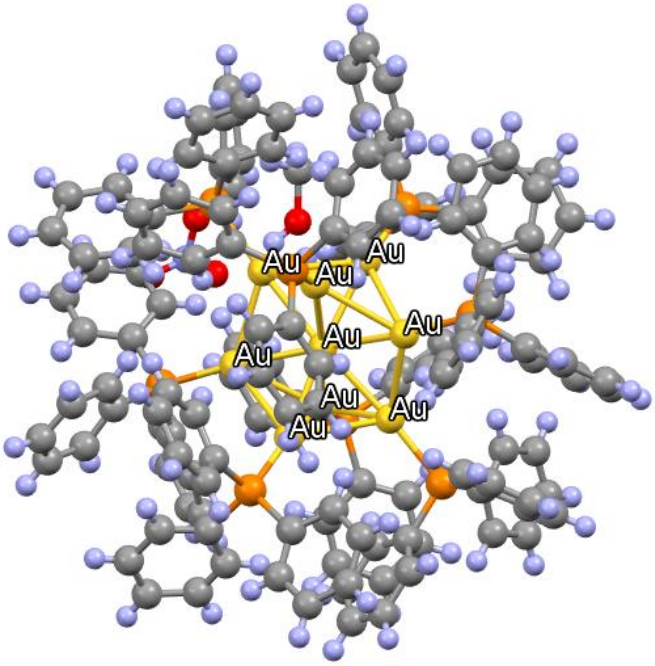

Figure 5-1 $Au_9(PPh_3)_8(NO_3)_3$ crystal structure obtained from F. Wen, U. Englert, B. Gutrath, and U. Simon, "Crystal Structure, Electrochemical and Optical Properties of [Au9(PPh3)8](NO3)3," *European Journal of Inorganic Chemistry,* vol. 2008, pp. 106-111, 2008. CCDC-645243, The Cambridge Crystallographic Data Center, https://dx.doi.org/10.5517/ccpnf91 [181].

5.2 Nanopyramid Fabrication

There are several steps in upright nanopyramid fabrications. A flow chart of the whole process is shown in Figure 5-2. To form the 3D pyramid structure on the glass substrate with nanoimprinting, a stamping mould needs to be fabricated first. The Si mould with inverted pyramids feature was first patterned with interference lithography described in section 3.1.2 on the photosensitive photoresist. The pattern is then transferred via dry etching, followed by anisotropic wet etching to

form the inverted pyramids in the Si substrate. The Si mould is then used as the stamping mould for upright nanopyramids with the UV curable photoresist.

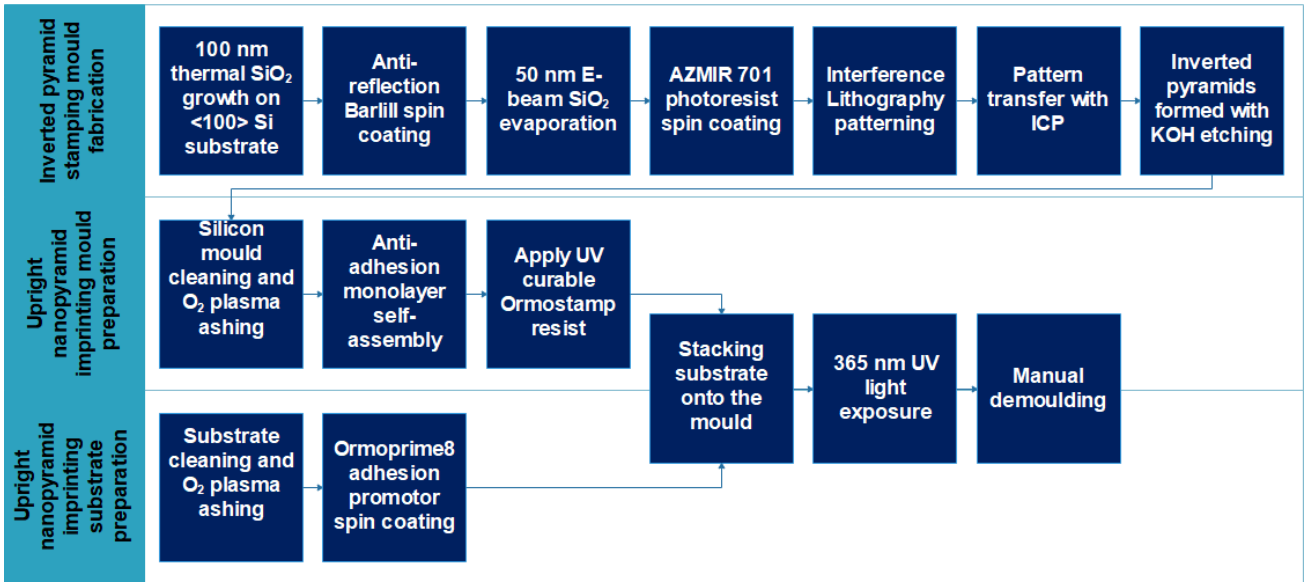

Figure 5-2 Upright nanopyramid fabrication flow chart. The Si mould is patterned with interference lithography and then formed the inverted pyramids with dry and wet etchings. The nanoimprinting of upright nanopyramids used the Si with inverted pyramids as the stamping mould to form the upright pyramids with UV curable Ormostamp resist.

5.2.1 Doping Ormostamp with $Au_9(PPh_3)_8(NO_3)_3$ Gold nanocluster

$Au_9(PPh_3)_8(NO_3)_3$ crystals were synthesized and obtained from Associate Professor Vladimir Golovko's research group. The crystals were synthesized following the recipe described by Anderson et al. [179] Figure 5-3 shows the process followed in this work for incorporating $Au_9(PPh_3)_8(NO_3)_3$ into the Ormostamp, the UV curable resist. The $Au_9(PPh_3)_8(NO_3)_3$ crystals were first dispersed in dichloromethane to obtain a homogeneous brown coloured solution. The mixture is then mixed with Ormostamp with a magnetic spinner for 5 minutes, resulting in a lighter brown coloured homogeneous mixture. The mixture was then placed in the fume hood to allow evaporation of the dichloromethane in the mixture at room temperature until the Au_9 doped polymer has a consistency that resembles the pure Ormostamp characteristics.

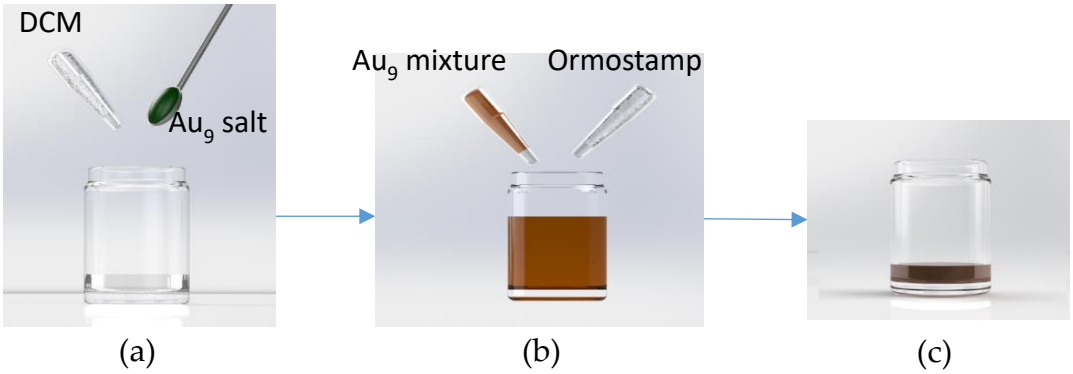

Figure 5-3 Doping method of Au_9 nanoclusters into Ormostamp UV curable resist: (a) Mix Au_9 with dichloromethane DCM, (b) Mix Au_9 solution with UV curable Ormostamp, and (c) leave to evaporate dichloromethane at room temperature

5.2.2 Silicon Mould Fabrication

6. Table 5-1 Thermal oxidation growth of SiO_2 on <100> silicon wafer with dry and steam assisted oxygen.

Dry	The furnace was fed with oxygen gas from an oxygen cylinder with 99.9% purity. The duration of this process is 5 minutes. This is to grow a high purity of SiO_2 at the interface of silicon and SiO_2.
Wet	Oxygen gas is bubbled through the 75 °C water then fed into the furnace tube. This way the oxygen gas is also carrying the water vapour into the furnace, increase the SiO_2 growth rate. The duration of this process is 10 minutes.
Dry	Once the required thickness of SiO_2 is reached, another 5 minutes of dry oxygen growth with the process explained above. This is to provide high quality SiO_2 at the interface of SiO_2 and the subsequent layer on the thermally grown SiO_2.

The method of fabricating silicon moulds for this research was established previously at our Nanofabrication laboratory as detailed by Sivasubramaniam et al. and Amalathas et al [138, 182]. It began with depositing, growing, and spinning the tri-layered films on top of the <100> oriented Si wafer before interference lithography patterning. A 100 nm of SiO2 was thermally grown on the Si

wafer using a high-temperature quartz tube furnace at 1000 °C with both dry and steam assisted oxygen, as shown in Table 5-1.

A 200 nm of AZ BARLiII (MicroChemicals GmbH) was then spin coated onto the wafer to eliminate the unwanted reflection from the Si substrate. Following that, another layer of 50 nm of SiO_2 was thermally evaporated on the BARLi Antireflection coating. After the evaporation of SiO_2, a thin layer of adhesion promoter, Hexamethyldisilazane (HMDS) and a layer of diluted AZMiR 701 photoresist (imaging layer) in PGMEA were spin coated onto the wafer before the lithography exposure.

Laser Interference Lithography (LIL) was used to pattern the sub-micron sized dots onto the photoresist explained in chapter 3. Two exposures at 90° angle difference, with exposure times ranging from 60 seconds to 80 seconds depending on the laser intensity, were used to form nanodots with $\lambda/2$ periodic pitch.

Table 5-2 ICP process recipe for transferring nanohole patterns from the photoresist to the silicon substrate. The whole process, including loading unloading samples, takes approximately 5 minutes to complete.

Layer to be etched	Process gases	Gas flow rate (sccm)	Process pressure (mTorr)	ICP power (W)	Substrate Table power (W)	Duration (seconds)
E-beam evaporated SiO_2	CHF_3	25	10	200	100	32
BarliII antireflection coating	O_2	50	5	250	100	32
Thermally grown SiO_2	CHF_3	25	10	200	100	120

Initial pattern transferring was done by using reactive ion etching (RIE) with either oxygen or CHF_3/Ar plasma in the research done previously [182]. For this research, the dry etching process has been switched to ICP, as described in section 3.3.2, with the process conditions shown in Table 5-2. For RIE dry etching, including pumping down and changing parameters for each layer, could take as long as an hour to complete the whole process. ICP dry etching reduces the time required to approximately 5 minutes, including loading/unloading and pumping down to the required vacuum

pressure.

A 30% Potassium hydroxide (KOH) in water was used to perform anisotropic etching on the exposed Si surface to form inverted pyramids. KOH will attack the <110> orientation 20 times more than the <111> orientation forming inverted pyramids. While most of the layers would be removed during the previous pattern transfer dry etching process, the thermally grown SiO_2 would remain as the masking layer during the KOH wet etching step. The remaining SiO_2 layer was finally removed using a buffer HF solution until the substrate surface appears to be hydrophobic.

5.2.3 Upright pyramid nanoimprinting

The silicon mould fabricated with a method described in section 5.2.2 was first cleaned with a mixture of sulfuric acid and hydrogen peroxide to remove organic materials from the mould, followed by a standard solvent ultrasonic clean of acetone, methanol then isopropanol alcohol. A 10 minute oxygen plasma treatment was used to further remove any remaining organics, and ensure that the mould is hydrophilic for the anti-adhesion coating deposition step. The mould was then placed in a vacuum desiccator for 2 hours to obtain a self-assembly monolayer of (1H, 1H, 2H, 2H-perfluorooctyl) trichlorosilane solution (F13-TCS) as the anti-adhesion coating.

Glass substrates were cleaned with solvents and treated with oxygen plasma to achieve a hydrophilic surface on the substrate. A layer of adhesion promoter, Ormoprime08 was spin coated onto the layer to enhance the adhesion between the substrate and the imprint resist. An imprint tool, shown in Figure 5-4 was used to secure the mould and substrate together during UV exposure.

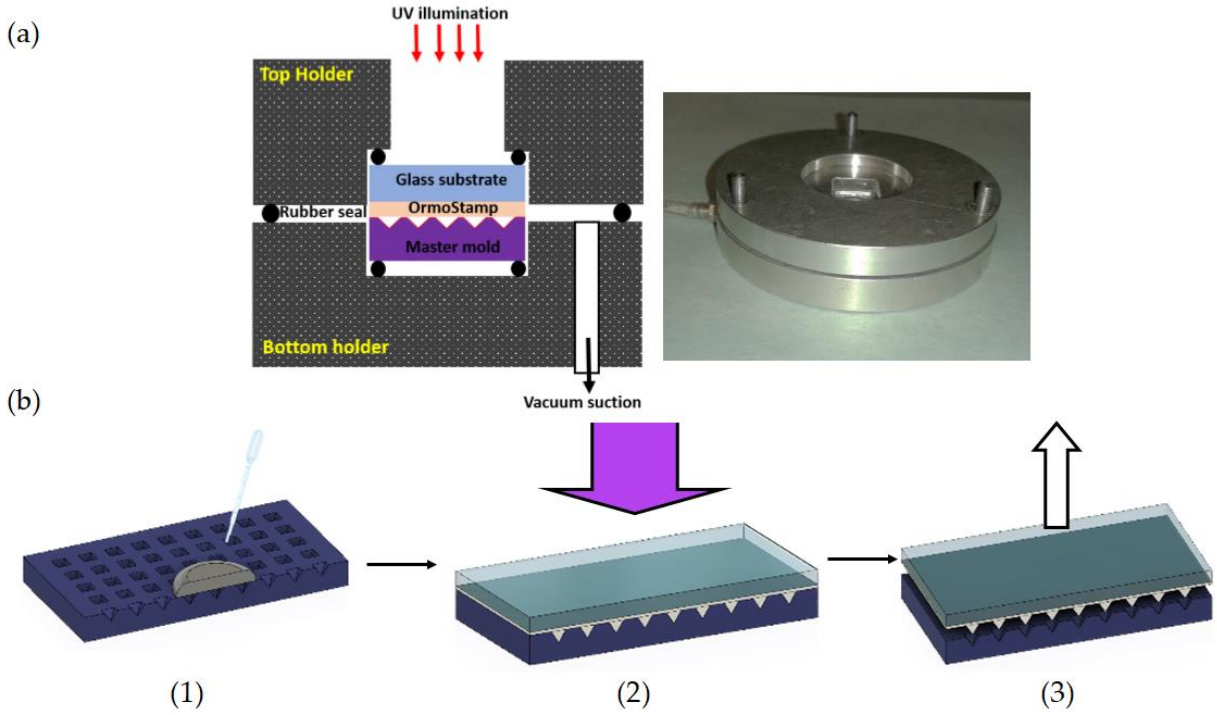

Figure 5-4 Nanoimprinting of nanopyramids: (a) Left: operating mechanism of the imprint tool; right: the imprint tool used at the nanofabrication laboratory, University of Canterbury. (b) Process of nanoimprinting upright nanopyramids: (1) UV curable resist Ormostamp dispense on the silicon mould, (2) Substrate placed on top of mould then followed by 4 minutes of UV flood exposure, and (3) manual demoulding of the sample from the silicon mould.

The mould was placed face-up on the holder with a drop of pure or $Au_9(PPh_3)_8(NO_3)_3$ doped Ormostamp dispensed in the centre of the mould. The substrate with the Ormoprime08 layer was placed directly on top of the mould. The weight of the substrate and the vacuum pressure of 4 mbar provided the required applied force for imprinting. The stack was exposed to UV light with approximately 5 mW/cm2 for 4 minutes to cure the resist and form the upright pyramids. Demoulding (separating the mould from the substrate) was done manually to separate the silicon mould and the substrate.

5.3 Perovskite Device Fabrication

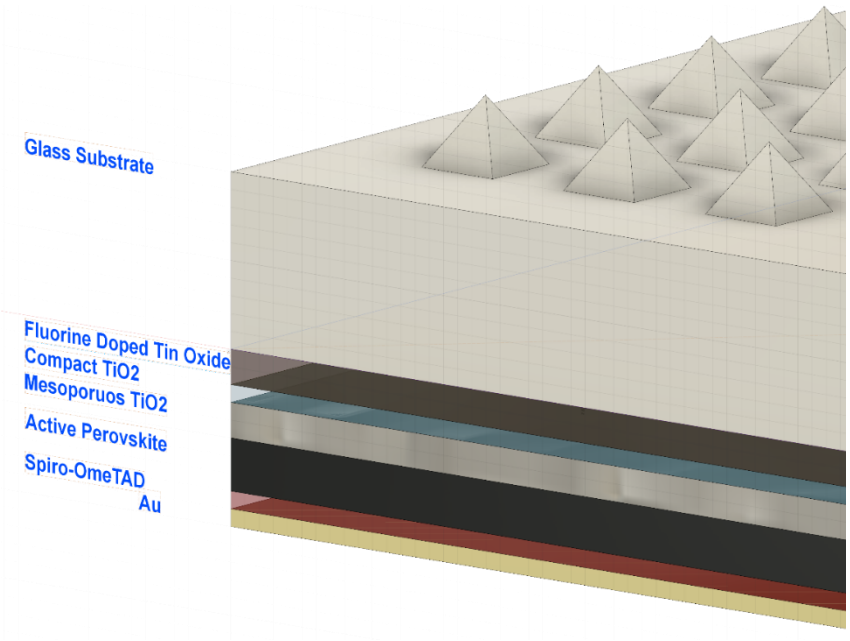

Figure 5-5 Basic structure of Perovskite solar cell with nanopyramids coated on the glass substrate. The pyramids are placed on the side that will be exposed to the sunlight

Figure 5-5 shows a typical basic structure of the device fabricated in this work. There are three main layers for most perovskite solar cells structure, the TiO_2 electrons transport layer, the active perovskite layer, and the Spiro-omeTAD holes transport layer. The fabrication of the perovskite solar cell for this chapter uses the fabrication processes optimized in Chapter 5.

5.3.3 Perovskite Precursor Preparation

TiO_2 precursor for mesoporous TiO_2 layer was prepared by diluting TiO_2 paste with TiO_2 nanoparticles (Great Solar Cell, average particle size 30 nm) in absolute Ethanol with 150 mg/mL concentration. The solution was stirred at 50 °C for at least 2 hours before use.

Precursor for the active perovskite layer was prepared by dissolving MAI (Great Solar Cell) and PbI_2 (Lumtec) in a mixed solvent of Dimethylformamide (DMF) and Dimethylsulfoxide (DMSO) with 1:1 molar ratio at 70 °C.

The Spiro-omeTAD for hole transporting layer (HTL) was prepared with a similar recipe mentioned

elsewhere [19, 56, 57]. 72 mg of Spiro-omeTAD (Lumtec) was dissolved in 1 mL of Chlorobenzene (CB) with 28.8 µL of 4-tert-Butylpyridine and 17.5 µL of 520mg/mL Bis(trifluoromethane)sulfonamide salt (Sigma Aldrich, 99.95 metal trace basis) in acetonitrile. The precursor was prepared immediately before spin coating the layer.

5.3.4 Device Fabrication

Unwanted section of fluorine-doped tin oxide (FTO) films on soda lime glass substrates (MSE supplies, 7-10 ohm/sq sheet resistance) was etched with Zinc powder and 2M Hydrogen chloride in DI water, followed by substrate cleaning with acetone, methanol, and isopropanol alcohol. The substrates were dried with nitrogen gas and stored in the oven set at 95 °C.

Before the deposition of compact TiO_2, the dehydrated substrates were further cleaned with oxygen plasma for 10 minutes. A 115 nm of compact TiO_2 layer was deposited via DC magnetron sputtering of Titanium target (Lesker,) at 200 W with a plasma of a mixture of Oxygen and Argon gas. The chamber background pressure was at approximately 4.8×10-6 Pa. The sputtering processing pressure was 3x10-3 Pa for the combination of Ar and O_2 gas. The flow rate of the Ar is set at 6 sccm whereas the flow rate for O_2 is set at 12 sccm, to maintain a ratio of 1:2 of Ar: O_2.

Mesoporous TiO_2 layer was deposited via spin coating the prepared precursor from Section 4.3.1 at 5000 rpm with 2500 rpm/second acceleration for 10 seconds. The samples were then annealed on the hotplate at 500 °C for 30 minutes with slow ramping, to obtain TiO_2 with anatase phased crystal structure.

The active perovskite layer was deposited via anti-solvent deposition under normal laboratory conditions, with humidity around 30 RH%. The prepared perovskite precursor was spin coated at 1000 rpm for 10 seconds, followed by 5000 rpm for 30 seconds. Approximately 150 µL of CB was dispensed on the sample 10 seconds before the spin coating is completed to wash off the DMF and DMSO. The sample was annealed at 100 °C for 1 hour to further remove the solvent in the film and improve the crystal quality [66, 183].

Once the samples have cooled down to room temperature, the prepared spiro-omeTAD precursor was spun coated onto the sample at 4000 rpm for 30 seconds. The samples were then rested in dark at humidity lower than 10 RH% for 7 to 8 hours before a 100 nm thick layer of gold evaporated with Electron beam evaporation. The completed device has an FTO conductive oxide front contact, TiO2 (Electron Transport Layer), Perovskite active layer, Holes Transport Layer, and Au rear contact.

5.4 Device Characterisation

Doping the Ormostamp UV curable resist from Microresist with gold nanoclusters raised the question such as whether the features formed by Ormostamp would remain as robust as the features without gold nanocluster doping. While it is preferred that the nanopyramids to be applied after the device fabrications, devices like perovskite solar cell is very sensitive to UV light and may induce active film degradation during curing the resist with UV light. Moreover, the long term stability of the UV cured nanopyramids in physical structure and optical characteristics have never been studied before. Part of this research looks at the long term stability of the nanoimprinted nanopyramids, doped and undoped with gold nanocluster The robustness of the nanopyramids will also be investigated and determine whether any subsequent semiconductor or thin film fabrications can be done after the application of nanopyramids.

5.4.3 Au nanocluster doped nanopyramid stability test

The suitability of the nanopyramids coating for solar cell applications was examined by subjecting the samples to temperatures at different time lengths, exposure to UV light, and testing the pyramid structures in the oxygen plasma. The pyramids were made of UV curable polymer, commercially available Ormostamp from Microresist.

The as-fabricated nanopyramids were placed on the hotplate at various temperatures ranging from 100 °C to 300 °C with different durations of time from 30 minutes to 2 hours. This test was used to understand any changes in the surface morphology and optical characteristics of the pyramids at

elevated temperature, and what are the thermal limits of the UV cured resist with sub-micron pyramids. A separate test on temperature ramping speed was conducted from 35 °C/hour to 450 °C/hour to investigate whether the polymer withstands thermal cycles and any changes in physical properties including cracks.

For the O_2 plasma treatment test, Ormostamp samples with pyramids imprinted were subjected to O2 plasma at different time durations ranging from 10 seconds to 10 minutes with the Plasma Asher (Tergeo Plasma Cleaner, 100W, 5 sccm O_2 flow rate). Plasma with different power levels ranging from 30 W to 100W was also tested to find the operating range of the UV curable polymer used in fabricating the nanopyramids coating.

Samples were also exposed to continuous UV light for over 5 hours with 40 mW/cm2 intensity to imitate the stability of nano pyramids under continuous sunlight exposure. The only light source that's available in the nanofabrication laboratory which has 100 mW is the solar simulator, which could not operate in long hours. Therefore, the alternative light source was used in this case. Moreover, studies showed that UV light is more detrimental than visible light and New Zealand is one of the countries that have higher UV intensity [184]. While the overall sunlight intensity is approximately 100 mW/ cm^2 across the whole UV-visible wavelength region at the midday of the equator, the UV intensity is approximately 5 mW/cm^2 for the extreme case. Using the UV light with 40 mW/cm^2 intensity could test the nanopyramid's long term stability in a much shorter time, since the intensity is approximately 20 times larger than the average UV intensity in Christchurch, with peak UV intensity between 2.75 mW/cm^2 and 3.5 mW/cm^2 in summer [185].

5.4.4 Surface Morphology and Optical Characterisations

The Submicron pyramid's morphology was examined and analyzed using atomic force microscopy (AFM) from Veeco. Images of the pyramids before and after each treatment were taken for comparison. Shimadzu UV-2600 spectrophotometer fitted with an integrating sphere was used to examine the optical transmittance of the nanopyramids, especially in the visible wavelength region,

before and after treatment. Contact angle measurement equipment was used to determine the change in the hydrophobic characteristic of the pyramids after treatments compared to as-cured samples. The experiment was repeated 3 times with DI water sample cleaning and dried with Nitrogen gas subsequently between experiments.

5.5 Results and Discussion

5.5.3 Nanopyramids physical morphology and optical characteristics

Figure 5-6 shows the AFM image and profile trace of the inverted pyramids silicon mould used for the nanoimprinting process and the replicated upright nanopyramids. The pyramids are approximately 300 nm in height, 500 nm in width, with 600 nm pitch on average. Direct replication and clean demoulding were achieved by ensuring the adhesion force at the interface of resist and mould was smaller than the adhesion force at the interface of resist and substrate by using the anti-adhesion agent. The optical transmittance of the upright pyramids coated on quartz is compared to the plain quartz substrate as shown in Figure 5-7. The total transmittance of the nanopyramids was maintained above 70 % in the visible wavelength range. High transmittance can be seen at a shorter wavelength range. The refractive index of Ormostamp after UV curing falls between 1.5 and 1.52 at the visible light wavelength range, according to the manufacturer's datasheet, which is very similar to glass, between 1.51 and 1.53.

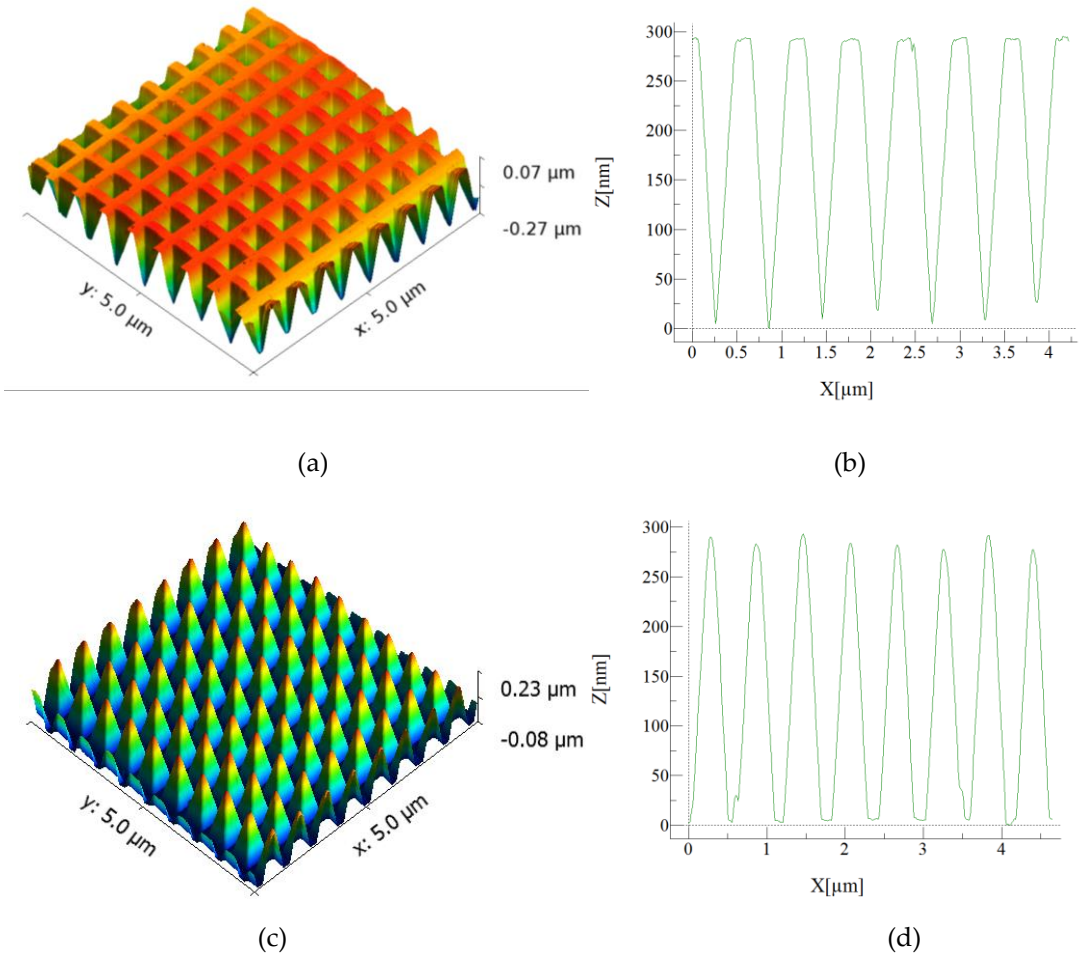

Figure 5-6 (a) and (b) are AFM images and profiles of silicon mould with inverted pyramids. (c) and (d) are AFM images and trace profiles of the upright nanoimprinted pyramids showing that the pyramids are 300 nm high and 500 micron nm in width.

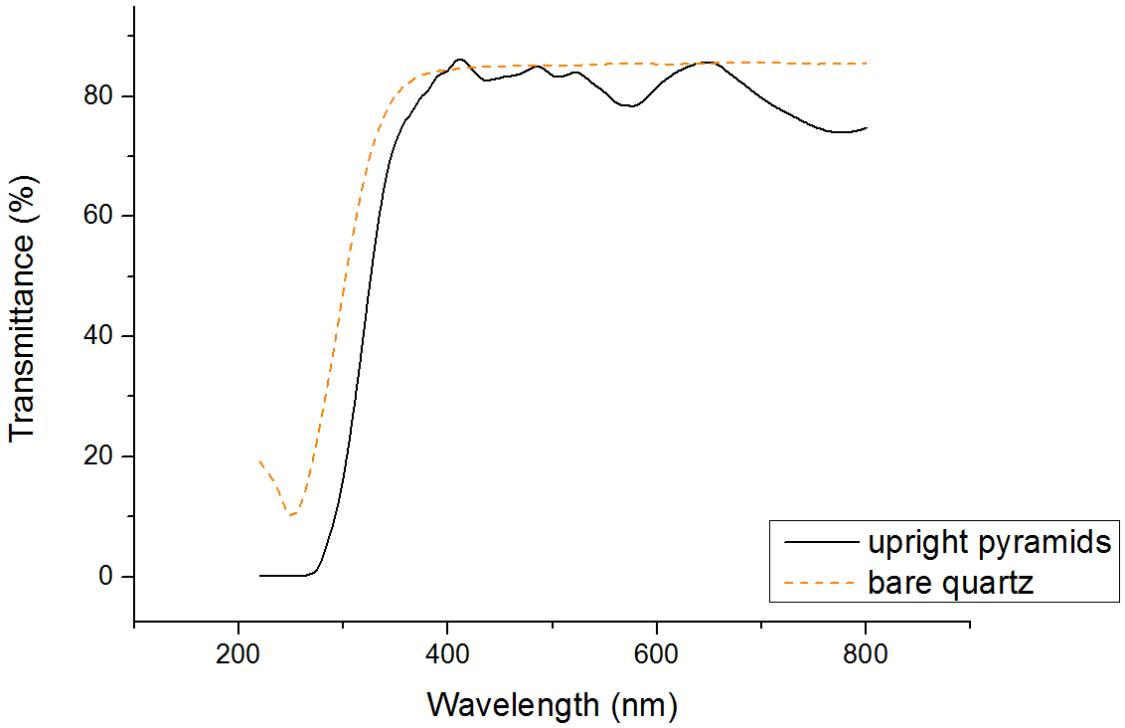

Figure 5-7 Optical transmittance of the nanoimprinted upright pyramids shown as a solid line.

5.5.4 Device Performance

The glass substrates used for device fabrication were approximately 1.1 mm thick. Figure 5-8 shows the improvement in UV-Vis absorbance with and without the nanopyramid light trapping feature. An increase in absorbance can be seen, especially in the shorter wavelength region, an increase of approximately 9 to 10 % of the device without nanopyramids at 450 nm wavelength range.

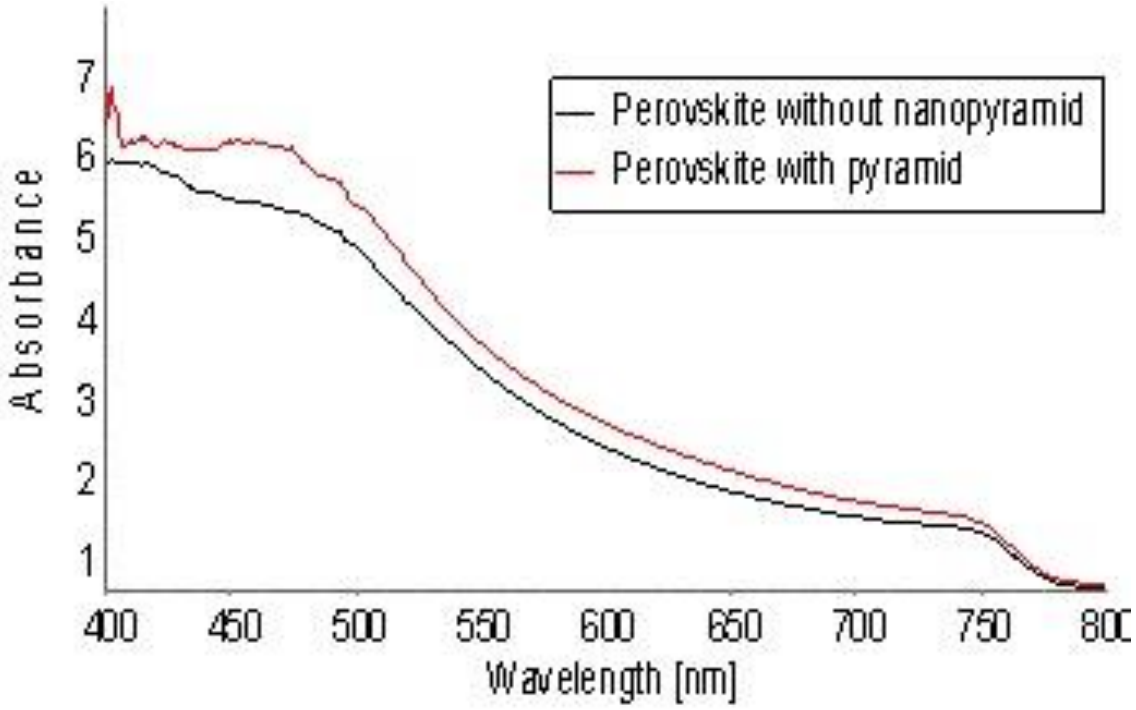

Figure 5-8 Absorbance of perovskite active layer when nanopyramids applied to the glass substrate

Figure 5-9 and Table 5-3 shows the current-voltage characteristics of the perovskite device, where the open circuit voltage, Voc, the short circuit current density Jsc, Fill factor FF, efficiency and series Rs and parallel Rsh resistances are calculated and measured for devices prepared with and without the nanopyramid coating. An increase in Jsc from 17.30 mA/cm^2 to 17.90 mA/cm^2 at the reverse scan could be observed, as well as an increase from 42.6% to 52% in fill factor (F.F) and reduction in series resistance Rs from 173.68 Ω to 83.29 Ω. Overall, a slight improvement in device performance was observed. Further improvement of device performance can be expected if the placement of nanopyramids is altered. With submicron pyramids, the light scattering usually happens at the area closer to the substrate surfaces. This works for silicon solar cells since the p-n junction of the silicon solar cell is usually relatively close to the substrate surface. For the perovskite solar cell, however, the light needs to travel pass through the transparent substrate, the FTO electrode, and TiO_2, the electron transport layer. Therefore, the light scattering effect needs to be much longer. This can be done by fabricating the nanopyramids at the interface of the glass substrate and the transparent electrode, reducing the optical path that the scattered light needs to travel to the photosensitive perovskite layer.

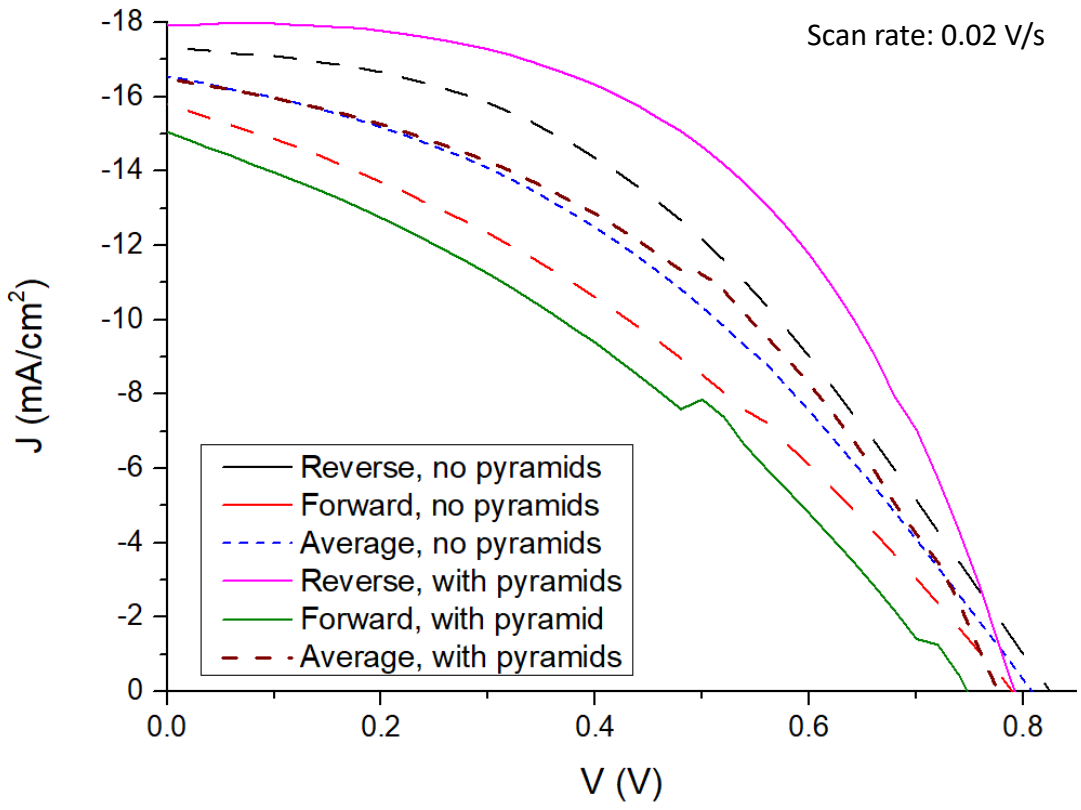

Figure 5-9 IV characteristics of perovskite with and without nanopyramids conducted in forward and reverse scans. The reverse scan is always higher than the forward scan in agreement with the hysteresis expected from perovskite solar cells. The active area of the cell is 0.1 mm^2, which is defined as the area where the gold electrode and FTO electrode overlap. 3 samples with 3 isolated cells each for each variable have been fabricated in the same batch to ensure the validity of the result.

Table 5-3 Performances of perovskite solar cells with or without nanopyramids.

Sample Description	Sweep direction	EFF (%)	FF (%)	Voc (mV)	Jsc (mA/cm2)	Vmax (mV)	Jmax (mA/cm2)	Isc (mA)	Rshunt (Ohm)	Rseries (Ohm)
No Pyramid	Forward	4.32	34.70	789.80	15.79	460.1	9.39	2.21	865.20	195.56
	Reverse	6.09	42.60	825.00	17.30	480.10	12.68	2.42	10001.00	173.68
	Average	**5.21**	**38.65**	**807.40**	**16.55**	**470.10**	**11.04**	**2.32**	**5433.10**	**184.62**
With Pyramid	Forward	3.93	34.90	747.70	15.05	500.10	7.85	2.11	686.87	139.48
	Reverse	7.38	52.00	792.00	17.94	540.10	13.67	2.51	28076.00	83.29
	Average	**5.66**	**43.45**	**769.85**	**16.50**	**520.10**	**10.76**	**2.31**	**14381.44**	**111.39**

5.5.5 Nanopyramids Thermal stability

5.5.5.1 Physical and Optical stability

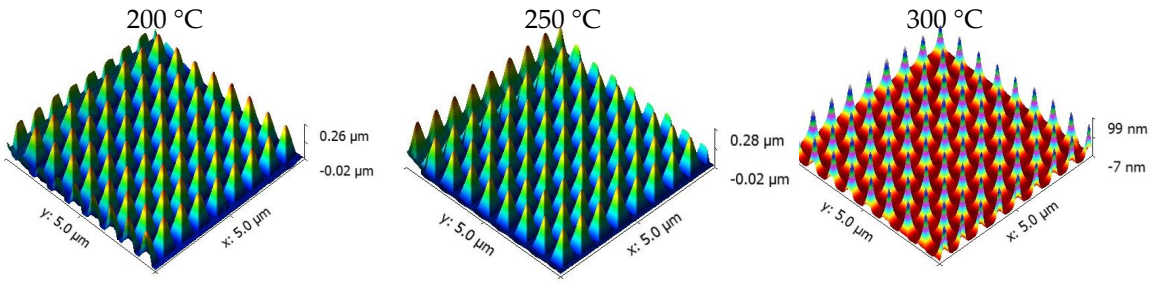

Figure 5-10 AFM images of nanopyramids after 1 hour of heat treatment at different elevated temperatures from 200 °C to 300 °C.

Figure 5-10 shows the AFM images of the nanopyramids nanoimprinted on 1 cm2 quartz substrates kept at different elevated temperatures for 1 hour. In comparison with the as-fabricated pyramids shown in Figure 5-6 (c), the pyramids' physical morphology/shape integrity was maintained up to 250 °C. As the temperature increased to 300 °C, the height of the pyramids decreased by approximately 33% of the original height. The side faces of the pyramids show more degradation (wrinkles) compared to the corners of the pyramids. Because of the optical transparency nature of Ormostamp resist, the UV light used for curing the polymer would also travel through the resist and get reflected by the silicon mould. This results in the resist receiving UV light at a higher intensity than the 4 mW measured. The resist receives higher UV light intensity at the corners where the faces of the pyramid connect due to the double UV light reflected by the two faces. In consequence, the cured resist is more robust at the corners of the pyramids compared with the faces. This study was the first to examine the temperature and oxygen stability of the Omostamp. The results obtained from this test helps in designing suitable process steps for coating the perovskite solar cells. Therefore, for perovskite solar cells with mesoporous TiO_2 as the electron transport layer, the nanopyramids need to be imprinted after the deposition of TiO_2. TiO_2 thin film deposition usually requires high temperature sintering to get the anatase crystal phase, which is the most

photocatalytic crystal phase for TiO_2. Fabricating the nanopyramids after the device is complete was not possible as well. This is because the UV light would either get absorbed by the photoactive layer or reflected by the metal electrode.

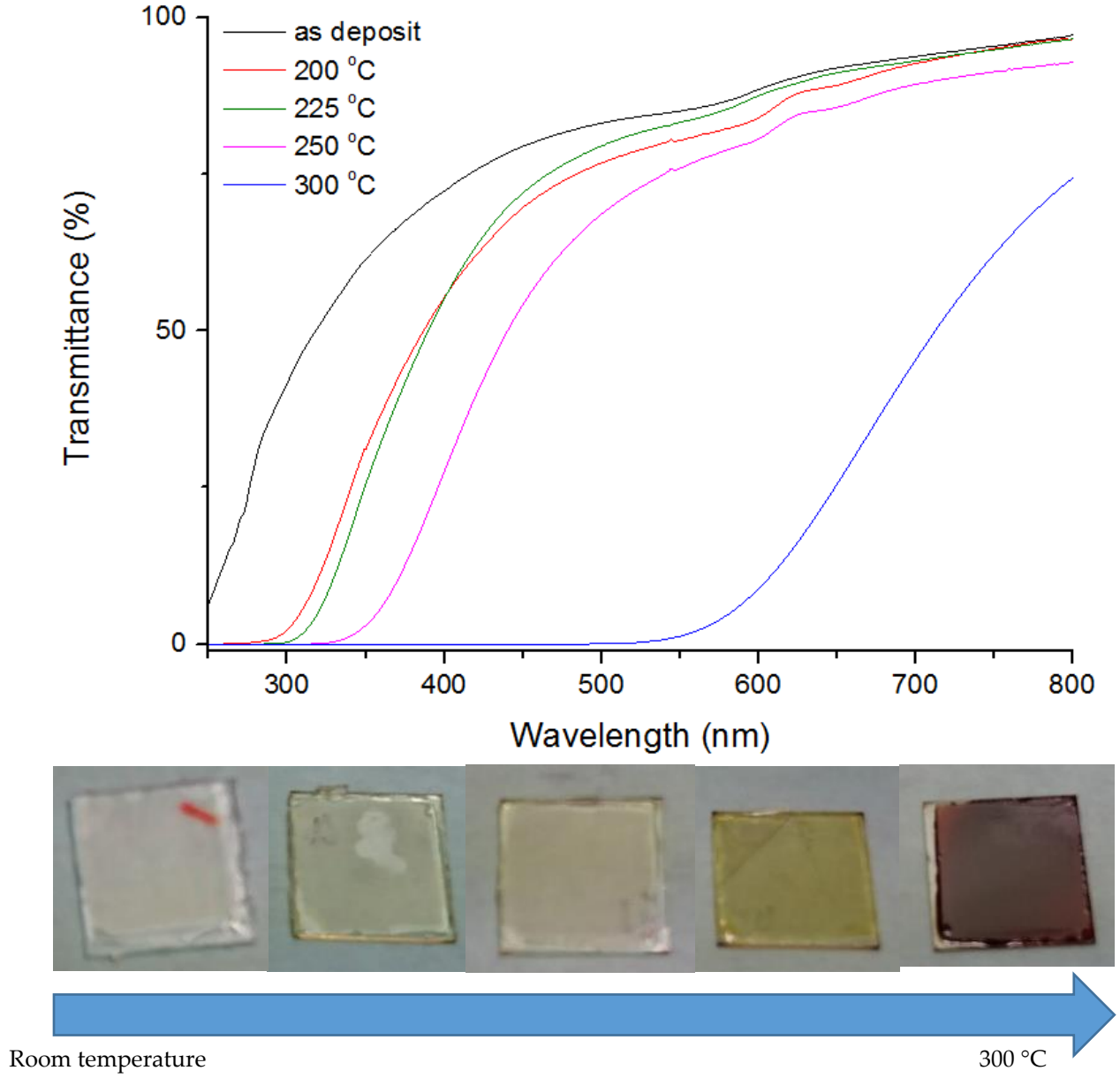

Figure 5-11 Optical transmittance comparison of the upright nanopyramids on quartz under different elevated temperatures for 1 hour.

The optical characteristics of the samples are shown in Figure 5-11. The nanopyramids have high transmittance at 500 nm to 800 nm wavelength when measured at ambient temperature (25 °C) and raised gradually to 250 °C. A huge drop in transmittance can be observed above 250 °C and higher. This is due to the polymers in the UV cured resist being burnt by the high heat.

5.5.5.2 Self-Cleaning characteristic stability

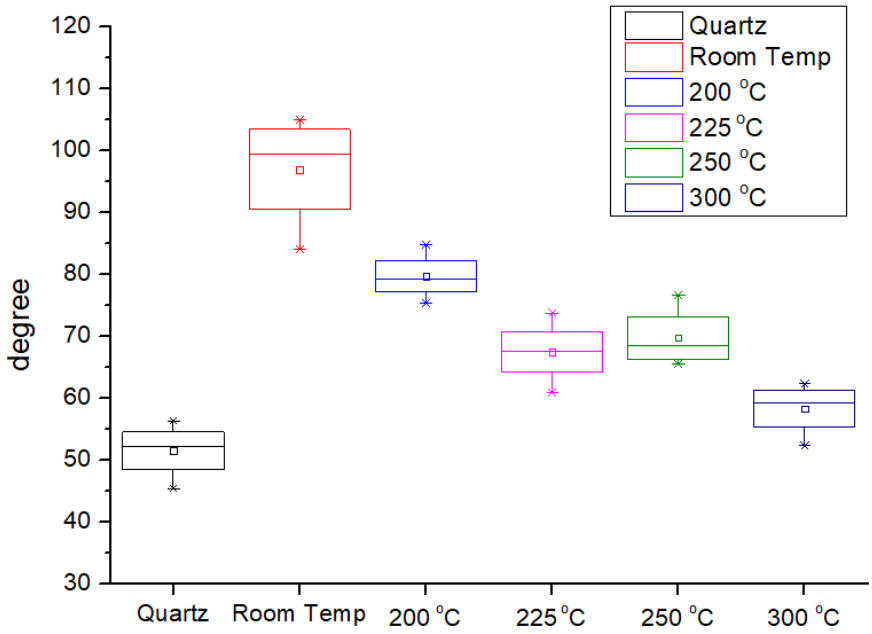

Figure 5-12 Changes in contact angle after exposure to different temperatures in air for 2 hours Each variable were tested at least 3 times with over 5 contact angles on both left and right side. The contact angle at the left and right side is then averaged to obtain the average value of the contact angle of each reading. The middle line of the box graph refers to the average of all contact angles measured from the sample. 75 % of the measured value is below the top edge of the box and 25% of the measured value is below the bottom edge of the box. The top and bottom whisker marks are the maximum and minimum of the measured contact angle.

The nanoimprinted pyramids surfaces are, in general, hydrophobic. This allows the surfaces to be washed easier and prevents the accumulation of dust from building up on their surfaces. Their Hydrophobic surface results in self-cleaning properties of devices coated with the nanopyramids adding another advantage to their antireflection properties. The characteristic is determined by measuring the contact angle of water droplets on the surface of nanopyramids. These characteristics also change as the ambient temperature changes. Figure 5-12 shows the changes in contact angles when the ambient temperature increases. The samples were tested three times with at least five readings for the contact angles at both the right and left sides of the droplets being recorded. While the nanopyramid's physical morphology maintains as the temperature increased to 200 °C, the contact angle of the water droplet on the substrate decreased. This indicates the loss of hydrophobicity of the textured substrate surface. As the temperature increased to 300 °C, the

contact angle drops to similar values as the plain, non-textured quartz substrate.

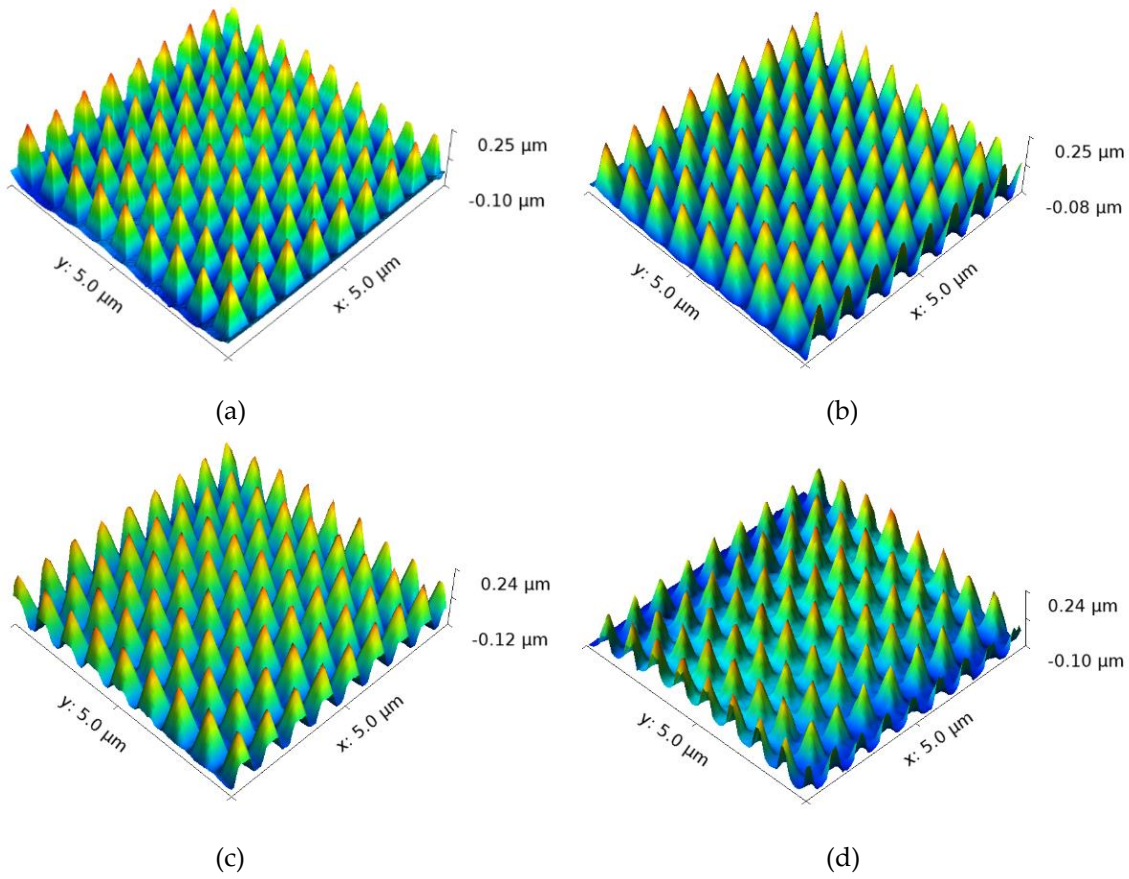

Figure 5-13 AFM 3D constructed image of the nanopyramids after they were subjected to different O_2 plasma duration: (a) 10 seconds, (b) 30 seconds, (c) 1 minute, and (d) 5 minutes.

O_2 plasma is often used to clean and remove organic materials on substrates. This O_2 plasma test is to determine the robustness of the pyramids, and whether the pyramids can be pre-coated before fabricating the perovskite solar cells. Figure 5-13 shows the changes in the physical morphology of nanopyramids after exposed to a short period of O_2 plasma. The result shows that the nanoimprinted pyramids could withstand O_2 plasma for up to 5 minutes. As the duration increased to over 5 minutes, the damage of O_2 plasma to the nanopyramids was visible.

The Nano pyramids are made of the UV curable Ormostamp and found that they can maintain their integrity when exposed to O_2 plasma for up to 5 minutes, temperature up to 250 °C, and UV light intensity for up to 5 hours.

5.5.6 Doping $Au_9(PPh_3)_8(NO_3)_3$ in Ormostamp

The Ormostamp UV curable resist for nanopyramids is optically transparent and allows all the light in the UV-Vis wavelength region to pass through. The possibility of doping the nanostructure with nanoparticles or nanoclusters to allow light with a certain wavelength to pass through has hardly been looked at in the past. The effect of the nanoparticles or nanostructures on the optical characteristics of the nanopyramids has been investigated. Moreover, whether doping the nanopyramids with nanoparticles or nanoclusters would result in a change in the physical characteristics of the nanopyramids is also being studied.

5.5.6.1 Physical and optical characteristics of Au_9 doped nanopyramids

The physical characteristic of Au_9 doped nanopyramid is measured with AFM imaging described in section 3.4.1. This is to determine whether identical nanopyramids could form when Ormostamp is doped with Au_9 nanoclusters. The optical characteristic of the doped nanopyramid has been investigated with UV-Vis spectrometry to understand how much effect of the nanoclusters on the nanopyramid's optical transparency. Figure 5-14 (b) shows the physical morphologies of $Au_9(PPh_3)_8(NO_3)_3$ nanoclusters doped nanopyramids and compares them with the plain nanopyramids (a). The result shows that adding Au_9 nanoclusters does not affect the physical structures of the nanoimprinted pyramids. There is, however, quite a bit of change in the optical transmittance when the pyramids contain different concentrations of Au_9 nanoclusters.

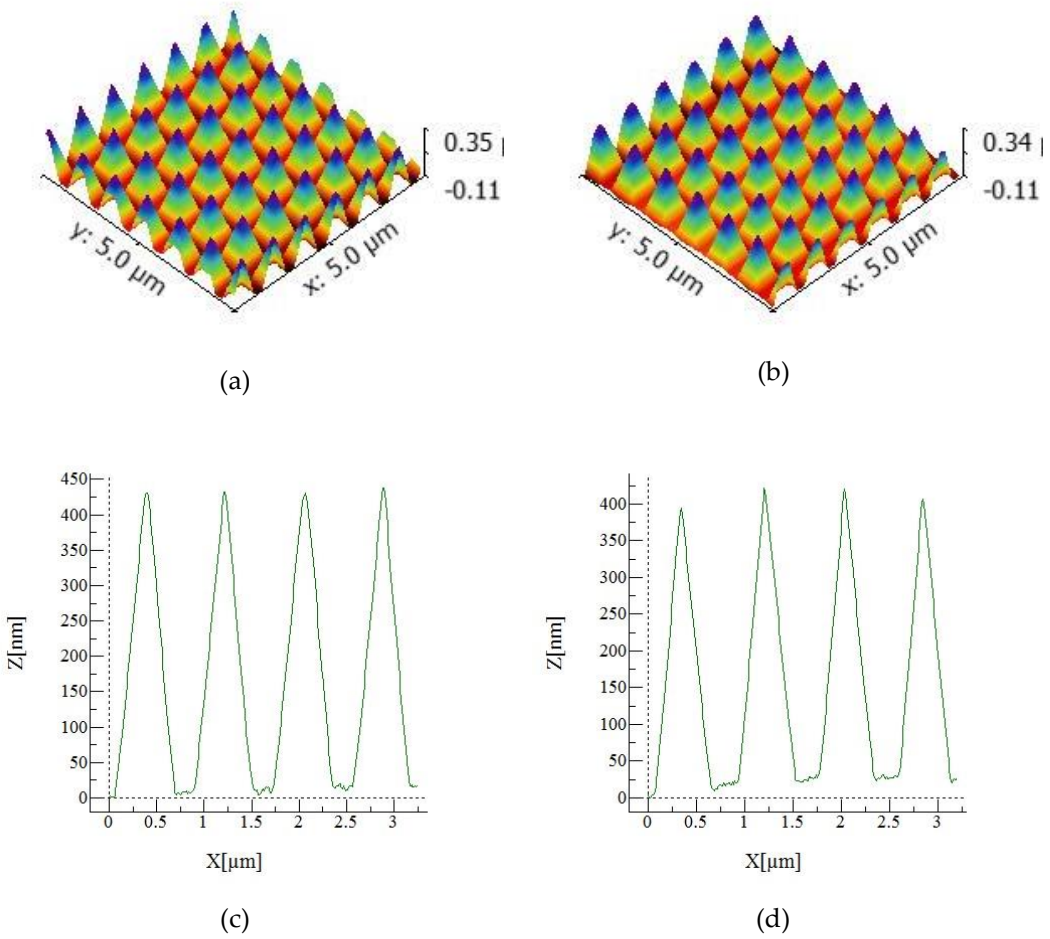

Figure 5-14 Surface morphology of nanopyramids with or without Au_9: (a) and (c) AFM image and trace profile of the nanopyramids without Au_9 nanoclusters; (b) and (d) AFM image and trace profile of Au_9 doped nanopyramids.

This is illustrated in Figure 5-15. Au_9 nanocluster has strong absorbance at the shorter wavelength region, which agrees with the literature. As the concentration increased the optical transmittance at a shorter wavelength drops dramatically. This is possibly due to a higher probability of agglomeration of the nanoclusters when the concentration was increased [180]. For photovoltaic applications, the concentration of Au_9 should be limited to below 2% of the total volume to maintain reasonable optical transmittance in the visible wavelength range.

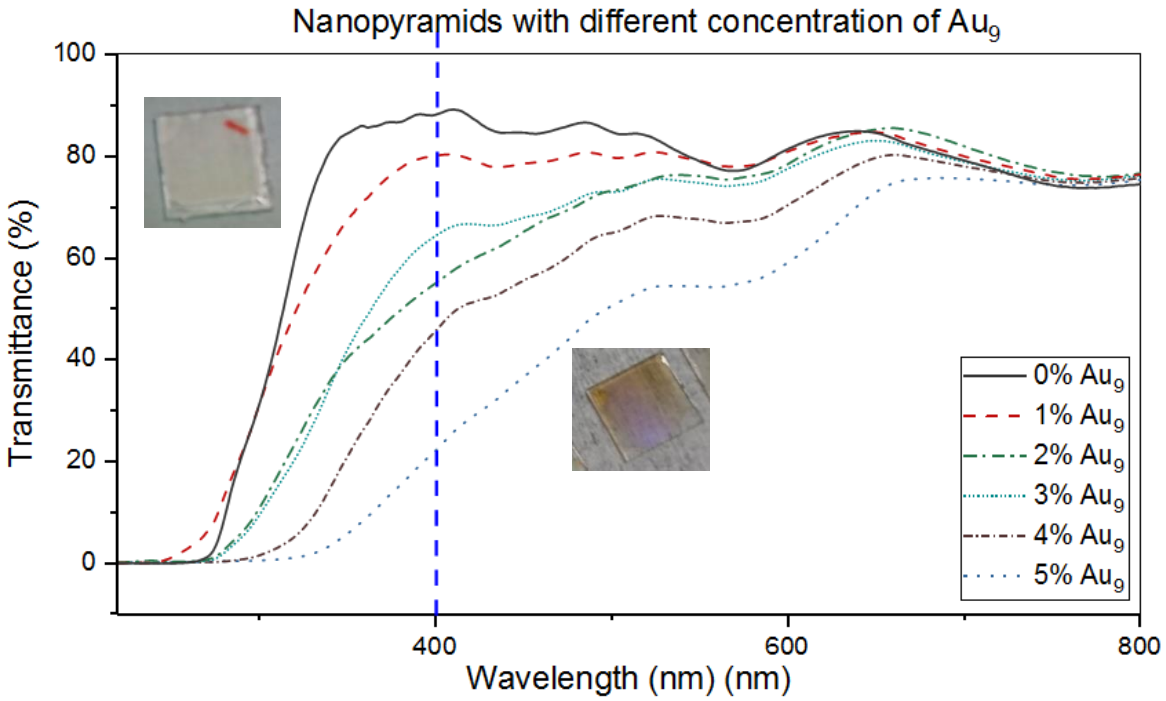

Figure 5-15 Optical transmittances of nanopyramids with different Au_9 concentrations, insert shows quartz samples coated with nanopyramids at two different Au_9 doping concentrations. The optical characteristics are measured with the Shimadzu UV-Vis spectrometer with an integrated sphere at the Department of Chemistry, University of Auckland.

5.5.6.2 Stability of Au_9 doped nanopyramids

The physical morphology of the Au_9 doped nanopyramids seems to be less affected by the elevated temperature up to 250 °C, as shown in Figure 5-16. While both doped and undoped nanopyramids could maintain their physical morphologies up 250 °C, the nanostructure size shrank when treated at 300 °C for an hour. The doped nanopyramids had their height reduced by 100 nm, whereas the height of the nanopyramids without Au_9 has reduced at double the rate.

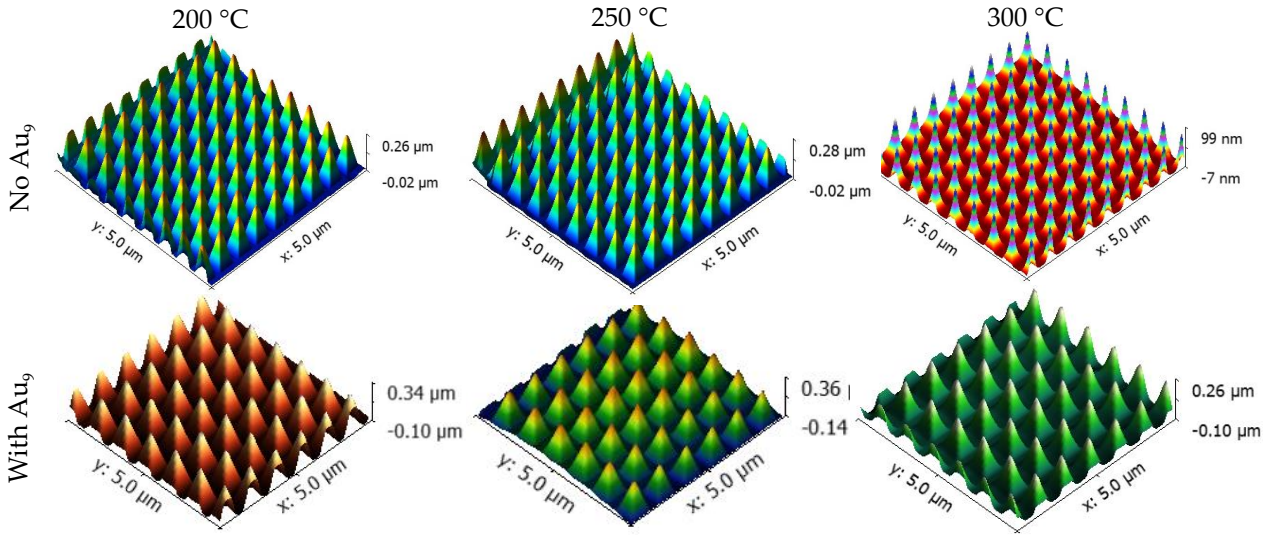

Figure 5-16 Nanopyramids physical morphologies subjected to elevated temperatures for one hour period.

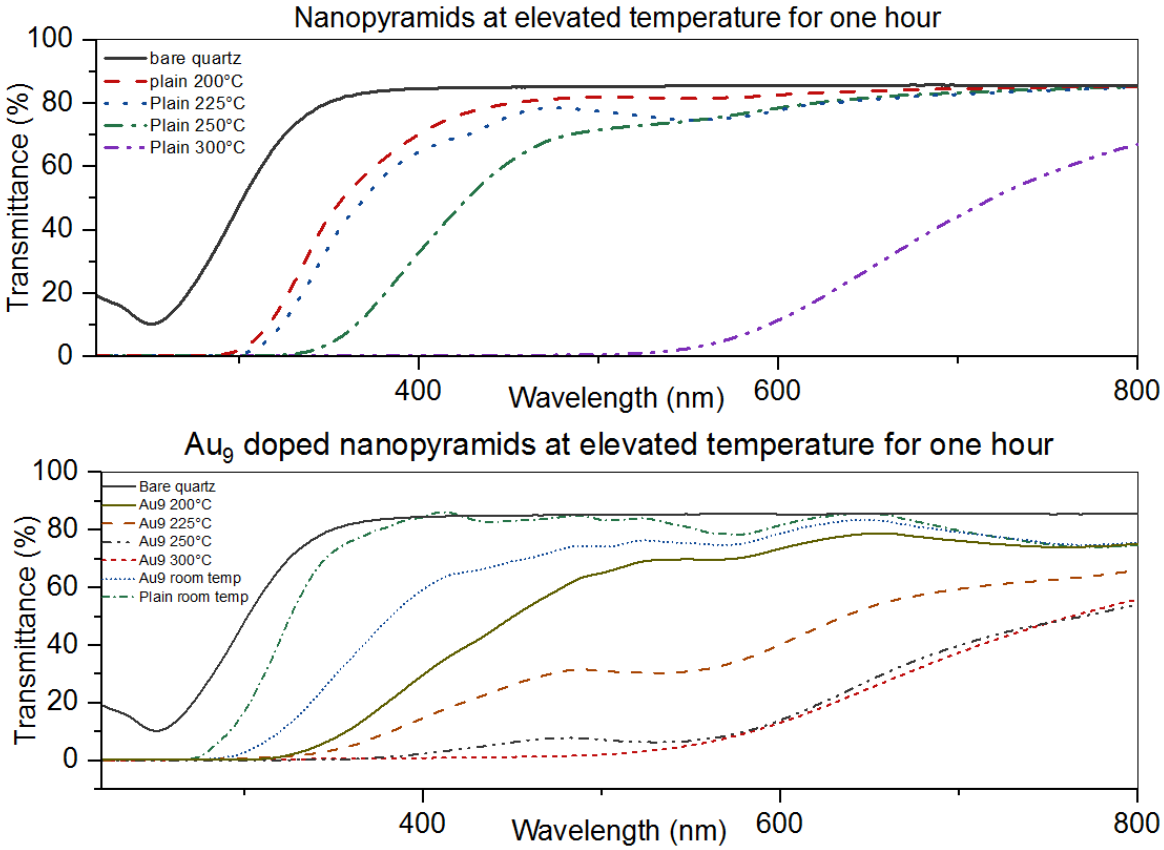

Figure 5-17 Total transmittance variation at various elevated temperature for Au_9 doped and undoped nanopyramids

The optical transmittance of samples at elevated temperatures is shown in Figure 5-17. Samples with Au_9 shows a rapid drop in transmittance when the temperature increased to 225 °C, whereas the undoped pyramids maintained its high transmittance when the samples were placed at 250 °C for one hour. This is possibly due to the ligands of Au_9 decomposing at temperatures above 200 °C. This indicates that fabricating perovskite solar cells with TiO_2 as the electronic transfer layer on

substrates coated with nanopyramids is not possible since the fabrication of TiO_2 usually requires high temperature annealing at around 500 °C. Substitute TiO_2 with other wide bandgap metal oxides such as ZnO or SnO_2 might be able to overcome this problem. Otherwise, the pyramid coating must be performed at the final stages of the fabrication process.

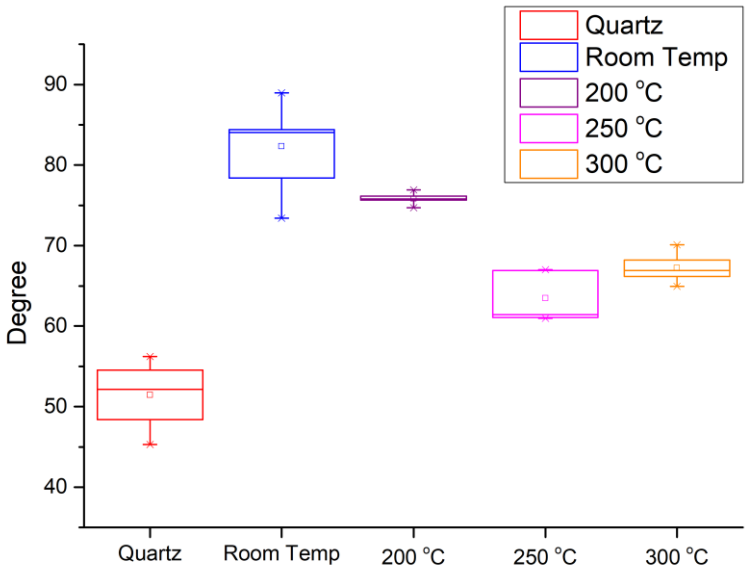

Figure 5-18 Contact angle measurement of Au_9 doped nanopyramids. The contact angle of the sample dropped to below 70 ° when the temperature increased to 250 °C, whereas the undoped sample could maintain around 70 ° at the same temperature.

The as-deposited Au_9 doped nanopyramids have an average contact angle around 80 °, as shown in Figure 5-18. This is approximately 20 ° lower than the pristine nanopyramids. This indicates that the nanocluster doped nanopyramids are less hydrophobic compared with the pristine nanopyramids. However, as the temperature is increased, the contact angle did not decrease as much as the pristine nanopyramids did. The Au_9 doped nanopyramids' contact angle was maintained at or above 60 ° whereas the undoped nanopyramids' contact angle dropped below 60°. Therefore, the processing temperature for any subsequent fabrication on substrates with nano pyramids needs to be below 250 °C.

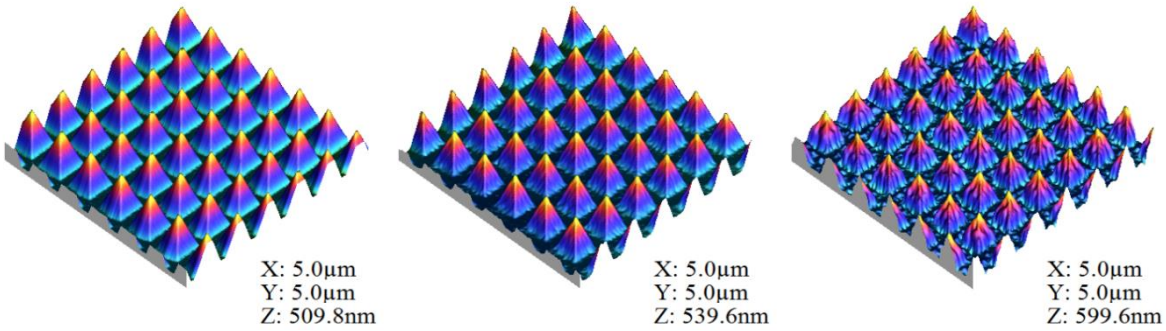

(a) (b) (c)

Figure 5-19 AFM images of nanopyramids (a) before O_2 plasma treatment, (b) plain pyramids after 5 minute O_2 plasma treatment, and (c) Au_9 doped and 5 minute O_2 plasma treatment

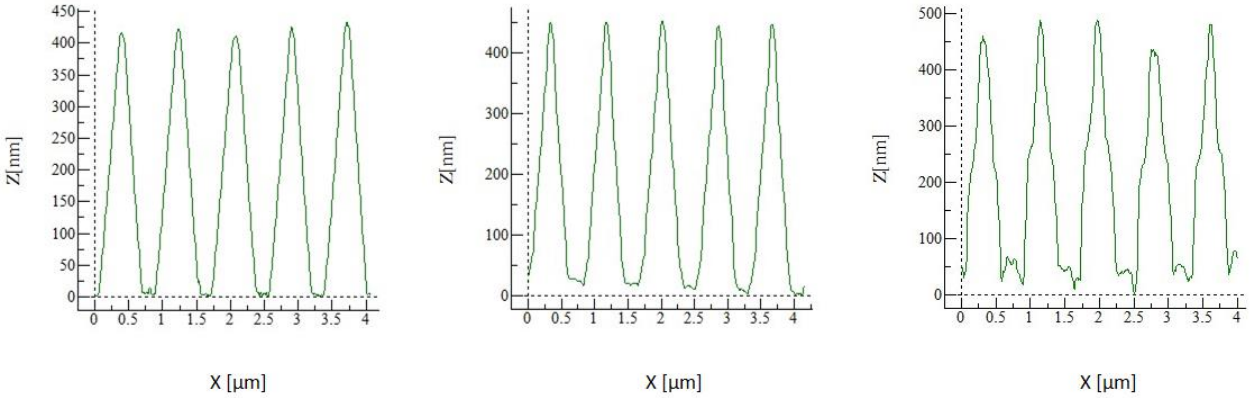

Figure 5-20 Profile of the nanopyramid samples shown in Figure 5-19. An increase in height from just over 400 nm to close to 500 nm for Au_9 doped nanopyramids. The side of the nanopyramids changed from smooth flat faces to rough and curved faces. This indicates the side surfaces of the pyramids have been attacked by the O_2 plasma and some UV cured resist has been etched.

The shape integrity of the nanopyramids was influenced and degraded after O_2 plasma treatment and was more pronounced for samples doped with Au_9 as shown in Figure 5-19. The increase in height, as shown in Figure 5-20 is possible due to the redepositing of the etched resist particles at the tip of the pyramids. It could also possibly because of the grooves between the pyramids being attacked by the plasma. The side faces of the pyramids made of Ormostamp showed very small degradation after 5 minutes of O_2 plasma, the side faces of Au_9 doped pyramids appeared to be affected more as evident by the wrinkle formed. These tests against, temperature, O_2 plasma, UV

exposure guide our fabrication process steps. For example, the Au_9 doped nanopyramids can be applied after the deposition of the active perovskite layer and can be cleaned with O_2 plasma provided it does not exceed 5 minutes. Undoped nanopyramids structures made from Ormostamp can withstand a harsher environment than the doped ones.

5.6 Conclusions

In this study, the feasibility of applying nanoimprint lithography of submicron pyramids on perovskite solar cells was examined, and the stability of the submicron pyramids' optical and physical characteristics under various environmental conditions was tested. An increase in reverse scan efficiency from 6 % to over 7 % and from 5.21 % to 5.66 % in the forward scan was obtained with the nanopyramids incorporated PSC device. The pyramids could maintain their physical morphology when ambient temperature increased up to 250 °C, with 75 % transmittance maintained at wavelengths longer than 550 nm. The pyramids textured features made of the Ormostamp were also stable in O_2 plasma for approximately 5 minutes without any change in physical morphology, suggesting that a short plasma clean of the substrates for device preparations is feasible. This indicates the possibility of fabricating nanopyramids on the substrate before the fabrication of perovskite solar cell thin films.

The successful use of Gold nanoclusters in the Ormostamp nanopyramids showed a strong absorbance in the UV region, showing the possibility of preventing the high energy UV light from damaging the photoactive layers. However, the thermal stability of Au_9 doped nanopyramids is not as stable as the undoped nanostructure. The optical transmittance of the nanopyramids was below 40 % at 400 nm wavelength when the temperature increased to 200 °C and dropped to 0 % when the temperature elevated to 250 °C. The Au_9 doped nanopyramids also appear to be more easily attacked by the O_2 plasma when compared with undoped samples, indicating that it is more difficult to prefabricate the nanopyramids on the substrate before the fabrication of solar cells.

6 Modifying Perovskite Compositions for wavelength selectivity

6.1 Introduction

For greenhouse research, the ability of solar cells to select the range of wavelengths to absorb or transmit is vital. Different plants required a slightly different energy level of light for each of the growth steps. To achieve that, one possible way is to tune the bandgap of the thin film solar cells, so that the device only absorbs certain wavelengths of light and allows the light that the plant needed to pass through. This section looks into the possibility of modifying the active perovskite layer's composition to achieve absorbing selectively wavelengths for photovoltaic conversion and let wavelengths essential for plants to pass through for plantation. The device fabricated for this part of the research is based on the mesoscopic structure with triple cation perovskite ($Cs_{0.05}(MA_{0.17}FA_{0.83})_{0.95}Pb(I_{0.83}Br_{0.17})_3$) composition used as the photoactive layer. Here, the cation refers to MA, $CH_3(NH_2)_2^+$ (FA), and caesium (Cs). Triple cation perovskite was proved to be able to achieve higher overall power conversion efficiency, with higher absorbance at the longer wavelength range and better stability [1].

6.2 Cesium doped Triple cation perovskite solar cell fabrication in humidity controlled chamber

Triple cation perovskite solar cell has proved to have better moisture stability compared to the original $CH_3NH_3PbI_3$ based solar cell [1]. While all the other films are similar to the device fabrication described in earlier sections, the deposition of the triple cation perovskite layer is based on the details published by Saliba et al [1, 41, 69]. This section provides a slightly modified deposition method for the triple cation perovskite layer. Due to the hygroscopic nature of most of

the materials in triple cation perovskite, the process is done in a low-cost humidity-controlled glovebox that's been described in detail in section 3.5. A spin coater that can pre-set 2 spinning steps were placed in the glovebox, with hot plates at both sides of the spin coater. Both perovskite and spiro-omeTAD layers were fabricated in the glovebox. The humidity is reduced down to less than 15% before depositing the perovskite layer. A temperature and humidity monitor was used to ensure the chamber's temperature is maintained below 28 °C and humidity below 15 % during perovskite film spin coating and annealing. A continuous purge of nitrogen with approximately 5 L/min is used during fabrication. A typical fabrication description of the triple cation perovskite active layer is shown in Table 6-1.

Table 6-1Triple cation perovskite fabrication

Triple cation perovskite with the anti-solvent method
Separate vials were used to dissolve FAI/MABr and PbI_2/$PbBr_2$ in a mixed solvent of DMF/DMSO (7:3). The two mixtures are then combined to achieve 1 mol of FAI, 0.2 mol of MABr, 1.1 mol of PbI_2, and 0.22 mol of $PbBr_2$ in the mixture. For dissolving PbI_2/$PbBr_2$, an elevated temperature of 150 °C is needed. A 5 % of 1.5 mol CsI in DMSO is then mixed with the solution to achieve a stoichiometry of $Cs_{0.05}(MA_{0.17}FA_{0.83})_{0.95}Pb(I_{0.83}Br_{0.17})_3$. The deposition of triple cation perovskite is using spin coating with the anti-solvent method, with a slight modification of the timing of chlorobenzene dispensing when compared to the one published by Saliba et al [41]. This is due to the consideration of the 10 to 15% humidity that's in the glovebox. The prepared precursor was spin coated on the substrate with 1000 rpm and 1000 rpm/second for 10 seconds, followed by 5000 rpm and 5000 rpm/second for 20 seconds. A 200 uL of chlorobenzene is then deposited on the spinning substrate 10 seconds before the spinning ends. The substrate was then immediately annealed at 100 °C for 1 hour to remove excess solvent and to promote the conversion of perovskite crystals [186].

6.2.1 *Perovskite precursor composition modification*

Unless stated otherwise, all materials were used directly as received from the supplier. Precursors with different amounts of Iodine, bromine, and chlorine were prepared based on the standard triple cation perovskite precursor preparation with a mixed solvent of 4:1 v/v DMF: DMSO. Here, X and Y refer to the anion of iodine, bromine, or chlorine, with X as the dominant anion in the mixture. A stock solution of 1.5 M CsX in DMSO was first prepared and stored in a dry and dark cabinet. The stock solution can be stored for a long time as long as it is stored in dry places. The preparation process is shown in Figure 6-1.

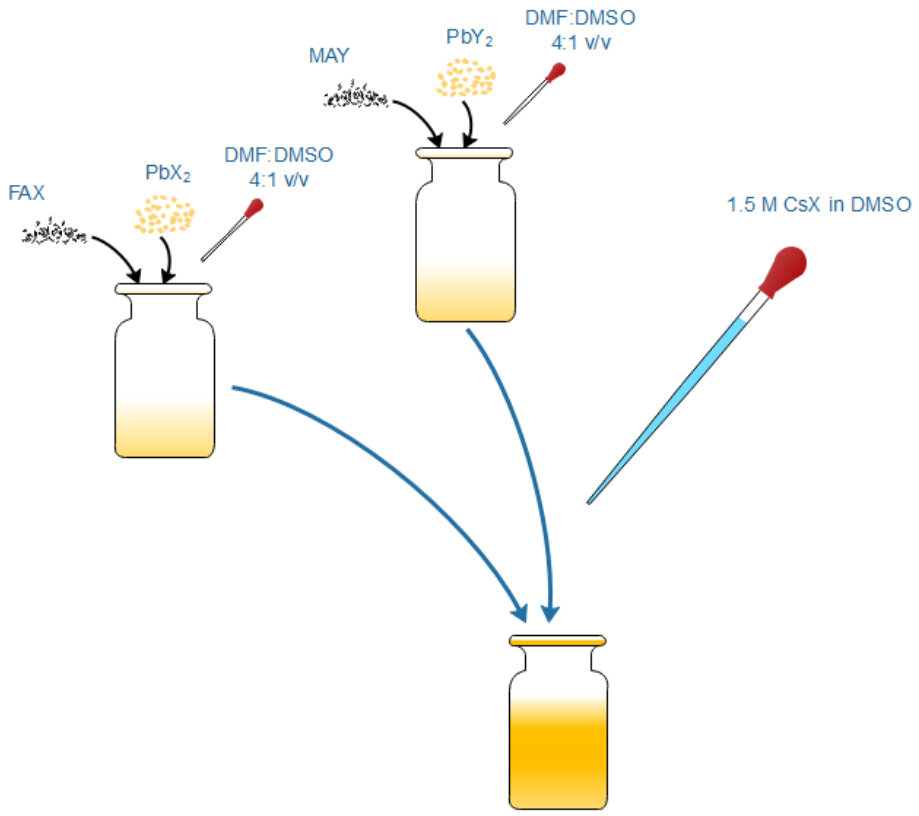

Figure 6-1 Perovskite precursor preparation: X and Y refer to the anion of iodine, bromine, and chlorine, where X is the dominant anion in the mixture.

Two separate vials were used to dissolve FAX+PbX_2 salt and MAY+PbY_2 salt with DMF: DMSO (4:1 v/v) mixed solvent at 100 °C to obtain homogeneous clear solutions. The solution was then allowed to cool down before mixing and become MAFAPbX_3Y_3. Finally, a CsX stock solution (5% of

the total mixture volume) was added to the mixture to achieve as close to the stoichiometry of $Cs_{0.05}MAFAPb(X_{0.83}Y_{0.17})_3$ as possible. The control sample based on the triple cation precursor preparation, described in Table 6-1, followed the procedure developed by Saliba et al [41]. To simplify the variables, the ratio of FA and MA were kept at 5:1 and the amount of caesium at 5% of the total precursor volume. The CsCl and CsBr powders are difficult to dissolve in the solvent, so approximately 100 µL of deionized water is first used to completely dissolve the powder, then DMF is added to obtain 1.5 mol of CsCl and CsBr solutions. The use of water to dissolve CsCl and CsBr was a concern initially since it is already confirmed that moisture affects the quality of perovskite film formed. However, currently, water is the only solvent that can dissolve CsCl and CsBr. Also, there are recently published results claiming that incorporating a small amount of water in precursor promotes the formation of good quality perovskite film [187, 188]. The molar ratios of each material in each sample were shown in Table 6-2. All precursors were prepared fresh before spin coating.

Table 6-2 compositions of the precursor materials in molar ratios (FA, MA, etc) and percentage (Cs materials) in the final precursor with 4:1 v/v DMF: DMSO mixed solvent

Sample #	Description	FAI (mol)	MAI (mol)	FABr (mol)	MABr (mol)	FACl (mol)	MACl (mol)	PbI2 (mol)	PbBr2 (mol)	PbCl2 (mol)	CsI (%)	CsBr (%)	CsCl (%)
Control	$Cs_{0.05}MAFAPb(I_{0.83}Br_{0.17})_3$	1.0			0.2			1.1	0.2		5.0		
1	$Cs_{0.05}MAFAPbI_3$	1.0	0.2					1.3			5.0		
2	$Cs_{0.05}MAFAPb(Br_{0.83}I_{0.17})_3$		0.2	1.0				0.2	1.1			5.0	
3	$Cs_{0.05}MAFAPbBr_3$			1.0	0.2				1.3			5.0	
4	$Cs_{0.05}MAFAPb(Br_{0.83}Cl_{0.17})_3$			1.0			0.2		1.1	0.2		5.0	
5	$Cs_{0.05}MAFAPb(Cl_{0.83}Br_{0.17})_3$				0.2	1.0			0.2	1.1			5
6	$Cs_{0.05}MAFAPb(I_{0.83}Cl_{0.17})_3$	1.0					0.2	1.1		0.2	5.0		
7	$Cs_{0.05}MAFAPb(Cl_{0.83}I_{0.17})_3$		0.2			1.0		0.2		1.1			5.0
8	$Cs_{0.05}MAFAPbCl_3$					1.0	0.2			1.3			5.0

6.2.2 Device Fabrication

Substrate preparation and both compact and mesoporous TiO_2 were deposited according to the procedure described in Chapter 4. Once the compact and mesoporous TiO_2 were deposited, the substrates were transferred to the glovebox for subsequent fabrication processes. The active perovskite layer was deposited via spin coating with the anti-solvent method with precursors prepared according to the composition described in Section 6.2.1, followed by annealing at 100 °C on the hotplate for 1 hour. Spiro-omeTAD was then deposited on the cooled down substrate via dynamic spin coating at 4000 rpm for 30 seconds. The samples were then rested in a dry cabinet with less than 10 % humidity, under dark, for at least 8 hours before depositing 100 nm of the gold electrode using electron beam evaporation. The completed devices were then stored overnight in a dry box, in dark before proceeding with device characterisations.

6.2.3 Device Characterization

Precursor modified perovskite thin films has been tested with Cary 6000i UV-Vis spectrometer to determine the absorbance of the thin films within the visible wavelength range. Photoluminescence spectrometer setup from Ocean Insight was also used to determine the excitation energy of each sample by looking at the standing peak position of the spectrum. Customized set up of spectral response measurement was arranged with Cary UV-Vis spectrometer for wavelength sweeping and a Keithley 2400 source meter for photocurrent measurement. A HIT reference solar cell was used to calibrate and determine the light intensity of the spectrometer.

6.3 Results and Discussions

6.3.1 Cesium contained triple cation perovskite solar cell performance

The completed device is measured with the ABET Sun 3000 solar simulator set up described in Section 2.4.1, with 100 mW/cm^2 light intensity. The sample performance under light shows that the open circuit voltage of triple cation perovskite solar cell can be boosted to 1 V, as shown in Table 6-3. A boost in short circuit current density was also seen in triple cation perovskite solar cell when compared with $MAPbI_3$ based perovskite solar cells. However, a huge hysteresis effect is present in the device, as shown in Figure 6-2. There is a 5 mA/cm^2 difference in short circuit current and over 35 % difference in fill factor values between forward and reverse sweeping. There was also an interesting decrease in the short circuit current when the sweeping voltage is less than 0.5 V. Similar effects have been observed in other published literature [189-191]. The exact reason for this decrease is unknown, but most likely to be caused by the electronic traps introduced by the electron transport layer. To minimise this effect, preconditioning the device with a forward bias voltage that's close to the open circuit voltage value for a very short time is required. This effect appeared to be minimised when testing the improved sample described in section 6.3.5, along with devices prepared with different perovskite compositions.

Table 6-3 Best performance of triple cation perovskite solar cell fabricated in humidity controlled glovebox with humidity kept at around 15 %.

		Reverse	**Forward**	**Average**
Efficiency	%	10.39	2.43	6.41
Fill Factor	%	58.50	21.30	39.90
Voc	mV	1009.30	909.80	959.55
Jsc	mA/cm2	17.61	12.57	15.09
Vmax	mV	580.10	360.10	470.10
Jmax	mA/cm2	17.91	6.75	12.33

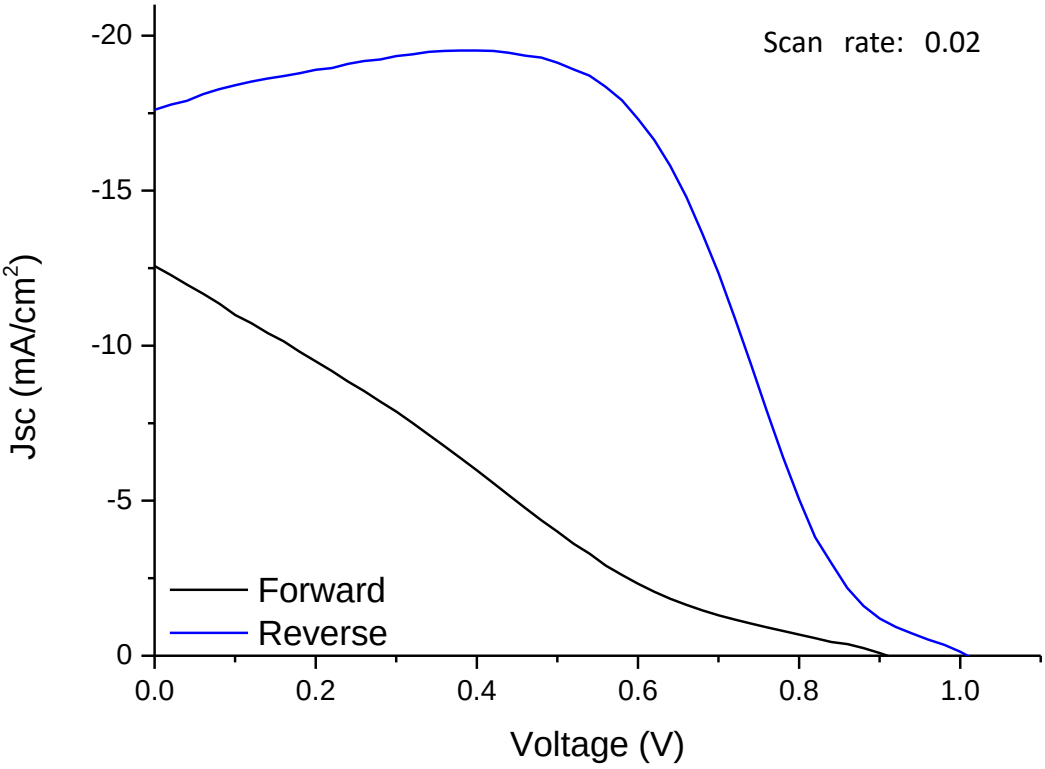

Figure 6-2 I-V relationship of triple cation perovskite solar cell with $Cs_{0.05}MAFAPb(I_{0.83}Br_{0.17})_3$. The recipe was based on Saliba et al.'s publication [1, 41].

6.3.2 *Fabrication of perovskite solar cells with different compositions*

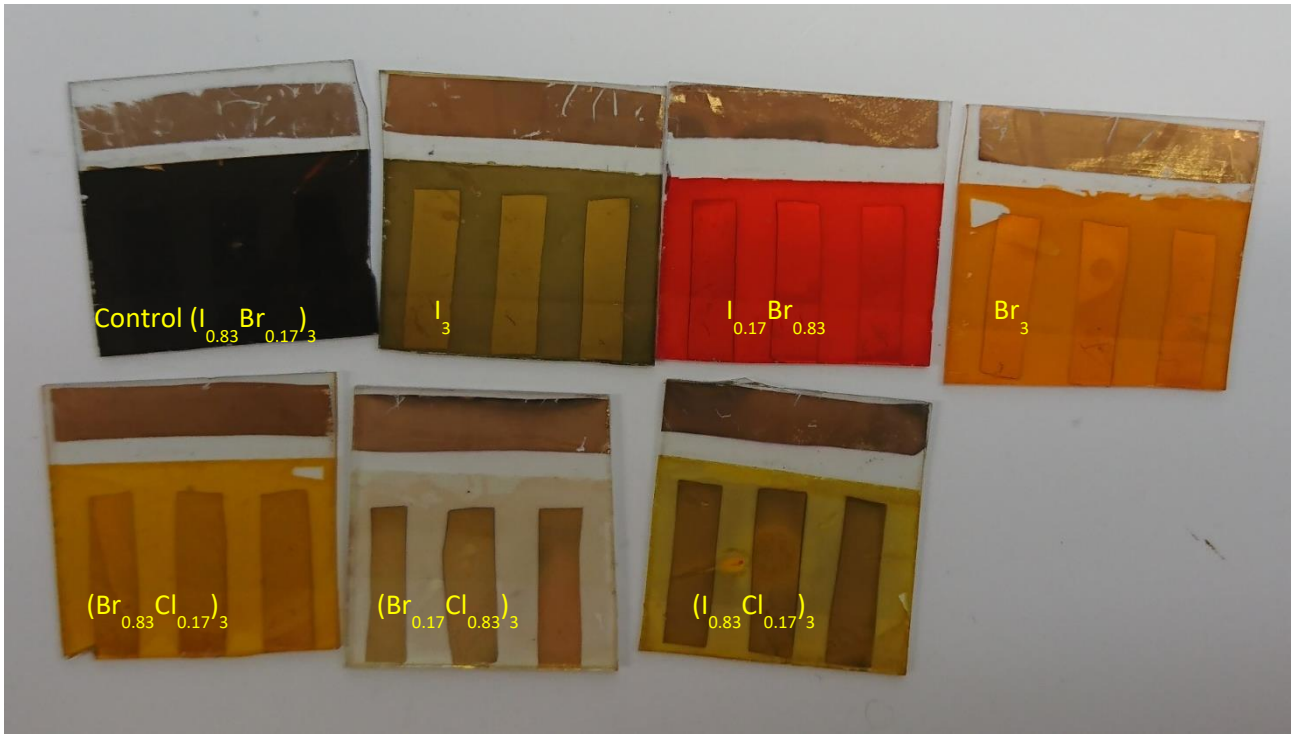

Figure 6-3 Perovskite solar cells with different iodine, bromine, and chlorine contents. The image was taken after characterisation with a solar simulator.

Figure 6-3 shows the completed devices with different iodine, bromine, and chlorine contents, with viewing from the FTO substrate side. The images were taken after the devices have been characterised with the solar simulator and spectral response measurements. Samples were store under a low vacuum before and between measurements. The colour of the samples changed from dark brown to red, orange, then towards yellow. This indicates the wavelength of the light being absorbed by the solar cell is shorter than the control sample.

6.3.3 *UV-Vis absorbance of perovskite with different compositions*

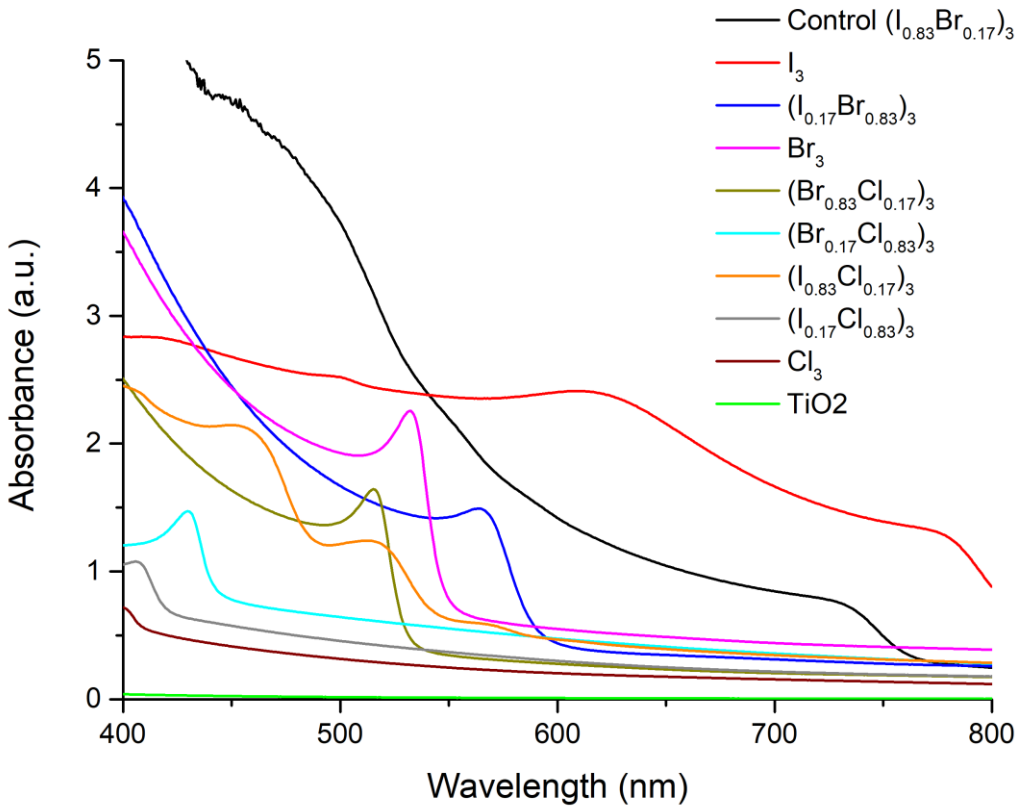

Figure 6-4 Absorbance of perovskite film with different anion concentration on TiO_2 coated quartz.

The modified perovskite films with different compositions were tested with the UV-Vis spectrometer to measure their absorbance wavelength range. The result is shown in Figure 6-4. Different perovskite compositions resulting in a change in light absorbance at the UV-Vis wavelength range. The addition of the anions such as bromine, chlorine, and iodine changes the size of the crystal structure and thus results in the modification in the bandgap potential. Iodine abundant perovskite film usually absorbs light better at longer wavelengths with wavelength above 600 nm. The addition of bromine in iodine abundant perovskite increases the material's absorbance at the shorter wavelength region. Increasing the amount of bromine while decreasing the iodine concentration results in a decrease in absorbance at the long wavelength range. The addition of chlorine blue shifts the light absorbance even more. This is due to the widening of the band gap

when bromine or chlorine is added to the mixture. This is confirmed with PL spectroscopy in section 6.3.4. Similar results with $MAPbI_{1-x}Br_x$ composition have been reported elsewhere, however, this could be the first time the triple cation perovskite with $CsMAFAPbX_3$ compositions incorporating different anion (X=I, Br, Cl, I/Br, Br/Cl or I/Cl) being reported.

Apart from the control and the sample that contains only Iodine has absorbance across the whole visible wavelength. All other samples absorb light at wavelengths shorter than 600 nm. All samples, except the control sample, have absorbance less than 4 at 400 nm wavelength. This is in agreement with the absorption spectrum that has been published in the literature [1, 109]. Samples containing more chlorine anions show the lowest absorbance and all absorbs wavelength shorter than 450 nm. Sample with $(I_{0.83}Cl_{0.17})_3$ anion composition shows two peaks in the absorbance spectrum at around 450 nm and 520 nm. The most possible explanation of the double peaks would be the segregation of iodine and chlorine atoms due to the crystal structure instability. There was no published report regarding the fabrication and characterization of triple cation perovskite with iodine and chlorine mixture. While there are reports regarding the characterization of perovskite with $MAPbI_{1-x}Cl_x$, the 2 peaks shown in Figure 6-4 were not seen in any of the literature [192]. Sharp peaks were also present in the bromine dominated samples, which have also been seen in MAPbIBr related in the published literature [183, 193, 194]. Therefore, this could confirm that the sharp peak is most likely come from the incorporation of bromine.

6.3.4 Photoluminescence measurements of perovskite films with different compositions

To ensure that the perovskite layers fabricated with the modified precursor are suitable for solar cell applications for selective wavelength, substrates coated with perovskite thin films and mesoporous TiO_2 underlayer were examined with photoluminescence spectroscopy (PL). This is to determine

changes in the bandgap of the composition modified perovskite and their possible use in wavelength selective solar cells. The set up for PL is explained and described in Section 2.4.2, employing the acquisition software Ocean View from Ocean optics. The 1 mW blue laser with 405 nm wavelength was used as the light source for PL measurement with a 1 mm diameter spot size. Some samples were more sensitive to the laser exposure, resulting in the number of photon counts exceeding the maximum photon counts that can be collected by the detector and the software. Therefore, filters with various optical densities were used to reduce the intensity of the laser, as shown in Table 6-4, so that peaks of the PL signals of each sample do not exceed the software limit. The integration time was kept at 750 ms to ensure enough photon counts can be collected from samples producing weak signals.

Table 6-4 Actual Incident laser intensity used for each sample. The optical density refers to how much energy of the incident light has been blocked by the filter. An O.D (1) filter allows only 10% of incident laser to be passed through. There is a limit on how much photon count could be recorded with the software. When the photon count exceeds the value, the signal would be saturated. The change in incident laser intensity is to ensure that the PL peaks versus wavelength of the sample could be recorded.

Sample #	Control	I_3	$(Br_{0.83}I_{0.17})_3$	Br_3	$(Br_{0.83}Cl_{0.17})_3$	$(Cl_{0.83}Br_{0.17})_3$	$(I_{0.83}Cl_{0.17})_3$	$(Cl_{0.83}I_{0.17})_3$
Optical density (O.D)	1.0	0.3	0.6	1.6	1.6	0.6	0.6	0.0
Laser output filtered (mW)	0.100	0.500	0.250	0.025	0.025	0.250	0.250	1.000
Laser Irradiance exposed to sample (mW/cm^2)	3.18	15.92	7.96	0.80	0.80	7.96	7.96	31.85

A Silicon detector was used to collect the photons generated by the laser exposed sample. Figure 6-5 shows the normalized PL peak position in photon counts versus the wavelength after 30 seconds of laser exposure in air. Perovskite films that were composed of pure chlorine did not give any PL peaks despite using the maximum laser output. This indicates that either the bandgap energy of

$Cs_{0.05}MAFAPbCl_3$ is higher than the incident laser, or $Cs_{0.05}MAFAPbCl_3$ is not a photoactive material. The control sample, based on the composition published by Saliba et al. [1], shows a PL peak around 762.61 nm wavelength. This agrees with the PL peak measured by Saliba's team. The addition of bromine and the reduction of iodine shows a blue shift of PL peak to 702 nm as expected. Surprisingly, there was not much redshift of the PL peak when there is 100 % iodine and 0% bromine in perovskite. The addition of chlorine in the composition provided further blue shift of the PL peaks in general. However, samples with more chlorine (anion composition of $(Cl_{0.83}Br_{0.17})_3$ and $(Cl_{0.83}I_{0.17})_3$) produce very weak PL peaks. Reasonable photon counts (2000 for $(Cl_{0.83}Br_{0.17})_3$ and less than 100 for the sample with $(Cl_{0.83}Br_{0.17})_3$ anion composition were collected with higher laser intensity. The bromine/chlorine mixture showed very little difference in peak positions, but there was a huge difference in the actual photon count collected. For bromine dominated sample such as the sample with $(Br_{0.83}Cl_{0.17})_3$ anion composition, the incident laser intensity used was 25 μW, producing a maximum of 3100 photon counts. At the same time, the maximum photon counts for chlorine dominated sample, the sample with $(Cl_{0.83}Br_{0.17})_3$ anion composition, excited with 250 μW laser intensity, is less than 200.

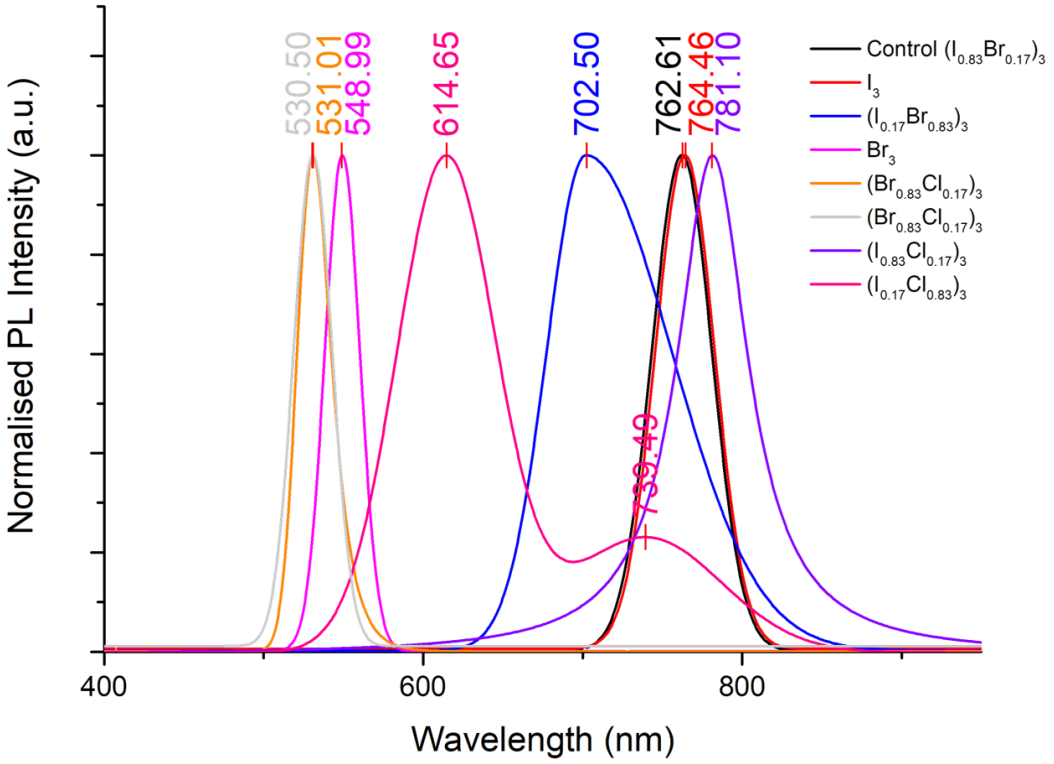

Figure 6-5 Normalised PL peak of different perovskite compositions after 30 seconds of laser exposure. Control sample refers to sample composition with $Cs_{0.05}MAFAPb(Br_{0.17}I_{0.83})_3$. Samples are labeled with different anion molar ratios. Increasing the concentration of bromine in the composition for iodine/bromine mixed samples blue shifts the peak towards a shorter wavelength. The small amount of chlorine mixing with bromine also blue shifts the PL peak slightly. Increasing the amount of chlorine in the composition reducing the intensity of the photoluminescence generated from the sample.

The wavelength shift under continuous exposure of the laser to the perovskite films was also examined, as shown in Figure 6-6, with a peak position at different times shown in Table 6-5. Due to the difference in incident laser intensity, it is difficult to compare between samples. Therefore this is used to look at every single sample's wavelength shift when it was exposed to the incident laser for up to 10 minutes.

Table 6-5 PL peak position of perovskite film with different compositions at different exposure times.

	Control	I_3	$(I_{0.17}Br_{0.83})_3$	Br_3	$(Br_{0.83}Cl_{0.17})_3$	$(Cl_{0.83}I_{0.17})_3$	$(Cl_{0.17}I_{0.83})_3$
30 seconds	763	764	703	531	530	615	782
1 minute	763	798	705	529	535	636	790
2 minute	763	797	720	530	535	635	789
5 minute	763	795	752	535	538	638	789
10 minute	765	794	763	541	536	734	787

Most of the samples did not show a rapid wavelength shift within the first 10 minute period when exposed to the laser continuously. However, when the wavelength shift occurs, it was always red-shifted, from higher energy to lower energy. The control sample shows the most stable peaks out of all the samples. Sample with the anion composition of I_3 containing only iodine as the anion in the composition, shows a slight redshift of the PL peak, from 760 nm to close to 800 nm. Moreover, the intensity of the PL peak was increased from 200 to 400 photon counts in 10 minutes. Sample with the anion composition of $(Br_{0.83}I_{0.17})_3$, with bromine dominating the bromine and iodine anion mixture, showed a wider redshift of the PL peak, from 700 nm to 766 nm, when compared with sample with I_3 composition. Sample with anion composition Br_3 contains Br anion only, showing the strongest PL intensity with no wavelength shifts. It was found that the incident laser intensity needed to be reduced down to 25 μW for this particular sample to ensure the maximum of the PL peak stays within the detector and software limits. Fewer wavelength shifts were seen in samples with anion composition of $(Br_{0.83}Cl_{0.17})_3$ and $(Cl_{0.83}Br_{0.17})_3$. The sample with iodine-chlorine combinations of $(Cl_{0.83}I_{0.17})_3$ shows a double peak, one at 614 nm and one at 739 nm when exposed to the 405 nm laser. Similar dual peaks could be seen in the sample with $(I_{0.83}Cl_{0.17})_3$ composition, with one peak at 680 nm and one peak at 775 nm. This phenomenon has been seen in other perovskite compositions with $MAPbBr_3$ or $MAPbI_3$ compositions but has not been seen in triple cation or mixed cation related perovskite compositions [195, 196]. There are no red-shift of the PL peak seen for sample 6 after 10 minutes of continuous laser exposure. For the sample with anion composition of $(Cl_{0.83}I_{0.17})_3$, however, the peak at around 600 nm red-shifted to close to 700 nm, with the intensity dropped from 200 photon counts to less than 100 photon counts.

The red-shift of the PL peaks are most likely be caused by the ion migration or ion segregation within the perovskite thin film [82, 125]. This is also one of the reasons that cause the hysteresis effect during device I-V measurements under light illumination. The cause of ion migration is yet to be confirmed, as various literature tried to explain the phenomenon [81, 84, 197]. This test can also be used to indicate the level of stability of the film under continuous laser light exposure.

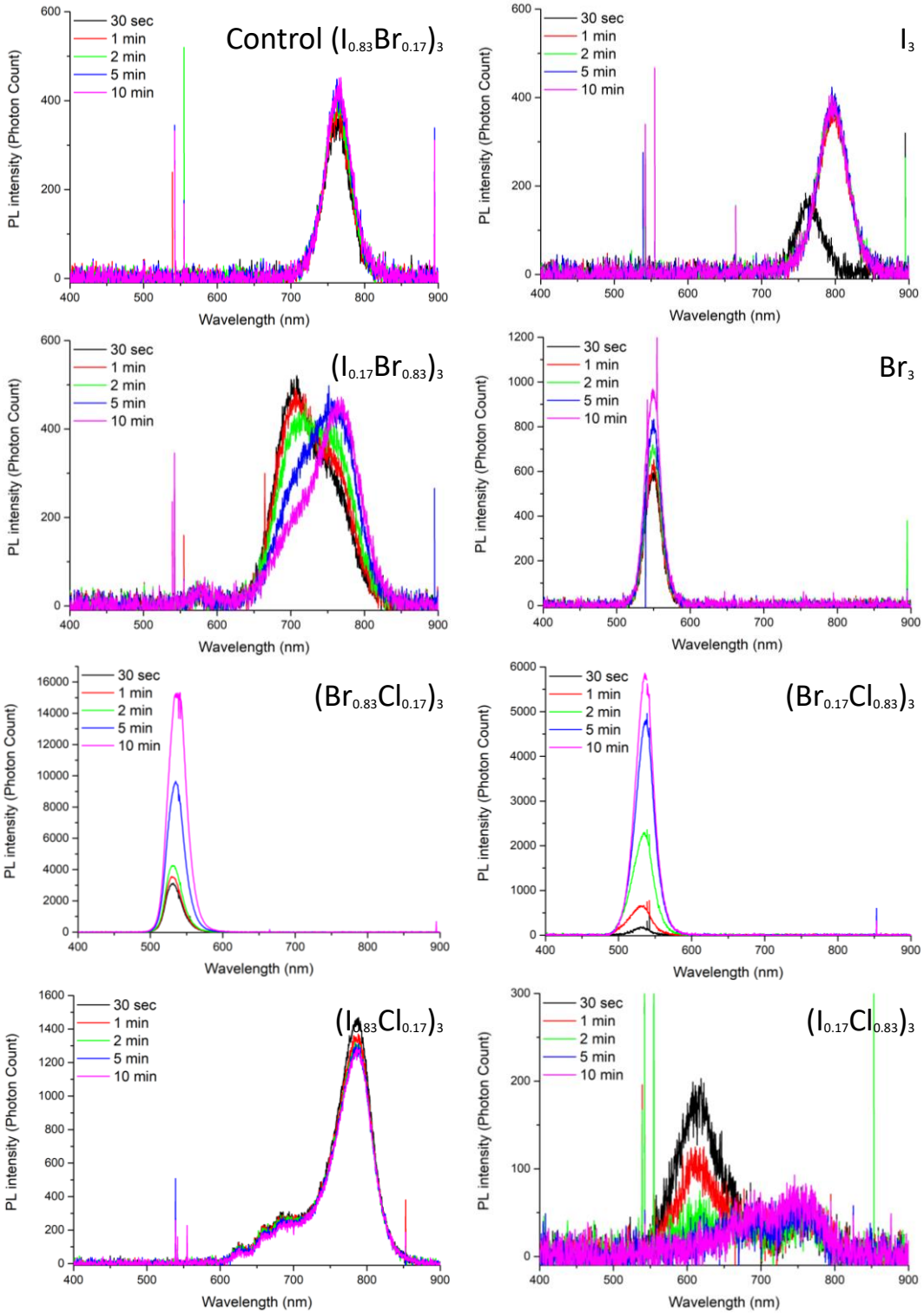

Figure 6-6 PL spectrum of samples with different iodine, bromine, or chlorine concentrations exposed to laser with different exposure times. Most of the samples show red-shift after exposure with laser exposure over time. The signal recorded from the sample with $(Cl_{0.83}I_{0.17})_3$ composition shows a high level of noise, due to the weak photon signal that was generated.

6.3.5 *Current-Voltage characteristics of devices with different perovskite compositions*

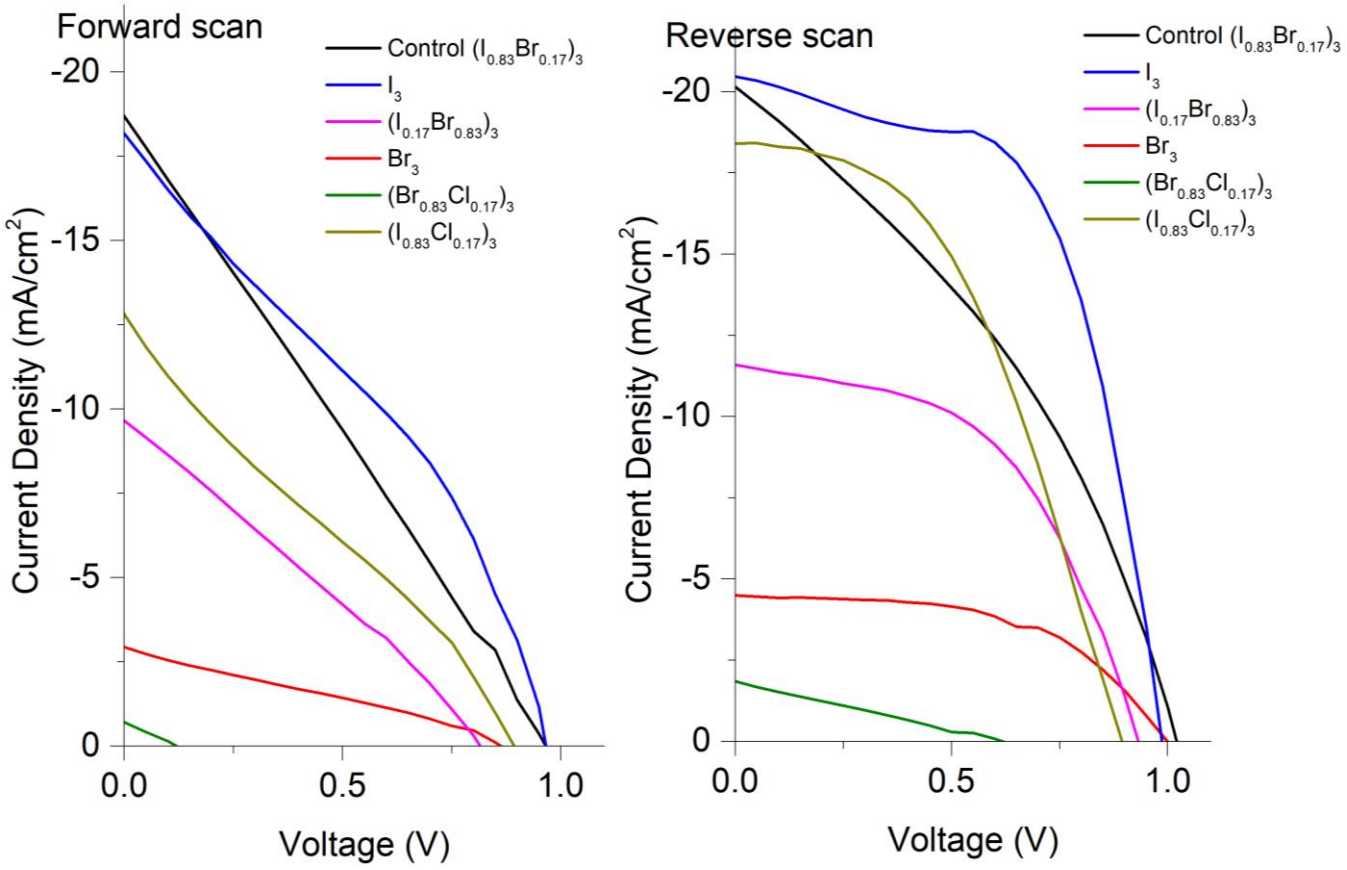

Figure 6-7 IV scan of perovskite solar cells with different perovskite compositions. Voltage sweep between -0.4 V to 1.2 V, with scan rate at 0.02 V/s. 3 samples with 3 isolated cells each for each variable have been fabricated in the same batch to ensure the validity of the result.

The mixed anion samples were then fabricated into a complete device with a typical mesoscopic structure shown in Figure 4-2 and tested with ABET 3000 solar simulator. To minimise the effect of the ambient light and humidity on the devices, all samples were fabricated in the same batch. All devices have been preconditioned with a forward bias voltage at 900 mV for 10 seconds under illumination immediately before the actual measurements. There is evidence that suggests by preconditioning the device with the solar simulator light and a bias voltage near the estimated open circuit voltage for few seconds can overcome the electronic charge trap redistribution within the

device structure, improving the actual measured open circuit voltage and the fill factor of the device [198, 199]. This results in a noticeable improvement in the overall device performance.

Table 6-6 Performance of devices with different perovskite compositions. 3 samples with 3 isolated cells each for each variable have been fabricated in the same batch to ensure the validity of the result.

		Efficiency (%)	Fill Factor (%)	Voc (mV)	Jsc (mA/cm^2)
Control $(Br_{0.17}I_{0.83})_3$	Reverse	7.47	36.30	1020.50	20.15
	Forward	4.69	26.00	965.80	18.69
	Average	6.08	31.15	993.15	19.42
I_3	Reverse	11.74	58.90	986.90	20.22
	Forward	6.08	34.20	964.20	18.43
	Average	8.91	46.55	975.55	19.33
$(Br_{0.83}I_{0.17})_3$	Reverse	5.48	50.70	932.40	11.60
	Forward	2.14	27.20	815.30	9.65
	Average	3.81	38.95	873.85	10.63
Br_3	Reverse	2.45	54.60	999.00	4.49
	Forward	0.71	28.10	863.00	2.94
	Average	1.58	41.35	931.00	3.72
$(Br_{0.83}Cl_{0.17})_3$	Reverse	0.29	25.00	619.70	1.86
	Forward	0.02	24.50	119.60	0.71
	Average	0.16	24.75	369.65	1.29
$(I_{0.83}Cl_{0.17})_3$	Reverse	7.52	45.70	894.60	18.41
	Forward	3.04	26.50	893.40	12.82
	Average	5.28	36.10	894.00	15.62

The IV performances of the devices with modified perovskite composition is shown in Figure 6-7 and Table 6-6. For this experiment, devices with chlorine abundant perovskite (samples with anion composition of $(Cl_{0.83}Br_{0.17})_3$, $(Cl_{0.83}I_{0.17})_3$, and Cl_3) show no photo-electric conversion when tested under solar simulator conditions of 100mW/cm2. Only the IV curves of the following 6 samples could be tested. Iodine abundant devices (control sample and samples with I_3 and $(I_{0.83}Cl_{0.17})_3$ compositions) show higher overall power efficiency when compared with other samples. The best performance is the sample with I_3 anion composition, with iodine as the only anion in the composition. The conversion efficiency of this device has reached over 11% at reverse sweeping, and close to 9% on average. The bromine abundant devices (samples with $(Br_{0.83}I_{0.17})_3$, Br_3, and $(Br_{0.83}Cl_{.17})_3$ anion compositions), although they are functional, have the least power conversion

efficiency when compared with the iodine abundant samples. This corresponds with the absorbance measurement shown in section 6.3.3, where the bromine abundant samples only absorb light under 600 nm, indicating lights longer than 600 nm would pass through the device for plantation. Light with wavelengths longer than 600 nm is the most important light for the photosynthesis system, as described in section 1.1.

6.3.6 Spectral Response of perovskite solar cells with different perovskite compositions

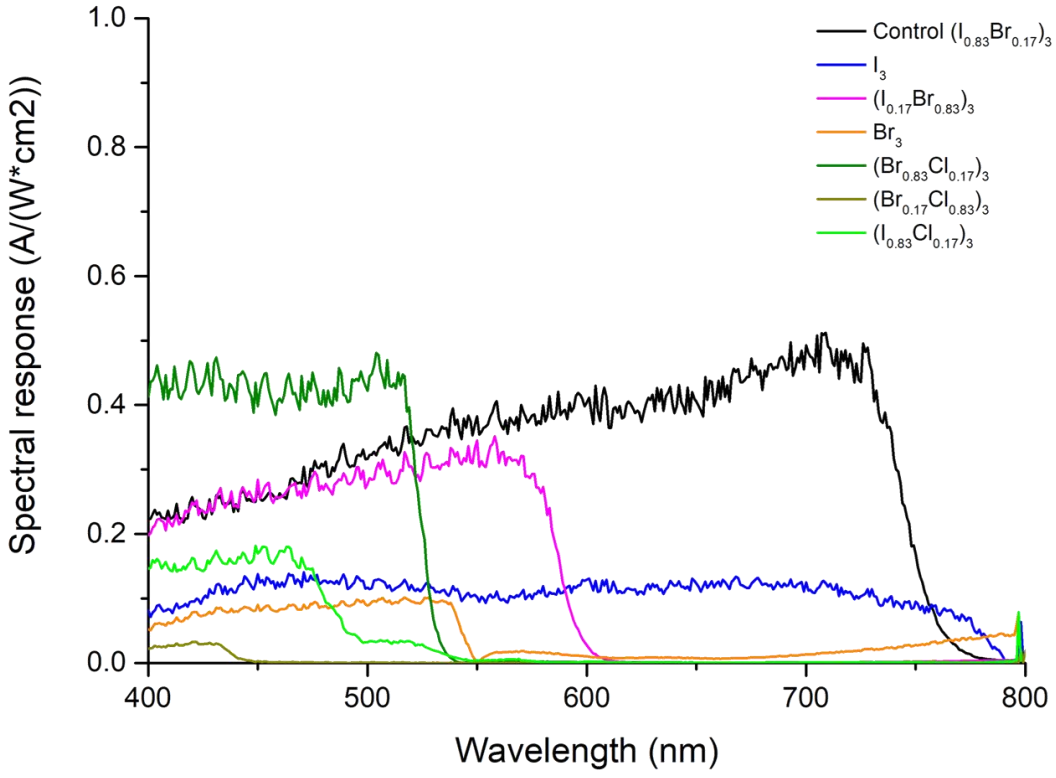

Figure 6-8 Spectral response in A/W versus incident light wavelength of perovskite solar cells with different perovskite compositions. 3 samples with 3 isolated cells each for each variable have been fabricated in the same batch to ensure the validity of the result.

As described in Section 2.4.3, the spectral response measurements for the perovskite modified devices was a customized set up using a UV-Vis spectrometer for monochromatic light exposure and

a source meter for short circuit current measurement. A reference cell with known external quantum efficiency, obtained from Taiwan Semiconductor Institute, NARLabs, Taiwan was used to determine the UV-Vis light source irradiance, as described in section 2.4.3. The calibration of the system light using the reference cell is also shown in section 2.4.3 The measured short circuit current at each wavelength is then converted to spectral response with the unit of Amp/Watt/cm^2, to determine the amount of current being generated from the solar cell, or the number of electrons excited per absorbed photons.

Figure 6-8 shows the spectral response of the devices with different perovskite compositions in the visible wavelength range. The control sample displays similar spectral responsivity when compared with the literature [200-202]. The measured spectral response is then used to calculate the expected short circuit current density (**Jsc**), using equation 2-10. The calculated **Jsc** for the control sample ($Cs_{0.05}(MA_{0.17}FA_{0.83})_{0.95}Pb(I_{0.83}Br_{0.17})_3$) is 18.33 mA/$cm^2$, whereas the measured **Jsc** is 19.33 mA/cm^2.

Sample with I_3 anion composition was able to generate the current across all visible wavelength range, but the responsivity level is relatively low when compared with the control sample. This may be because the composition, $Cs_{0.05}(MA_{0.17}FA_{0.83})_{0.95}PbI_3$, is less stable when compared with the control sample. The bromine abundant devices show relatively good spectral response at wavelengths shorter than 600 nm, but no current generated when the wavelength is longer than 600 nm. This agrees with both the absorbance and Photoluminescence measurement presented in section 6.3.3 and section 6.3.4. This indicates that the bromine abundant samples could potentially allow light with a longer wavelength to pass through for plantation applications. Sample with Br_3 anion composition shows similar spectral responsivity as the published literature with $MAPbBr_3$ composition [201]. The addition of the Cs and FA cations in $Cs_{0.05}(MA_{0.17}FA_{0.83})_{0.95}PbI_3$ did not affect the current generation on a longer wavelength. The huge drop of short circuit current density of the 3 devices in section 6.3.5 is probably because the samples could only generate current partially in the UV-Vis wavelength range. For chlorine abundant

devices (anion composition of $(Cl_{0.83}Br_{0.17})_3$, $(Cl_{0.83}I_{0.17})_3$, and Cl_3), only sample 5 displays very weak spectral responsivity at short wavelength regions, when the wavelength is shorter than 450 nm. This might be why it was not possible to measure the current-voltage for chlorine abundant samples.

6.4 Conclusions

Solar cell color tuning for rooftop perovskite solar cells has been quite popular for both aesthetic and functional purposes. Furthermore, greenhouse plantation requires different light for different plant's growth stage. One of the most popular ways is to modify the bandgap of the photosensitive perovskite layer so that only part of the light is being absorbed and utilized by the solar cell and the rest could be passed on to the plants. In this research, caesium contained triple cation solar cells with different ratios of Iodine, Bromine, and chlorine as the anion mixtures for the active perovskite solar cell have been investigated. When the bromine anion concentration increased for the samples with I/Br mixture, the optical absorbance of the device blue shifts from absorbing the whole visible wavelength spectrum to absorbing lights with wavelengths shorter than 550 nm. The chlorine contained samples show much weaker absorbance within the visible wavelength range. The PL measurement of perovskite thin film samples with different anion mixtures agrees with the measurement of the optical absorbance in the visible wavelength. The position of PL peak blue shifts to a shorter wavelength as the bromine concentration increased in the composition for the I/Br mixture. The Photon count of the PL peaks for the chlorine abundant samples is a lot weaker when compared with bromine abundant or Iodine abundant samples. The perovskite thin film with chlorine as the only anion in the composition does not emit any photons for the system to detect.

7 Research Summary

Perovskite solar cells is have attracted large attention from both the academic and industry communities since its discovery in 2009 due to the high efficiency achieved in a short time. Due to its transparent nature and strong photosensitivity in the visible range, it is possible to utilize perovskite solar cells for various applications, such as on glass windows and in greenhouses which is the aim of this work. The idea is to design wavelength-selective solar cells that absorb part of the solar spectrum and transmit other wavelengths that are important for plant growth such as the UV and IR wavelengths. The main limitations of the PSC are their stability both during fabrication and during operation which are greatly affected by the moisture in the air and under prolonged light exposure. For greenhouse applications, typical perovskite solar cells have good light absorbance across the whole visible wavelength range. This indicates that the light reaching the plants may not be enough. Different plants require different wavelength range to grow at a different stage of their life cycle, and therefore the ability to select which wavelength to reach the plants would be very important and desirable.

This research explores methods for fabricating perovskite solar cells under the usual laboratory environment and compares it with glove box prepared cells. This includes optimization of the electron transport layer and the active photon absorbing perovskite layer. To improve the overall light absorption and reduce reflections from the front surface, Nano pyramids were applied as the light trapping and scattering features. In addition, the nanopyramids were doped with gold nanoclusters to explore the possibility of increasing the light absorbance at particular wavelengths. The final part of this research looks into the possibility of changing the colour absorption spectrum of the perovskite solar cells by changing the composition of the active perovskite layer to achieve wavelength selectivity. This allows light with particular wavelengths to be used by the plantation, while the unwanted wavelengths are absorbed by perovskite solar cells for electricity generation.

7.1 Fabrication of perovskite solar cell without humidity control

In this study, various methods were employed and tested based on $MAPbI_3$ perovskite solar cell fabrication. The initial attempt on the PSC device preparation, with spin coated compact TiO_2, produced less than 0.1 % in power conversion efficiency. After changing the deposition method of compact TiO_2 from spin coating to DC sputtering, the overall efficiency of the device improved to over 3%. This was further improved by first applying a bilayer mesoporous TiO_2, with 2 different particle sizes. The overall efficiency was increased to over 5% when the TiO_2 layers are optimized further. This was later on modified to utilize single layer mesoporous TiO_2 with 30 nm particle size, to achieve an increase in short circuit current density, which was able to improve from approximately 11 mA/cm^2 to as high as 17 mA/cm^2.

Different deposition methods were tried for the active photon absorbing $MAPbI_3$ layer and compared for materials properties and device performance. The anti-solvent method shows the best performance, with minimal cracks and pinholes as indicated through the SEM and AFM imaging. The overall efficiency of the cells reached an average of over 8% for the anti-solvent method, which is a significant increase from where this research began. The surface morphologies of the thin film were also imaged with SEM, showing that the grains of the $MAPbI_3$ film deposited with the anti-solvent method are tightly connected, whereas thin films deposited with other methods have a large number of pinholes in the film. The amount used and timing for dispensing during spin coating of the chlorobenzene was also examined. The best timing of dispensing the chlorobenzene to remove the excess solvent is approximately 20 seconds before the high speed spin coating speed is finished, with 250 µL of chlorobenzene results in better overall power conversion efficiency, with improved fill factor, open circuit voltage, and short circuit density.

There was also evidence that the characterization method for the IV curve with the solar simulator

can greatly affect the performance testing of the device. Preconditioning the cell with light and biased voltage near open circuit voltage for at least 30 seconds could increase the short circuit current from 15 mA/cm^2 or less to over 18 mA/cm^2, and open circuit voltage from less than 800 mV to close to 1 V. The modification of sweeping direction from single forward sweeping to double sweeping with forward and reverse sweeping gave a more accurate measurement of perovskite solar cell's IV characteristics, due to the hysteresis effect.

A comparison between devices fabricated in a controlled environment and the devices fabricated in this section. A noticeable improvement in short circuit current density and open circuit voltage can be seen. This results in an improvement in average power conversion efficiency from approximately 4.5 % to 7.5 %.

7.2 Gold nanocluster doped nanopyramids for perovskite solar cells

In this study, the feasibility of applying nanoimprint lithography of submicron pyramids on perovskite solar cells was examined, and the stability of the submicron pyramids' optical and physical characteristics under various environmental conditions was tested. When the Perovskite solar cells were coated with nanopyramids, an increase in reverse scan efficiency from 6 % to over 7 % and from 5.21 % to 5.66 % in the forward scan was obtained. The pyramids could maintain their physical morphology, ie height, sidewalls, overall size to up to 250 °C, but the optical transparency was dropped 60 %, from approximately 75% transmittance to 25 % transmittance at 400 nm light wavelength, as the temperature increased to 200 °C, but maintained above 75 % transmittance at wavelengths longer than 550 nm. The pyramids textured features made of the Ormostamp were also stable in O_2 plasma for approximately 5 minutes without any change in physical morphology. This suggests the possibility of a short plasma clean of the substrates (if required) for device preparations without losing the integrity of the structures.

The successful use of Gold nanoclusters in the Ormostamp nanopyramids showed a strong absorbance in the UV region. This could be used to prevent the high energy UV light from damaging the photoactive layers. It is possible, in the future, to incorporate different sizes of nanoclusters or nanoparticles, or a mixture of different sizes to block/allow different wavelengths depending on the applications. However, the thermal stability of Au_9 doped nanopyramids is not as stable as the undoped nanostructure. The optical transmittance of the nanopyramids was below 40 % at 400 nm wavelength when the temperature increased to 200 °C and dropped to 0 % when the temperature elevated to 250 °C. The Au_9 doped nanopyramids also appear to be more easily attacked by the O_2 plasma since the physical morphology, measured with AFM for the samples before and after the 5 minutes immersion in O_2 plasma. This indicates that it is more difficult to prefabricate the nanopyramids on the substrate before the fabrication of solar cells.

7.3 Wavelength selectivity with different perovskite solar cell compositions

The final part of the research looks into changing the composition of the active perovskite layer to achieve wavelength selectivity. The original composition of the device as the control sample is based on caesium contained triple cation perovskite solar cell published by Saliba et al. [1] Different concentrations of iodine, bromine, and chlorine were used in an attempt to change the absorbance of the film at different wavelength regions. The thin films' absorbance and photoluminescence excitation were tested and showed that by changing the amount of bromine and iodine in the composition shift in the PL peak to shorter wavelength was achieved, but could only reach around 550 nm. The mixture of chlorine and bromine was able to push the PL peak slightly further to 530 nm, but the more chlorine added to the composition, the less stable the sample is. This is proved by the weak PL signal which disappeared after the sample being exposed

to laser for only a short period. Moreover, the more chlorine added to the composition, the less luminescent it is. The sample with $Cs_{0.05}MAFAPbCl_3$ composition shows no PL peaks over a range of the laser source intensity. This agrees with the absorbance measured, which has an absorbance of less than 0.5 across the whole UV-Vis spectrum when compared with other samples with iodine/bromine compositions which has an absorbance of over 1 for wavelengths longer than 600 nm and over 2 at 400 nm wavelength. Chlorine abundant samples have the least absorbance when compared with other samples. The measured PL peaks of the samples were also red-shifted when exposed to the laser continuously for 10 minutes. This is due to the ion migration caused by laser exposure. The actual reason for the ion migration is yet to be explored.

8 Future Works

This research provides the starting point for perovskite solar cell fabrication research at the nanofabrication laboratory, University of Canterbury. We also have shown the possibility of achieving the application of nanostructures on perovskite solar cells for light trapping, as well as the wavelength selectivity by changing the composition of perovskite solar cells. Further improvements in the perovskite solar cell fabrication process and characterizations are still in need. Moreover, the possibility of making tandem solar cells could also be looked at for better performance of the device.

8.1 Perovskite solar cell S.O.P.

While the perovskite solar cell fabricated in this research does work and can be compared with some of the emerging solar cell performances, it has not yet reached the performance that is close to the published champion records. Moreover, the fabrication process of the perovskite is greatly dependent on manual handling during the deposition, which could incur human handling errors very easily and ends up with low repetitive results (reproducibility problems).

Several ways are possible to explore improving the performance of the device further. For example, using SnO_2 instead of TiO_2 for the electron transport layer could be a good start. There are published reports that proposed SnO_2 might be a better choice than TiO_2 for the electron transport layer since SnO_2 does not degrade like TiO_2 under UV light exposure [42, 51, 52]. Furthermore, there are reports that the hysteresis effect of the solar cell's IV characteristics for devices fabricated with SnO_2 as the electron transport layer has been minimised. Moreover, SnO_2 does not require high temperature annealing like anatase TiO_2, saving the energy used for device fabrication.

The compact TiO_2 layer for this work was deposited with DC sputtering, which could take up to 4 hours for deposition time. While it produces dense TiO_2 thin films, the time consuming is its downside. Switching from DC sputtering to other deposition methods such as spray pyrolysis

would help reduce the fabrication time required.

Alternatively, improving the hole transport layer for the perovskite solar cells is another way to boost the device's performance further. While the composition of spiro-omeTAD doped with Li^+ ions for this research remains the same, there are reports showing that including some other additives such as adding the cobalt ions, apart from lithium ions could improve the performance of the solar cells [203, 204].

To improve the reproducibility of the perovskite solar cells fabricated with the same process and conditions, minimizing manual handling is probably one of the most important parts. The dispensing of the materials for removing the solvent in the thin films is usually done manually. Developing an implementation on the spin coater that automatically dispenses the material during spin coating would help eliminate the uncontrollable uncertainties such as the critical timing, more precise anti-solvent amount, and the pressure during dispensing.

8.2 Stability

The hysteresis effect of the device needs to be studied more regarding where it came from. From the literature studied for this research, the improvement of hysteresis could be improved by reducing the thickness of compact TiO_2 while maintaining a dense thin film with high quality. One common deposition method for the compact TiO_2 is spraying TiO_2 precursor [205], with oxygen gas as the carrier gas. The substrate has to be heated to 500 °C to form ultra-thin layers of compact TiO_2. However, due to the health and safety restrictions, it is difficult to set up a spray station at the nanofabrication laboratory at the University of Canterbury. Therefore, alternative methods need to be researched. This could include evaporating TiO_2 with electron beam evaporation [146, 206], and mist chemical vapor deposition. [207] Alternatively, SnO_2 [42], or ZnO [49] are possible substitute material for compact TiO_2.

8.3 Doping nanopyramids with nanoclusters or nanoparticles

Since doping the nanoimprinted nanopyramids with nanoclusters proved possible, different size nanoparticles or nanoclusters can also be tested. While the gold nanoclusters with an average of 1.8 nm in size improved the UV light absorbance, solvent-based nanoparticles or nanoclusters with different sizes that have absorption peaks at different wavelengths could also be tested. Larger nanoparticle size tends to absorb at slightly longer wavelengths

Moreover, due to the high temperature required during TiO_2 fabrication and the high absorbance of perovskite at a shorter wavelength, the nanopyramids need to be fabricated after the TiO_2 deposition and before the perovskite deposition. This could introduce impurities at the interface between the TiO_2 and the perovskite layer, resulting in traps that would cause the recombination of electron-hole pairs. An alternative method of applying the nanopyramids such as using Ormostamp to fabricate transparent imprint mould with inverted pyramids first then use it for nanoimprinting the upright pyramids on the substrate with the completed device.

8.4 Optimization of the different perovskite compositions

This research demonstrated that by changing the composition of triple cation perovskite, it is possible to fabricate devices that absorb highly in particular wavelengths. Optimization of each composition is still required to fine tune the absorption and transmission oat each wavelength. Moreover, due to the difficulty in dissolving CsBr and CsCl in the solvent, the actual CsBr and CsCl in the composition were predicted to be less than expected. More research needs to be performed into alternative ways of blending CsBr and CsCl in the composition to account for a more accurate concentration of chlorine in the composition.

Moreover, to ensure the light unused by the device can be passed through for plantation, non-

transparent metal counter electrode such as gold or aluminium is not a good choice. Transparent electrodes such as ITO, Al doped ZnO, FTO, etc are better choices for this type of application. Due to the polymer characteristics of Spiro-omeTAD, some fabrication methods, especially plasma related fabrication techniques such as sputtering, are not suitable to deposit the material on spiro-omeTAD. More research into methods on fabricating high quality transparent electrode on Spiro-omeTAD without causing degradation of Spiro-omeTAD is needed.

8.5 Tandem solar cells and self-powered perovskite LED with perovskite solar cell

Perovskite solar cell is one of the new generation solar cell with great potentials. Research regarding the device's applications has been quite popular. The tandem solar cell combining 2 or more same or different types of solar cells for overall power efficiency improvements has been very popular in recent years. One of the most successful cases is to apply the semi-transparent 2D perovskite solar cell on top of the silicon solar cell, with overall power efficiency exceeding 27 %, overpassing the 26.7 % record set by crystalline silicon solar cell alone [208, 209]. Other possibility includes Perovskite/CIGS tandem solar cells, perovskite/perovskite solar cells [29, 210]. Most of these tandem cells utilized perovskite solar cells for shorter visible wavelength spectrum, and silicon or CIGS solar cell for longer visible wavelength and near IR spectrum. Therefore, the completed device can convert light from as short as near UV light (350 nm) to near IR (1100 nm).

With the perovskite/perovskite tandem solar cell as the basis of the idea, it may be possible to fabricate a self-powered perovskite LED with perovskite solar cells. The perovskite solar cell will absorb the sunlight and provide electricity for the perovskite based LED to emit light at a different wavelength for plantation. This is possible to allow perovskite solar cell to absorb all the light in visible wavelength range but provide essential light with particular wavelengths for plants at different stages of the lifecycle. There are crystalline solar cell powered LED in the market, which

involves the wiring of a complete solar panel and the LED. With a self-powered perovskite LED, it is possible to fabricate the complete device in one go.

References

[1] M. Saliba *et al.*, "Cesium-containing triple cation perovskite solar cells: improved stability, reproducibility and high efficiency," *Energy & Environmental Science,* 10.1039/C5EE03874J vol. 9, no. 6, pp. 1989-1997, 2016, doi: 10.1039/C5EE03874J.

[2] F. NZ, "Retail price of tomatoes in New Zealand," ed, 2019.

[3] F. NZ, "Retail price of cucumber in New Zealand," ed, 2019.

[4] E. P. Thompson *et al.*, "Tinted Semi-Transparent Solar Panels Allow Concurrent Production of Crops and Electricity on the Same Cropland," *Advanced Energy Materials,* https://doi.org/10.1002/aenm.202001189 vol. 10, no. 35, p. 2001189, 2020/09/01 2020, doi: https://doi.org/10.1002/aenm.202001189.

[5] W. E. I. Sha, X. Ren, L. Chen, and W. C. H. Choy, "The efficiency limit of CH3NH3PbI3 perovskite solar cells," *Applied Physics Letters,* vol. 106, no. 22, p. 221104, 2015/06/01 2015, doi: 10.1063/1.4922150.

[6] B. Cai, Y. Peng, Y.-B. Cheng, and M. Gu, "4-fold photocurrent enhancement in ultrathin nanoplasmonic perovskite solar cells," *Opt. Express,* vol. 23, no. 24, pp. A1700-A1706, 2015/11/30 2015, doi: 10.1364/OE.23.0A1700.

[7] N. R. E. Laboratory. "Best Research-Cell Efficiency Chart." National Renewable Energy Laboratory. https://www.nrel.gov/pv/cell-efficiency.html (accessed.

[8] A. Kojima, K. Teshima, Y. Shirai, and T. Miyasaka, "Organometal Halide Perovskites as Visible-Light Sensitizers for Photovoltaic Cells," *Journal of the American Chemical Society,* vol. 131, no. 17, pp. 6050-6051, 2009/05/06 2009, doi: 10.1021/ja809598r.

[9] H.-S. Kim *et al.*, "Lead Iodide Perovskite Sensitized All-Solid-State Submicron Thin Film Mesoscopic Solar Cell with Efficiency Exceeding 9%," *Scientific Reports,* Article vol. 2, p. 591, 08/21/online 2012, doi: 10.1038/srep00591
http://www.nature.com/articles/srep00591#supplementary-information.

[10] G. Overton. "EPFL perovskite solar cells reach 21% efficiency." http://www.laserfocusworld.com/articles/2015/12/epfl-perovskite-solar-cells-reach-21-efficiency.html (accessed.

[11] J. H. Noh, S. H. Im, J. H. Heo, T. N. Mandal, and S. I. Seok, "Chemical Management for Colorful, Efficient, and Stable Inorganic–Organic Hybrid Nanostructured Solar Cells," *Nano Lett.,* vol. 13, no. 4, pp. 1764-1769, 2013/04/10 2013, doi: 10.1021/nl400349b.

[12] D. M. Jang *et al.*, "Reversible Halide Exchange Reaction of Organometal Trihalide Perovskite Colloidal Nanocrystals for Full-Range Band Gap Tuning," (in English), *Nano Lett.,* Article vol. 15, no. 8, pp. 5191-5199, Aug 2015, doi: 10.1021/acs.nanolett.5b01430.

[13] S. A. Kulkarni, T. Baikie, P. P. Boix, N. Yantara, N. Mathews, and S. Mhaisalkar, "Band-gap tuning of lead halide perovskites using a sequential deposition process," *Journal of Materials*

Chemistry A, 10.1039/C4TA00435C vol. 2, no. 24, pp. 9221-9225, 2014, doi: 10.1039/C4TA00435C.

[14] L. L. Bu *et al.*, "Semitransparent Fully Air Processed Perovskite Solar Cells," (in English), *ACS Appl. Mater. Interfaces,* Article vol. 7, no. 32, pp. 17776-17781, Aug 2015, doi: 10.1021/acsami.5b04040.

[15] G. M. Kim and T. Tatsuma, "Semi-transparent Perovskite Solar Cells Developed by Considering Human Luminosity Function," *Scientific Reports,* vol. 7, no. 1, p. 10699, 2017/09/06 2017, doi: 10.1038/s41598-017-11193-1.

[16] "Encapsulation for improving the lifetime of flexible perovskite solar cells," Available online 19 October 2015 2015, doi: 10.1016/j.nanoen.2015.10.006.

[17] S. M. Iftiquar and J. Yi, "Numerical simulation and light trapping in perovskite solar cell," *Journal of Photonics for Energy,* vol. 6, no. 2, pp. 1-10, 10, 2016. [Online]. Available: https://doi.org/10.1117/1.JPE.6.025507.

[18] C. O. Ramírez Quiroz, C. Bronnbauer, I. Levchuk, Y. Hou, C. J. Brabec, and K. Forberich, "Coloring Semitransparent Perovskite Solar Cells via Dielectric Mirrors," *ACS Nano,* vol. 10, no. 5, pp. 5104-5112, 2016/05/24 2016, doi: 10.1021/acsnano.6b00225.

[19] Z. Lu *et al.*, "Plasmonic-enhanced perovskite solar cells using alloy popcorn nanoparticles," *RSC Advances,* 10.1039/C4RA16385K vol. 5, no. 15, pp. 11175-11179, 2015, doi: 10.1039/C4RA16385K.

[20] A. Cannavale, G. E. Eperon, P. Cossari, A. Abate, H. J. Snaith, and G. Gigli, "Perovskite photovoltachromic cells for building integration," (in English), *Energy & Environmental Science,* Article vol. 8, no. 5, pp. 1578-1584, 2015, doi: 10.1039/c5ee00896d.

[21] S. Gholipour and M. Saliba, "Chapter 1 - Bandgap tuning and compositional exchange for lead halide perovskite materials," in *Characterization Techniques for Perovskite Solar Cell Materials*, M. Pazoki, A. Hagfeldt, and T. Edvinsson Eds.: Elsevier, 2020, pp. 1-22.

[22] B. Philipp *et al.*, "Triple cation mixed-halide perovskites for tunable lasers," *Opt. Mater. Express,* vol. 7, no. 11, pp. 4082--4094, 2017, doi: 10.1364/OME.7.004082.

[23] "Visible spectrum of light," in *Encyclopaedia Britannica*, ed: Encyclopaedia Britannica, 2012.

[24] H. Wollaeger and E. Runkle. "Green light: Is it important for plant growth?" Michigan State University Extension. http://msue.anr.msu.edu/news/green_light_is_it_important_for_plant_growth (accessed.

[25] Illumitex. "Wavelength Influence on Plants." https://www.illumitex.com/impacts-colored-light-plants/ (accessed.

[26] D. Singh, C. Basu, M. Meinhardt-Wollweber, and B. Roth, "LEDs for energy efficient greenhouse lighting," *Renewable and Sustainable Energy Reviews,* vol. 49, pp. 139-147, 2015, doi: http://dx.doi.org/10.1016/j.rser.2015.04.117.

[27] Boundless, *Boundless Biology* (The Phytochrome System and Red Light Response). 2016.

[28] "Solutions for horticulture lightning-LEDs for efficient and reliable luminaire design-ensuring sustainable growth of plants," ed: OSRAM, 2016.

[29] R. Lin *et al.*, "Monolithic all-perovskite tandem solar cells with 24.8% efficiency exploiting comproportionation to suppress Sn(ii) oxidation in precursor ink," *Nature Energy,* vol. 4, no. 10, pp. 864-873, 2019/10/01 2019, doi: 10.1038/s41560-019-0466-3.

[30] R. Coontz. (2013) Science's Top 10 Breakthroughs of 2013. *Science Magazine*.

[31] S. D. Stranks and H. J. Snaith, "Metal-halide perovskites for photovoltaic and light-emitting devices," (in English), *Nature Nanotechnology,* Review vol. 10, no. 5, pp. 391-402, May 2015, doi: 10.1038/nnano.2015.90.

[32] M. Muzammal uz Zaman *et al.*, "Potassium doped methylammonium lead iodide (MAPbI3) thin films as a potential absorber for perovskite solar cells; structural, morphological, electronic and optoelectric properties," *Physica B: Condensed Matter,* vol. 522, pp. 57-65, 2017/10/01/ 2017, doi: https://doi.org/10.1016/j.physb.2017.07.067.

[33] J.-H. Im, C.-R. Lee, J.-W. Lee, S.-W. Park, and N.-G. Park, "6.5% efficient perovskite quantum-dot-sensitized solar cell," *Nanoscale,* 10.1039/C1NR10867K vol. 3, no. 10, pp. 4088-4093, 2011, doi: 10.1039/C1NR10867K.

[34] M. M. Lee, J. Teuscher, T. Miyasaka, T. N. Murakami, and H. J. Snaith, "Efficient Hybrid Solar Cells Based on Meso-Superstructured Organometal Halide Perovskites," *Science,* 10.1126/science.1228604 vol. 338, no. 6107, pp. 643-647, 2012. [Online]. Available: http://science.sciencemag.org/content/338/6107/643.abstract.

[35] M. Gratzel, "The light and shade of perovskite solar cells," (in English), *Nature Materials,* Article vol. 13, no. 9, pp. 838-842, Sep 2014. [Online]. Available: <Go to ISI>://WOS:000341343500002.

[36] M. A. Green, A. Ho-Baillie, and H. J. Snaith, "The emergence of perovskite solar cells," *Nat Photon,* Review vol. 8, no. 7, pp. 506-514, 07//print 2014, doi: 10.1038/nphoton.2014.134.

[37] M. Liu, M. B. Johnston, and H. J. Snaith, "Efficient planar heterojunction perovskite solar cells by vapour deposition," *Nature,* Letter vol. 501, no. 7467, pp. 395-398, 09/19/print 2013, doi: 10.1038/nature12509.

[38] N. J. Jeon *et al.*, "Compositional engineering of perovskite materials for high-performance solar cells," *Nature,* Letter vol. 517, no. 7535, pp. 476-480, 01/22/print 2015, doi: 10.1038/nature14133.

[39] D. Limited, "EPFL Achieves 21% Efficiency for Perovskites," D. Limited, Ed., ed, 2015.

[40] C. Manspeaker, S. Venkatesan, A. Zakhidov, and K. S. Martirosyan, "Role of interface in stability of perovskite solar cells," *Current Opinion in Chemical Engineering,* vol. 15, pp. 1-7, 2017/02/01/ 2017, doi: https://doi.org/10.1016/j.coche.2016.08.013.

[41] M. Saliba *et al.*, "How to Make over 20% Efficient Perovskite Solar Cells in Regular (n–i–p) and Inverted (p–i–n) Architectures," *Chemistry of Materials,* vol. 30, no. 13, pp. 4193-4201, 2018/07/10 2018, doi: 10.1021/acs.chemmater.8b00136.

[42] Y. Chen *et al.*, "SnO2-based electron transporting layer materials for perovskite solar cells: A review of recent progress," *Journal of Energy Chemistry,* vol. 35, pp. 144-167, 2019/08/01/ 2019, doi: https://doi.org/10.1016/j.jechem.2018.11.011.

[43] X. Liu *et al.*, "20.7% highly reproducible inverted planar perovskite solar cells with enhanced fill factor and eliminated hysteresis," *Energy & Environmental Science,* 10.1039/C9EE00872A vol. 12, no. 5, pp. 1622-1633, 2019, doi: 10.1039/C9EE00872A.

[44] J. Y. Ahn *et al.*, "Designed Synthesis and Stacking Architecture of Solid and Mesoporous TiO2 Nanoparticles for Enhancing the Light-Harvesting Efficiency of Dye-Sensitized Solar Cells," *ACS Appl. Mater. Interfaces,* vol. 6, no. 2, pp. 903-909, 2014/01/22 2014, doi: 10.1021/am4041866.

[45] M. Abdi-Jalebi *et al.*, "Impact of a Mesoporous Titania–Perovskite Interface on the Performance of Hybrid Organic–Inorganic Perovskite Solar Cells," *The Journal of Physical Chemistry Letters,* vol. 7, no. 16, pp. 3264-3269, 2016/08/18 2016, doi: 10.1021/acs.jpclett.6b01617.

[46] A. Hernández-Granados *et al.*, "Optically uniform thin films of mesoporous TiO2 for perovskite solar cell applications," *Optical Materials,* vol. 88, pp. 695-703, 2019/02/01/ 2019, doi: https://doi.org/10.1016/j.optmat.2018.12.044.

[47] N. Shibayama *et al.*, "All-inorganic inverse perovskite solar cells using zinc oxide nanocolloids on spin coated perovskite layer," *Nano Convergence,* vol. 4, no. 1, p. 18, 2017/07/28 2017, doi: 10.1186/s40580-017-0113-2.

[48] J. You *et al.*, "Improved air stability of perovskite solar cells via solution-processed metal oxide transport layers," *Nat Nano,* Article vol. advance online publication, 10/12/online 2015, doi: 10.1038/nnano.2015.230
http://www.nature.com/nnano/journal/vaop/ncurrent/abs/nnano.2015.230.html#supplementary-information.

[49] K. Schutt, P. K. Nayak, A. J. Ramadan, B. Wenger, Y.-H. Lin, and H. J. Snaith, "Overcoming Zinc Oxide Interface Instability with a Methylammonium-Free Perovskite for High-Performance Solar Cells," *Advanced Functional Materials,* vol. 29, no. 47, p. 1900466, 2019, doi: 10.1002/adfm.201900466.

[50] Y. Cheng *et al.*, "Decomposition of Organometal Halide Perovskite Films on Zinc Oxide Nanoparticles," *ACS Appl. Mater. Interfaces,* vol. 7, no. 36, pp. 19986-19993, 2015/09/16 2015, doi: 10.1021/acsami.5b04695.

[51] G. Martínez-Denegri, S. Colodrero, M. Kramarenko, and J. Martorell, "All-Nanoparticle SnO2/TiO2 Electron-Transporting Layers Processed at Low Temperature for Efficient Thin-Film Perovskite Solar Cells," *ACS Applied Energy Materials,* vol. 1, no. 10, pp. 5548-5556, 2018/10/22 2018, doi: 10.1021/acsaem.8b01118.

[52] Y. Li *et al.*, "Mesoporous SnO2 nanoparticle films as electron-transporting material in perovskite solar cells," *RSC Advances,* 10.1039/C5RA01540E vol. 5, no. 36, pp. 28424-28429, 2015, doi: 10.1039/C5RA01540E.

[53] W. Ahmad *et al.*, "Physisorption of Oxygen in SnO2 Nanoparticles for Perovskite Solar Cells," *IEEE Journal of Photovoltaics,* vol. 9, no. 1, pp. 200-206, 2019, doi: 10.1109/JPHOTOV.2018.2877002.

[54] W. Ke and M. G. Kanatzidis, "Prospects for low-toxicity lead-free perovskite solar cells," *Nature Communications,* vol. 10, no. 1, p. 965, 2019/02/27 2019, doi: 10.1038/s41467-019-08918-3.

[55] B.-w. Park *et al.*, "Chemical engineering of methylammonium lead iodide/bromide perovskites: tuning of opto-electronic properties and photovoltaic performance," *Journal of Materials Chemistry A,* 10.1039/C5TA05470B vol. 3, no. 43, pp. 21760-21771, 2015, doi: 10.1039/C5TA05470B.

[56] R. Schölin, M. H. Karlsson, S. K. Eriksson, H. Siegbahn, E. M. J. Johansson, and H. Rensmo, "Energy Level Shifts in Spiro-OMeTAD Molecular Thin Films When Adding Li-TFSI," *The Journal of Physical Chemistry C,* vol. 116, no. 50, pp. 26300-26305, 2012/12/20 2012, doi: 10.1021/jp306433g.

[57] A. Abate *et al.*, "Lithium salts as “redox active” p-type dopants for organic semiconductors and their impact in solid-state dye-sensitized solar cells," *Physical Chemistry Chemical Physics,* 10.1039/C2CP44397J vol. 15, no. 7, pp. 2572-2579, 2013, doi: 10.1039/C2CP44397J.

[58] J.-Y. Jeng *et al.*, "CH3NH3PbI3 Perovskite/Fullerene Planar-Heterojunction Hybrid Solar Cells," *Adv. Mater.,* vol. 25, no. 27, pp. 3727-3732, 2013, doi: 10.1002/adma.201301327.

[59] W.-C. Lai, K.-W. Lin, T.-F. Guo, P. Chen, and Y.-Y. Liao, "Efficient CH3NH3PbI3 perovskite/fullerene planar heterojunction hybrid solar cells with oxidized Ni/Au/Cu transparent electrode," *Applied Physics Letters,* vol. 112, no. 7, p. 071103, 2018, doi: 10.1063/1.5006513.

[60] J. C. Yu *et al.*, "Highly efficient and stable inverted perovskite solar cell employing PEDOT:GO composite layer as a hole transport layer," *Scientific Reports,* vol. 8, no. 1, p. 1070, 2018/01/18 2018, doi: 10.1038/s41598-018-19612-7.

[61] C. Wang *et al.*, "Energy level and thickness control on PEDOT:PSS layer for efficient planar heterojunction perovskite cells," *Journal of Physics D: Applied Physics,* vol. 51, no. 2, p. 025110, 2017/12/20 2017, doi: 10.1088/1361-6463/aa9d30.

[62] J.-Y. Jeng *et al.*, "Nickel Oxide Electrode Interlayer in CH3NH3PbI3 Perovskite/PCBM Planar-Heterojunction Hybrid Solar Cells," *Adv. Mater.,* vol. 26, no. 24, pp. 4107-4113, 2014, doi: 10.1002/adma.201306217.

[63] P.-K. Kung *et al.*, "A Review of Inorganic Hole Transport Materials for Perovskite Solar Cells," *Advanced Materials Interfaces,* vol. 5, no. 22, p. 1800882, 2018, doi: 10.1002/admi.201800882.

[64] S. Liu *et al.*, "17% efficient printable mesoscopic PIN metal oxide framework perovskite solar cells using cesium-containing triple cation perovskite," *Journal of Materials Chemistry A,* 10.1039/C7TA07660F vol. 5, no. 44, pp. 22952-22958, 2017, doi: 10.1039/C7TA07660F.

[65] F. Xu, T. Zhang, G. Li, and Y. Zhao, "Mixed cation hybrid lead halide perovskites with enhanced performance and stability," *Journal of Materials Chemistry A,* 10.1039/C7TA00042A vol. 5, no. 23, pp. 11450-11461, 2017, doi: 10.1039/C7TA00042A.

[66] A. Binek, F. C. Hanusch, P. Docampo, and T. Bein, "Stabilization of the Trigonal High-

Temperature Phase of Formamidinium Lead Iodide," *The Journal of Physical Chemistry Letters,* vol. 6, no. 7, pp. 1249-1253, 2015/04/02 2015, doi: 10.1021/acs.jpclett.5b00380.

[67] H. Fujiwara *et al.*, "Organic-Inorganic Hybrid Perovskite Solar Cells," in *Spectroscopic Ellipsometry for Photovoltaics: Volume 1: Fundamental Principles and Solar Cell Characterization*, H. Fujiwara and R. W. Collins Eds. Cham: Springer International Publishing, 2018, pp. 463-507.

[68] Y. Hu, M. F. Aygüler, M. L. Petrus, T. Bein, and P. Docampo, "Impact of Rubidium and Cesium Cations on the Moisture Stability of Multiple-Cation Mixed-Halide Perovskites," *ACS Energy Letters,* vol. 2, no. 10, pp. 2212-2218, 2017/10/13 2017, doi: 10.1021/acsenergylett.7b00731.

[69] C. Dong, Z.-K. Wang, and L.-S. Liao, "Progress of Triple Cation Organometal Halide Perovskite Solar Cells," *Energy Technology,* vol. n/a, no. n/a, p. 1900804, doi: 10.1002/ente.201900804.

[70] B. Philippe *et al.*, "Chemical Distribution of Multiple Cation (Rb+, Cs+, MA+, and FA+) Perovskite Materials by Photoelectron Spectroscopy," *Chemistry of Materials,* vol. 29, no. 8, pp. 3589-3596, 2017/04/25 2017, doi: 10.1021/acs.chemmater.7b00126.

[71] E. Mosconi, A. Amat, M. K. Nazeeruddin, M. Grätzel, and F. De Angelis, "First-Principles Modeling of Mixed Halide Organometal Perovskites for Photovoltaic Applications," *The Journal of Physical Chemistry C,* vol. 117, no. 27, pp. 13902-13913, 2013/07/11 2013, doi: 10.1021/jp4048659.

[72] B. Cao, L. Yang, S. Jiang, H. Lin, N. Wang, and X. Li, "Flexible quintuple cation perovskite solar cells with high efficiency," *Journal of Materials Chemistry A,* 10.1039/C8TA11945G vol. 7, no. 9, pp. 4960-4970, 2019, doi: 10.1039/C8TA11945G.

[73] L. Chen *et al.*, "Toward Long-Term Stability: Single-Crystal Alloys of Cesium-Containing Mixed Cation and Mixed Halide Perovskite," *Journal of the American Chemical Society,* vol. 141, no. 4, pp. 1665-1671, 2019/01/30 2019, doi: 10.1021/jacs.8b11610.

[74] H. J. Snaith *et al.*, "Anomalous Hysteresis in Perovskite Solar Cells," *The Journal of Physical Chemistry Letters,* vol. 5, no. 9, pp. 1511-1515, 2014/05/01 2014, doi: 10.1021/jz500113x.

[75] B. Chen, M. Yang, S. Priya, and K. Zhu, "Origin of J–V Hysteresis in Perovskite Solar Cells," *The Journal of Physical Chemistry Letters,* vol. 7, no. 5, pp. 905-917, 2016/03/03 2016, doi: 10.1021/acs.jpclett.6b00215.

[76] T. Leijtens, G. E. Eperon, N. K. Noel, S. N. Habisreutinger, A. Petrozza, and H. J. Snaith, "Stability of Metal Halide Perovskite Solar Cells," *Advanced Energy Materials,* vol. 5, no. 20, pp. n/a-n/a, 2015, Art no. 1500963, doi: 10.1002/aenm.201500963.

[77] M. V. Khenkin *et al.*, "Consensus statement for stability assessment and reporting for perovskite photovoltaics based on ISOS procedures," *Nature Energy,* vol. 5, no. 1, pp. 35-49, 2020/01/01 2020, doi: 10.1038/s41560-019-0529-5.

[78] J. A. Christians, J. S. Manser, and P. V. Kamat, "Multifaceted Excited State of CH3NH3PbI3. Charge Separation, Recombination, and Trapping," (in English), *Journal of Physical Chemistry Letters,* Article vol. 6, no. 11, pp. 2086-2095, Jun 2015, doi: 10.1021/acs.jpclett.5b00594.

[79] S. Meloni *et al.*, "Ionic polarization-induced current-voltage hysteresis in CH3NH3PbX3

perovskite solar cells," *Nat Commun,* Article vol. 7, 02/08/online 2016, doi: 10.1038/ncomms10334.

[80] K.-M. Lee, C.-J. Lin, B.-Y. Liou, S.-M. Yu, C.-C. Hsu, and V. Suryanarayanan, "Effect of anti-solvent mixture on the performance of perovskite solar cells and suppression hysteresis behavior," *Organic Electronics,* vol. 65, pp. 266-274, 2019/02/01/ 2019, doi: https://doi.org/10.1016/j.orgel.2018.08.048.

[81] P. Calado *et al.*, "Evidence for ion migration in hybrid perovskite solar cells with minimal hysteresis," *Nature Communications,* vol. 7, no. 1, p. 13831, 2016/12/22 2016, doi: 10.1038/ncomms13831.

[82] M. Wenmei, Y. Dongwen, L. Tianshu, Z. Lijun, and D. Mao-Hua, "Formation and Diffusion of Metal Impurities in Perovskite Solar Cell Material CH3NH3PbI3: Implications on Solar Cell Degradation and Choice of Electrode," *Advanced Science,* vol. 5, no. 2, p. 1700662, 2018, doi: doi:10.1002/advs.201700662.

[83] Z. Shi and A. H. Jayatissa, "Perovskites-Based Solar Cells: A Review of Recent Progress, Materials and Processing Methods," (in eng), *Materials (Basel),* vol. 11, no. 5, p. 729, 2018, doi: 10.3390/ma11050729.

[84] D. Lan, "The physics of ion migration in perovskite solar cells: Insights into hysteresis, device performance, and characterization," *Progress in Photovoltaics: Research and Applications,* vol. n/a, no. n/a, doi: 10.1002/pip.3203.

[85] Y. Rong *et al.*, "Tunable hysteresis effect for perovskite solar cells," *Energy & Environmental Science,* 10.1039/C7EE02048A vol. 10, no. 11, pp. 2383-2391, 2017, doi: 10.1039/C7EE02048A.

[86] G. Niu, X. Guo, and L. Wang, "Review of recent progress in chemical stability of perovskite solar cells," *Journal of Materials Chemistry A,* 10.1039/C4TA04994B vol. 3, no. 17, pp. 8970-8980, 2015, doi: 10.1039/C4TA04994B.

[87] Y. C. Chern, H. R. Wu, Y. C. Chen, H. W. Zan, H. F. Meng, and S. F. Horng, "Reliable solution processed planar perovskite hybrid solar cells with large-area uniformity by chloroform soaking and spin rinsing induced surface precipitation," (in English), *Aip Advances,* Article vol. 5, no. 8, p. 11, Aug 2015, Art no. 087125, doi: 10.1063/1.4928516.

[88] Z. H. Lin, C. Y. Jiang, C. X. Zhu, and J. Zhang, "Development of Inverted Organic Solar Cells with TiO2 Interface Layer by Using Low-Temperature Atomic Layer Deposition," (in English), *ACS Appl. Mater. Interfaces,* Article vol. 5, no. 3, pp. 713-718, Feb 2013, doi: 10.1021/am302252p.

[89] W.-n. S. Taame Abraha Berhe , Ching-Hsiang Chen , Chun-Jern Pan , Juhsaing Cheng , Hong-Ming Chen , Mon-che Tsai , Liang-Yih Chen Amare Aregahegn Dubale and Bing Joe Hwang, "Organometal Halide Perovskite Solar Cells: Degradation and Stability," (in en), doi: 10.1039/C5EE02733K.

[90] H. C. Weerasinghe, Y. Dkhissi, A. D. Scully, R. A. Caruso, and Y.-B. Cheng, "Encapsulation for improving the lifetime of flexible perovskite solar cells," *Nano Energy*, doi:

http://dx.doi.org/10.1016/j.nanoen.2015.10.006.

[91] M. Shirayama *et al.*, "Degradation mechanism of CH3NH3PbI3 perovskite materials upon exposure to humid air," *Journal of Applied Physics,* vol. 119, no. 11, p. 115501, 2016, doi: doi:http://dx.doi.org/10.1063/1.4943638.

[92] A. M. A. Leguy *et al.*, "Reversible Hydration of CH3NH3PbI3 in Films, Single Crystals, and Solar Cells," *Chemistry of Materials,* vol. 27, no. 9, pp. 3397-3407, 2015/05/12 2015, doi: 10.1021/acs.chemmater.5b00660.

[93] N. Arora *et al.*, "Perovskite solar cells with CuSCN hole extraction layers yield stabilized efficiencies greater than 20%," *Science,* vol. 358, no. 6364, p. 768, 2017, doi: 10.1126/science.aam5655.

[94] G. Grancini *et al.*, "One-Year stable perovskite solar cells by 2D/3D interface engineering," *Nature Communications,* vol. 8, no. 1, p. 15684, 2017/06/01 2017, doi: 10.1038/ncomms15684.

[95] F. Bella *et al.*, "Improving efficiency and stability of perovskite solar cells with photocurable fluoropolymers," *Science,* vol. 354, no. 6309, p. 203, 2016, doi: 10.1126/science.aah4046.

[96] S. Kazuhiko, F. Akihiro, and Y. Yuji, "Theoretical limit of power conversion efficiency for organic and hybrid halide perovskite photovoltaics," *Japanese Journal of Applied Physics,* vol. 54, no. 8S1, p. 08KF04, 2015. [Online]. Available: http://stacks.iop.org/1347-4065/54/i=8S1/a=08KF04.

[97] Y. Li *et al.*, "High-efficiency robust perovskite solar cells on ultrathin flexible substrates," *Nat Commun,* Article vol. 7, 01/11/online 2016, doi: 10.1038/ncomms10214.

[98] T. M. Schmidt, T. T. Larsen-Olsen, J. E. Carle, D. Angmo, and F. C. Krebs, "Upscaling of Perovskite Solar Cells: Fully Ambient Roll Processing of Flexible Perovskite Solar Cells with Printed Back Electrodes," (in English), *Advanced Energy Materials,* Article vol. 5, no. 15, p. 9, Aug 2015, Art no. 1500569, doi: 10.1002/aenm.201500569.

[99] B. Susrutha, L. Giribabu, and S. P. Singh, "Recent advances in flexible perovskite solar cells," (in English), *Chemical communications (Cambridge, England),* vol. 51, no. 79, pp. 14696-707, 2015 Sep 2015, doi: 10.1039/c5cc03666f.

[100] K. M. Boopathi *et al.*, "Preparation of metal halide perovskite solar cells through a liquid droplet assisted method," (in English), *Journal of Materials Chemistry A,* Article vol. 3, no. 17, pp. 9257-9263, 2015, doi: 10.1039/c4ta06392a.

[101] Y. H. Deng, E. Peng, Y. C. Shao, Z. G. Xiao, Q. F. Dong, and J. S. Huang, "Scalable fabrication of efficient organolead trihalide perovskite solar cells with doctor-bladed active layers," (in English), *Energy & Environmental Science,* Article vol. 8, no. 5, pp. 1544-1550, 2015, doi: 10.1039/c4ee03907f.

[102] S. Hong *et al.*, "A facile and low-cost fabrication of TiO2 compact layer for efficient perovskite solar cells," (in English), *Current Applied Physics,* Article vol. 15, no. 5, pp. 574-579, May 2015, doi: 10.1016/j.cap.2015.01.028.

[103] F. M. Li *et al.*, "A facile spray-assisted fabrication of homogenous flat CH3NH3PbI3 films for

high performance mesostructure perovskite solar cells," (in English), *Mater. Lett.,* Article vol. 157, pp. 38-41, Oct 2015, doi: 10.1016/j.matlet.2015.05.106.

[104] A. Yella, L. P. Heiniger, P. Gao, M. K. Nazeeruddin, and M. Gratzel, "Nanocrystalline Rutile Electron Extraction Layer Enables Low-Temperature Solution Processed Perovskite Photovoltaics with 13.7% Efficiency," (in English), *Nano Lett.,* Article vol. 14, no. 5, pp. 2591-2596, May 2014, doi: 10.1021/nl500399m.

[105] C.-S. Jiang *et al.*, "Carrier separation and transport in perovskite solar cells studied by nanometre-scale profiling of electrical potential," *Nat Commun,* Article vol. 6, 09/28/online 2015, doi: 10.1038/ncomms9397.

[106] W. Zhang *et al.*, "Enhancement of Perovskite-Based Solar Cells Employing Core–Shell Metal Nanoparticles," *Nano Lett.,* vol. 13, no. 9, pp. 4505-4510, 2013/09/11 2013, doi: 10.1021/nl4024287.

[107] Y. Jiang *et al.*, "Optical analysis of perovskite/silicon tandem solar cells," *Journal of Materials Chemistry C,* 10.1039/C6TC01276K vol. 4, no. 24, pp. 5679-5689, 2016, doi: 10.1039/C6TC01276K.

[108] B. Niesen, A. Walter, C.-H. Weng, and J. Werner. "Perovskite Cells for Tandem Applicatiopns." (accessed.

[109] J. Chen, S. Zhou, S. Jin, H. Li, and T. Zhai, "Crystal organometal halide perovskites with promising optoelectronic applications," *Journal of Materials Chemistry C,* 10.1039/C5TC03417E vol. 4, no. 1, pp. 11-27, 2016, doi: 10.1039/C5TC03417E.

[110] R. Ganesan *et al.*, "Tuning the band gap of hybrid lead free defect perovskite nano crystals for solar cell applications," *New Journal of Chemistry,* 10.1039/C9NJ03902C vol. 43, no. 38, pp. 15258-15266, 2019, doi: 10.1039/C9NJ03902C.

[111] K.-T. Lee, J.-Y. Jang, N. Y. Ha, S. Lee, and H. J. Park, "High-performance colorful semitransparent perovskite solar cells with phase-compensated microcavities," *Nano Research,* journal article vol. 11, no. 5, pp. 2553-2561, May 01 2018, doi: 10.1007/s12274-017-1880-0.

[112] S. Sun, Z. Xie, G. Qin, and L. Xiao, "Light trapping nano structures with over 30% enhancement in perovskite solar cells," *Organic Electronics,* vol. 75, p. 105385, 2019/12/01/ 2019, doi: https://doi.org/10.1016/j.orgel.2019.105385.

[113] B. Lipovšek, J. Krč, and M. Topič, "Light-Management Mechanisms of Optimized Micro-Textured Foils in Perovskite Solar Cells," in *2018 IEEE 7th World Conference on Photovoltaic Energy Conversion (WCPEC) (A Joint Conference of 45th IEEE PVSC, 28th PVSEC & 34th EU PVSEC)*, 10-15 June 2018 2018, pp. 0085-0088, doi: 10.1109/PVSC.2018.8547594.

[114] P. Spinelli, B. K. Newman, and A. Polman, "Photovoltaics: Light-Trapping in Crystalline Silicon and Thin-Film Solar Cells by Nanostructured Optical Coatings," in *Nanotechnology for Energy Sustainability*, P. B. Raj, P. M. V. d. Voorde, and D. Y. Mahajan Eds., 2017, pp. 163-180.

[115] C. S. Solanki and H. K. Singh, "Principle of Texturization for Enhanced Light Trapping," in *Anti-reflection and Light Trapping in c-Si Solar Cells*, C. S. Solanki and H. K. Singh Eds. Singapore: Springer Singapore, 2017, pp. 65-82.

[116] Z. Tang, W. Tress, and O. Inganäs, "Light trapping in thin film organic solar cells," *Materials Today,* vol. 17, no. 8, pp. 389-396, 2014/10/01/ 2014, doi: https://doi.org/10.1016/j.mattod.2014.05.008.

[117] J. Vladislav *et al.*, "Light trapping in periodically textured amorphous silicon thin film solar cells using realistic interface morphologies," *Opt. Express,* vol. 21, no. S4, pp. A595--A606, 2013, doi: 10.1364/OE.21.00A595.

[118] Q. G. Du, G. Shen, and S. John, "Light-trapping in perovskite solar cells," *AIP Advances,* vol. 6, no. 6, p. 065002, 2016/06/01 2016, doi: 10.1063/1.4953336.

[119] M. Jošt *et al.*, "Efficient Light Management by Textured Nanoimprinted Layers for Perovskite Solar Cells," *ACS Photonics,* vol. 4, no. 5, pp. 1232-1239, 2017/05/17 2017, doi: 10.1021/acsphotonics.7b00138.

[120] J. Hao *et al.*, "Hybrid organic-inorganic perovskite metamaterial for light trapping and photon-to-electron conversion," (in English), *Nanophotonics,* vol. 9, no. 10, pp. 3323-3333, 01 Sep. 2020 2020, doi: https://doi.org/10.1515/nanoph-2020-0071.

[121] A. Lin *et al.*, "The external light trapping for perovskite solar cells using nanoimprinted polymer metamaterial patterns," in *2016 IEEE 43rd Photovoltaic Specialists Conference (PVSC)*, 5-10 June 2016 2016, pp. 0334-0337, doi: 10.1109/PVSC.2016.7749605.

[122] Y. Han, X. Yu, D. Wang, and D. Yang, "Formation of Various Pyramidal Structures on Monocrystalline Silicon Surface and Their Influence on the Solar Cells," *Journal of Nanomaterials,* vol. 2013, 2013.

[123] S. J. Fonash, "Chapter 3 - Light-Trapping Structures," in *Light Trapping in Solar Cell and Photo-Detector Devices*, S. J. Fonash Ed. Boston: Academic Press, 2015, pp. 33-48.

[124] M. Soldera, Q. Wang, F. Soldera, V. Lang, A. Abate, and A. F. Lasagni, "Toward High-Throughput Texturing of Polymer Foils for Enhanced Light Trapping in Flexible Perovskite Solar Cells Using Roll-to-Roll Hot Embossing," *Advanced Engineering Materials,* https://doi.org/10.1002/adem.201901217 vol. 22, no. 4, p. 1901217, 2020/04/01 2020, doi: https://doi.org/10.1002/adem.201901217.

[125] H. Zhang *et al.*, "Phase segregation due to ion migration in all-inorganic mixed-halide perovskite nanocrystals," *Nature Communications,* vol. 10, no. 1, p. 1088, 2019/03/06 2019, doi: 10.1038/s41467-019-09047-7.

[126] J. Hao *et al.*, "Light Trapping Effect in Perovskite Solar Cells by the Addition of Ag Nanoparticles, Using Textured Substrates," *Nanomaterials,* vol. 10, no. 8, 2018;.

[127] S. Sivasubramaniam, D. Kumar, V. Golovko, and M. Alkaisi, *Current density enhancement in inverted nanopyramid textured crystalline silicon solar cell using gold nanoparticles* (SPIE Micro+Nano Materials, Devices, and Applications). SPIE, 2013.

[128] I. Díez *et al.*, "Color Tunability and Electrochemiluminescence of Silver Nanoclusters," *Angewandte Chemie International Edition,* vol. 48, no. 12, pp. 2122-2125, 2009, doi: 10.1002/anie.200806210.

[129] L. Ai *et al.*, "Copper inter-nanoclusters distance-modulated chromism of self-assembly

induced emission," *Nanoscale,* 10.1039/C7NR06918A vol. 9, no. 47, pp. 18845-18854, 2017, doi: 10.1039/C7NR06918A.

[130] M. Zhou, C. Zeng, Q. Li, T. Higaki, and R. Jin, "Gold Nanoclusters: Bridging Gold Complexes and Plasmonic Nanoparticles in Photophysical Properties," *Nanomaterials,* vol. 9, no. 7, p. 933, 2019. [Online]. Available: https://www.mdpi.com/2079-4991/9/7/933.

[131] M. K. Basher, "Fabrication and characterization of monocrystalline silicon solar cell," Master of Philosophy, Department of materials and metallurgical engineering, Bangladesh University of Engineering and Technology, Bangladash, 2016.

[132] B. H. Hamadani and B. Dougherty, "Solar Cell Characterization," in *Semiconductor Materials for Solar Photovoltaic Cells*, M. P. Paranthaman, W. Wong-Ng, and R. N. Bhattacharya Eds. Cham: Springer International Publishing, 2016, pp. 229-245.

[133] M. Kelzenberg. "I-V software." http://mkelzenb.caltech.edu/software/IV/index.html (accessed.

[134] "Perovskites and Perovskite solar cells: An Introduction." Ossila. https://www.ossila.com/pages/perovskites-and-perovskite-solar-cells-an-introduction (accessed 2020).

[135] S. Viswanathan *et al.*, "Graphene–protein field effect biosensors: glucose sensing," *Materials Today,* vol. 18, no. 9, pp. 513-522, 2015/11/01/ 2015, doi: https://doi.org/10.1016/j.mattod.2015.04.003.

[136] P. M. Ushasree and B. Bora, "CHAPTER 1 Silicon Solar Cells," in *Solar Energy Capture Materials*: The Royal Society of Chemistry, 2019, pp. 1-55.

[137] C. Mack, *Fundamental Principles of Optical Lithography : The Science of Microfabrication*. Newy York, UNITED KINGDOM: John Wiley & Sons, Incorporated, 2007.

[138] S. Sivasubramaniam and M. M. Alkaisi, "Inverted nanopyramid texturing for silicon solar cells using interference lithography," *Microelectronic Engineering,* vol. 119, pp. 146-150, 2014/05/01/ 2014, doi: https://doi.org/10.1016/j.mee.2014.04.004.

[139] W. Wang and A. Freundlich, "Rapid sub-wavelength texturing for III–V solar cells by laser interference lithography and wet etching," in *2015 IEEE 42nd Photovoltaic Specialist Conference (PVSC)*, 14-19 June 2015 2015, pp. 1-5, doi: 10.1109/PVSC.2015.7355658.

[140] A. P. Amalathas and M. M. Alkaisi, "Upright nanopyramid structured cover glass with light harvesting and self-cleaning effects for solar cell applications," *Journal of Physics D: Applied Physics,* vol. 49, no. 46, p. 465601, 2016/10/20 2016, doi: 10.1088/0022-3727/49/46/465601.

[141] A. Peter Amalathas and M. M. Alkaisi, "Efficient light trapping nanopyramid structures for solar cells patterned using UV nanoimprint lithography," *Materials Science in Semiconductor Processing,* vol. 57, pp. 54-58, 2017/01/01/ 2017, doi: https://doi.org/10.1016/j.mssp.2016.09.032.

[142] S. Razza *et al.*, "Perovskite solar cells and large area modules (100 cm(2)) based on an air flow-assisted PbI2 blade coating deposition process," (in English), *Journal of Power Sources,* Article vol. 277, pp. 286-291, Mar 2015, doi: 10.1016/j.jpowsour.2014.12.008.

[143] Y. Wu *et al.*, "Consecutive Morphology Controlling Operations for Highly Reproducible Mesostructured Perovskite Solar Cells," (in English), *ACS Appl. Mater. Interfaces,* vol. 7, no. 37, pp. 20707-13, 2015 Sep 23 (Epub 2015 Sep 2015, doi: 10.1021/acsami.5b05576.

[144] L. Dreesen, F. Cecchet, and S. Lucas, "DC Magnetron Sputtering Deposition of Titanium Oxide Nanoparticles: Influence of Temperature, Pressure and Deposition Time on the Deposited Layer Morphology, the Wetting and Optical Surface Properties," *Plasma Processes and Polymers,* vol. 6, no. S1, pp. S849-S854, 2009, doi: 10.1002/ppap.200932201.

[145] J. Zheng, S. Bao, Y. Guo, and P. Jin, "TiO2 films prepared by DC reactive magnetron sputtering at room temperature: Phase control and photocatalytic properties," *Surface and Coatings Technology,* vol. 240, pp. 293-300, 2014/02/15/ 2014, doi: https://doi.org/10.1016/j.surfcoat.2013.12.044.

[146] M. F. Hossain, S. Naka, and H. Okada, "Annealing effect of E-beam evaporated TiO2 films and their performance in perovskite solar cells," *Journal of Photochemistry and Photobiology A: Chemistry,* vol. 360, pp. 109-116, 2018/06/01/ 2018, doi: https://doi.org/10.1016/j.jphotochem.2018.04.025.

[147] T. Wahl, J. Hanisch, and E. Ahlswede, "Comparison of the Al back contact deposited by sputtering, e-beam, or thermal evaporation for inverted perovskite solar cells," *Journal of Physics D Applied Physics,* vol. 51, April 01, 2018 2018. [Online]. Available: https://ui.adsabs.harvard.edu/abs/2018JPhD...51m5502W.

[148] M. P. Tian, *Thin Film Technology and Materials*. 2009.

[149] H. Sharifi and G. Gardner, "Plasma RIE etching fundamentals and applications," ed. Indiana USA: Discovery park, Purdue University, 2008.

[150] N. Heikkilα, "Influence of ambient working conditions on the performance of planar and mesoscopic perovskite solar cell architectures," Master of science, Chemistry, Tampere University of Technology, Finland, 2017.

[151] C. o. Wikipedia. "Perovskite." Wikipedia, The Free Encyclopedia. https://en.wikipedia.org/wiki/Perovskite (accessed.

[152] T. e. o. E. Britannica, "Perovskite," E. Britannica, Ed., ed: Encyclopaedia Britannica, Inc., 2018.

[153] X. Dai, K. Xu, and F. Wei, "Recent progress in perovskite solar cells: the perovskite layer," *Beilstein Journal of Nanotechnology,* vol. 11, pp. 51-60, 2020, doi: 10.3762/bjnano.11.5.

[154] M. Becker and M. Wark, "Recent Progress in the Solution-Based Sequential Deposition of Planar Perovskite Solar Cells," *Crystal Growth & Design,* vol. 18, no. 8, pp. 4790-4806, 2018/08/01 2018, doi: 10.1021/acs.cgd.8b00686.

[155] D. G. Lee *et al.*, "Effect of TiO2 particle size and layer thickness on mesoscopic perovskite solar cells," *Applied Surface Science,* vol. 477, pp. 131-136, 2019/05/31/ 2019, doi: https://doi.org/10.1016/j.apsusc.2017.11.124.

[156] G. Namkoong, A. A. Mamun, T. T. Ava, K. Zhang, and H. Baumgart, "Impact of perovskite precursor solution temperature on charge carrier dynamics and photovoltaic performance of perovskite based solar cells," *Organic Electronics,* vol. 42, pp. 228-233, 2017/03/01/ 2017,

doi: https://doi.org/10.1016/j.orgel.2016.12.047.

[157] S. L. Triana, Kusumandari, and R. Suryana, "Effect of wet etching process on the morphology and transmittance of fluorine doped tin oxide (FTO)," *Journal of Physics: Conference Series,* vol. 776, p. 012005, 2016/11 2016, doi: 10.1088/1742-6596/776/1/012005.

[158] W. H. Nguyen, C. D. Bailie, E. L. Unger, and M. D. McGehee, "Enhancing the Hole-Conductivity of Spiro-OMeTAD without Oxygen or Lithium Salts by Using Spiro(TFSI)2 in Perovskite and Dye-Sensitized Solar Cells," *Journal of the American Chemical Society,* vol. 136, no. 31, pp. 10996-11001, 2014/08/06 2014, doi: 10.1021/ja504539w.

[159] C. Xiao *et al.*, "Inhomogeneous Doping of Perovskite Materials by Dopants from Hole-Transport Layer," *Matter,* vol. 2, no. 1, pp. 261-272, 2020/01/08/ 2020, doi: https://doi.org/10.1016/j.matt.2019.10.005.

[160] J. P. Correa Baena *et al.*, "Highly efficient planar perovskite solar cells through band alignment engineering," *Energy & Environmental Science,* 10.1039/C5EE02608C vol. 8, no. 10, pp. 2928-2934, 2015, doi: 10.1039/C5EE02608C.

[161] Z. Hawash, L. K. Ono, S. R. Raga, M. V. Lee, and Y. Qi, "Air-Exposure Induced Dopant Redistribution and Energy Level Shifts in Spin-Coated Spiro-MeOTAD Films," *Chemistry of Materials,* vol. 27, no. 2, pp. 562-569, 2015/01/27 2015, doi: 10.1021/cm504022q.

[162] C.-H. Wei and C.-M. Chang, "Polycrystalline TiO_2 Thin Films with Different Thicknesses Deposited on Unheated Substrates Using RF Magnetron Sputtering," *MATERIALS TRANSACTIONS,* vol. 52, no. 3, pp. 554-559, 2011, doi: 10.2320/matertrans.M2010358.

[163] R. d. A. Ramos Jr, M. H. Boratto, M. S. Li, and L. V. d. A. Scalvi, "Emission Properties Related to Distinct Phases of Sol-Gel Dip-Coating Titanium Dioxide, and Carrier Photo-Excitation in Different Energy Ranges," *Materials Research,* vol. 20, pp. 866-873, 2017. [Online]. Available: http://www.scielo.br/scielo.php?script=sci_arttext&pid=S1516-14392017000400866&nrm=iso.

[164] B. Karunagaran, R. T. Rajendra Kumar, V. Senthil Kumar, D. Mangalaraj, S. K. Narayandass, and G. Mohan Rao, "Structural characterization of DC magnetron-sputtered TiO2 thin films using XRD and Raman scattering studies," *Materials Science in Semiconductor Processing,* vol. 6, no. 5, pp. 547-550, 2003/10/01/ 2003, doi: https://doi.org/10.1016/j.mssp.2003.05.012.

[165] C. Li *et al.*, "Mesoporous TiO2 aggregate photoanode with high specific surface area and strong light scattering for dye-sensitized solar cells," *Journal of Solid State Chemistry,* vol. 196, pp. 504-510, 2012/12/01/ 2012, doi: https://doi.org/10.1016/j.jssc.2012.07.014.

[166] C.-H. Tsai *et al.*, "Influences of Stacking Architectures of TiO_2 Nanoparticle Layers on Characteristics of Dye-Sensitized Solar Cells," vol. 2013, 2013.

[167] Y. Wang *et al.*, "Stitching triple cation perovskite by a mixed anti-solvent process for high performance perovskite solar cells," *Nano Energy,* vol. 39, pp. 616-625, 2017/09/01/ 2017, doi: https://doi.org/10.1016/j.nanoen.2017.07.046.

[168] J. Troughton, K. Hooper, and T. M. Watson, "Humidity resistant fabrication of CH3NH3PbI3 perovskite solar cells and modules," *Nano Energy,* vol. 39, pp. 60-68, 2017/09/01/ 2017, doi:

https://doi.org/10.1016/j.nanoen.2017.06.039.

[169] H.-S. Kim and N.-G. Park, "Parameters Affecting I–V Hysteresis of CH3NH3PbI3 Perovskite Solar Cells: Effects of Perovskite Crystal Size and Mesoporous TiO2 Layer," *The Journal of Physical Chemistry Letters,* vol. 5, no. 17, pp. 2927-2934, 2014/09/04 2014, doi: 10.1021/jz501392m.

[170] A. A. F. Husain, W. Z. W. Hasan, S. Shafie, M. N. Hamidon, and S. S. Pandey, "A review of transparent solar photovoltaic technologies," *Renewable and Sustainable Energy Reviews,* vol. 94, pp. 779-791, 2018/10/01/ 2018, doi: https://doi.org/10.1016/j.rser.2018.06.031.

[171] P. K. Basu, A. Khanna, and Z. Hameiri, "The effect of front pyramid heights on the efficiency of homogeneously textured inline-diffused screen-printed monocrystalline silicon wafer solar cells," *Renewable Energy,* vol. 78, pp. 590-598, 2015/06/01/ 2015, doi: https://doi.org/10.1016/j.renene.2015.01.058.

[172] A. Peer, R. Biswas, J.-M. Park, R. Shinar, and J. Shinar, "Light management in perovskite solar cells and organic LEDs with microlens arrays," *Opt. Express,* vol. 25, no. 9, pp. 10704-10709, 2017/05/01 2017, doi: 10.1364/OE.25.010704.

[173] B. Shi *et al.*, "Enhanced light absorption of thin perovskite solar cells using textured substrates," *Solar Energy Materials and Solar Cells,* vol. 168, pp. 214-220, 2017/08/01/ 2017, doi: https://doi.org/10.1016/j.solmat.2017.04.038.

[174] D. I. Kim, S.-H. Nam, K.-H. Hwang, Y.-M. Lee, and J.-H. Boo, "Glass Texturing Affects Optical Properties of Perovskite Solar Cells: Comparison Study between Mesoscopic and Planar Structure," *Chemical Engineering Transactions,* vol. 52, pp. 367-372, 2016, doi: 10.3303/CET1652062.

[175] M. Kambe, N. Taneda, A. Takahashi, and T. Oyama, "Transparent Conductive Oxide Film Coated Glass Substrates for Silicon Based Thin Film Solar Cells," in "Research Reports Asahi Glass Co., Ltd," 621.383.51﷯539.234, 2010, vol. 60. [Online]. Available: https://www.agc.com/innovation/library/pdf/60-02.pdf

[176] M. M. Tavakoli *et al.*, "Highly Efficient Flexible Perovskite Solar Cells with Antireflection and Self-Cleaning Nanostructures," *ACS Nano,* vol. 9, no. 10, pp. 10287-10295, 2015/10/27 2015, doi: 10.1021/acsnano.5b04284.

[177] V. Neder, S. L. Luxembourg, and A. Polman, "Efficient colored silicon solar modules using integrated resonant dielectric nanoscatterers," *Applied Physics Letters,* vol. 111, no. 7, p. 073902, 2017, doi: 10.1063/1.4986796.

[178] Y. Zhang *et al.*, "Improved multicrystalline Si solar cells by light trapping from Al nanoparticle enhanced antireflection coating," *Opt. Mater. Express,* vol. 3, no. 4, pp. 489-495, 2013/04/01 2013, doi: 10.1364/OME.3.000489.

[179] D. P. Anderson *et al.*, "Chemically-synthesised, atomically-precise gold clusters deposited and activated on titania," *Physical Chemistry Chemical Physics,* 10.1039/C3CP44005B vol. 15, no. 11, pp. 3917-3929, 2013, doi: 10.1039/C3CP44005B.

[180] G. Andersson *et al.*, "Phosphine-stabilised Au9 clusters interacting with titania and silica

surfaces: The first evidence for the density of states signature of the support-immobilised cluster," *The Journal of Chemical Physics,* vol. 141, 06/01 2014, doi: 10.1063/1.4884642.

[181] F. Wen, U. Englert, B. Gutrath, and U. Simon, "Crystal Structure, Electrochemical and Optical Properties of [Au9(PPh3)8](NO3)3," *European Journal of Inorganic Chemistry,* vol. 2008, no. 1, pp. 106-111, 2008, doi: 10.1002/ejic.200700534.

[182] A. Amalraj Peter and M. A. Maan, "Fabrication and Replication of Periodic Nanopyramid Structures by Laser Interference Lithography and UV Nanoimprint Lithography for Solar Cells Applications," 2018, doi: 10.5772/intechopen.72534.

[183] R. A. Scheidt and P. V. Kamat, "Temperature-driven anion migration in gradient halide perovskites," *The Journal of Chemical Physics,* vol. 151, no. 13, p. 134703, 2019, doi: 10.1063/1.5120270.

[184] M. S. Jones, "Effects of UV Radiation on Building Materials," Building Research Association of New Zealand (BRANZ), 2002.

[185] "UV levels." Environmental Health Indicators New Zealand. https://www.ehinz.ac.nz/indicators/uv-exposure/daily-uv-levels/ (accessed 2020).

[186] A. Dualeh, N. Tétreault, T. Moehl, P. Gao, M. K. Nazeeruddin, and M. Grätzel, "Effect of Annealing Temperature on Film Morphology of Organic–Inorganic Hybrid Pervoskite Solid-State Solar Cells," *Advanced Functional Materials,* vol. 24, no. 21, pp. 3250-3258, 2014, doi: 10.1002/adfm.201304022.

[187] K. Zhang *et al.*, "A prenucleation strategy for ambient fabrication of perovskite solar cells with high device performance uniformity," *Nature Communications,* vol. 11, no. 1, p. 1006, 2020/02/21 2020, doi: 10.1038/s41467-020-14715-0.

[188] Z. Li *et al.*, "Moisture-Induced Crystallinity Improvement for Efficient CsPbI3–xBrx Perovskite Solar Cells with Excess Cesium Bromide," *The Journal of Physical Chemistry Letters,* vol. 10, no. 16, pp. 4587-4595, 2019/08/15 2019, doi: 10.1021/acs.jpclett.9b01822.

[189] A. K. Jena, A. Kulkarni, and T. Miyasaka, "Halide Perovskite Photovoltaics: Background, Status, and Future Prospects," *Chemical Reviews,* vol. 119, no. 5, pp. 3036-3103, 2019/03/13 2019, doi: 10.1021/acs.chemrev.8b00539.

[190] A. J. Bett *et al.*, "Low temperature perovskite solar cells with an evaporated TiO2 compact layer for perovskite silicon tandem solar cells," *Energy Procedia,* vol. 124, pp. 567-576, 2017/09/01/ 2017, doi: https://doi.org/10.1016/j.egypro.2017.09.293.

[191] R. Kottokkaran, H. A. Gaonkar, B. Bagheri, and V. L. Dalal, "Efficient p-i-n inorganic CsPbI3 perovskite solar cell deposited using layer-by-layer vacuum deposition," *Journal of Vacuum Science & Technology A,* vol. 36, no. 4, p. 041201, 2018, doi: 10.1116/1.5029253.

[192] Q.-Y. Xu, D.-X. Yuan, H.-R. Mu, F. Igbari, Q. Bao, and L.-S. Liao, "Efficiency Enhancement of Perovskite Solar Cells by Pumping Away the Solvent of Precursor Film Before Annealing," *Nanoscale Research Letters,* vol. 11, no. 1, p. 248, 2016/05/12 2016, doi: 10.1186/s11671-016-1467-9.

[193] D. P. McMeekin *et al.*, "A mixed-cation lead mixed-halide perovskite absorber for tandem

solar cells," *Science,* vol. 351, no. 6269, p. 151, 2016, doi: 10.1126/science.aad5845.

[194] T. Zhang *et al.*, "Bication lead iodide 2D perovskite component to stabilize inorganic α-CsPbI₃ perovskite phase for high-efficiency solar cells," *Science Advances,* vol. 3, no. 9, p. e1700841, 2017, doi: 10.1126/sciadv.1700841.

[195] K. Schötz *et al.*, "Double peak emission in lead halide perovskites by self-absorption," *Journal of Materials Chemistry C,* 10.1039/C9TC06251C vol. 8, no. 7, pp. 2289-2300, 2020, doi: 10.1039/C9TC06251C.

[196] M. I. Dar *et al.*, "Origin of unusual bandgap shift and dual emission in organic-inorganic lead halide perovskites," *Science Advances,* vol. 2, no. 10, p. e1601156, 2016, doi: 10.1126/sciadv.1601156.

[197] J.-W. Lee, S.-G. Kim, J.-M. Yang, Y. Yang, and N.-G. Park, "Verification and mitigation of ion migration in perovskite solar cells," *APL Materials,* vol. 7, no. 4, p. 041111, 2019, doi: 10.1063/1.5085643.

[198] J. A. Christians, J. S. Manser, and P. V. Kamat, "Best Practices in Perovskite Solar Cell Efficiency Measurements. Avoiding the Error of Making Bad Cells Look Good," *The Journal of Physical Chemistry Letters,* vol. 6, no. 5, pp. 852-857, 2015/03/05 2015, doi: 10.1021/acs.jpclett.5b00289.

[199] D. A. Egger, E. Edri, D. Cahen, and G. Hodes, "Perovskite Solar Cells: Do We Know What We Do Not Know?," *The Journal of Physical Chemistry Letters,* vol. 6, no. 2, pp. 279-282, 2015/01/15 2015, doi: 10.1021/jz502726b.

[200] T. Zhang *et al.*, "High Speed and Stable Solution-Processed Triple Cation Perovskite Photodetectors," *Advanced Optical Materials,* vol. 6, no. 13, p. 1701341, 2018, doi: 10.1002/adom.201701341.

[201] A. A. Khan, Z. Yu, U. Khan, and L. Dong, "Solution Processed Trilayer Structure for High-Performance Perovskite Photodetector," *Nanoscale Research Letters,* vol. 13, no. 1, p. 399, 2018/12/06 2018, doi: 10.1186/s11671-018-2808-7.

[202] Y. Fu *et al.*, "High performance photomultiplication perovskite photodetectors with PC60BM and NPB as the interlayers," *Organic Electronics,* vol. 51, pp. 200-206, 2017/12/01/ 2017, doi: https://doi.org/10.1016/j.orgel.2017.09.028.

[203] A. Pellaroque *et al.*, "Efficient and Stable Perovskite Solar Cells Using Molybdenum Tris(dithiolene)s as p-Dopants for Spiro-OMeTAD," *ACS Energy Letters,* vol. 2, no. 9, pp. 2044-2050, 2017/09/08 2017, doi: 10.1021/acsenergylett.7b00614.

[204] Q. Wang, "Influence of a cobalt additive in spiro-OMeTAD on charge recombination and carrier density in perovskite solar cells investigated using impedance spectroscopy," *Physical Chemistry Chemical Physics,* 10.1039/C8CP00008E vol. 20, no. 15, pp. 10114-10120, 2018, doi: 10.1039/C8CP00008E.

[205] A. Möllmann *et al.*, "Highly Compact TiO2 Films by Spray Pyrolysis and Application in Perovskite Solar Cells," *Advanced Engineering Materials,* vol. 21, no. 4, p. 1801196, 2019, doi: 10.1002/adem.201801196.

[206] W. Qiu *et al.*, "An electron beam evaporated TiO2 layer for high efficiency planar perovskite solar cells on flexible polyethylene terephthalate substrates," *Journal of Materials Chemistry A,* 10.1039/C5TA07515G vol. 3, no. 45, pp. 22824-22829, 2015, doi: 10.1039/C5TA07515G.

[207] Q. Zhang and C. Li, "Pure Anatase Phase Titanium Dioxide Films Prepared by Mist Chemical Vapor Deposition," (in eng), *Nanomaterials (Basel),* vol. 8, no. 10, p. 827, 2018, doi: 10.3390/nano8100827.

[208] T. Duong *et al.*, "High Efficiency Perovskite-Silicon Tandem Solar Cells: Effect of Surface Coating versus Bulk Incorporation of 2D Perovskite," *Advanced Energy Materials,* vol. 10, no. 9, p. 1903553, 2020, doi: 10.1002/aenm.201903553.

[209] M. A. Green, Y. Hishikawa, E. D. Dunlop, D. H. Levi, J. Hohl-Ebinger, and A. W. Y. Ho-Baillie, "Solar cell efficiency tables (version 51)," *Progress in Photovoltaics: Research and Applications,* vol. 26, no. 1, pp. 3-12, 2018, doi: 10.1002/pip.2978.

[210] H. Degans, "Perovskite/CIGS tandem cell with Record Efficiency of 24.6 percent Paves the Way for Flexible Solar Cells and High-Efficiency Building-Integrated PV," ed: Imec, 2018.